TUL

KOKA 2024

55. MEZINÁRODNÍ VĚDECKÁ KONFERENCE ZAMĚŘENÁ NA VÝZKUMNÉ A VÝUKOVÉ METODY V OBLASTI VOZIDEL A JEJICH POHONŮ

5. – 6. 9. 2024
Liberec

WWW.TUL.CZ

Recenzent: doc. Ing. Lubomír Moc, CSc.

ISBN 978-80-7494-711-7

PŘÍPRAVNÝ A ORGANIZAČNÝ VÝBOR KONFERENCE:

Ing. Robert Voženílek, Ph.D., Technická univerzita v Liberci
Ing. Pavel Brabec, Ph.D., Technická univerzita v Liberci
Ing. Aleš Dittrich, Ph.D., Technická univerzita v Liberci
Ing. Josef Bříoušek, Ph.D., Technická univerzita v Liberci
Ing. Tomáš Petr, Technická univerzita v Liberci
Ing. Radek Procházka, Technická univerzita v Liberci
Jitka Baudyšová, Technická univerzita v Liberci

OBSAH

55. mezinárodní vědecká konference zaměřená na výzkumné a výukové metody v oblasti vozidel a jejich pohonů

září 5. - 6., 2024 – Liberec, Česká republika
Technická univerzita v Liberci
Fakulta strojní, Katedra vozidel a motorů

IMPROVEMENT OF WOSCHNI'S HEAT TRANSFER COEFFICIENT FOR SI ENGINES

Karel Páv [1]

Abstract
This paper deals with investigation on the heat transfer coefficient for SI engines. The accurate determination of the heat losses is required for the computational engine modeling due to its influence on the engine efficiency lowering. Both the Woschni's and Bargende's correlations for the heat transfer coefficient were evaluated on a naturally aspirated three-cylinder SI engine in wide range of engine operational conditions. Significant discrepancies in expected and calculated heat transfer were found at low and high engine speeds for both correlations, and at low engine loads for the Woschni's correlation. The expected heat transfer within the high-pressure period of the cycle was calculated by means of the thermodynamic analysis of the measured in-cylinder pressure. The evaluation was based on comparison of the calculated heat, released from the combustion during the working cycle, with the heat energy contained in the fuel. Since the Woschni's correlation is relatively simple and allows making its correction in a feasible way, this correlation was chosen for the improvement consisting in adjustment of the combustion effect on turbulence intensity. Finally, the improved Woschni's correlation was proposed and verified with acceptable results.

[1] Doc. Ing. Karel Páv, Ph.D., Technická univerzita v Liberci, Katedra vozidel a motorů, Studentská 2, Liberec 461 17, Czech Republic, karel.pav@tul.cz

1. INTRODUCTION

A modeling of the combustion process in an internal combustion engine is widely used practice during initial phase of engine development as well as during further engine optimization. Besides the air charge amount calculation, the most important part of the engine modeling is the combustion process producing indicated work. Therefore, its mathematical description should be as accurate as possible. The combustion process itself can be modeled by using state of art combustion adaptive models [2, 5, 12] with very good approximation to measurement, but the heat transfer from the cylinder charge to combustion chamber walls is doubtful. Since the heat losses decrease producing indicated work, their accurate determination is demanded.

2. CORRELATIONS FOR HEAT TRANSFER COEFFICIENT

For the calculation of the cylinder wall heat transfer on the gas side in the combustion chamber is commonly used Newton's law although this assumption is not fully valid for non-steady heat transfer [3]

$$\frac{dQ_w}{dt} = -\alpha \cdot A \cdot (T - T_w) \tag{1}$$

where α is the heat transfer coefficient, A is the corresponding surface area, T is the mean cylinder bulk gas temperature and T_w is the wall temperature which is usually assumed constant throughout the engine working cycle but different for several combustion chamber areas. When the combustion chamber is split into five areas following substitution is used

$$\begin{aligned} A \cdot (T - T_w) = A_{head} \cdot (T - T_{head}) + A_{in.valve} \cdot (T - T_{in.valve}) + A_{ex.valve} \cdot (T - T_{ex.valve}) + \\ + A_{cyl} \cdot (T - T_{cyl}) + A_{piston} \cdot (T - T_{piston}) \end{aligned} \tag{2}$$

Several recommended semi-empirical correlations for the heat transfer coefficient α assuming spatially averaged combustion chamber heat flux are widely used [4, 5, 6, 10, 11, 18]. The most widespread approximations used for modeling of spark ignition (SI) combustion engine are Woschni's and Bargende's correlations.

2.1 Woschni's correlation

The Woschni's correlation was originally intended for compression ignition (CI) engines where the heat flux to the wall is besides a convection transfer accompanied by substantial radiation. Afterwards in 1981, the correlation was modified and extended in order to be applicable for SI engines as well [11, 19]

$$\alpha = 130 \cdot D^{-0.2} \cdot p^{0.8} \cdot T^{-0.53} \cdot w^{0.8} \qquad [\mathrm{Wm^{-2}K}, \mathrm{m}, \mathrm{bar}, \mathrm{K}, \mathrm{ms^{-1}}] \tag{3}$$

where D is the cylinder bore, p is the cylinder pressure, T is the mass averaged cylinder gas temperature and w is the velocity term varying for different periods of the cycle. This velocity term, interpreted as the average cylinder gas velocity, is expressed as

$$w = C_1 \cdot \overline{S}_p + C_2 \cdot \frac{V_d \cdot T_r}{p_r \cdot V_r} \cdot (p - p_m) \qquad [\mathrm{ms^{-1}}, 1, \mathrm{ms^{-1}}, \mathrm{ms^{-1}K^{-1}}, \mathrm{m^3}, \mathrm{K}, \mathrm{bar}] \tag{4}$$

where $\overline{S}_p$ is the mean piston speed, V_d is the cylinder displaced volume, p_r, T_r, V_r are

the gas pressure, temperature, and volume at some reference state, usually inlet valve closing or start of combustion, and p_m is the motored cylinder instantaneous gas pressure at the same crank angle as the gas pressure p. The first term reflects the cylinder charge motion which is proportional to the mean piston speed while the second term involves the effect of the combustion process leading to increasing of the turbulence intensity. The contribution of these terms is given by constants C_1 and C_2 respectively. For CI engines as well as for SI engines without swirl were determined following constants:

$$\begin{aligned} &C_1 = 6.18\,, \quad C_2 = 0\ \mathrm{m s^{-1} K^{-1}} && \text{for the gas exchange period} \\ &C_1 = 2.28\,, \quad C_2 = 0\ \mathrm{m s^{-1} K^{-1}} && \text{for the compression period} \\ &C_1 = 2.28\,, \quad C_2 = 3.24 \cdot 10^{-3}\ \mathrm{m s^{-1} K^{-1}} && \text{for the combustion and expansion period} \end{aligned} \tag{5}$$

Some works [8, 9, 17] show that the Woschni's correlation provides too low values for cases when the engine is dragged, or the engine load is low. For this reason, some modifications of the second term in equation (4) are proposed.

2.2 Bargende's correlation

In 1991 Bargende published improved correlation for the heat transfer coefficient [1]. This correlation is intended for SI engines for high pressure period of the engine cycle. Like the Woschni's correlation, it is based on dimensionless numbers (Nusselt, Reynolds, Prandtl) but there are improvements considering some additional influencing factors.

$$\alpha = 253.5 \cdot V^{-0.073} \cdot p^{0.78} \cdot \overline{T}^{-0.477} \cdot w^{0.78} \cdot \Delta \qquad [\mathrm{W m^{-2} K},\ \mathrm{m^3},\ \mathrm{bar},\ \mathrm{K},\ \mathrm{m s^{-1}}] \tag{6}$$

The characteristic diameter D in equation (3) is here substituted by the instantaneous cylinder volume V which represents the characteristic sphere diameter. The influence of the cylinder pressure p remains nearly unchanged but the relevant gas temperature at which the gas properties in boundary layer are evaluated is given by arithmetical average of the mean cylinder bulk gas temperature T and the overall averaged wall temperature $\overline{T}_w$

$$\overline{T} = \frac{T + \overline{T}_w}{2} \tag{7}$$

Instead of the mean piston speed, the instantaneous piston speed S_p and the average turbulent kinetic energy $\overline{k}$ is embedded in the velocity term w [4]

$$w = \frac{1}{2} \cdot \sqrt{\frac{8}{3} \cdot \overline{k} + S_p^2} \tag{8}$$

The turbulent kinetic energy is provided by a simple global $\overline{k} - \varepsilon$ turbulence model [1]. For the engine with flat piston design without squish effect the time derivative of the turbulent kinetic energy is given by

$$\frac{d\overline{k}}{dt} = -\frac{2}{3} \cdot \frac{\overline{k}}{V} \cdot \frac{dV}{dt} - 2.184 \cdot \overline{k}^{1.5} \cdot \left(\frac{6}{\pi} \cdot V \right)^{-\frac{1}{3}} \tag{9}$$

whereas the initial turbulent kinetic energy $\overline{k}$ at inlet valve closing is estimated from average inlet valve seat velocity [10]

$$\bar{k}_{ivc} = \frac{1}{32} \cdot \left(\frac{\bar{S}_p \cdot D^2 \cdot \eta_{ch}}{n_{iv} \cdot D_{iv} \cdot h_{iv} \cdot \sin 45°} \right)^2 \tag{10}$$

where n_{iv}, D_{iv}, h_{iv} are the number of inlet valves, valve diameter, and maximum inlet valve lift respectively. The engine overall charging efficiency η_{ch} is related to inlet manifold conditions. The last term Δ in equation (6) reflects the combustion effect on the heat transfer which considers splitting the combustion chamber into burned and unburned zone

$$\Delta = (A + B)^2 \tag{11}$$

$$A = x_b \cdot \frac{T_b}{T} \cdot \frac{T_b - \bar{T}_w}{T - \bar{T}_w} \tag{12}$$

$$B = (1 - x_b) \cdot \frac{T_u}{T} \cdot \frac{T_u - \bar{T}_w}{T - \bar{T}_w} \tag{13}$$

The combustion term Δ comprises two sub-terms A and B considering mass averaged gas temperature of burned zone T_b and unburned zone T_u at given burned mass fraction x_b, and its related heat transfer areas approximated by $x_b \cdot T_b/T$ and $(1-x_b) \cdot T_u/T$ ratios respectively. The squaring of $(A+B)$ term is given empirically to get the best agreement with numerous experiments [1]. For the calculation of the gas temperature in burned zone is proposed relation

$$T_b = \frac{T + (x_b - 1) \cdot T_u}{x_b} \tag{14}$$

whereas the gas temperature of unburned zone T_u is calculated from the polytropic (close to adiabatic) compression.

For the final heat transfer calculation according to equations (1) and (2) Hohenberg [7], Bargende [1] and Lejsek [10] suggest enlarging the surface area by the quarter of the crevice area over the first piston ring. Thus, both the cylinder liner and the piston area in equation (2) are enlarged accordingly.

3. EVALUATION PROCEDURE

The goal of the investigation is the heat transfer coefficient verification and its appropriate correction. A direct measurement of the heat flux to the combustion chamber walls is very difficult and time demanding task with some non-explicit results [3, 10]. A simple comparison of the measured and calculated total heat flux to the coolant is also unreliable because of the measurement error which exceeds required accuracy [16]. Hence, the most favourable solution seems to be utilisation of the indirect approach for the heat transfer correction. The principle is based on comparison of the calculated heat, released from the combustion during the working cycle, with the heat energy contained in the fuel. The heat Q_b released from the burned air-fuel mixture is calculated from the energy balance conservation

$$\frac{dQ_b}{dt} = \frac{dU}{dt} + p \cdot \frac{dV}{dt} - \frac{dQ_w}{dt} - \sum_i \dot{m}_i \cdot h_i \tag{15}$$

where U is the internal energy of the cylinder charge, and $\dot{m}_i$ is the gas mass flow entering (positive) or leaving (negative) the cylinder with its stagnation specific

enthalpy h_i. The used 0-D calculation tool for the cylinder pressure analysis [15] considers semi-2-zone model which splits the cylinder charge into two zones with different thermodynamic properties, but the gas temperature used for general calculation is the same for both zones. However, the calculation of the instantaneous combustion efficiency which is due to dissociation processes strongly temperature dependent takes into account the mass averaged temperature in burned zone. On the other hand, the calculation of blow-by gas mass flow and its composition which is primarily formed by unburned air-fuel mixture [13] considers the mass averaged temperature in unburned zone until the combustion is finished. For the correct thermodynamic analysis of the measured in-cylinder pressure according to equation (15) is necessary to determine the residual gas mass fraction in the cylinder and relevant wall temperatures used for the heat transfer calculation according to equations (1)-(5). These quantities were calculated by means of the same calculation tool [15], but in this case the modeling section for the simulation of entire working cycle including gas exchange period was used. In fact, both sections of this calculation tool communicate between each other in an iterative manner, but only the calculated residual gas mass fraction and combustion chamber wall temperatures were handed over from the simulation section to the analysis section. Since the piezoelectric pressure sensors were used for the in-cylinder pressure measurement, the pressure offset had to be adjusted in order to provide the best coincidence of the modeled and measured gas pressure within the gas exchange and compression period. The procedure of the Woschni's heat transfer coefficient correction is demonstrated on an example in *Figure 1*. The achievable heat energy from the air-fuel mixture is given by the fuel mass in cylinder at inlet valve closing $m_{f\text{-}ivc}$ lowered by escaping fuel mass from the cylinder in blow-by gas $m_{f\text{-}bb}$. The fuel lower heating value Q_{LHV} is deteriorated by the overall combustion efficiency η_c considering incomplete combustion due to dissociation processes and flame quenching. If the calculated released heat Q_b does not reach the target value, the heat transfer Q_w is not determined properly. The most favorable tuning parameter for the heat transfer coefficient is the constant C_2 in equation (4) which quantifies the combustion effect on turbulence intensity. Thus, the constant C_2 is adjusted in order to match the heat released from the burned air-fuel mixture Q_b with the target value. The heat transfer coefficient is then changed accordingly as can be seen in *Figure 1*.

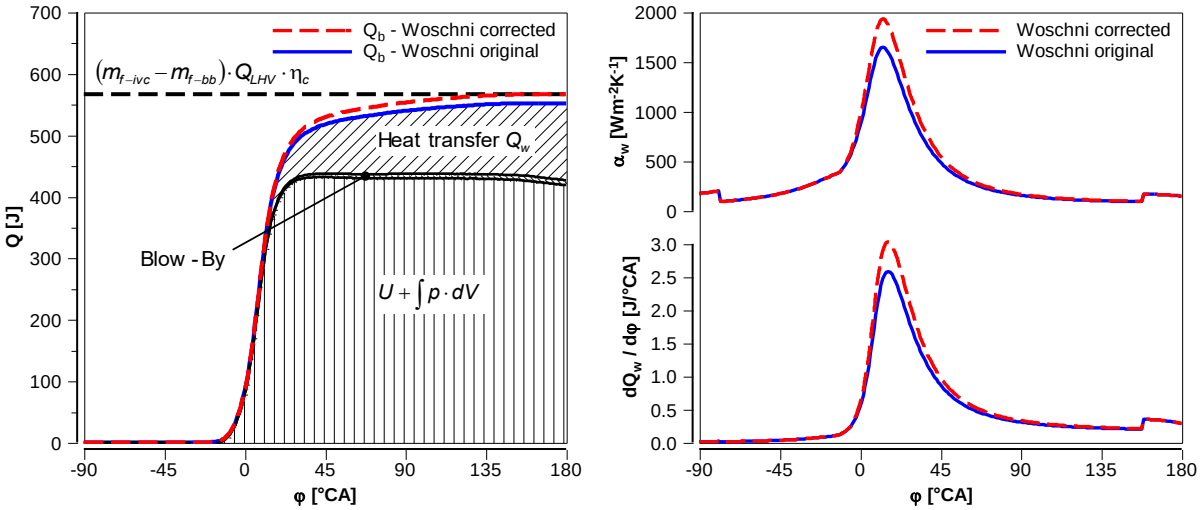

Figure 1: *Correction of Woschni's heat transfer coefficient by adjustment of the constant C_2 in equation (4).*

This tailoring procedure is carried out for more engine operational points in order to cover all possible cases from the statistical point of view. Afterwards, when the corrected traces of the heat transfer coefficient are known for all selected engine operational points, the corrected instantaneous heat transfer according to equations (1) and (2) is recalculated to $dQ_w/d\varphi$. Finally, the entire batch of corrected heat transfer traces $dQ_w/d\varphi$ then undergoes the calculation procedure where a new general expression of the constant C_2 in equation (4) is tried to find. For solving this problem, the gradient method minimizing the mean square error value was used.

3.1 Engine description

As a subject of investigation, the naturally aspirated engine has been chosen. The main reason for choosing a non-turbocharged engine is the simple engine modeling and subsequent verification. Basic parameters of used three-cylinder gasoline engine with port fuel injection and variable valve timing with late inlet valve closing strategy are stated in *Table 1*.

Number of cylinders	3	Fuel	Gasoline
Number of valves	2 + 2	Eq. formula	$C_{6.86}\ H_{12.66}\ O_{0.148}$
Bore	74.5 mm	RON	96.2
Stroke	76.4 mm	LHV	41.63 MJ/kg
Compression ratio	11.68	Air-fuel mixture	$\lambda = 1$

Table 1: *Engine parameters.*

The combustion chamber is split into five areas with different surface temperatures calculated by means of simplified heat transfer model incorporating main engine parts. The individual surface areas are shown in *Figure 2*, whereas the quarter of the crevice area over the first piston ring is not included for the Woschni's correlation compared to the Bargende's correlation.

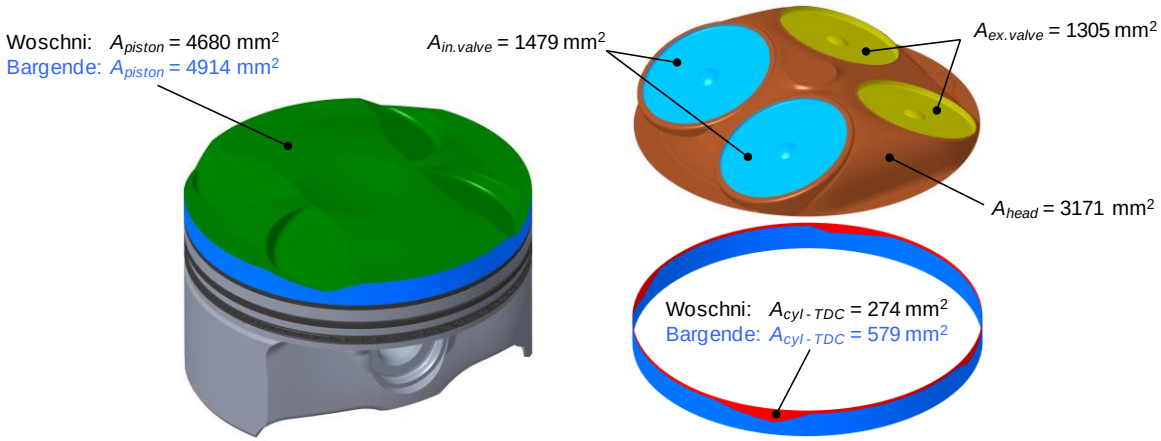

Figure 2: *Relevant combustion chamber surface areas.*

The engine was equipped with the couple of pressure sensors at each cylinder for the gas pressure indicating. Spark plugs KISTLER 6115BFD65 with integrated piezoelectric pressure sensors and water-cooled piezoelectric pressure sensors AVL QC34D were used at the same time. This configuration allowed the check of the measured cylinder pressure focused on the temperature drift and vibration intrusion during the measurement. Finally, the water-cooled AVL sensor at first cylinder was

chosen for the analysis. The measured fuel mass flow, as a one of the main inputs for the analysis, was supposed to be evenly distributed among cylinders. The capacitive TDC sensor KISTLER 2629C and crack angle encoder AVL 365C was used for dynamic piston top dead center determination.

3.1 Model calibration

The engine cycle was modeled in 0-D calculation tool [15] with appropriate combustion chamber geometry, mechanical friction and measured inlet and exhaust valve discharge coefficients with actual variable valve timing. The exhaust manifold backpressure was emulated by equivalent volume and orifice. The combustion process was approximated by the adaptive combustion model [14] calibrated in accordance with the measurement. A special attention was paid to determination of the combustion chamber wall temperatures. This issue was solved by simplified heat transfer model incorporating parts shown in *Figure 2*. The heat transfer among these parts and to coolant was tuned by several heat transfer factors in order to reach the real wall temperatures according to the measurement. The target average wall temperatures of the representative parts of the combustion chamber for selected engine operational points used for model calibration are shown in *Figure 3*. Significant change in piston crown temperature at engine speed transition from 3000 1/min to 4000 1/min is caused by activation of oil jets for the piston cooling. As the calculated wall temperature depends on the wall heat flux given by the heat transfer coefficient and the wall temperature itself, the model calibration was done iteratively, and of course, separately for the applied specific heat transfer coefficient (i.e., Woschni original, Woschni improved, Bargende).

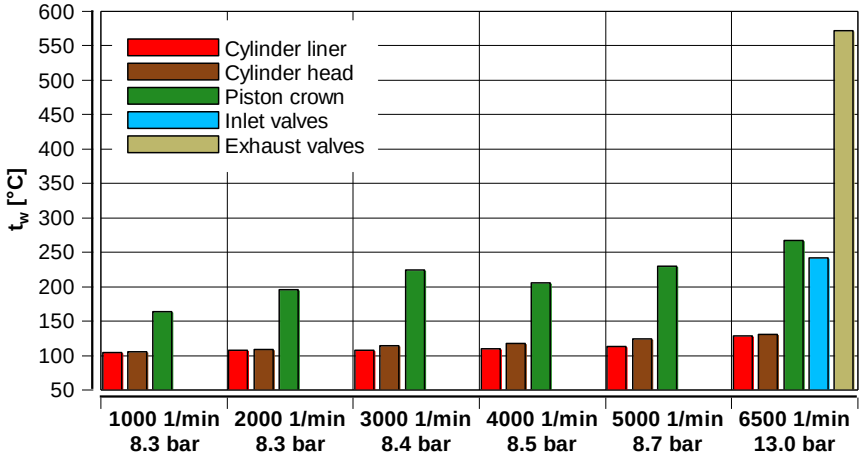

Figure 3: *Average wall temperatures of representative parts of the combustion chamber at different engine speed and IMEP used for model calibration.*

3.2 Improvement of Woschni's correlation

The complex assessment of the applied heat transfer coefficient is possible only when the statistically enough engine operational points are considered. The uniform scatter of points in the engine map is also recommended. The heat transfer analysis was carried out for engine operational points at different engine speed and load with focus to cover the engine map in as large as possible range – see *Figure 4*. The engine full load measurements were abandoned due to the engine tendency to knock

since the ignition angle has been changed intentionally in each point to consider different combustion timing as well. Finally, the analysis was made for 75 points in total: 25 engine load points with three different combustion timings (advanced, normal, and retarded combustion). As the modification of the heat transfer coefficient is related to the combustion and expansion period solely, the relevant crank angle range is given by the inlet and exhaust valve timing. The crank angles at inlet valve closing and exhaust valve opening are shown in *Figure 4*.

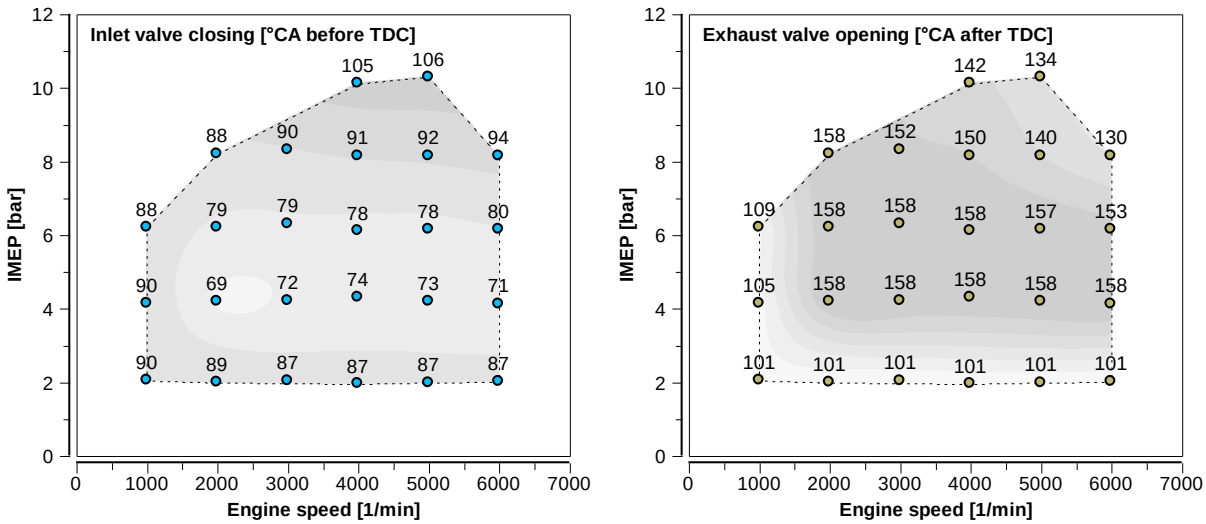

Figure 4: *Engine operational points and applied valve timing used for the verification / modification of the heat transfer coefficient.*

At each operational point, the averaged cylinder pressure trace from approximately 30 cycles was used for the heat transfer analysis. The only cycles with low scatter in combustion timing were selected from the batch for the averaging. The advanced, normal, and retarded combustion is characterized by the crank angle at 50% of mass fraction burned (MFB50%). The intermediate results in terms of required change of the constant C_2 in equations (4) and (5) are shown in *Figure 5*. The trend of the correction factor adjusting the constant C_2 is obvious. Generally, the factor increases with engine speed, and besides that much more at very low engine load.

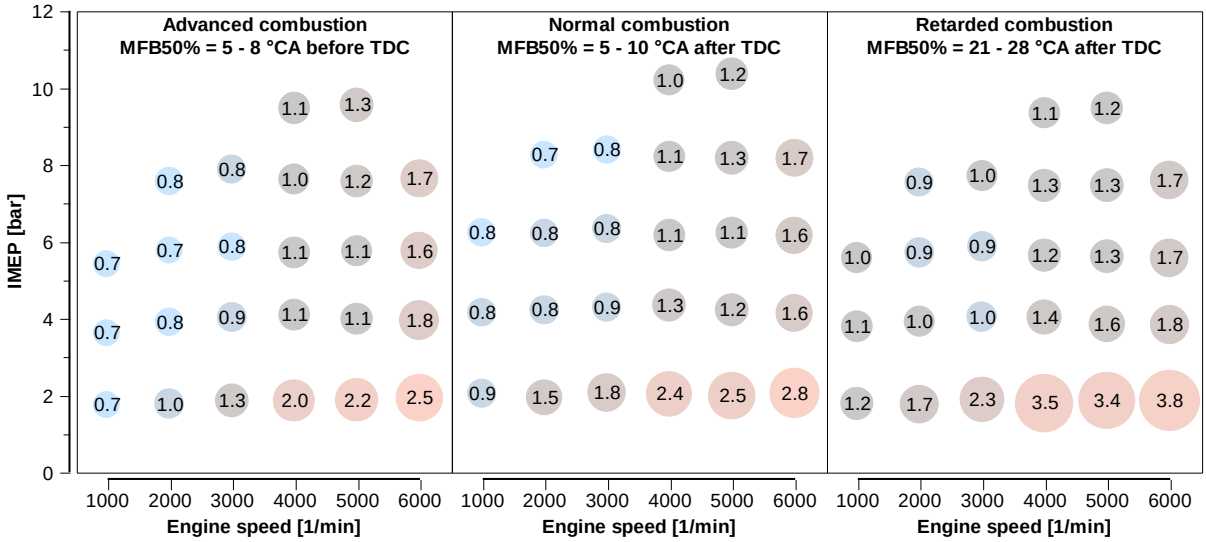

Figure 5: *Required correction factors for the constant C_2 in equations (4) and (5).*

The main goal of this investigation is to improve the current Woschni's correlation for the heat transfer coefficient in a reasonable way. After the collection of all corrected heat transfer traces $dQ_w/d\varphi$ for all 75 points, the new expression for C_2 has been found by means of the gradient method minimizing the mean square error comparing the corrected and the calculated heat transfer traces. The recommended expression for C_2 in equations (4) and (5) for the combustion and expansion period is

$$C_2 = 4.8 \cdot 10^{-3} \cdot p^{-0.3} \cdot \left(\frac{V_c}{V}\right)^{0.2} \left(1 + 0.14 \cdot \overline{S}_p\right) \qquad [\mathrm{ms^{-1}K^{-1}}, \mathrm{bar}, \mathrm{m^3}, \mathrm{ms^{-1}}] \qquad (16)$$

where p is the instantaneous cylinder pressure, V_c is the compression volume, V is the instantaneous cylinder volume, and $\overline{S}_p$ is the mean piston speed. The presented structure of the formula for C_2 has been chosen as a trade-off between accuracy and real applicability for an extrapolation out of the verified range. The embodied cylinder pressure rectifies the original scheme ($p - p_m$) in equation (4), the required effect of the mean piston speed is obvious from *Figure 5*, while the ratio V_c/V suppresses the combustion influence on the turbulence intensification in later expansion period.

4. VALIDATION

The comprehensive check of the proposed formula for C_2 in equation (16) consists of two parts. The first part compares the calculated total wall heat transfer within the high-pressure period with a target value for all engine operational points used for the analysis. The target value is calculated from equations (1)-(5), whereas the constant C_2 in equation (5) is multiplied by the correction factor from *Figure 5*. The new proposal for the calculation of C_2 according to equation (16) improves the calculated wall heat transfer mainly at low and high engine speed compared to the original Woschni's correlation. Despite the overall improvement there are still certain margins at very low engine load as can be seen in *Figure 6*. It could be reduced even more by using more complex formula for C_2 but the trade-off representation has been chosen for its simplicity and robustness.

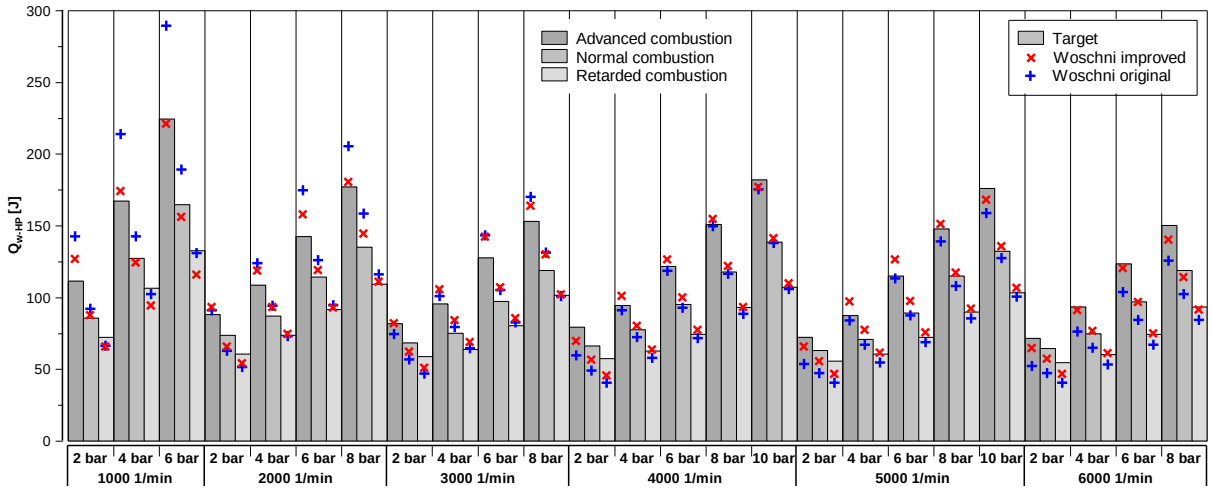

Figure 6: *Comparison of the wall heat transfer within the high-pressure period for the original and improved Woschni's correlation with the target value from the thermodynamic analysis, the single points are specified by engine speed and round IMEP.*

The second part of the validation is more complex. The indicated mean effective pressure (IMEP) from the measurement is compared with the calculated one from the models with different correlations for the heat transfer coefficient. The most important input value for the calculation is the fuel mass in the cylinder which was assumed in accordance with the measurement. The combustion process was modeled with respect to its timing dependence using the calibrated adaptive combustion model [12]. The most effective way for the comprehensive validation within a wide range of engine operational conditions is doing a transient measurement during which the engine speed and the inlet manifold pressure are fixed while the ignition angle solely is continuously changing. As the naturally aspirated engine is investigated the almost constant inlet manifold pressure can be simply ensured by setting of the throttle flap to a locked position. However, the ignition timing transition is accompanied by small changes in the engine charging efficiency, but it can be easily compensated in the calculation model. During the transient change of the ignition angle which lasted from 20 to 40 seconds depending on the engine speed (the lower engine speed the longer time) the in-cylinder pressure was recorded and subsequently evaluated in order to calculate the single cycle IMEP and the crank angle at MFB50% according to simplified approach

$$MFB = \frac{C}{n-1} \cdot \int_{\varphi_{ign}}^{\varphi} \left(n \cdot p \cdot dV + V \cdot dp \right) \tag{17}$$

where *MFB* is the instantaneous mass fraction burned over the crank angle φ, and *C* is the constant fulfilling the condition max(*MFB*) = 1. The integration starts at the crank angle of spark ignition and ends at the exhaust valve opening crank angle. The choice of the polytropic exponent for $n = 1.29$ provides sufficient matching with the exact calculation procedure assuming the real gas properties, heat transfer, and blow-by gas losses as well. After determination of the constant *C* the crank angle at MFB50% can be found for $MFB = 0.5$. This simplified approach was used for both measured and calculated pressure traces to get fully comparable results. The comparison of the measured and calculated IMEP as a function of the crank angle at MFB50% for all investigated engine operational points is shown in *Figure 7*. Besides the original and improved Woschni's correlation for the heat transfer coefficient there are also calculation results from the model using the Bargende's correlation. In order to get comparable results, the Bargende's correlation was used for the compression, combustion, and expansion period only. The Woschni's correlation was used during the gas exchange period in all cases.

The comparison of calculation results in *Figure 7* confirms the previously presented figures from the first validation part. The most significant discrepancies in the measured and calculated IMEP with the original Woschni's correlation for the heat transfer coefficient are at low and high engine speeds. The utilization of the improved Woschni's correlation brings closer matching with the experiment especially at the engine speed 1000 1/min, where the improvement is quite obvious. Despite the overall positive effect of the improved Woschni's correlation, there is still too low wall heat transfer calculated for the engine loads at IMEP = 2 bar. The shape of the IMEP curve is also very important for the suitability assessment of the heat transfer coefficient. With both the original Woschni's correlation and Bargende's correlation the optimum crank angle at MFB50% at which the maximum IMEP is reached does not match the experiment at low engine speeds in contrast to improved Woschni's correlation.

The carried-out validation confirmed the benefits of the proposed improved Woschni's correlation. The substitution of the fixed constant C_2 by the expression in equation (16) giving variable figures for C_2 is a feasible way for the more accurate heat transfer calculation.

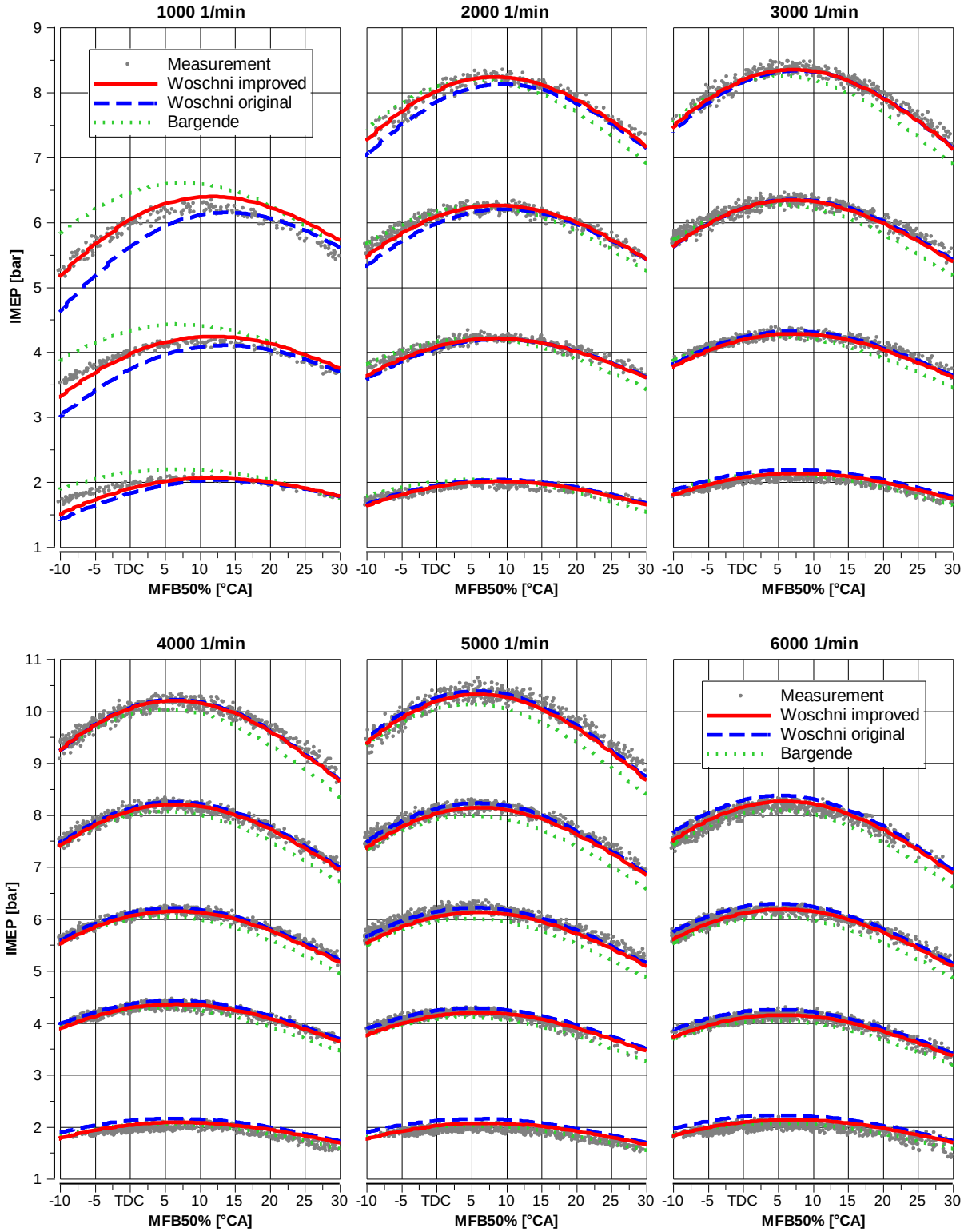

Figure 7: *IMEP as a function of the crank angle at MFB50% for all investigated engine operational points, results from the measurement and from the calculation models with different heat transfer coefficients.*

5. CONCLUSION

The investigation proved that neither the Woschni's correlation nor Bargende's correlation for the heat transfer coefficient on the gas side in the combustion chamber is not generally valid for all engine operational conditions. The most significant discrepancies were found at very low engine speed. Therefore, the prediction of the indicated mean effective pressure by contemporary calculation models is deteriorated, and the computational optimization of the combustion timing is limited as well. Compared to the Woschni's correlation, the Bargende's correlation gives higher magnitudes of the wall heat transfer at higher engine speeds which leads to decreasing of the calculated indicated mean effective pressure. This phenomenon is especially significant when the combustion is retarded. The Woschni's correlation is commonly respected and widely used for its transparency. The explicitness of that correlation allows making its correction in a relatively simple way. The new expression for the constant C_2 affecting the combustion influence on the turbulence intensity was proposed and verified with acceptable results. However, there are still some margins to be eliminated mainly at very low engine load. The proposed form of the improved Woschni's correlation comes from the experiments on the naturally aspirated SI engine, so it should be yet validated on a supercharged SI engine, where the higher indicated mean effective pressure is achievable.

REFERENCES

[1] BARGENDE, M.: Ein Gleichungsansatz zur Berechnung der instationären Wandwärmeverluste im Hochdruckteil von Ottomotoren, Dissertation Thesis, TH Darmstadt, 1991

[2] BERETTA, G. P., RASHIDI, M., KECK, J. C.: Turbulent Flame Propagation and Combustion in Spark Ignition Engines, Combustion and Flame, pp. 217 - 245, Elsevier, 1983

[3] CARUANA, C.: Incylinder Heat Transfer and Friction Analysis in Pressurised Motored Compression Ignition Engine, Dissertation Thesis, University of Malta, 2020

[4] CHIODI, M., BARGENDE, M.: Improvement of Engine-Heat Transfer Calculation in the Three-Dimensional Simulation Using a Phenomenological Heat-Transfer Model, SAE 2001-01-3601, 2001

[5] GT-Suite: Engine Performance Application Manual, Version 2021, Gamma Technologies, 2021

[6] HEYWOOD, J. B.: Internal Combustion Engines Fundamentals, McGraw-Hill, ISBN 0-07-028637-X,1988

[7] HOHENBERG, G.: Experimentelle Erfassung der Wandwärme von Kolbenmotoren, Habilitation Thesis, TU Graz, 1980

[8] HUBER, K.: Der Wärmeübergang schnellaufender, direkt einspritzender Dieselmotoren, Dissertation Thesis, TU München ,1990

[9] HUBER, K., WOSCHNI, G., ZEILINGER, K.: Investigations on Heat Transfer in Internal Combustion Engines under Low Load and Motoring Conditions, SAE Paper 905018, 1991

[10] LEJSEK, D.: Berechnung des instationären Wandwärmeübergangs im Hochlauf von Ottomotoren mit Benzin-Direkteinspritzung, Dissertation Thesis, Technical University of Darmstadt, 2009

[11] MERKER, G. P., TEICHMANN, R.: Grundlagen Verbrennungsmotoren, Springer Vieweg, 2014

[12] PÁV, K.: Adaptive Combustion Model for SI Engines, XLVII. International Scientific Conference of Czech and Slovak University Departments and Institutions Dealing with the Research of Combustion Engines, pp. 149-156, Brno, ISBN 978-80-214-5379-1, 2016

[13] PÁV, K.: Blowby Gas Composition in SI Engines, MECCA – Journal of Middle European Construction and Design of Cars, Vol. 8, No. 3, pp. 1-7, Praha, ISSN 1214-0821, 2015

[14] PÁV, K.: Implication of cycle-to-cycle variability in SI engines, MECCA – Journal of Middle European Construction and Design of Cars, Vol. 16, No. 1, pp. 10 - 17, Praha, ISSN 1214-0821, 2018

[15] PÁV K.: Simulace pracovního oběhu 4T, Calculation software – Microsoft Excel, 2017-2024

[16] PÁV, K., RYCHTÁŘ, V., VOREL, V.: Heat Balance of Contemporary Automotive Engines, MECCA – Journal of Middle European Construction and Design of Cars, Vol. 10, No. 2, pp. 6-13, Praha, ISSN 1214-0821, 2012

[17] VOGEL, CH.: Einfluss von Wandablagerungen auf den Wärmeübergang im Verbrennungsmotor, Dissertation Thesis, TU München, 1995

[18] TWARDOWSKI, T.: Abgasturboaufladung eines 3-Zylinder Ottomotors – Evaluierung der Leistungssteigerung und Bestimmung von Wandwärmeverlusten, Projektarbeit, TU Bergakademie Freiberg, 2002

[19] WOSCHNI, G., FIEGER, J.: Experimentelle Bestimmung des örtlich gemittelten Wärmeübergangskoeffizienten im Ottomotor, MTZ 42/6, pp. 229-234, 1981

55. mezinárodní vědecká konference zaměřená na výzkumné a výukové metody v oblasti vozidel a jejich pohonů

září 5. - 6., 2024 – Liberec, Česká republika
Technická univerzita v Liberci
Fakulta strojní, Katedra vozidel a motorů

MANUFACTURING TECHNOLOGY OF ROOTS BLOWERS DESIGNED FOT SUPERCHARGING TXO-STROKE ENGINES

Marek Žák [1], Martin Tobiáš [2]

Abstract
This paper presents the second generation of a prototype supercharger for a two-stroke engine. The design is based on a modified solution of the Roots blower, featuring a compressor with two four-lobe rotors. The article outlines design changes resulting from the modified requirements of the combustion engine and the optimization of the production technology, which significantly affects the resulting parameters.

1. INTRODUCTION

[1] Ing. Marek Žák, Ph.D., Mendel University in Brno, Faculty od AgriSciences, Department of Technology and Automobile Transport, Zemědělská 1, 613 00 Brno, Czech Republic, marek.zak@mendelu.cz
[2] Ing. Martin Tobiáš, Mendel University in Brno, Faculty od AgriSciences, Department of Technology and Automobile Transport, Zemědělská 1, 613 00 Brno, Czech Republic, martin.tobias@mendelu.cz

In 2021, at the 52nd KOKA conference, the authors Žák and Čupera presented a design solution for a two-stroke internal combustion engine with a timing system that used a rotating disc [1]. In 2022, at the 53rd KOKA conference, the same authors, along with Stanislav Mitáš, followed up with a paper on the design of a mechanical blower for this engine [2]. As the powertrain specification expanded from a 598cc inline-twin to a 1195cc four-cylinder engine, the original supercharger with its displacement of 583 ccm/rev became inadequate. The second generation was not only dimensionally modified according to the requirements of the drive unit, but there was also an effort to optimize the production technology based on the knowledge gained from the operation of the GEN1 compressor, both from the perspective of the required parameters and production costs. Small series production is always expensive, and in the case of mechanical blower rotors with their specific shape and precision requirements, this is doubly true. Nevertheless, thanks to modern technologies, it is possible to find very interesting solutions with acceptable costs, which can also offer solutions that would otherwise be difficult to implement. For example, precision casting technology can currently become an interesting alternative for small-series and prototype production, which is normally realized by multi-axis machining.

2. BODY OF PAPER

The engine for which the compressor is intended is, with its light, compact solution and high specific power, intended primarily for use in aviation applications, therefore weight is one of the crucial parameters.

2.1 Changing compressor parameters

The demand for a significant increase in the supplied amount of air can be achieved in many ways. Due to set priorities such as the uniformity of the supplied pressure, compact dimensions regarding the installation, and weight, our options were quite limited. Considering the uniformity of the charge air pressure, the number of lobes was not reduced, which would have led to an increase in volumetric efficiency, but the dimensions of the rotors were changed. The design of the rotors, therefore, remained the same as for Gen1, i.e., four lobes (Figure 1), but the increase in diameter required a small optimization of the surfaces and a reduction of the maximum revolutions.The demand for a drastic increase in the supplied amount of air can be achieved in many ways. Due to the set priorities such as the uniformity of the supplied pressure, compact dimensions with regard to the installation and weight, our options were quite limited.
With regard to the uniformity of the charge air pressure, the number of lobes was not reduced, which would lead to an increase in volumetric efficiency, but the dimensions of the rotors were changed. The design of the rotors therefore remained the same as for Gen1, i.e. 4 lobes (figure 1), but the increase in diameter still required a small optimization of the surfaces and a reduction of the maximum revolutions. Of course, this reduction had to be taken into account.

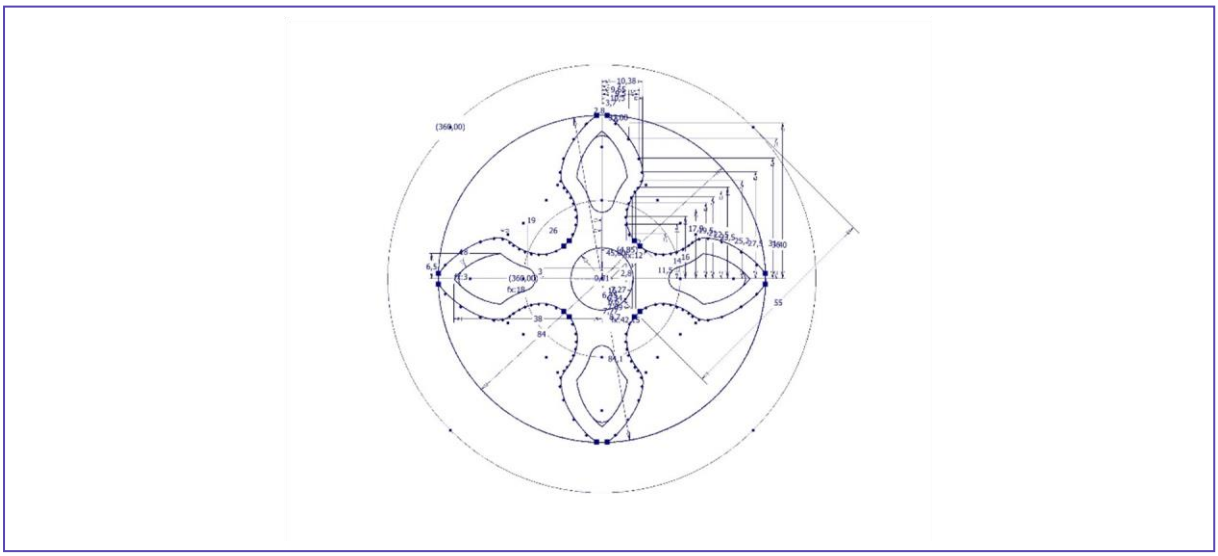

Figure 1: *For lobe rotor profile*

The resulting transported volume increased from 583 to 930 ccm/rev. The optimization of the dimensions was carried out considering the installation space of the drive unit, increasing both the diameter of the rotors (from 75 to 84 mm) and their length (from 120 to 150 mm). The tilt of the rotors remained at 0.4 °/mm.
As this is a prototype/small batch production of components, the rotors for Gen1 were produced by CNC machining. The rotors are made of high-strength aluminium alloy EN-AW 7075, chosen for its weight and the assumption of reaching up to 24.000 revolutions per minute (rpm), aiming to reduce the moment of inertia. The rotors were pressed onto shafts made of 15142 steel. Such a rotor was then mounted in the rotor carrier on one side by means of a 7204 high-speed bearing with angular contact and on the other side by means of a needle bearing NK 17/16 in the intake cover. To avoid the need for expensive heat treatment and grinding of the shaft, the inner race for the needle bearing was provided by pressing the bearing ring IR 14x17x17.
For the second generation (Gen2), using the same rotor production technology would result in a 51% weight increase and an 87.5% increase in the moment of inertia, which was unacceptable. Simulations showed that hollow rotor lobes would significantly reduce the increase in weight and moment of inertia. This design solution is used on Roots blowers with two- and three-lobe rotors of larger dimensions, where the rotors are straight or with a small tilt, and the relief is usually made by drilling (see Figure 2).

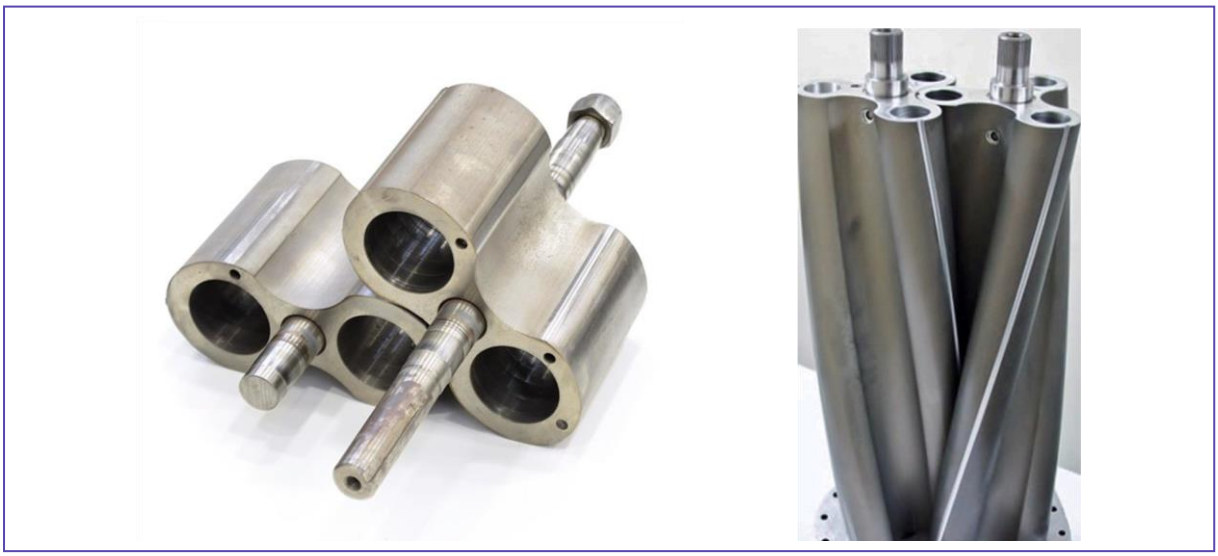

Figure 2: *Lightweight rotors*

Given the dimensional parameters of the rotors, drilling would be complicated and would not bring the significant improvement expected. The designed shape of the relief, seen in Figure 1, could be achieved with additive manufacturing (3D metal printing), but it remains very expensive.For the given dimensional parameters of the rotors, the drilling of the rotors would be complicated and would not bring the significant improvement of the parameters that was expected.
The designed shape of the relief, which can also be seen in Figure 1, could of course be achieved nowadays with an additive manufacturing method (3d metal printing), but it is still very expensive.

2.2 Change in production technology

Another goal for Gen2 was to optimize production costs. The results of testing the first generation showed unnecessary oversizing of bearings with diagonal contact, necessitating an expensive high-speed variant for the given dimension. Therefore, for the second generation, despite the increased dimensions of the rotors, the bearings were reduced from 7204 (shaft diameter 20 mm) to 7202 (shaft diameter 15 mm), allowing the use of a normal series instead of a high-speed one. This optimization enabled the use of a more suitable clamping sleeve for the assembly of gears, ensuring mutual non-contact delimitation of the rotors.
The production of the Gen1 compressor also demonstrated that due to the chaining of production tolerances, relatively narrow tolerance bands of sub-components were necessary to achieve the required clearance between the rotors and the compressor block, logically increasing production costs. Thus, we aimed to reduce the number of processes requiring prescribed interrelationships of components. In cooperation with the Institute of Manufacturing Technology – Brno University of Technology, we designed the technology of casting a fusible/burnable model into a ceramic shell – Investment Casting (IC). At the same time, the hollow rotors are cast directly onto the steel shaft, reducing undesirable rotor parameters and eliminating the need to precisely position the rotor on the shaft, as both components are machined together..

2.1.1 Technology – Investmen Casting

Investment casting (IC), also known as fusible model casting, has a long history dating back thousands of years. This ancient technique involves creating a wax model, coating it with ceramic, melting the wax to create a cavity, and pouring molten metal into the mold [3]. The origins of precision casting technology can be traced to ancient Mesopotamia and Egypt, where artisans used the lost mold process to make jewelry, figurines, and other decorative objects.

Today, precision casting is widely used for producing parts with precise dimensions and complex shapes, such as turbines, engine parts, and jewelry, where manual machining would be impractical and uneconomical. It has evolved into a commonly used technology that meets customer requirements for shape and dimensional accuracy and material requirements of castings. It is also widely used for rapid prototyping, speeding up the production process. The development is further accelerated by integrating digital technologies and automation, making it a versatile and cost-effective manufacturing method for various components [3][4].

2.1.2 Combination of Rapid Prototyping and Investment casting technologies

3D printing is increasingly used in industry for its sustainability, efficiency, and ability to create complex parts with minimal material waste. Especially in Industry 4.0, it plays a key role in supporting automation, digitization, and the development of smart materials, enabling the creation of an autonomous industrial environment. 3D printing is used to produce prototypes, assembly aids, spare parts, and components for production equipment. In addition to plastic, metals and special materials can be printed for use in IC instead of wax [5][6].

Rapid Prototyping (RP) technology, not only used in foundry, enables flexible rapid design changes and prototyping without molds or tooling, ideal for testing new designs and quickly bringing products to market [7].

2.1.3 Castings in machine parts

In order to meet the requirements for weight savings and low production costs, many machine parts that were previously made entirely of one material are now produced by casting lighter alloys supplemented with castings made of another material in places where, for example, higher strength is required. This results in a so-called bimetallic component, the main advantage of which is, among other things, a significant reduction in weight, which leads to improved production efficiency. However, if it is not a connection of only metals, but e.g. wood and metal, the more accurate term composite component is suggested. [8] [9]

2.2 Manufacturing process

A universally designed shaft made of ČSN 15 142 steel was used as a casting, which can be machined into any desired final shape. On a 3d printer, a model of the rotor with an inlet condition was created from the PolyCast material (Figure 3), which was then pushed onto the shaft. To create the shell, this assembly was alternately dipped in a ceramic suspension and then sprinkled with ceramic material.

Figure 3: *Rotor assembly with inlet system and shaft*

The primary coating is crucial, as the overall quality of the casting surface depends on it; hence, the finest dusting and highly wetting slurry are used. Reinforcement packages strengthen the shell for further handling and resistance to high temperatures, using coarser sprinkle material and less wetting suspension. Eight casing layers were created instead of the usual six, allowing the shell to withstand increased fusing temperature and differential thermal expansion of the model and ceramic shell. The PolyCast models must be melted at a higher temperature than usual to achieve rapid melting on the shell wall (Flash Fire), allowing the entire model to be fired with minimal residual ash. Since aluminum alloy was chosen as the rotor material, the shell (Figure 4) did not need to be annealed before casting but was preheated just before casting.

Figure 4: *Finished shell with an inserted shaft*

3. CONCLUSION

The result of the proposed technology can be seen in Figure 5, and the parameters of the rotors that were achieved are summarized in Table 1. The parameters are compared here with the first generation compressor, and in parentheses are the parameters corresponding to the original production technology by machining without relief. It is noticeable that thanks to the new technology of manufacturing rotors with lightened lobes, there is only a 3.8% increase in the weight of the rotors and a 21% increase in the moment of inertia of the rotors with a 46% increase in the maximum transported amount of air. In the case of using the original production technology, the mass increase would be 51.2% and the moment of inertia increase by 87.5%. Compared to solid machined rotors, the cast ones are 31.3% lighter and have a 35.4% lower moment of inertia.

Figure 5: *Cast after shell removal*

	Gen1	Gen2	Unit	Change
Displacement volume	583	930	ccm/rev	+60 %
Maximum rpm	24000	22000	rpm	-8,3 %
Number of lobes	4	4	-	
Diameter of the rotor	75	84	mm	+12 %
Rotor length	120	150	mm	+25 %
Rotor tilt	0,4	0,4	°/mm	
Rotor weight	572	594 (865)	g	+3,8 (+51,2) %
Inertia moment	314,1	380,2 (589)	kg/mm2	+21 (+87,5) %
Tip gap	0.1	0.1	mm	
Lobe gap	0.08	0.08	mm	

Table 1: *Parameters Gen1 vs. Gen2*

REFERENCES

[1] ŽÁK, M., ČUPERA, J. Supercharged two-stroke spark ignition engine. In: KOKA 2021: LII. International Scientific Conference of the Czech and Slovak Universities and Institutions Dealing with Research of Internal Combustion Engines. 2021, Czech University of Life Sciences Prague, pp. 229-235. ISBN 978-80-213-3132-7.

[2] ŽÁK, M., ČUPERA, J., MITÁŠ, S. Design and Construction of a compressor for supercharging a two-stroke engine. In: KOKA 2022: LIII. International Scientific Conference of the Czech and Slovak Universities and Institutions Dealing with Research of Motor Vehicles and Powertrains. 2022, Slovak University of Technology in Bratislava, ISBN 978-80-227-5215-2

[3] HORÁČEK, Milan. LATEST TRENDS IN INVESTMENT CASTING TECHNOLOGY, 2008 available: <https://blayson.com/wp-content/uploads/2020/05/2010-Milan-Horacek-Latest-Trends-in-Investment-Casting-Technology.pdf>.

[4] PATTNAIK, Sarojrani; JHA, Pradeep Kumar a KARUNAKAR, D Benny. A reviewof rapid prototyping integrated investment casting processes. Online. *Proceedings ofthe Institution of Mechanical Engineers, Part L: Journal of Materials: Design and Applications*. 2014, roč. 228, č. 4, s. 249-277. ISSN 1464-4207. available: https://doi.org/10.1177/1464420713479257.

[5] JANDYAL, Anketa; CHATURVEDI, Ikshita; WAZIR, Ishika; RAINA, Ankush a ULHAQ, Mir Irfan. 3D printing – A review of processes, materials and applications in industry 4.0. Online. *Sustainable Operations and Computers*. 2022, roč. 3, s. 33-42. ISSN 26664127. available: https://doi.org/10.1016/j.susoc.2021.09.004.

[6] PRASHAR, Gaurav; VASUDEV, Hitesh a BHUDDHI, Dharam. Additive manufacturing: expanding 3D printing horizon in industry 4.0. Online. *International Journal on Interactive Design and Manufacturing (IJIDeM)*. 2023, roč. 17, č. 5, s. 2221-2235. ISSN 1955-2513. available: https://doi.org/10.1007/s12008-022-00956-4.

[7] VIVEK, Tiwary; ARUNKUMAR, P.; DESHPANDE, A. S.; VINAYAK, Malik; KULKARNI, R. M. et al. Development of polymer nano composite patterns using fused deposition modeling for rapid investment casting process. Online. In: . 020110-aavaile https://doi.org/10.1063/1.5029686.

[8] FERRO, Paolo; FABRIZI, Alberto; BONOLLO, Franco a BERTO, Filippo. Influence of aluminum casting alloys chemical composition on the interaction with a 304L stainless steel insert. Online. *Procedia Structural Integrity*. 2021, roč. 33, s. 189-197. ISSN 24523216. available: https://doi.org/10.1016/j.prostr.2021.10.023.

[9] VIALA, J.C; PERONNET, M; BARBEAU, F; BOSSELET, F a BOUIX, J. Interfacechemistry in aluminium alloy castings reinforced with iron base insertsOnline. *Composites Part A: Applied Science and Manufacturing*. 2002, roč. 33, č. 10, s. 1417-1420. ISSN 1359835X. available: https://doi.org/10.1016/S1359- 835X(02)00158-6.

ACKNOWLEDGEMENT

Projekt Super2Stroke v **rámci systémového projektu** č**. FX01010001 „Technologická inkubace“**

55. mezinárodní vědecká konference zaměřená na výzkumné a výukové metody v oblasti vozidel a jejich pohonů

září 5. - 6., 2024 – Liberec, Česká republika
Technická univerzita v Liberci
Fakulta strojní, Katedra vozidel a motorů

ON-BOARD DIAGNOSTICS AS A SUPPORT TOOL FOR CHASSIS DYNAMOMETERS

Jiří Čupera[1], Martin Fajman[2], Zdeněk Ředina[3], Stanislav Mitáš[4]

Abstract
This paper explores the utilization of On-board Diagnostics (OBD) as a support tool for chassis dynamometers in modern vehicle testing laboratories. As vehicles transition from mechanical to electronic control systems, testing methodologies must evolve to address these changes. The integration of OBD-II protocols provides critical real-time data essential for accurate and comprehensive vehicle diagnostics during dynamometer tests. The study examines the specific challenges faced when testing electric vehicles, which often require proprietary diagnostic protocols due to limited information from standard OBD-II systems. By leveraging software solutions like Hella Gutmann Mega MacsX, this research highlights the importance of integrating advanced diagnostic tools to enhance the accuracy and efficiency of vehicle testing. The findings indicate significant improvements in data acquisition and test reliability,

[1] Jiří Čupera, Mendel University in Brno, Zemědělská 1, 613 00 Brno, Czechia, jiri.cupera@mendelu.cz
[2] Martin Fajman, Mendel University in Brno, Zemědělská 1, 613 00 Brno, Czechia, fajman@mendelu.cz
[3] Zdeněk Ředina, Mendel University in Brno, Zemědělská 1, 613 00 Brno, Czechia, xredina@mendelu.cz
[4] Stanislav Mitáš, Zetor Tractors a.s., Trnkova 111, 62800 Brno, SMitas@zetor.com

emphasizing the necessity for adaptive testing systems in the rapidly evolving automotive landscape.

Keywords: On-board Diagnostics, chassis dynamometers, electric vehicles, vehicle testing, OBD-II protocol, Hella Gutmann Mega MacsX.

1. INTRODUCTION

The contemporary vehicle testing lab necessitates an evolved approach to the tested subject – the vehicle. This procedural shift is driven by the transition from purely mechanical methods of vehicle system regulation to electronically implemented controllers, requiring a testing methodology that encompasses the specificities of such regulations. Automotive systems now exhibit a myriad of implementation methods, ranging from linear continuous control via PID to nonlinear controllers, fuzzy logic systems, and even AI applications. Modern automobiles, particularly passenger cars, display a diverse array of propulsion systems, with a notable shift towards purely electric propulsion, where the increased cost is justified by the integration of additional sophisticated systems. The rapid pace of development also introduces various types of errors, from design flaws and technological issues to cybersecurity threats. The aim of this paper is not to engage in a debate regarding the current situation, where the predominant factors influencing the market expansion of electric vehicles are political-legislative measures or, more critically, EU regulations. It is imperative to acknowledge the current state. Somewhat ironically, car manufacturers are compelled to globally mitigate the impacts of conventional vehicle operations while simultaneously subsidizing electric vehicle production. The dismal perspective on the quantity of added value in specific regions, unfortunately, does not apply to the Czech Republic in Asia. Policymakers, legislators, and the general populace should occasionally shift from declarative slogans to straightforward reasoning inspired by natural principles. Biodiversity in nature follows a simple survival strategy, a logic that should be mirrored in the development of propulsion systems, respecting resource availability and their rational use. The purpose of this conference paper is to compile a body of knowledge in the realm of vehicle testing, with chassis dynamometers being pivotal equipment. The critical question remains whether these electrically powered vehicles can undergo standardized tests, which are integral to homologation processes. It is crucial to recognize that the vehicle development cycle spans approximately four years. However, this period is insufficient for the development and manufacturing of testing equipment that must serve for several decades. The software development of vehicle systems progresses at a much faster pace. Although technologies like OTA enable flexible reconfiguration of software blocks, including internal diagnostic processes, this presents a significant challenge for testing and inspection equipment.

In the past decade, systems capable of reading parameter values from onboard diagnostics have proven to be highly effective and essential tools for tests conducted on chassis dynamometers. These systems typically rely on reading parameters from the OBD-II protocol, which all vehicles are required to be equipped with. The utilization of the OBD-II protocol is extensive and is frequently presented at KOKA conferences e.g [4]. Apart from our previously published conclusions, we were inspired by Jouanne et al. (2020), who describe the same issue of integrating vehicle data and test stand data for driving test simulations of electric vehicles. Although they mention the term real-time, our experience so far defines occasional to stochastic latencies in the onboard diagnostics system. Dimitros Rampas et al. (2020) present a very simple

method (as a proof of concept) for monitoring fuel consumption under different loads, which are determined by the nature of real-world driving. Campoverde (2020) used OBD data measured during performance tests (while compiling the full engine speed map) to develop a machine learning model. At the chassis testing facility at Mendel University in Brno, either an in-house system based on the Automotive Diagnostic Toolkit, which is part of the NI LabVIEW development environment (the entire test facility is programmed in this environment), is used. For older vehicles that do not use the CAN-BUS, it is necessary to connect an external system provided by AVL. This system can acquire data from other physical layers – ISO9141, ISO14230, SAE J1850, etc. However, the situation is dire for electric vehicles, where the mandated OBD-II protocol provides only basic information. The solution to this unfortunate situation lies in integrating proprietary diagnostic protocols into the software architecture of vehicle test benches. This is hindered by vehicle manufacturers who, in many cases, equip their diagnostic tools with mechanisms that prevent external access to the data. This may involve hardware keys or, more recently, online authentication methods for the diagnostic tool or even the vehicle. This online method is often accompanied by vehicle cybersecurity measures, usually referred to as Cyber-Security-Management (CSM). Until the time of writing this contribution, there were only a few diagnostic devices for personal cars from various manufacturers available on the market that allowed access to manufacturers' servers directly or through their own access to authorization servers. The dominant companies in this field include Bosch and Hella. The method of data acquisition will be presented on the platform of the second mentioned company – Hella Gutmann Mega MacsX.

2. BODY OF PAPER

2.1 Chassis dynamometer

Chassis dynamometers are specialized devices designed to simulate real-world operating conditions as accurately as possible within a laboratory setting. This paper does not aim to differentiate the general construction of chassis dynamometers, as there is currently significant diversity in the arrangement of rollers, their drives, and their regulation. However, fundamentally, these devices are based on the transfer of force from the wheel's circumference to the roller (in the case of a single-roller design) or to the rollers (in the case of paired rollers, which may be mechanically linked by chains, belts, etc., for higher force transfer area).The basic physical relationship for determining power lies in knowing the speed and force, where their product, applied to the roller's circumference, gives the power also on the roller's circumference. The relationship is straightforward and does not involve any constants, which come into play only when determining passive losses in test devices that cannot measure their own losses or those of the vehicle. This test concept is entirely unsuitable for laboratory tests and does not allow for many important tests in the motor quadrant. The chassis dynamometer at the Department of Technology and Automobile Transport of the Faculty of AgriSciences at Mendel University in Brno is a true laboratory device, evidenced by its two-year calibration cycle. The MENDELU chassis dynamometer underwent significant modernization between 2020-2023. Firstly, it was necessary to adjust the recuperation system, which exhibited anomalies in the sinusoidal current drawn by the MENDELU network. It was more of a trapezoidal shape, common in simple DC-AC converters. The cause of this was likely found in high-power converters,

where a significant quantization effect occurred at a specific moment related to the temperature gradient, causing the entire regulator to oscillate. This irregular AC current then frequently caused failures in power sources with PFC correction, especially in control computers. The solution was dynamic compensation with autonomous control, which only removes artifacts on the recuperation side and does not affect the chassis dynamometer's regulation processes. Figure 1 shows the MENDELU test facility along with the tested vehicle produced by Škoda Auto a.s.

Figure 1: *The tested Škoda Enyaq - electric vehicle on the BR4VDM chassis dynamometer located at Mendel University in Brno (Source: author)*

A significant change occurred in the automation of the entire test facility. The entire DC drive and roller system used analog signals, meaning the currents from the DC drives to the DC motors were controlled by analog signals, as were their feedback loops. This was also true for rotational feedback, where the drives and rollers used incremental IRC sensors from the Czech company LARM, but their output led to 5B modules that transformed the frequency signal into an analog 0-10V signal. The entire low-level software part was replaced by a solution from NI (formerly National Instruments), relying not only on an RTOS based on Linux but also extensively utilizing FPGA elements from XILINX for precise timing. Some systems have FPGA clocked at 80 MHz, which is incomparable to the original MS-DOS timer set at 55 ms (just under 20 Hz). All communications are handled by the EtherCAT protocol, not only between NI control systems but also between digital converters for DC drives from Control Techniques (Mentor). These converters have an autonomous communication system where they exchange a range of information about their current values. All the above-described changes have resulted in a fundamental change in the concept of request transfer and allow regulation in speed mode with an accuracy of 0.02 km/h. At this

point, this represents absolute precision below the resolution of all known driving assistant systems. Emphasis on this value is placed due to the potential mutual influence of regulators, where any interference from the ESP system could destabilize the dynamometer regulator. Further modifications to the chassis dynamometer have occurred in the external measurement section, which, being based again on NI technologies, is scalable to hundreds of analog and digital signals, expandable with data from onboard CAN, CAN FD, OBD protocols, Ethernet, etc. The storage of such heterogeneous data, where some are not time-equidistant, is accomplished using the native TDMS format (and the NI DIADEM environment with export capabilities to Excel). The parameters of MENDELU chassis dynamometer are given in the Table 1.

Parameter	Value
Max. Testing Speed [kph]	200
Max. Power per Axle [kW]	240
Max. Weight per Axle [kg]	2000
Diameter of Rollers [m]	12
Width of Rollers [mm]	600
Gap Between Rollers [mm]	900
Surface of Rollers	Roughness equivalent to RAA 1.6
Inertial Mass of Rollers (each axle) [kg]	1130
Min. Wheelbase [mm]	2000
Max. Wheelbase [mm]	3500
Load Capacity of Covering	
At the Driving Area [kg]	2000
At the Walking Area [kg]	500
Compressed Air [bar]	min. 4
Speed Measurement Range [kph]	0 – 200
Force Measurement/Control Range [kN]	4x ± 5
Speed Measurement Accuracy [kph]	± 0.01
Force Measurement Accuracy [%]	± 0.05
Speed Control Accuracy [kph]	± 0.02
Force Control Accuracy [%]	± 0.1

Table 1: *Technical parameters of chassis dynamometer*

2.2 Testing vehicle

The representative electric vehicle used as a test car prepared for tests on the chassis dynamometer was a car produced by Škoda Auto a.s., specifically the Škoda Enyaq iV 80 (odometer: 130 638 km). In Table 2, the basic technical parameters of the vehicle type are provided. Additional detailed information, particularly related to the identification of electric components, is shown in Figure 2, which was obtained by querying the hybrid battery management parameter.

Parameter	Value
Power	150 kW
Torque	310 Nm
Number of Motors	1

Drive	Rear
0-100 km/h Acceleration	8.6 seconds
Maximum Speed	160 km/h
Real Range	440 km
Battery	
Battery Type	Lithium-ion
Nominal Battery Capacity	82.0 kWh
Number of Cells	288
Architecture	400 V
Battery Warranty	8 years or 160,000 km
Actual Usable Battery Capacity	77.0 kWh
Cathode Material	NCM712
Pack Configuration	96s3p
Nominal Voltage	350 V
Charging	
Standard Charger (Onboard)	11 kW
AC Charging Time (0 to 440 km)	8 hours and 15 minutes
Fast Charging (CCS port)	
Maximum Fast Charging Power	143 kW (10-80%: 125 kW)
Fast Charging Time (44 to 352 km)	27 minutes
Energy Consumption	
Real Range	440 km (175 Wh/km)
WLTP Rating	
Range	548 km
Rated Consumption	167 Wh/km
Vehicle Consumption	141 Wh/km

Table 2: *Skoda Enyaq iV 80 Specifications*

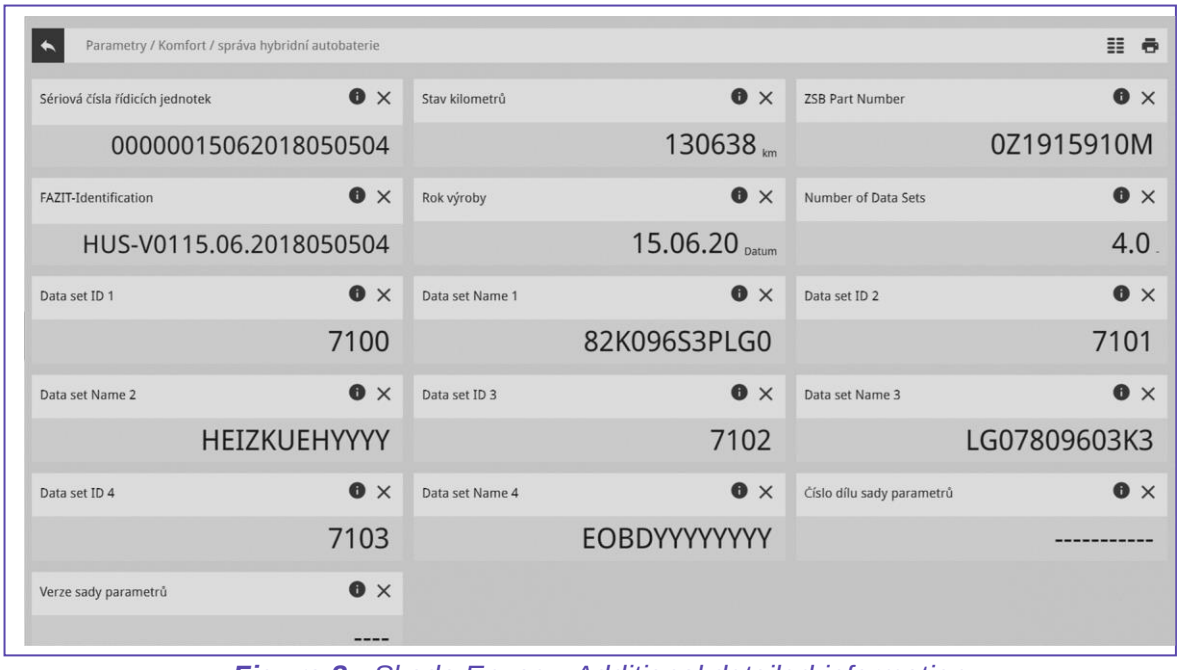

Figure 2: *Skoda Enyaq - Additional detailed information*

2.3 HellaDiag – software development

As mentioned above, "live" onboard diagnostic data can provide a wealth of insights into the results of tests conducted on a chassis dynamometer. Given that no manufacturers of diagnostic tools provide any data output that could be integrated into the test system, it was necessary to devise a concept that, even in a non-standard way, would allow data acquisition. Preferred solutions would rely on communication output, such as via the TCP/IP protocol over Ethernet; however, this is not feasible. The solution adopted by Hella is attractive not only for the user, who can choose the diagnostic device or general system and only needs to comply with a browser compatible with modern HTML5, CSS, and JS standards, but also because the data flows through standard ports. This makes it possible to use methods for data collection from web technologies, though it is clear that this does not constitute a deterministic system and cannot guarantee that the outputs will be equidistant. Since all the software for the test facility and additional external support systems are controlled through NI LabVIEW, an essential requirement for development was to create the system within this environment. A crucial question in developing the concept was how to programmatically proceed so that data from the Hella system could be acquired, processed, and saved to a file or further shared. It should be noted that there were several options ranging from OCR methods (too complex and unreliable) to reverse engineering (data on the CAN bus is relatively difficult to identify and initial frame analysis suggests some might be encrypted) to selecting data from HTML code. The last option presents the best available solution, although it is not very efficient in terms of the necessary application performance. Unfortunately, due to the current concept of diagnostic procedures, the cooperation of the diagnostic system with human operators is always required. Therefore, the developed system necessarily requires a certain degree of functional control. A positive aspect for operators might be the method of virtual control or settings via remote access to software developed on the LabVIEW platform, which the company itself refers to as Remote Front Panels. The reason for the necessary interaction is illustrated, for example, in Figure 3, where access to certain modules requires authorization from the person invoking the functions. Once authentication on the Hella server is complete, it is possible to proceed further. However, to initiate this process, it is necessary to log in with a Hella Gutmann account username and password.

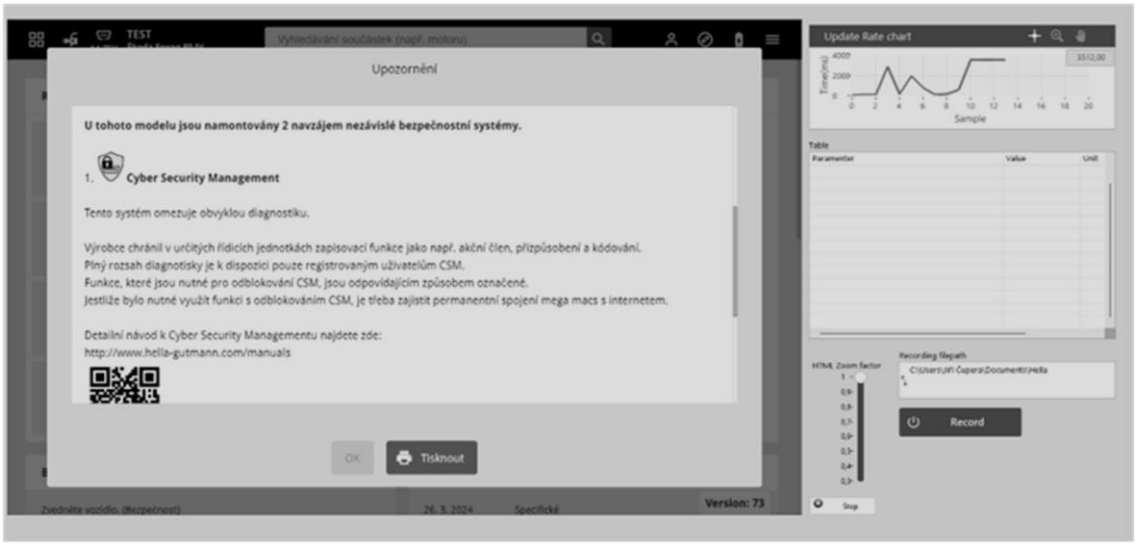

Figure 3: *Authorization of a person in the cybersecurity system*

The development of the application was quite time-consuming, although the result is a relatively simple solution. However, it involved a thorny programming journey, starting with an ambitious initial step to develop a complete system capable of displaying HTML code as web browsers do. For simple systems, the initially chosen solution might have been effective, but with the structure provided by the Hella Gutmann diagnostic device's web server, it was not possible to maintain the necessary graphical level. The reason is the source code, which is automatically generated and did not provide a "readable" structure. It was full of DIV tags, whose locations are too complex, and the naming is handled by very long tokens. From a programmer's perspective, it can be stated that the creator did not optimize the structure at all; I would unabashedly call this waste of application performance. Simply put, it can be interpreted that the necessary data constitute only a few percent of the total code of the webpage content carrying the information. Unfortunately, as the programming proceeds, the entire HTML code, including cascading styles and internal JavaScripts, must be processed. This seems to be the biggest drawback of the created system. Unfortunately, despite numerous consultations and attempts with AI tools like ChatGPT or MS Copilot, a more efficient solution was not found. The departure from programming a custom web browser for the code provided by the diagnostic device came with the discovery that third-party components could be used, integrating many necessary functions. Generally, the components are based on technologies like ActiveX (an older but still used developer platform) or .NET (a modern Microsoft-supported developer "ecosystem"). Choosing from free platforms shared with programmers under open licenses, the component directly from Microsoft named WebView2 was used. The WebView2 component allows hosting web content in native applications using the Microsoft Edge rendering engine based on Chromium, which is essentially the current standard incorporating HTML5, XHTML, CSS3, and support for extensive JavaScripts. A positive experience with this component is worth noting, as no errors on its part were recorded over several months.

The graphic illustrations below, depicting the diagnostic process state, are created from the final compiled application in the NI LabVIEW environment. A simple guide is the right side of the graphical interface, where the "Response Time" graph is visible, showing how long it took to process the command request (e.g., listing parameters). Programmatically, it is necessary to handle the timeout, as for some (non-)electric vehicles, the process of scanning valid addresses can take several tens of seconds. The image below, Figure 4, shows the diagnostic system screen, displaying the most important and necessary current value data. On the left is the Hella Gutmann diagnostic system screen. On the right, the parameters are read and displayed in the environment programmed in the NI LabVIEW environment. Below the table are options for saving files from the top table, and the HTML Zoom factor is a WebVIEW2 function that allows user setting of the web page content size. This function was added to the application after testing on several devices, where less standard display resolutions caused deformation of graphical elements. Changing the zoom factor can eliminate the deformation.

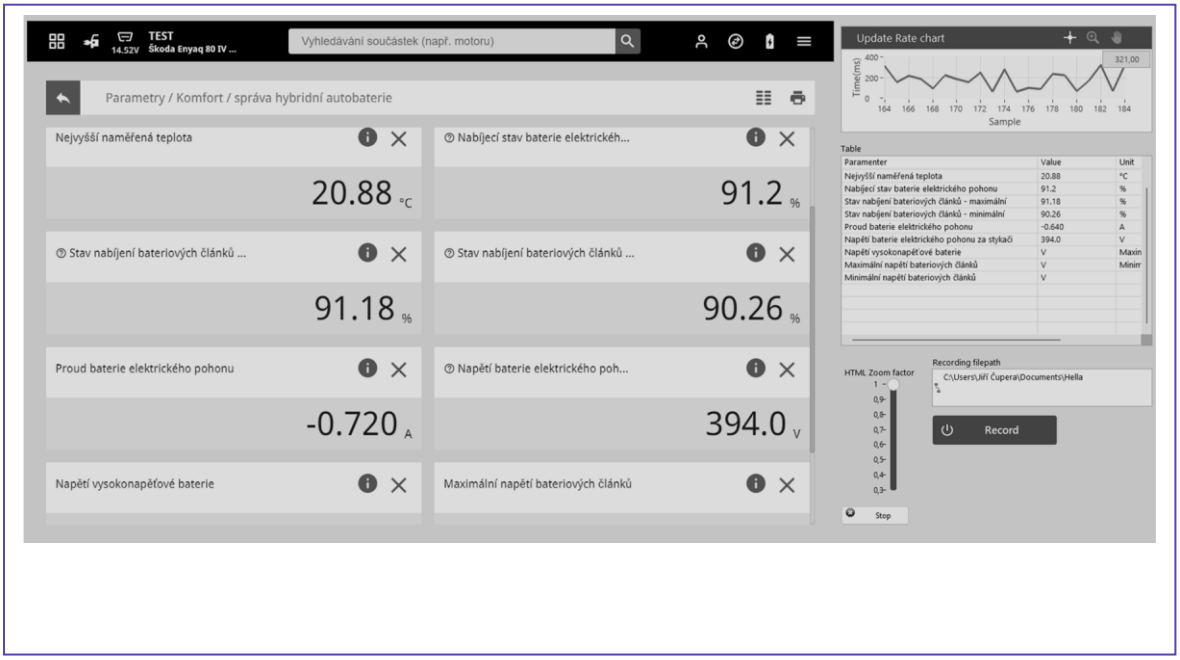

Figure 4: *Example of live data that can be saved by the system*

2.3 Skoda Enyaq – case study

The methodologies for tests conducted on the MENDELU chassis dynamometer were intentionally chosen with parameters corresponding to testing a car with a combustion engine. However, a fundamental aspect is the completely different torque characteristics between a combustion engine and an electric drive, in the case of the test vehicle, a synchronous electric motor. This characteristic is described in the construction chapter, showing that the maximum torque values are reached at zero engine RPM. Unfortunately, the dynamometer drive "fails" here, as its maximum force value is 5 kN in both motor and generator modes, or quadrants. From comparing the characteristics, it was clear and evident that a higher speed needed to be chosen for the first test point, as at lower speeds, the dynamometers' current protection would activate. This "starting" speed point was set at 60 km/h. The test procedure then proceeds by waiting for the vehicle to reach the starting speed, which the vehicle operator does using the accelerator pedal. Once the dynamometer registers the starting speed, the operator again uses the accelerator pedal to set the maximum value, effectively demanding the maximum torque. The regulator then takes over the test process, striving to minimize the speed control deviation (further evaluated). After the defined parameter recording period, the dynamometer, or its regulator, moves to the next speed point, stabilizes the speed again, and subsequently records and averages the force value. The setup for this configuration with the Škoda Enyaq was 60–150 km/h. The methodology for static power measurement, aside from the previous paragraph describing the necessary first speed point at 60 km/h due to significant forces on the roller surface, also differed in the operating mode of the test bench. Electric vehicles generally integrate very innovative driver support systems (ADAS), at a minimum including the second generation of ESP, which is highly sensitive to the accuracy of input variables. Therefore, for power tests, it is essential to ensure the same circumferential speed on each wheel. If this is not the case, the vehicle's control

system will intervene and disrupt the consistency of the test procedure.There was some uncertainty here because all rollers are independently controlled by their regulators in the test bench exciter, which share information about test parameterization, control mode, and current variables via the EtherCAT network. In the event of control "overshoots," which would otherwise have no impact on the test results in terms of test bench data, the vehicle could enter one of its emergency modes and generate substitute values. In real-world driving dynamics regulation, this would result in a situation where, based on the difference in wheel speeds and lack of knowledge of the actual driving state due to zero changes on the accelerometer or gyroscope, the system would repeatedly test with brake support and monitor the changes made. The oscillation of one regulator would cause oscillation in the other. However, the quality of the rotational or speed control of the test bench proved to be very high (even during testing).

The graph in Fig. 5 is the result of measuring the characteristics of the Škoda Enyaq vehicle drive. It is necessary to comment on the fact that, in the case of internal combustion engines, the X-axis would represent the rotational speed of the crankshaft, in other words, the engine RPM. However, for the Enyaq vehicle, we were unable to determine the drive RPM not only from the vehicle's onboard instruments but also from the Hella onboard diagnostics. For this reason, the graph is not titled in accordance with the usual graphical representation of RPM characteristics. Instead of engine RPM, I have retained a parameter that is somewhat equivalent, which is the roller speed corresponding to the wheel speed. The maximum measured value was 146.5 kW at a speed of 70 km/h. Subsequently, it decreased to 70 kW at a speed of 150 km/h. This is due to power limitation, which is time-defined by the manufacturer. However, it can be assumed that a multidimensional analysis of other parameters, especially electrical and thermal, is necessary. Unfortunately, it is not possible to find documentation of the vehicle drive controller to make the result valid.

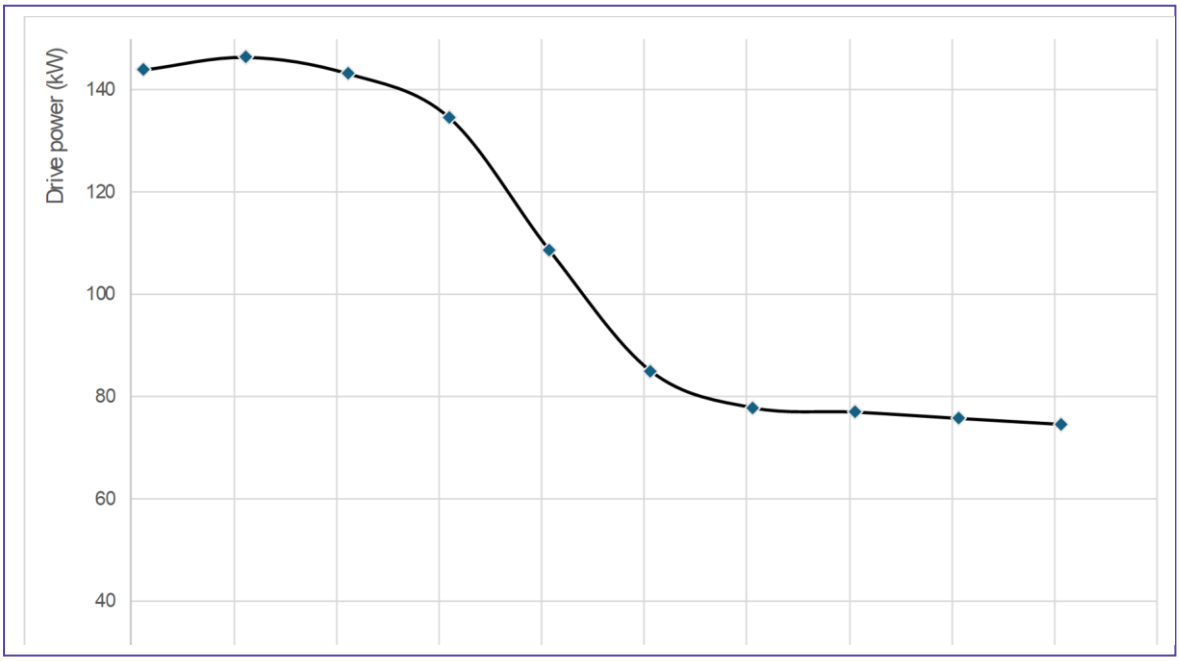

Figure 5: *Power curve – Skoda Enyaq*

From the above, it is evident that presenting the power characteristics in relation to RPM is not reliable. It is highly necessary to present the stability of power over time, as is apparent from the graph in Figure 6.

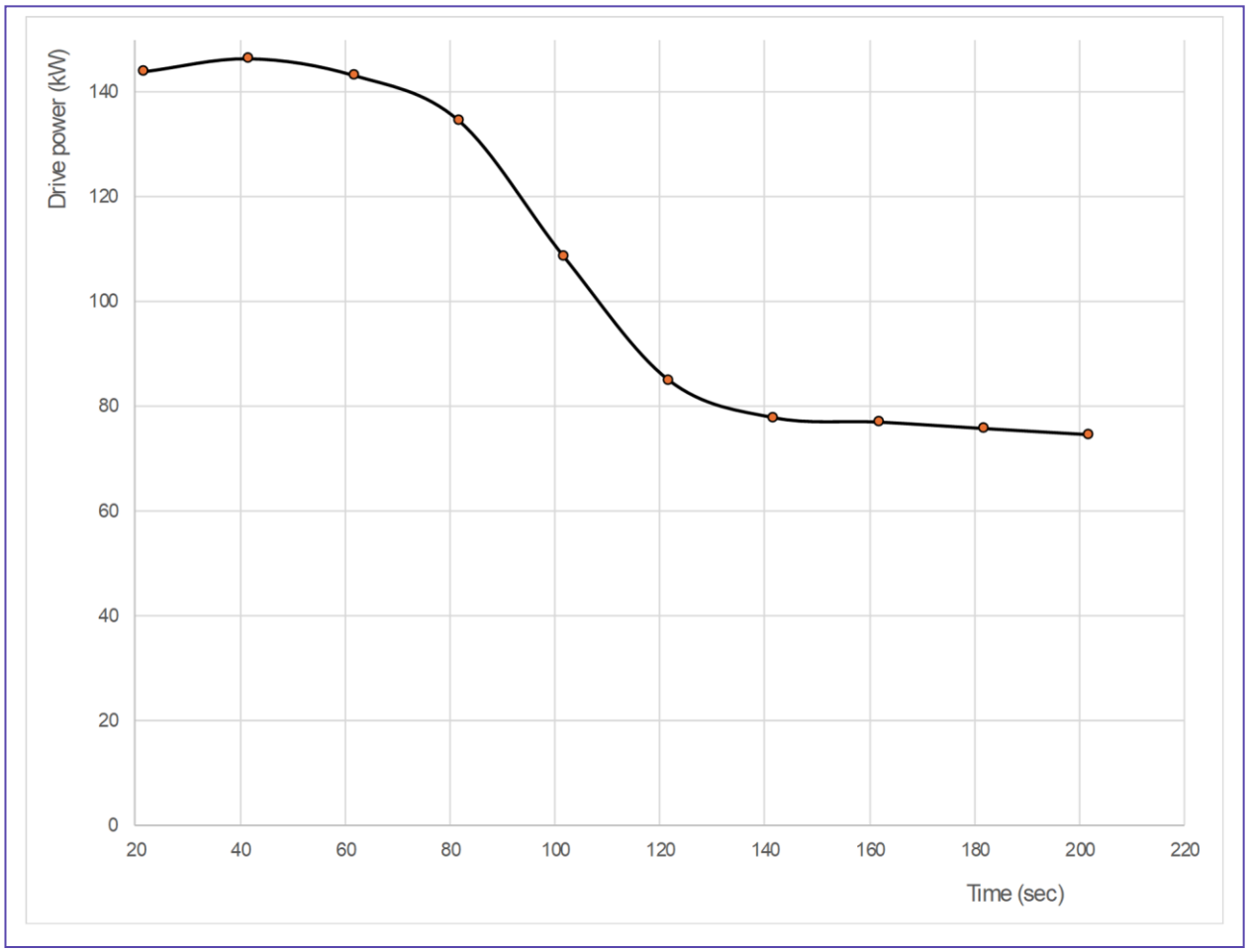

Figure 6: *Power curve (time) – Skoda Enyaq*

3. CONCLUSION

Given that the developed software was deliberately tested on an electric vehicle, the following section will discuss the facts related to the execution of test procedures and the use of OBD-II and the battery vehicle. Based on the theoretical analysis of vehicle testing methodologies conducted using a chassis dynamometer, it was found that there are no significant differences in the direct execution of test procedures between electric vehicles and those powered by conventional hydrocarbon fuels. It is true that challenges arose during the experiment. These were not primarily related to the powertrain itself, but rather to the driver assistance systems (ADAS), which caused various issues before and during testing. For example, the radar system was “obscured” by the test rig’s mounting equipment, and the camera system was blocked by the control screen, etc. Changes in the setup should eliminate these complications. However, the situation remains problematic for the vehicle's inertial measurement system, as wheel acceleration will not be accompanied by a translational acceleration signal. The following text details the procedure for conducting the tests and possible measures.

Identified differences in methodologies implemented for electrically driven vehicles:

Torque and Speed Characteristics - From the review of electric drives used in electric vehicles, it is evident that there is an "overlap" of torque characteristics of the vehicle test bench dynamometers. In other words, a critical part of the torque characteristics in the initial phase, which can be defined approximately at wheel speeds up to about 3 km/h, encounters limits in processing and signal consistency from the wheel speed sensors. This combination of methods on a vehicle secured on a chassis dynamometer creates a situation that cannot occur on the road. My work does not involve validating methods for determining the vehicle's kinematic state; however, I can generally outline the factors contributing to the inconsistency of test results between laboratory and real-world vehicle operation. Detection of the direction of rotation uses a combination of differential wheel speed sensors for ABS/ESP, signal comparison from ABS/ESP speed sensors, and supplementary information from inertial systems based on accelerometer and gyroscope outputs, possibly including monitoring the Earth's magnetic field. In static testing, where wheels rotate but the body does not move, no "support" from the IMU can be expected. Although the IMU sensor cluster detects very fine levels of vehicle acceleration, the signal analysis, which filters out disturbances defined by the direction change in the positive and negative quadrants of influence, oversees the signal. Generating torque through electric current is problematic without knowing the speed or the second derivative of the signal—acceleration—and relies on a rigid motion equation model, where at zero speed, a defined and fixed value of electric current is set (static at least within a certain range of conditions where temperature and other regulations do not enter current regulation). Current studies do not focus on knowledge at zero speeds for vehicle electric drives. In road vehicles, the quality of the model is crucial, where missing feedback must be replaced by the result from a predictive model; currently, so-called virtual sensors, which provide a range of kinematic and dynamic information based on complex calculations from diverse signals, are the topic. The above aspects contribute to certain torque artifacts, which manifest in torque overshoots and collapse of both control algorithms, leading to fluctuation in torque decrement and increment limited by speed limits.

Regenerative Modes - During dynamic tests, where it is necessary to monitor the forces acting in the deceleration quadrant, known as coast-down testing, it is essential to deactivate the vehicle's regenerative modes. For example, in a dynamic power test, where torque is calculated as the product of the rotational system's moment of inertia and angular acceleration. This involves accelerating from minimum to maximum speed and then measuring during the descending coast-down test to determine passive vehicle losses, i.e., complementary rolling resistances.

Defining Boundary Points of Characteristics - Currently, the speed characteristic is presented within the range of usable engine speeds. Unlike the internal combustion engine, which has zero torque at zero speed, the electric motor (synchronous) has maximum torque at zero speed. Unfortunately, there is a discrepancy between the concept of the chassis dynamometer and the electric motor of the vehicle, where the low engine speed of the vehicle can significantly exceed the maximum braking torque. For this reason, the characteristic must be shifted to speeds where this situation does not occur. At the opposite end of the speed range, the situation differs from the conventional setup for internal combustion engines, as the vast majority of electric vehicles are speed-limited within the range of 140–200 km/h. Typically, the characteristic in chassis dynamometer software is set so that engine speed is a function of roller speed. Torque is then calculated from power. However, for the specific tested vehicle, engine speed was not available, so it had to be interpreted as a speed characteristic. Jouanne et al. (2020) present an approach and integration of OBD-II parameters for electric vehicles for chassis dynamometers. This conclusion can be agreed upon, especially if the parameters are used to simulate driving tests for estimating emissions load or, in this case, determining consumption. However, based on knowledge of the OBD-II protocol, I cannot agree with the designation of real-time data access. The request for data is normatively limited to 50 ms, followed by an indeterminate time for the ECU response, meaning system latency can be quite significant. Unfortunately, the range of required parameters is not mentioned, so the problem of determining speed remains.

Testing Battery Pack Parameters - To extend tests conducted on a chassis dynamometer, the integration of tests defined and supported by standards for battery pack cycling, including part of the cycle with the support of an external charging device, is directly suggested. Vaidya et al. (2009), in cooperation with the Indian vehicle manufacturer TATA, focused on automating tests on the chassis dynamometer to define and objectify vehicle battery load tests and aimed for the greatest possible reproducibility and repeatability of the tests conducted. As shown in their results, it is possible to regulate a wide range of vehicle processes via the CAN bus. This is demonstrated in a fairly extensive test of an electric vehicle battery, where the outcome is an assessment of the parameters of li-ion cell cycling.

The source code is free for all purposes:
https://www.utad.cz/helladiag/

REFERENCES

[1] Malekian, R., Moloisane, N., Nair, L., Maharaj, B., & Chude-Okonkwo, U. (2017). Design and Implementation of a Wireless OBD II Fleet Management System. IEEE Sensors Journal, 17, 1154-1164. https://doi.org/10.1109/JSEN.2016.2631542.

[2] Jouanne, A., Adegbohun, J., Collin, R., Stephens, M., Thayil, B., Li, C., Agamloh, E., & Yokochi, A. (2020). Electric Vehicle (EV) Chassis Dynamometer Testing. 2020 IEEE Energy Conversion Congress and Exposition (ECCE), 897-904. https://doi.org/10.1109/ECCE44975.2020.9236288.

[3] Campoverde, J. (2019). Driving Mode Estimation Model Based in Machine Learning Through PID's Signals Analysis Obtained From OBD II. , 80-91. https://doi.org/10.1007/978-3-030-42520-3_7.

[4] ČUPERA, Jiří; HAVLÍČEK, Miroslav; SEDLÁK, Pavel; 2005. Integrace OBD-2 do systému zkoušení vozidel na válcovém dynamometru.. In: Sborník přednášek XXXVI. mezinárodní konference kateder a pracovišť spalovacích motorů českých a slovenských vysokých škol. Technická 4, 166 07 Praha, Česká republika: České vysoké učení technické v Praze, Fakulta strojní, ISBN 80-01-03293-0.

[5] VAIDYA, V., & BHERE, H., 2009. Driverless chassis dynamometer testing of electric vehicles. ATZ worldwide, 111, pp. 12-15. https://doi.org/10.1007/BF03225155.

55. mezinárodní vědecká konference zaměřená na výzkumné a výukové metody v oblasti vozidel a jejich pohonů

září 5. - 6., 2024 – Liberec, Česká republika
Technická univerzita v Liberci
Fakulta strojní, Katedra vozidel a motorů

ON THE RUNNING SMOOTHNESS OF THE IN-LINE SPARK-IGNITION ENGINE FOR NON-EUROPEAN MARKETS

Lubomír Drápal[1], Kateřina Fridrichová[2], Jozef Dlugoš[3]

Abstract
The right choice of power train layout is a key prerequisite for success in the chosen market. However, the operating conditions and driving modes of passenger vehicle power trains differ in different markets. The paper presents a study of the influence of the layout and other design modifications of the crank train of an in-line spark-ignition engine on the running smoothness at atypically low engine speeds and high engine load. Several design proposals of the crank train are assessed from this point of view and compared based on the results of dynamics simulations using a discrete torsional model with lumped masses which is solved in the frequency domain.

[1] Lubomír Drápal, Institute of Automotive Engineering, Brno University of Technology, Technická 2896/2, 616 69, Brno, Czech Republic, e-mail: drapal@fme.vutbr.cz
[2] Kateřina Fridrichová, Institute of Automotive Engineering, Brno University of Technology, Technická 2896/2, 616 69, Brno, Czech Republic, e-mail: Katerina.Fridrichova@vutbr.cz
[3] Jozef Dlugoš, Institute of Automotive Engineering, Brno University of Technology, Technická 2896/2, 616 69, Brno, Czech Republic, e-mail: jozef.dlugos@vutbr.cz

1 INTRODUCTION

During the development of a new power unit, in addition to the required performance parameters, applicable emission standards, costs, installation space, etc., the potential specifics of the target markets must also be considered. When examining the operating modes of internal-combustion engines sold in the Indian and Southeast Asian markets, it was found that they quite often have a peculiar high load mode at very low engine speeds, sometimes even lower than idle. This mode has a negative effect on NVH as well as transmission fatigue life. This paper describes how to improve the running smoothness of a 1.2 L in-line three-cylinder gasoline engine in this mode at the lowest possible manufacturing costs, comparing the torsional dynamics of its crank train with a four-cylinder engine of the same displacement and with the initial three-cylinder 1.0 L engine, from which the three-cylinder 1.2 L engine is derived.

The dynamics of the crank train can be simulated using advanced MBS (Multi-Body System) tools including modally reduced elastic bodies [1, 2]. These computational models can also include various types of nonlinearities [3], or allow the study of detailed stresses of individual parts in terms of fatigue life [4].

Computational models with lumped mass are used for simulations in the case where the output is, for example, only torsional dynamics of the system [5, 6]. The advantages are lower complexity of the computational model, much faster simulation time and easier incorporation of frequency-dependent parameters.

The thermodynamics of such an internal combustion engine can be simulated in the phase of its development using 1-D computational tools, for example [7, 8]. The obtained results can be used as excitation effects of the aforementioned computational models of forced vibration of the crank train.

2 DESIGN MODEL OF A CRANK TRAIN

From the point of view of the running smoothens at low engine speeds and high engine load, several design variants are compared, see Figure 1.

		1.0 MPI	1.2 MPI I3	1.2 MPI I3 *EF*	1.2 MPI I3 *BF1*	1.2 MPI I3 *BF2*	1.2 MPI I4
		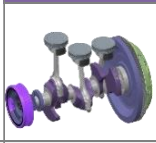	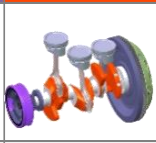	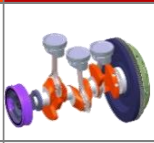	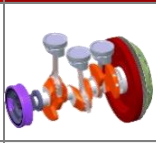	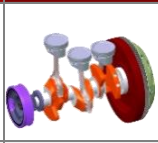	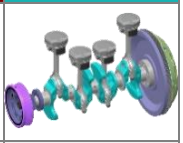
Mass rel. diff.	[%]	0	+5.5	+8.2	+17.8	+24.5	+3.6
Inertia moment rel. diff.	[%]	0	+5.4	+10.2	+28.5	+41.3	-7.6

Figure 1: *The design of the crank train of the compared variants, the relative difference in the mass of the crank train and the axial moment of inertia (including the clutch)*

The default design is the initial mass-produced three-cylinder 1.0 MPI, which serves as a reference in this comparison. The new 1.2 MPI I3 three-cylinder engine derived from it is equipped with either a mass-produced flywheel, a flywheel enlarged as part of the standard installation space – *EF*, a large flywheel allowing the same running smoothness as in the case of the 1.0 MPI engine with a combustion chamber pressure corresponding to the original engine 1.0 MPI – *BF1* and a large flywheel to achieve the same running smoothness as the 1.0 MPI with combustion chamber pressure corresponding to the larger cylinder unit 1.2 MPI I3 – *BF2*. The four-cylinder 1.2 MPI I4 engine is also included in the comparison, however its overall mass, costs and dynamic parameters are not as suitable for the target market as in the case of three-cylinder engines. Table 1 summarizes the basic dimensions of the crank train of the compared engines.

Table 1: *Basic dimensions of the crank train of the compared variants*

		1.0 MPI	1.2 MPI I3	1.2 MPI I4
Bore	[mm]	74.5	76.5	71
Stroke	[mm]	76.4	86.9	75.6
Connecting rod length	[mm]	145	140	145
Cylinder distance	[mm]	82	82	82
Crankshaft offset	[mm]	0	0	0

3 COMPUTATIONAL MODEL OF THE TORSIONAL DYNAMICS

For the needs of this project, the simulation of the torsional vibration of the system is performed using a 1-D dynamic model with lumped masses, see Figure 2. The inertia effects of the individual parts of the system are lumped in the respective disc with an equivalent moment of inertia. Torsional stiffness of the individual parts is represented by the corresponding stiffness of the intangible shaft connecting the adjacent discs.

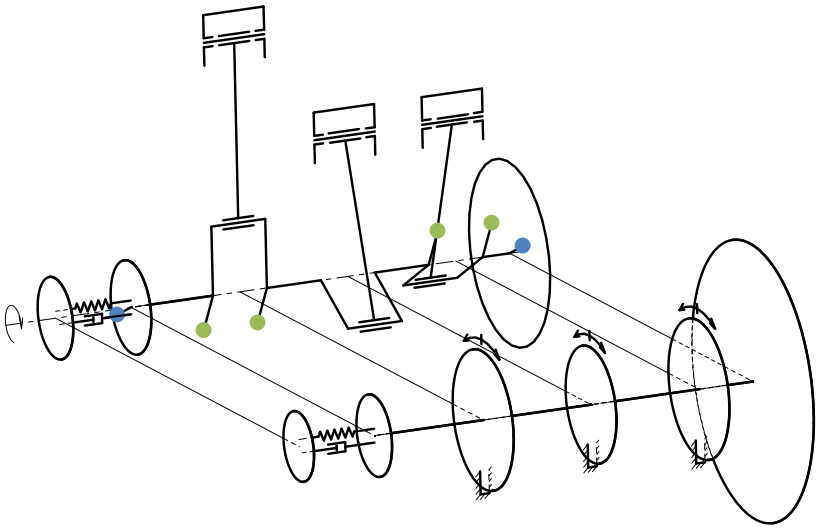

Figure 2: *Computational model of the torsional dynamics with lumped masses*

Torsional stiffness of individual parts is determined analytically, e.g. according to [9], torsional stiffness of crankshaft throws is determined according to equations derived by Ker Wilson [10].

The response of a steady damped system to time-varying forced torsional excitation can be determined from the equation system:

$$\mathbf{M}\ddot{\mathbf{q}} + \mathbf{B}\dot{\mathbf{q}} + \mathbf{C}\mathbf{q} = \mathbf{Q}, \tag{1}$$

where $\mathbf{M}$ is the mass matrix, $\mathbf{q}$ is the vector of generalized torsional coordinates, $\mathbf{B}$ is the damping matrix, $\mathbf{C}$ denotes the stiffness matrix and $\mathbf{Q}$ is the excitation vector. The simulation of this type of vibration is performed in the frequency domain on an in-house computational model created in the FORTRAN environment. The model is excited by the torque of inertia forces of the reciprocating parts and by the pressure in the combustion chamber. The pressure in the combustion chamber originates in a thermodynamic 1-D simulation in a GT-POWER environment. The thermodynamic model is based on a modified and verified computational model of the initial three-cylinder engine 1.0 MPI.

A hysteresis damping model is used to simulate the internal damping. However, the damping in the rubber parts has the most significant effect. The rubber part is the torsional damper in this case. The connection of the crank train with the dynamometer rotor is simulated in this computational model by a very soft torsional spring with negligible damping. The damping of the crank train relative to the construction frame (i. e. to the engine block) is modelled to be proportional to the estimated friction mean effective pressure.

Due to the simulation in the frequency domain, when the mutual independence of the individual harmonic orders of the requested quantities is assumed and the frequency-dependent parameters (damping of the torsional damper) can be calculated directly, the simulation time is extremely short compared to the simulations in the time domain. For this reason, this method is also suitable for more extensive parametric studies. This is used precisely for the design of the large flywheels *BF1* and *BF2*, see the next chapter. A certain limitation of the described computational model is the fact that it is linear, however this does not limit its applicability in this case.

4 SIMULATION RESULTS

The computational model described in the previous chapter enables the recalculation of the investigated quantities back into the time domain. In this way, it is possible to obtain, for example, values of the angular displacement of individual members of the torsional model, the relative deformation between individual members, or the torque acting between them. From these results, the angular displacement of the flywheel is the most important for evaluating the running smoothness of the crank train. Figure 3 shows this for the compared variants in the form of half peak-to-peak value of the flywheel angular displacement. The results show a significant deterioration in the running smoothness of the three-cylinder variants compared to the four-cylinder one, which is caused by the larger firing angular gap

of the three-cylinder variants. Due to the larger cylinder unit and higher performance parameters, the largest value of half peak-to-peak value of the angular displacement of the flywheel is achieved in the 1.2 MPI I3 version. The increase of its flywheel within the existing installation space (variant *EF*) will improve the running smoothness by 4 % compared to the initial design 1.0 MPI, however only a substantial increase in the moment of inertia of the flywheel by 55 % will bring the 1.2 I3 MPI variant the same running smoothness as the 1.0 MPI.

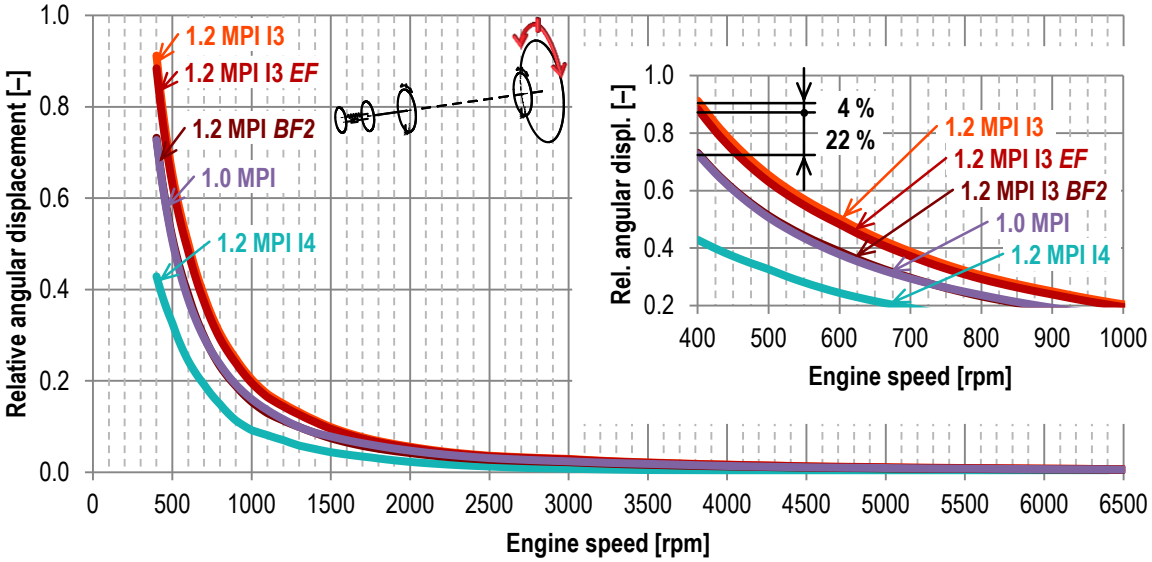

Figure 3: *Half peak-to-peak value of flywheel torsional vibration*

Figure 4 shows the same results in the case where all variants are excited by in-cylinder pressure of the initial 1.0 MPI version.

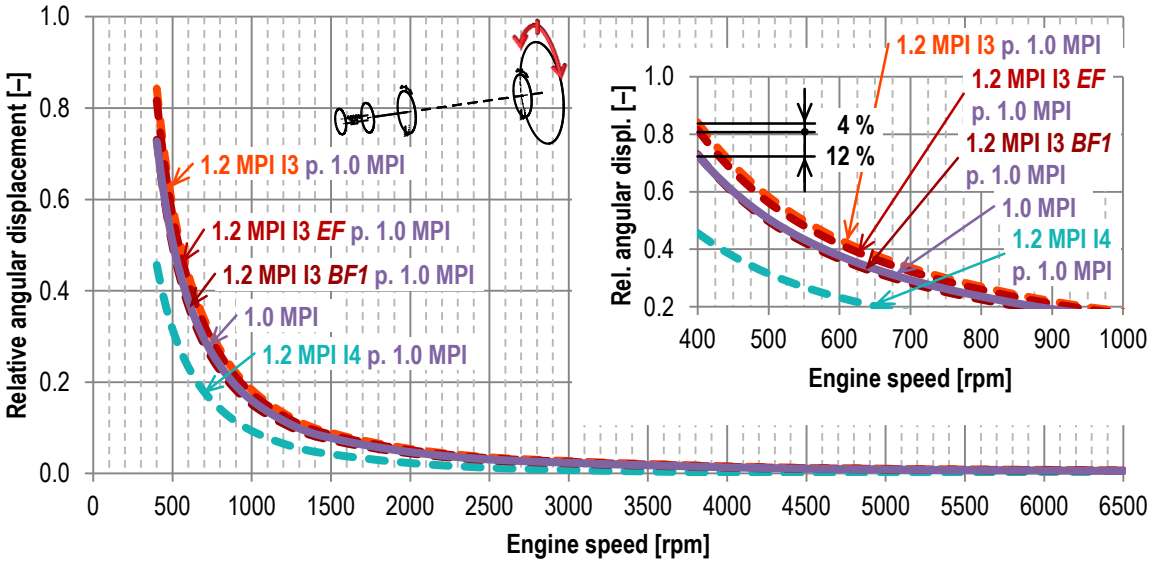

Figure 4: *Half peak-to-peak value of flywheel torsional vibration when the computational model is excited by the in-cylinder pressure of the initial variant 1.0 MPI*

It is obvious that the running smoothness will improve in this case, as the 1.0 MPI design achieves significantly lower values of pressure in the combustion chamber in the range of engine speeds (400–1800) rpm. The flywheel of the 1.2 MPI I3 *BF1* variant thus has a moment of inertia greater by only 35 %, therefore that this design reaches the level of smoothness of the initial 1.0 MPI variant.

During parametric studies of the influence of the moment of inertia of the flywheel torsional vibration at low engine speeds, when one harmonic order completely dominates (for a three-cylinder 1½, for a four-cylinder 2), a practically perfectly logarithmic dependence of these quantities is observed. This can be used by approximating this dependence for a given engine design, e.g. using the method of least squares. After finding out the constants of this function, the moment of inertia of the flywheel can be designed directly for the required flywheel angular displacement.

5 CONCLUSION

In general, a computational model of the most appropriate level should be chosen for each simulation. The presented method for the design of the flywheel for the chosen level of running smoothness of the crank train is time effective and relatively easy to use. It can also be used to determine the influence of the thermodynamics of the combustion process and the geometry of the crank train on its running smoothness. In addition, it can also provide information on the torsional stress of crankshaft parts, the effect of the torsional damper, etc.

The results show that, in terms of the mass and moment of inertia of the crank train, or rather the flywheel, in order to achieve greater running smoothness, it is more advantageous to adjust the combustion process so that the excitation of the crank train at the lowest engine speeds decreases. To further increase the running smoothness of the 1.2 MPI I3 engine, however, increasing the flywheel is necessary.

REFERENCES

[1] MOURELATOS Z. P. A crankshaft system model for structural dynamic analysis of internal combustion engines. Computers and Structures, 2001, Vol. 79(20), pp. 2009–2027. DOI: 10.1016/S0045-7949(01)00119-5. ISSN 0045-7949.

[2] VANDENPLAS B., GOTOH K., DUTRE, S. Predictive Analysis for Engine/Driveline Torsional Vibration in Vehicle Conditions using Large Scale Multi Body Model. SAE Technical Paper. Warrendale (PA): SAE, 2003. DOI: 10.4271/2003-01-1726. ISSN 0148-7191.

[3] NOVOTNÝ P., PÍŠTĚK V. New Efficient Methods for Powertrain Vibration Analysis. Proceedings of the Institution of Mechanical Engineers, Part D, Journal of Automobile Engineering. 2010, Vol. 224, No. 5, pp. 611–629. DOI: 10.1243/09544070JAUTO1277. ISSN 0954-4070.

[4] ORTJOHANN T., REBBERT M., MAASSEN F., ROBERS M. 3D-Durability Analysis of Crankshafts via Coupled Dynamic Simulation including Modal Reduction. SAE Technical Paper. Warrendale (PA): SAE, 2006. DOI: 10.4271/2006-01-0823. ISSN 0148-7191.

[5] MILASINOVIC A., MILOVANOVIC Z., KNEŽEVIĆ D., MUJANIĆ I. Determination of Differential Equations of Motion and Parameters of an Elastic Internal Combustion Engine Crankshaft. Transactions of FAMENA. 2016, Vol. 40, No. 7, pp. 83–95. DOI: 10.21278/TOF.40207. ISSN 1333-1124.
[6] ÖSTMAN F., TOIVONEN H. T. Torsional system parameter identification of internal combustion engines under normal operation. Mechanical Systems and Signal Processing, May 2011, Vol. 25(4), pp. 1146–1158. DOI: 10.1016/j.ymssp.2010.11.001. ISSN 0888-3270.
[7] NORTHROP W. F., ZARLING D. One-Dimensional Modeling of a Thermochemical Recuperation Scheme for Improving Spark-Ignition Range Extender Engine Efficiency. SAE International Journal of Advances and Current Practices in Mobility. Warrendale (PA): SAE, 2020, pp. 543–550. DOI: 10.4271/2019-24-0066. ISSN 2641-9637.
[8] VASUDEVAN D., SARAVANA VENKATESH R., KRISHNAN S., VARATHAN, K. K. Simulation and Experimental Study of Intake Air Flow Pulsation and Resolution for a 2-Cylinder Uneven Firing (0°-540°) Naturally Aspirated and Turbocharged CPCB II Diesel Engine. SAE Technical Paper. Warrendale (PA): SAE, 2012. DOI: 10.4271/2019-01-1171. ISSN 0148-7191.
[9] NESTORIDES, E. J. A Handbook on Torsional Vibration. B.I.C.E.R.A. Cambridge: Cambridge University Press, 1958.
[10] [71] KER WILSON, W. Practical Solution of Torsional Vibration Problems. Vol. 1, London: Chapmann Hall, 1942.

ACKNOWLEDGEMENT

This work was supported by the Faculty of Mechanical Engineering, Brno University of Technology. The authors gratefully acknowledge funding from the specific research on BUT FSI–S-23-8235.

55. mezinárodní vědecká konference zaměřená na výzkumné a výukové metody v oblasti vozidel a jejich pohonů

září 5. - 6., 2024 – Liberec, Česká republika
Technická univerzita v Liberci
Fakulta strojní, Katedra vozidel a motorů

BEYOND VEHICLE ELECTRIFICATION: LIFE CYCLE ASSESSMENT, MINERALS, ENERGY CHALLENGES AND THEIR IMPACT ON COMPONENTS DESIGN AND CAR ARCHITECTURE

Guillaume HÉBERT[1]

Abstract
In the race towards vehicles electrification, optimizing the products (the vehicles) may not be good enough. First of all, because a "tank to wheel" approach only captured a part of the total emissions required to manufacture and operate. Second of all, because it fails to consider resources availability e.g., minerals, energy.
Therefore, cars should not be considered as a system on their own, but rather as a "system of systems" which requires wider consideration to be operational.

1. INTRODUCTION

The last decade has seen a push towards Battery Electric Vehicles (BEV's). The two main technical goals being reduction of carbon dioxide (CO2) and pollutants i.e., particulates matter, nitrogen oxides (NOx)… The last ones are toxic but latest enhancements in combustion and after-treatments have reduced the issue to very low

[1] Guillaume Hébert, Hanon Systems Autopal Services s.r.o., Závodní 1007, 687 25 HLUK, Czech Republic, ghebert4@hanonsystems.com

level [1]. Hence, the main focus has been on CO2 improvements through massive BEV's introduction to the passenger fleet at first, possibly later to medium and heavy duty (and further later to other transportation systems as aviation).
When different solutions were initially investigated by scientists and engineers, politicians from several countries e.g., European Union, United Kingdom, California [2] etc., have pre-empted BEV's as a silver bullet technology to cope with climate change emergency, as far as personal transportation is concerned, including coercive ("zero emissions" city zones) and incentive (bonus to buy BEV's) measures to persuade or force consumers to that direction.
However, those decisions are still being discussed [3] and BEV's sales seem to be lagging vs. exponential predictions of electric proponents. Why that? From the author point of view, there are four main arguments to explain questions on the electrification path:

A. Users anxiety: range vs charging and price
B. Industry anxiety: sovereignty and cost competitiveness, especially US / EU vs China
C. The ecological interest of BEV's, including CO2 Life Cycle Assessment (LCA) in real conditions
D. The question of resource availability i.e., energy (electricity generation) and minerals, to support electrification

Point A has been in deep discussed, including the author itself [4]. Point B goes far beyond technical question and can be seen as an economical consequence of the two last points, which will therefore be discussed in the rest of this paper, presenting the current context and trying to draft what should be done if the pre-empted BEV technical choice has to make sense.

2. THE LIMITS OF BEV'S ECOSYSTEM

2.1 Life Cycle Assesment (LCA) of electric vehicles

Current status of legislations is mostly based on "Tank to Wheels" approach i.e., considering solely the emission being created by vehicle powertrain usage [5]. Even some new regulations tend to extend the definition by including other sources (e.g., tyres and breaks [6]), it still fails to capture the full scope of emissions related to this usage (including production of the vehicle, generation of the energy carrier and recycling). Advantage of the "Tank to Wheels" is that it is pretty simple to implement. Conclusion of such approach is pretty in favour of BEV's, which can be wrongly considered as "Zero Emissions Vehicles". However, simple LCA as proposed by Morkus et al. [7] demonstrates that the condition of such results are more complex and may not be quickly achievable everywhere and quickly. Burton et al. [8] have reached similar conclusions, introducing further sophisticated considerations on electricity grids exchange in the USA.

In a previous paper [9], the author listed the main factors impacting the mileage to be driven by a BEV's to be CO2 beneficial in regards of other powertrains (pure gasoline, Full Hybrid and Plug-In Hybrid) for the same vehicle type (similar mass and aerodynamics):

- Intra-automotive factors (i.e., fully resulting from vehicle engineering):

- Battery capacity C_{batt}: ranging from 30 to 130 kWh
- Vehicle energy consumption, *CONSO*: from 12 to 20 kWh/100km
- Energy lost for heating and cooling, η_{AC_heat}: from 7 to 30%

- Border line factors (i.e., partially under automive engineers technical choices):
  - Energy intensity of batteries production, α: from 50 to 200 kWh to produce 1 kWh of battery capacity. Depends of the manufacturing processes as well as the chemistry choice (e.g., LFP vs NMC, hence a clear link to the minerals)
  - Energy lost during charging, $\eta_{charging}$: from 6 to 18%. Depends of the type and design of the charging station, on-board power-electronic design, as well as consumer habits (e.g., low speed home AC charging vs high speed public DC)

- Fully external factors (i.e., not under automotive engineers control):
  - Electricity carbon intensity at the batteries production site, f_{prod}: from 35 to 500 gCO2eq./kWh
  - Electricity carbon intensity during usage, f_{usage}: from 35 to 500 gCO2eq./kWh

The extremes values for each factor have been chosen to represent what is currently the best (red) and worst (Blue) achievable scenarios (typically the range indicated abive). A sensitivity analysis, presented in *Figure 1*, displays the effect of those extreme inputs to the breakeven point (mileage after which a BEV displays lower overall CO2 emissions that Spark ignition equivalent) when compared to a KIA NIRO baseline (0% line) of the following characteristics:

- C_{batt} = 64.8 kWh [10]
- *CONSO* = 14.1 kWh/100 km [10]
- η_{AC_heat} = 1.1 [9]
- α = 111 [7]
- $\eta_{charging}$ = 1.15 [9]
- f_{prod} = 250 gCO2eq./kWh, which represents current EU average
- f_{usage} = 250 gCO2eq./kWh, which represents current EU average

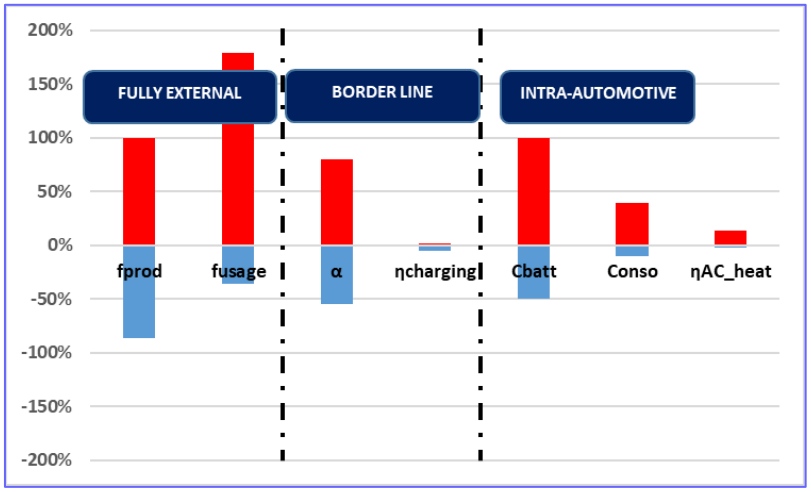

Figure 1: *BEV's CO2 footprint LCA conditions sensibility analysis*

If we focus on the four most sensible parameters, only one of them (C_{batt}) is purely in the hands of automotive engineers. Said differently: the most optimized BEV considered separately, out of its "ecosystem", may not provide significant benefits (in terms of CO2 emissions) if factors external to the scope are degraded to a point that overrun the advantages.
If BEV transition has to be a success, in term of significantly reduced CO2 emissions, then only if the system "vehicle" is considered as a sub-part of a "system of systems", which includes on top electricity generation and distribution, charging infrastructure, availability of required minerals etc. What has to be optimized is the "system of system" as a whole and not the sub-system "vehicle" only.

Therefore, the rest of this paper will focus on two main technical limitations: the availability of low-carbon electricity and of the necessary minerals to manufacture, at scale, BEV's, systems for generation, transport and distribution of electricity.

2.2 Limitations on electricity generation

As seen in previous section, the CO2 intensity factor of electricity consumed during BEV usage, *f*, is a significant factor impacting their carbon footprint. But how to calculate it? The easiest and very often used way is to consider average number e.g., yearly, for the country / region considered. But this approach is not satisfactory for different reasons that we will explore.

As a started, let's remind the condition of electricity grid stability (in tension and frequency):

$$Demand\ [W] = Supply\ [W] = Production + \left(Storage_{depealing} - Storage_{charging}\right) + (Import - Export) \quad (1)$$

Let's now deep dive into the term of the equation. The baseline is that, at each time t, the demand equals the supply. This most obvious solution is to adapt the production to meet the demand. But it is not always possible when the demand is high (exceeding maximum installed capacity) or low (some generation means need to continue to generate at minimum load) or too fast.
Hence, there are s-called interconnections between national grid, enabling European balancing at continental scale (in the equation this is the term IMPORT – EXPORT).
Last but not least, operators may dispose of possibilities to store a certain amount of energy.

Massive introduction of BEV's and renewable electricity sources create some issues:

- Demand increase (as other usage will not stop because of BEV's introduction). Requires production strong increase, as the import from interconnections will probably not be available, each countries facing same challenges without too much reserve [11]
- As it can be seen in *Figure 2*, increasing demand lead to call less clean generation means on the grid, more often, through merit increase (operators first called on the grid clean / less expensive generation means and only called the expensive / more emitting ones if needed). Leading to a degradation of the factor *f*. This marginal effect (f linked to the incremental demand > f average > f

average before the demand increase) has to be considered as a factor in BEV's LCA calculation

- Often prospective studies are just extrapolating past trends to project carbon intensity future reduction. However, as the deployment of BEV's can be much faster than deploying new energy (power generation units, grids…) infrastructures, brutal demand increase may not drive to any reduction
- Energy storage, even Li-Ions Giga packs of V2G, will remain insignificant to the total amount of energy consumed
- Massive renewable sources adaption create significant additional variability on supply and also demand (when PV produce, you want to inject to the grid with priority. But when not, then the grid is missing your input + your auto-consumption)

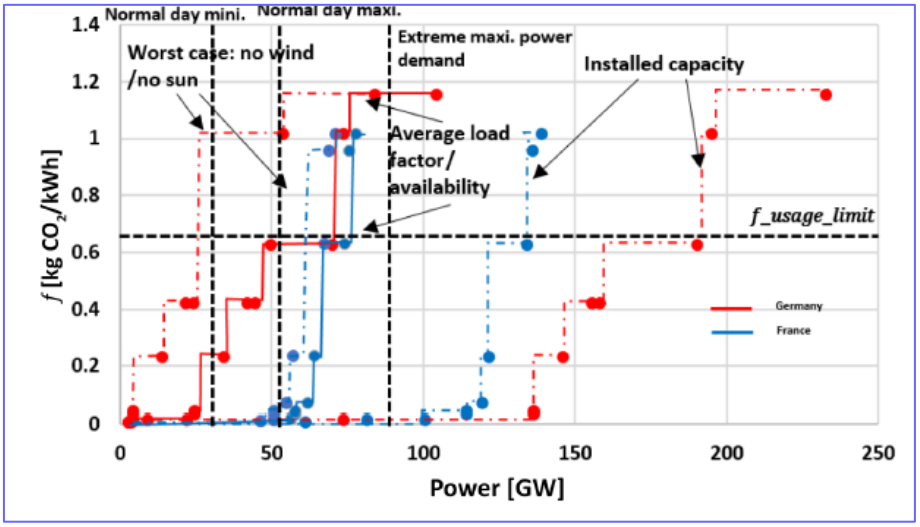

Figure 2: *Aggregated power generation curve, per merit order for France and Germany [9]*

Therefore, current electric system has a maximum limit for BEV adoption if we still want to carbon balance to be beneficial vs conventional powertrains, as it can be seen in *Figure 3*.

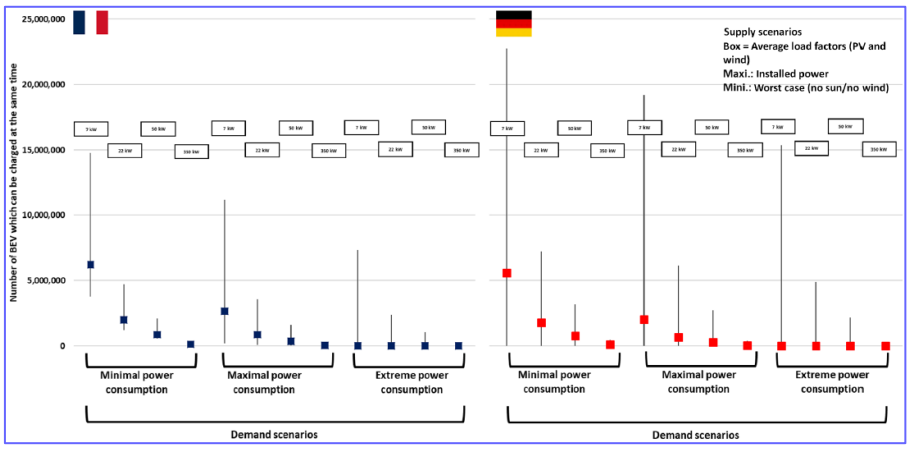

Figure 3: *Amount of BEV's that can be charged at same moment to fulfil condition f ≤ f_usage_limit, for different supply and demand conditions [9]*

2.3 Limitations on minerals

In collective imagination, mining is connected to the industrial revolution, deep, messy, dangerous work, liked in Emile Zola's novel *Germinal*. Also, former mining areas (as well as heavy industry like metallurgy) are often connected with ecological burdens. Therefore, it is understandable that the western world has pushed mining far from itself, thanks to globalization of the economy. "Out of sight, out of mind": was the problem solved?

Nowadays, two things are fundamentally changing our view on mining and minerals:

- Electrification of everything will require much more minerals, including for BEV's manufacturing as shown in *Figure 4*.
- New geopolitical tensions in parallel of demand growth for relatively rare resources (at least for the deposit which are sufficiently concentrated, easy enough to be economically exploited). Coupled with not even distribution of those resources and the industrial tools to exploit and transform them, the situation raised to what is called a "race for minerals", described in *Figure 5* & *Figure 6*. Some countries got early situation awareness and have set-up adequate strategy to secure value chain, as demonstrated by this famous quote from former Chinese president Deng Xiaoping in 1987: "The Middle East has oil, China has rare earths"

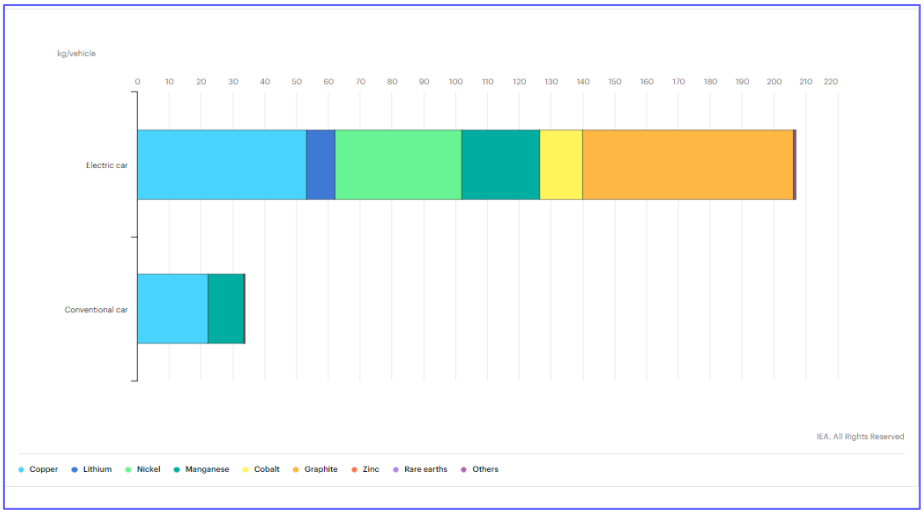

Figure 4: *Metal and mineral necessary - Comparison EVs vs ICE [12]*

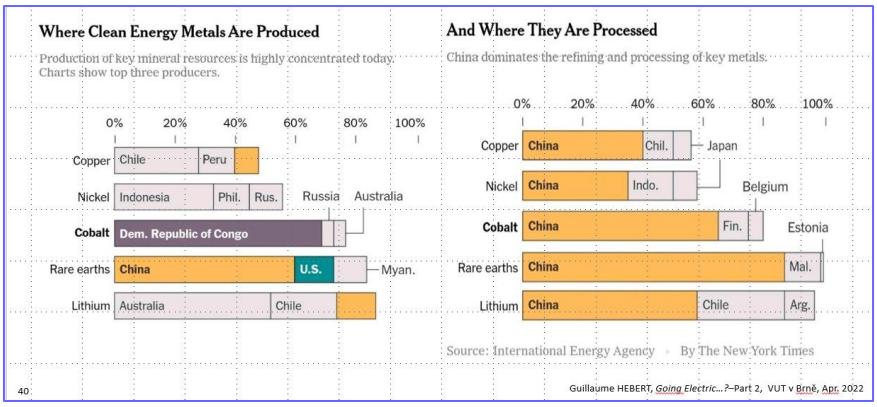

Figure 5: *Critical elements for clean energy transition [13]*

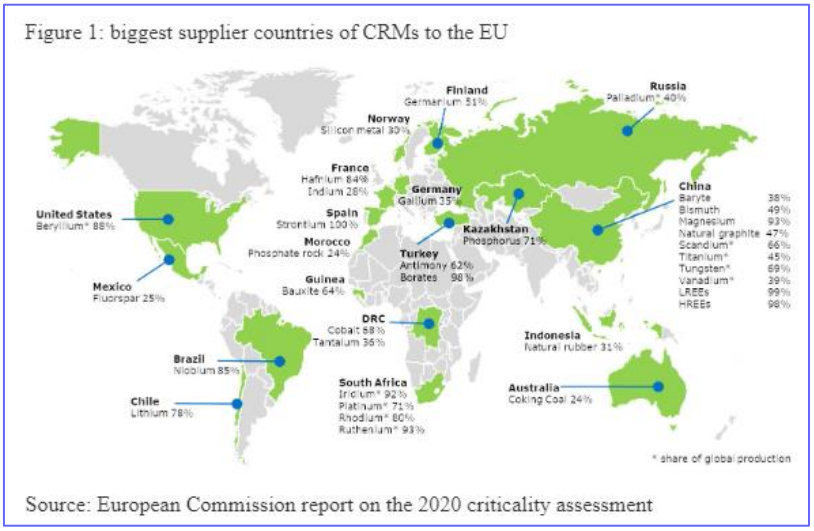

Figure 6: *Biggest supplier countries of CRM's to the EU [14]*

This drove certain consequences that we are starting to see in practice and highly impact the whole industry and in particular automotive:

- Establishment in various region of list of Critical Raw Materials, as per *Figure 7*.
- Update the geological inventory of mineral resources, a premiere since half century for certain countries like France for instance
- Plan to open new mines e.g., lithium in France [16]. However, it comes with various complications:
    - Long lead time (up to 15 years) between exploration and operation of a new mines, hence it requires anticipation
    - Project acceptance. Paradoxically, environmentalist groups are not in support of new mines needed to electrify everything, despite the fact that electrification is seen as a major path toward climate change mitigation…
- Securization of value chains. Example of Li-ions batteries for automotive: diplomacy (agreement with governments of countries having resources) is a prerequisite to the exploration and the extraction of the resource. But complete value chain securization should also including refining, manufacturing of cells (using several minerals), manufacturing of modules & packs and finally assembly on vehicle. The numerous projects being celebrated in mass media as "giga-factories" start mostly with cells or modules production. If this is better than nothing, it is by far not securing the supply to European industry!

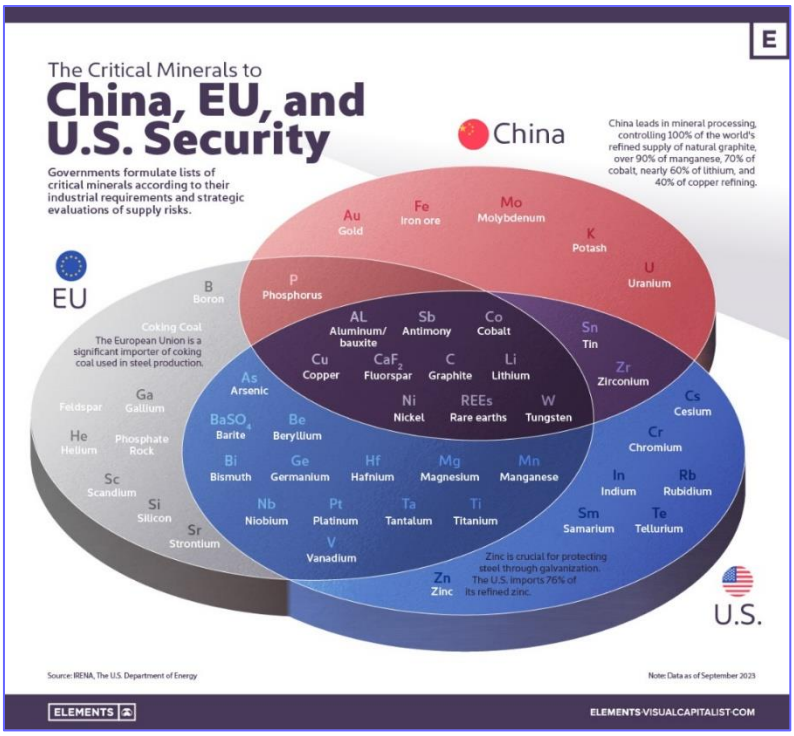

Figure 7: *The critical Minerals to China, EU, and U.S. Security [15]*

Reducing dependency to mineral resources does not only pass through securing new deposits but should also go through 4R (Repaire / Reuse / Recycle / Reduce). Below is an example of this method applied to an automotive radiator:

- Repaire = change isolators / manifolds if deformed during low speed crash
- Reuse = if the vehicle is scrapped and radiator OK = re-use it as spare part
- Recycle = Aluminium to be separated and use back in alloy to make new parts. It is necessary to make a distinction between re-cycling for the same usage or not (conservation of mechanical properties) which leads to different process: mechanical or chemical recycling [18]
- Reduce: reduce Aluminium usage through down-gaging or size reduction by improving thermal efficiency

In other way, we should also think of closing the loop. From this perspective, example of other area, liked Uranium cycle [19] can be inspiring.

3. CONCLUSION

Contrary to a generally accepted opinion, electrification of mobility, and especially BEV's, is neither good nor bad. Making it beneficial in the context of fighting global warming requires certain conditions to be fulfilled: marginal carbon intensity at both battery production and usage sites to be as low as possible, lowest energy intensive process for battery cells production, limited battery capacity, optimized vehicles energy consumption including in cold and hot weather, for the most significant ones.
When some are under automotive R&D control, others are not: therefore the system "car" should holistically considered in a system of systems which at minimum should include considerations on electricity generation and distribution and minerals mining and processing.

It is interested to note, that car makers are pushing that directions: they do already require minimum level of recycles metals, minimum level of parts to be re-usable or recycled and quota of renewable energy consumption. However, suppliers and their supply-chain do have huge problems to commit. Just to quote an example, there is not enough amount of high value recycled aluminium to already fulfil the demand as per today.
This tension is easily explained by the different dynamics behind automotive, energy and mining sectors: when the 2035 ICE-ban target corresponds roughly to 2 generations of vehicles, giving room for optimization, it is hardly enough to bring new electricity generation supplies or open new mines and refining facilities.
Further to that, the “electrify everything” strategy, does not only drive automotive but other sectors as heavy industry, domestic application (replacement of natural gas heaters), creating competitions between those fields in a context of faster increasing demand vs supply.

REFERENCES

[1] Study of Euro 6d-TEMP emissions – IFPEN for DGEC, IFPEN, 2020. https://www.ifpenergiesnouvelles.fr/sites/ifpen.fr/files/inline-images/Innovation%20et%20industrie/Motorisations%20thermiques/Study-of-Eudo-6%20d-TEMP-emissions_IFPEN-DGEC_SynthesisReport_Dec2020.pdf

[2] International Energy Agency. Gobal EV outlook 2023: policy developments , IEA, 2023. https://www.iea.org/reports/global-ev-outlook-2023/policy-developments

[3] VELA J.H., POSANER J. Top EU commissioner calls for ‘no taboos’ review of 2035 car ban, in POLITICO, 2022. https://www.politico.eu/article/breton-says-u-turn-on-eus-2035-car-engine-ban-isnt-taboo/

[4] HEBERT G. What are the peoples waiting to buy BEV vehicles ?, self-published, 2019. https://www.linkedin.com/pulse/what-peoples-waiting-buy-bev-vehicles-guillaume-hebert/?trackingId=M2auEry7SlCTBnDaBaWsbA%3D%3D

[5] European Commision, CO_2 emission performance standards for cars and vans (EU) 2019/631, https://climate.ec.europa.eu/eu-action/transport/road-transport-reducing-co2-emissions-vehicles/co2-emission-performance-standards-cars-and-vans_en

[6] European Council, Euro 7: Council adopts new rules on emission limits for cars, vans and trucks, 2024. https://www.consilium.europa.eu/en/press/press-releases/2024/04/12/euro-7-council-adopts-new-rules-on-emission-limits-for-cars-vans-and-trucks/

[7] MORKUS J., MACEK J. *Kam kráčíš, elektromobilito?* Czech Technical University in Prague, 2020. https://www.fs.cvut.cz/verejnost/pr-media/pribehy-z-ustavu/kam-kracis-elektromobilito/

[8] Burton, T., Powers, S., Burns, C., Conway, G. et al., "A Data-Driven Greenhouse Gas Emission Rate Analysis for Vehicle Comparisons," SAE Int. J. Elec. Veh. 12(1):2023, https://doi.org/10.4271/14-12-01-0006.

[9] Hébert, G., “Light-Duty Vehicles Electrification: Carbon Dioxide Reduction Impact Potential and Considerations of Its Effect on Electricity Generation System,” SAE Technical Paper 2023-01-5054, 2023, doi:10.4271/2023-01-5054. https://www.sae.org/publications/technical-papers/content/2023-01-5054/

[10] KIA. (2020b, January 1). https://www.kia.com/cz/modely/niro-ev/objevte/?cmpid=ppc|Kia_Search-Longterm_DFD_2020-01-01_2020-12-31_CZE_EEU_KML_CSK_Models|google|generic|147705784447

[11] Futurs énergétiques 2050 : les scénarios de mix de production à l’étude permettant d’atteindre la neutralité carbone à l’horizon 2050. (2022). In Rte. Rte. Retrieved February 13, 2023, from https://www.rte-france.com/analyses-tendances-et-prospectives/bilan-previsionnel-2050-futurs-energetiques

[12] International Energy Agency, Minerals used in electric cars compared to conventional cars, 2021. https://www.iea.org/data-and-statistics/charts/minerals-used-in-electric-cars-compared-to-conventional-cars

[13] International Energy Agency, The Role of Critical Minerals in Clean Energy Transitions, 2021. https://www.iea.org/reports/the-role-of-critical-minerals-in-clean-energy-transitions

[14] European Union, Critical raw materials, 2023. https://single-market-economy.ec.europa.eu/sectors/raw-materials/areas-specific-interest/critical-raw-materials_en

[15] VENDITTI Bruno, ABOULAZM Zack, The Critical Minerals to China, EU, and U.S. National Security, Visual Capitalist, 2023. https://elements.visualcapitalist.com/the-critical-minerals-to-china-eu-and-u-s-national-security/

[16] Ce granite pourrait servir à fabriquer des batteries - Monsieur Bidouille, 2024. https://www.youtube.com/watch?v=Vhgih6ft6es

[17] Commisariat à l’Energie Atomique, Comment recycler les matériaux des batteries, 2021. https://www.youtube.com/watch?v=WuRw8wn3JaY

[18] HEBERT G., Uranium Cycle, in Mister G. (self published), 2024. https://www.instagram.com/p/C4EHewaMWms/?igsh=eTF3MmU0Y3NvOXR3

55. mezinárodní vědecká konference zaměřená na výzkumné a výukové metody v oblasti vozidel a jejich pohonů

září 5. - 6., 2024 – Liberec, Česká republika
Technická univerzita v Liberci
Fakulta strojní, Katedra vozidel a motorů

DYNAMIC SIMULATIONS OF ELECTRIC MOTOR FOR MILD-HYBRID POWERTRAIN

Kateřina Fridrichová[1], Lubomír Drápal[2], Michal Ušiak[3]

Abstract
Dynamic simulations of mild-hybrid powertrains tend to focus on internal combustion engines due to higher NVH compared to electric motors. On the contrary, this paper focuses on the effects of radial and tangential forces of a specific electric motor that is used in mild-hybrid powertrain. This motor is usually connected via belt on the front end of the crankshaft. The aim of the paper is also to provide comparison of two approaches to the dynamic simulations and to evaluate the influence of using flexible bodies in this kind of analysis.

[1] Kateřina Fridrichová, Institute of Automotive Engineering, Brno University of Technology, Technická 2896/2, 616 69, Brno, Czech Republic, e-mail: Katerina.Fridrichova@vutbr.cz
[2] Lubomír Drápal, Institute of Automotive Engineering, Brno University of Technology, Technická 2896/2, 616 69, Brno, Czech Republic, e-mail: drapal@fme.vutbr.cz
[3] Michal Ušiak, Institute of Automotive Engineering, Brno University of Technology, Technická 2896/2,616 69, Brno, Czech Republic, e-mail: Michal.Usiak@vutbr.cz

1. INTRODUCTION

Electric motors are widely used in automotive applications. Recent rise of production of battery electric vehicles (BEV) and hybrid electric vehicles (HEV) leads to new challenges and areas that need more attention. The most common type of electric motor used in vehicles is permanent magnet motor. It has been implemented to the powertrain due to high efficiency, high power/torque density and low vibration and noise [1].

The main sources of NVH issues for electric motors are magnetostriction of core lamination, mechanical noise and the radial forces acting on stator [2]. Torque is produced by applying a current to one of the phase windings which pulls the rotor into a new position. The stator resonates with a damped vibration at its natural frequency. The tangential forces are smaller than radial forces, however, they should not be neglected. Tangential motions of tooth tips are often many times larger than the radial motions in important natural modes of machine vibration [3]. Tangential load can interact with radial load in a complex way depending on the associated spatial order [4].

The electromagnetic vibration is a parasitic effect of electric motors. The vibration is created by the Maxwell pressure (electromagnetic forces) which is applied to the interface between the air gap and stator inner surface [4]. The importance of stator vibration is a design consideration. The engineers should predict accurately the vibration that would be associated with a given design.

Dynamic analyses of hybrid powertrain usually focus on the internal combustion engine, however, the excitation of mechanical structure of the motor by electromagnetic exciting force and its harmonics should be also further investigated to understand the complexity of the system. Even though some researchers have already published studies dealing with vibration of electric motors, the topic is still not well-covered and it needs further investigation. A finite element multi-physics model is necessary for this kind of investigation [5].

The study described in the paper is a part of dynamic analysis of the whole hybrid powertrain with cylinder deactivation. The motor should help to mitigate vibration of internal combustion engine by torque smoothing [6]. The multi-physics model of this motor should also help to create methodology for evaluating dynamics of electric motors. This electric motor is a belt starter/generator used in mild-hybrid powertrains with 48V technology. The whole system consists of 48V battery, low-voltage DC/DC converter and the permanent magnet synchronous motor that is connected via belt to a pulley on the crankshaft. The peak power of the motor is 9 kW for motor mode and 12 kW for generator mode. The peak torque of the motor is 40 N·m.

2. DYNAMIC SIMULATIONS

Multibody simulations are an effective tool for studying vibration, friction losses, bearing loads and the like. Additionally, electromagnetic simulations must be conducted to obtain the necessary input data.

2.1 Electromagnetic simulations

These simulations are carried out in Ansys Maxwell. The stator and rotor geometry is imported from CAD and the stator winding is added in the Ansys environment. The stator has 96 slots with two conductors in each slot. It is U-Pin rectangular hairpin winding with two star couplings. Three phases are used for motor mode and three for generator mode. The angle between them is 30°. The model could be seen in Figure 1.

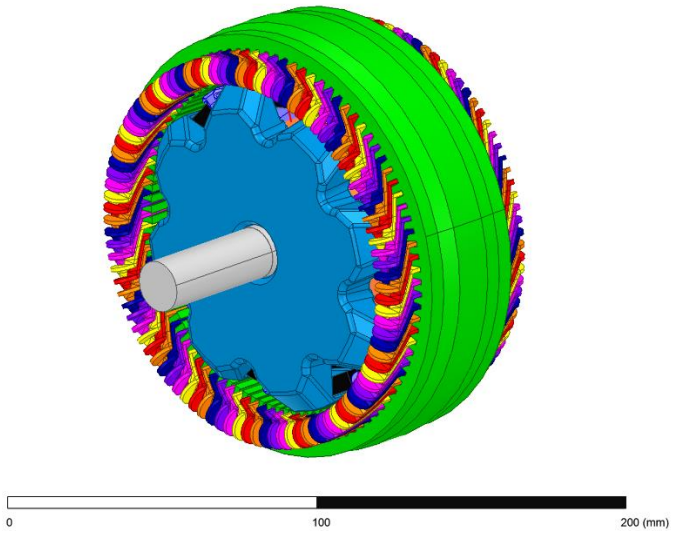

Figure 1: *Model of electric motor in Ansys Maxwell*

The rotor is similar to standard alternator rotor with claws. Figure 2 shows the rotor with outlined stator. There is a coil in the middle of the rotor part as well as 16 magnets placed between the claws. The connection was modelled in Maxwell Circuit Editor. Ansys Maxwell uses its own meshing algorithm. The mesh in the air gap has to be refined.

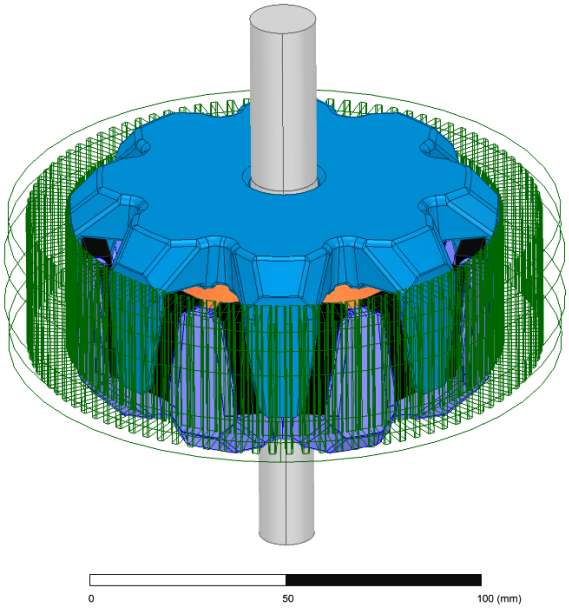

Figure 2: *Rotor including coil (orange) and magnets (black)*

The aim of this simulation is to obtain radial and tangential forces that act on stator teeth. These forces as well as the torque of the motor are exported and used as an input for multibody simulations.

2.2 Multibody simulations

The results are obtained by simulations using FEV Virtual Dynamics software, which uses the core technology of Hexagon Adams. The model contains flexible bodies meshed in ANSA and the modal reduction was carried out in Nastran. The meshed rotor is shown in Figure 3. The parts of the meshed rotor (the coil, the magnets and the shaft) are connected with RBE2 elements and the model contains three interface nodes, two for bearings and one for force application. Interface nodes are nodes for load application in multibody simulations and they are connected via RBE3 elements with the structure.

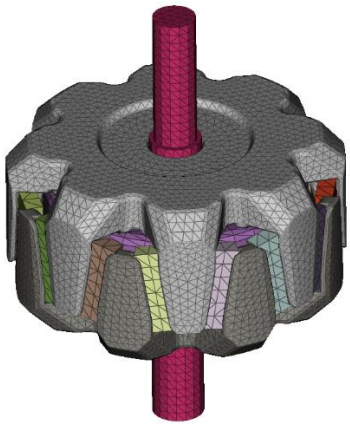

Figure 3: *Meshed rotor assembly*

The stator itself is connected to the housing with contact. The two parts of the housing are connected via RBE2 elements. The stator model includes two interface nodes for bearings, two for mounting the motor and 96 interface nodes for force application on each of the stator teeth. The meshed assembly and the separate stator are shown in Figure 4.

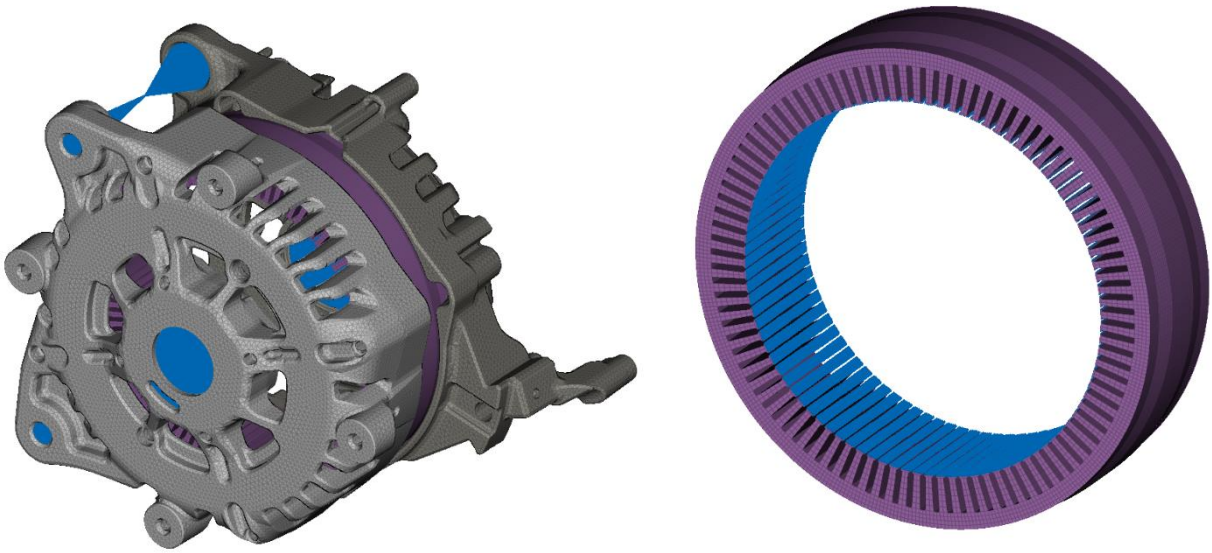

Figure 4: *Meshed stator (left) and meshed rotor (right) with RBE3 elements (blue)*

The multibody model is firstly modelled only with rigid bodies. The stator and rotor are then replaced by obtained modal neutral files. Radial and tangential forces data are determined for each stator tooth separately. The flexible stator is necessary for this load application. The final computational model is shown in Figure 5.

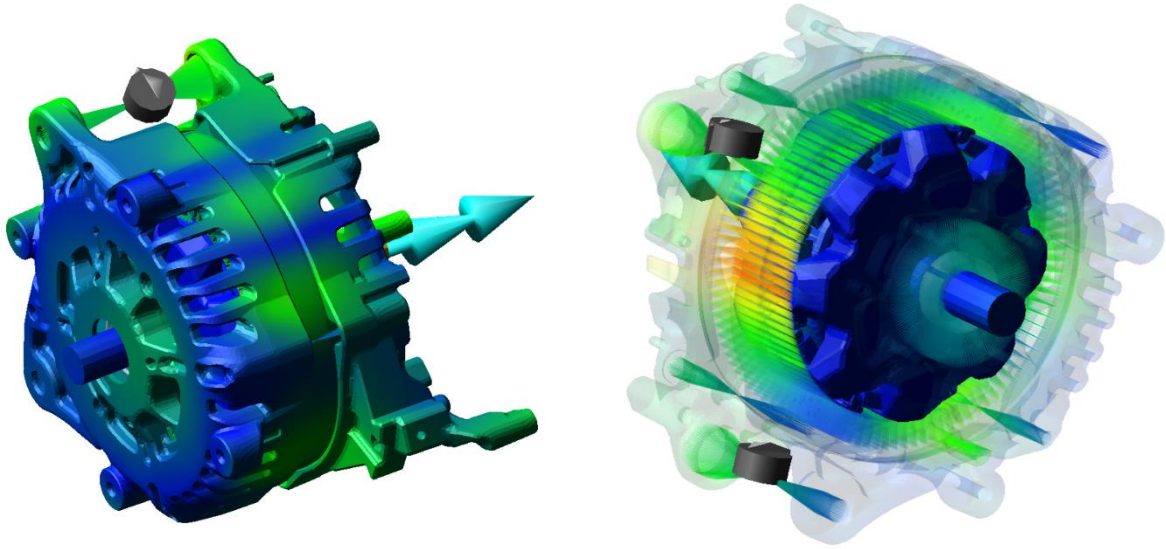

Figure 5: *Multibody model in Virtual Dynamics environment*

2.3 Results

The main goal is to study the effect of radial and tangential forces on torsional vibration. The simulation with rigid bodies does not include these forces. The current simulation with flexible bodies shows a noticeable ripple in angular velocity of the shaft caused by radial and tangential forces. However, this model does not include eccentricity yet. This effect should be added in later stage of the study. The presented results of the steady-state simulation for 6000 rpm are shown in Figure 6.

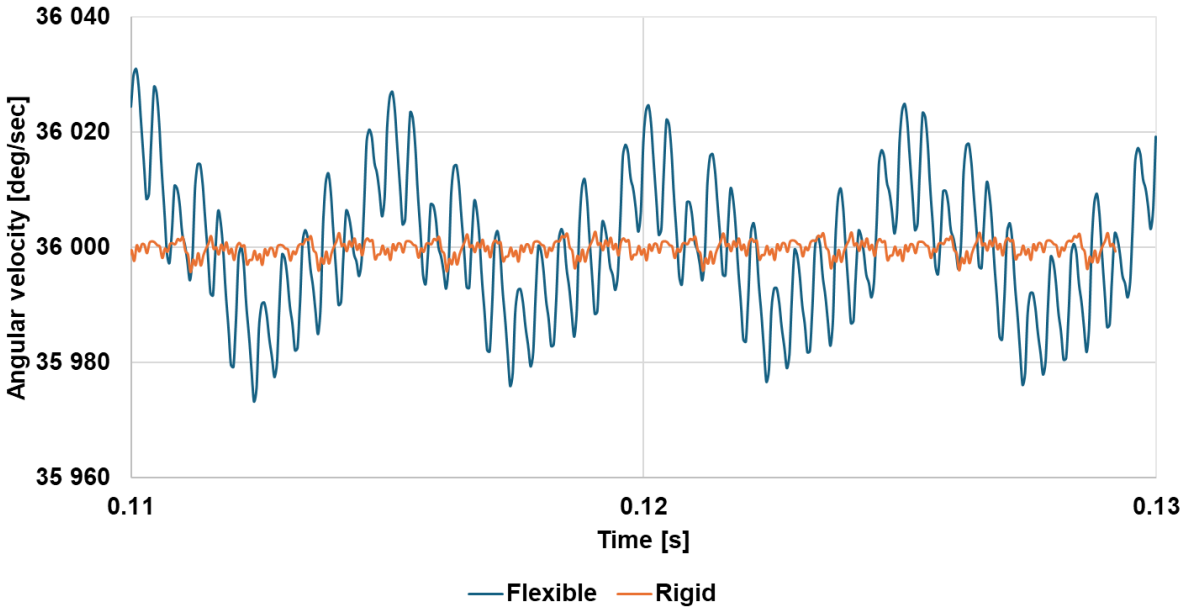

Figure 6: *Angular velocity of the rotor shaft (near pulley) at 6000 rpm*

The electric motor is a part of a hybrid powertrain. The corresponding engine speed would be approximately 2400 rpm. The torque of the system is set as the maximum possible torque for the given angular velocity, in this case 15 N·m. The simulation is carried out for different angular velocities, however, the trend of the results remains the same. As an example, the results for 3000 rpm is shown in Figure 7.

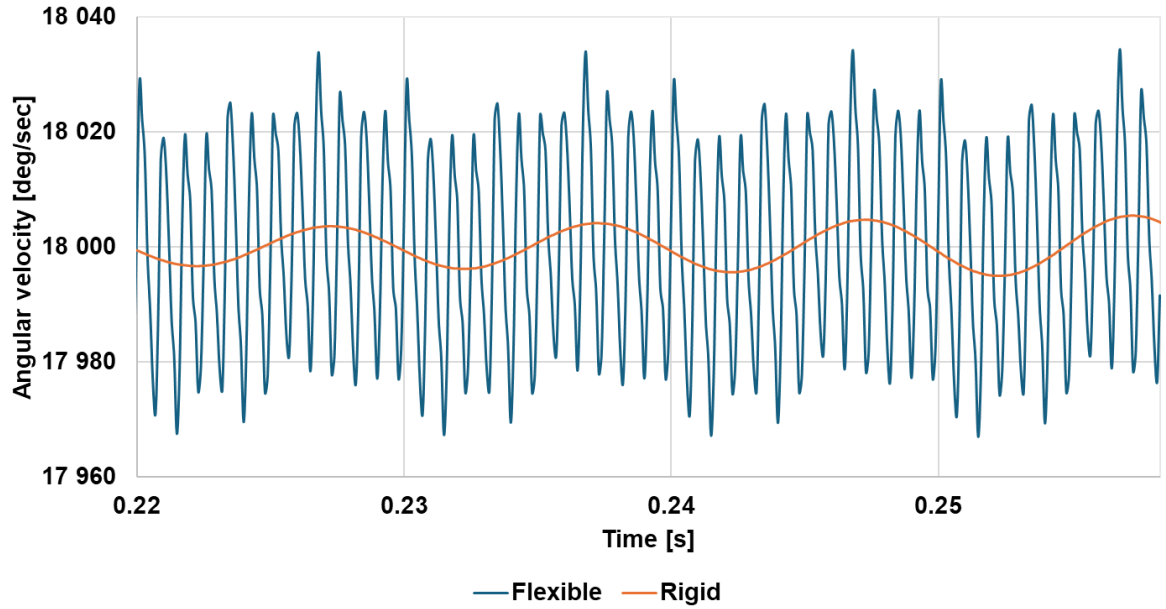

Figure 7: *Angular velocity of the rotor shaft (near pulley) for 3000 rpm*

Multibody simulations could be a useful tool for assessing the load on bearings. The bearing loads for 6000 rpm are shown in Figure 8.

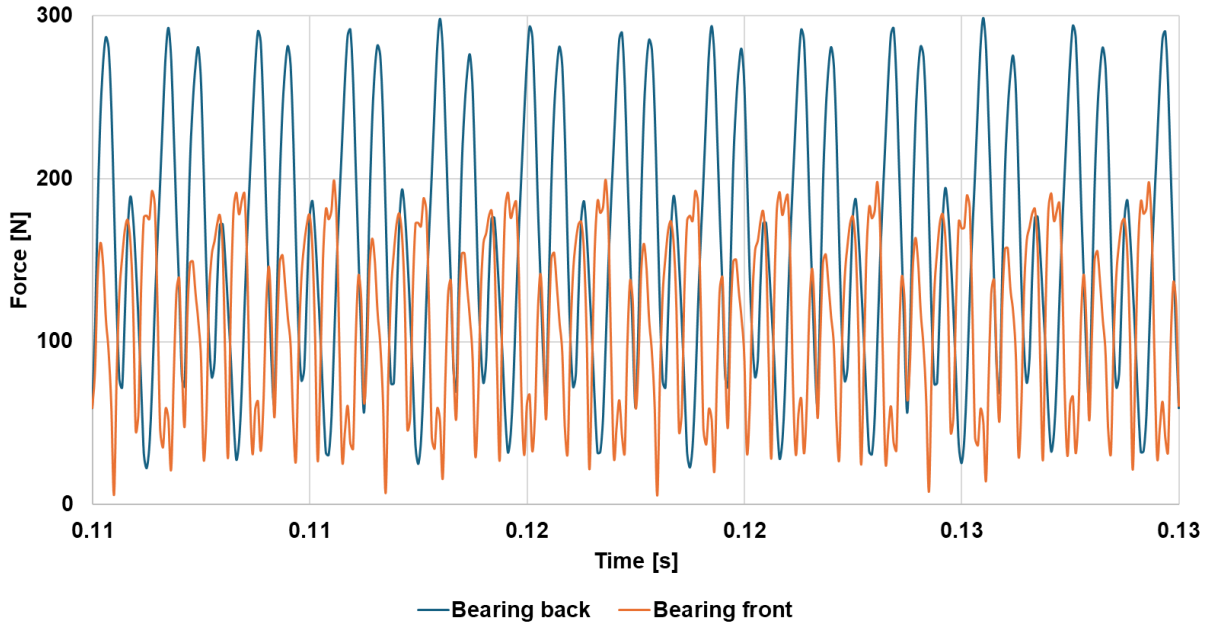

Figure 8: *Force magnitudes acting on rotor shaft bearings*

3. CONCLUSION

The multibody analysis proved to be a useful tool for assessing the dynamics of electric motors. The difference between the simulation with rigid and flexible bodies show the necessity of including the radial and tangential forces in the computational model. The results could be further used for harmonic analysis to describe better the torsional vibration of the system. This project serves more as a tool for creating a methodology due to the fact that the vibration of this motor in mild-hybrid powertrain would be negligible compared to the internal combustion engine. This is only an early stage of the project. The next steps would include refining the electromagnetic model and assessing the torsional vibration in more detailed manner.

REFERENCES

[1] WU Z., FAN Y., CHEN H., WANG X., LEE C. H. T. Electromagnetic Force and Vibration Study of Dual-Stator Consequent-Pole Hybrid Excitation Motor for Electric Vehicles. IEEE Transactions on Vehicular Technology. 2021, 70(5), pp. 4377-4388. ISSN 0018-9545. DOI: 10.1109/TVT.2021.3075461

[2] JIAN L., XUEGUAN S., YUNHYUN C. Comparison of 12/8 and 6/4 Switched Reluctance Motor: Noise and Vibration Aspects. IEEE Transactions on Magnetics. 2008, 44(11), pp. 4131-4134. ISSN 0018-9464. DOI: 10.1109/TMAG.2008.2002533

[3] GARVEY S.D. Tangential forces matter. 9th International Conference on Electrical Machines and Drives. 1999, pp. 174-178. ISBN 0852967209. DOI: 10.1049/cp:19991013

[4] HALLAL J.; RASID A. H., DRUESNE F., LANFRANCHI V. Comparison of radial and tangential forces effect on the radial vibrations of synchronous machines. 2019 IEEE International Conference on Industrial Technology (ICIT). 2019, pp. 243-248. ISBN 978-1-5386-6376-9. DOI: 10.1109/ICIT.2019.8755241

[5] HONG J. F., GUI L., CAO J. C. An Investigation of Tangential Force and Radial Force in PM Motor by means of FEM-simulation. 2022 International Conference on Electrical Machines (ICEM). 2022, pp. 2009-2014. ISBN 978-1-6654-1432-6. DOI: 10.1109/ICEM51905.2022.9910714

[6] WILCUTTS M., NAGASHIMA M., EISAZADEH-FAR K., YOUNKINS M., CONFER K. Electrified Dynamic Skip Fire (eDSF): Design and Benefits. 2018, DOI: 10.4271/2018-01-0864

ACKNOWLEDGEMENT

This work was supported by the Faculty of Mechanical Engineering, Brno University of Technology. The authors gratefully acknowledge funding from the specific research on BUT FSI–S-23-8235.

55. mezinárodní vědecká konference zaměřená na výzkumné a výukové metody v oblasti vozidel a jejich pohonů

září 5. - 6., 2024 – Liberec, Česká republika
Technická univerzita v Liberci
Fakulta strojní, Katedra vozidel a motorů

INFLUENCE OF A CASING TREATMENT ON OPERATING PARAMETERS OF A CENTRIFUGAL COMPRESSOR

Jiří Vacula[1], Pavel Novotný[2], Petr Kudláček[3], František Kocman[4]

Abstract
Application of a casing treatment to centrifugal compressors is a possible way to influence their operating parameters such as compression, efficiency or aerodynamic noise. Based on experimental results, the implemented casing treatment showed an increase in isentropic efficiency at selected operating points and affected the compressor map width as well. These results are in an agreement with numerical simulations that predict this effect. The selected casing treatment design also affected the sound pressure level measured during the compressor operation. It is thus shown that casing treatment represent an interesting way leading to a noticeable influence on the compressor map.

[1] Jiří Vacula, BUT, Technická 2896/2, 616 69 Brno, Czech Republic, jiri.vacula@vutbr.cz
[2] Pavel Novotný, BUT, Technická 2896/2, 616 69 Brno, Czech Republic, novotny.pa@fme.vutbr.cz
[3] Petr Kudláček, BUT, Technická 2896/2, 616 69 Brno, Czech Republic, petr.Kudlacek@vutbr.cz
[4] František Kocman, BUT, Technická 2896/2, 616 69 Brno, Czech Republic, frantisek.Kocman@vutbr.cz

1. INTRODUCTION

Manufacturers of rotating machines try to ensure their high efficiency, reliability and trouble-free operation and low noise level. The requirement for low noise levels is now becoming increasingly important, particularly in the automotive sector. However, all requirements for the best possible performance of a given device are almost always confronted with production costs. In the case of the centrifugal compressor, which is the subject of the research here, improvements in operating parameters can be achieved through changes in the aerodynamic design. The standard procedure for aerodynamic design consists of an analytical analysis, the experience of the designer and subsequent detailed calculations using computational fluid dynamics tools. These include modifications to the shape of the impeller channel and the shape of the blades, selection of their number and other changes to other flow components. With regard to manufacturing and a certain conventionality, these shapes are usually smooth. However, do smooth walls represent the most aerodynamically favourable class of surfaces in terms of efficiency? An analysis of the dissipation of energy generated in the flowing fluid does not allow a clear conclusion to be reached, and instead suggests a certain complexity.

The fluid flow in centrifugal compressors is rather complex. It is well known that the aerodynamic conditions in, for example, axial compressors or turbines, are considerably less complex than in the case of a centrifugal compressors. A centrifugal compressor consists of an inlet pipe, impeller, diffuser and a volute. It is the impeller region that can be considered as a key part determining the operating parameters, since the impeller region is the place where the energy is transferred from the rotating surfaces of the impeller to the working fluid. It is therefore reasonable to assume that it is the impeller space that offers the greatest potential for increased efficiency and, in general, for changes in aerodynamic parameters.

Centrifugal compressors are, with few exceptions, almost exclusively designed as unshrouded wheels primarily to reduce their weight. Tip leakage losses are thus present in all operating conditions and their importance is higher in those operating conditions where the pressure difference between the pressure and suction sides of the impeller is dominant. The aerodynamic conditions in the tip clearance (TC) are characterised by very high velocities at the blade tip. This circumferential velocity is reduced to zero on the stator surface in a very small region, typically on the order of tens of millimetres. The velocity gradient is thus very high at this location. Therefore, it can be assumed that the TC offers the potential to influence the flow field inside the impeller channel.

Isentropic efficiency $\eta_{\mathrm{T-T}}$ is defined as

$$\eta_{\mathrm{T-T}} = \frac{\Delta H_{\mathrm{is}}}{\Delta H_{\mathrm{real}}}, \tag{1}$$

where ΔH_{is} and ΔH_{real} are ideal (isentropic) and real enthalpy differences between outlet and inlet of the compressor. The possible visual significance of defining the efficiency $\eta_{\mathrm{T-T}}$ can be seen in ***Figure 1***. It is worth noting that efficiency can also be defined as a ratio of enthalpy (or temperature) gradients based on static flow parameters or a combination of total and static values. These other definitions are based, for example, on whether or not the kinetic energy leaving the diffuser is viewed as lossy.

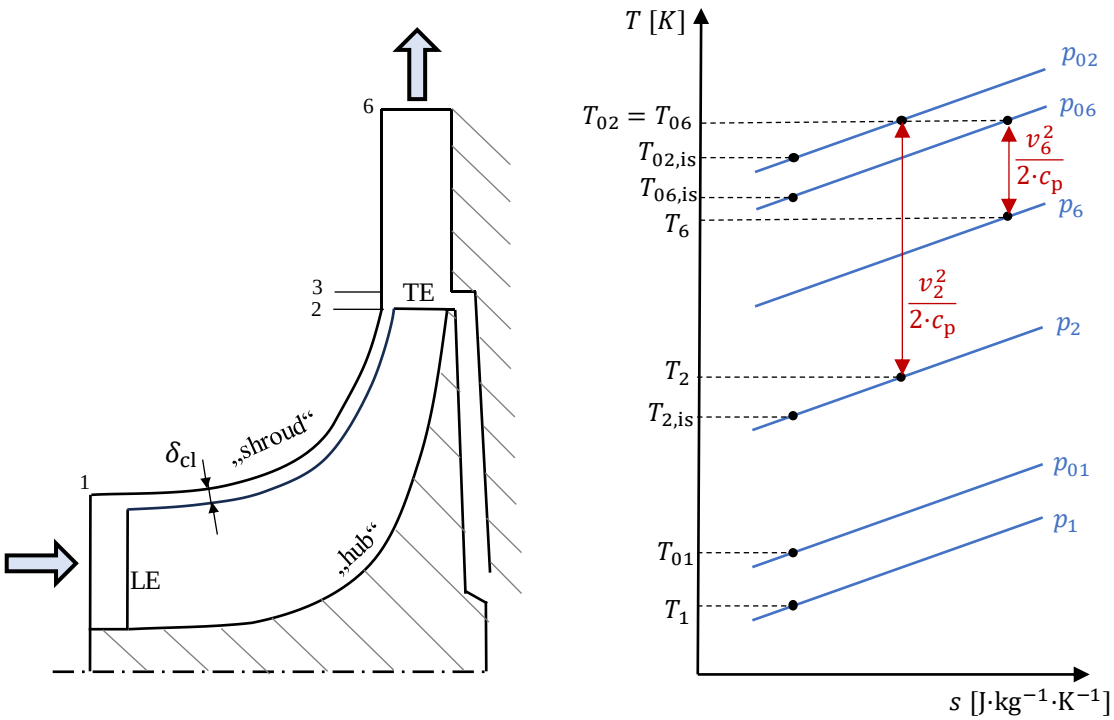

Figure 1 Basic scheme of a centrifugal compressor (left) and thermodynamic variables (right). Adopted from [1]***.***

2. METHODS

The effect of casing treatment is physically justified, as significant velocity gradients are present at this region. While a high circumferential velocity is present at blade tip, the velocity is zero at the stator. In addition, a significant static pressure gradient in the circumferential direction, i.e. between the pressure and suction sides of the blade, should also be mentioned.

2.1 State of the art

In the case of axial compressors, there are quite a few papers dealing with local modifications of the stator surface. This is mostly very extensive research carried out within the NASA organisation, which has subsequently been followed up by other research teams around the world. For example, as reported by Greitzer [2], in axial compressors, the design of grooves or even perforations of the stator surface at the point of interaction of the rotor blade with this stator has a beneficial effect on the stability of compressor operation. Based on a study conducted by Prince et al. [3], a positive effect has also been demonstrated when stator surface modification is used, with the most favourable effect assumed to be achieved when the stator modification accounts for 65% to 75% of the area in the nominal stator area without modification. In the comprehensive work of Osborn et al. [4], several casing treatments were experimentally tested in an axial compressor, see ***Figure 2***. Based on these results, it was concluded that, circumferentially grooved casing not only leads to a shift in the limit of stable compressor operation, but also may lead to a significant increase in efficiency. For example, on the speed line corresponding to 90 % of the design speed, there is an improvement in efficiency of 4 % and at the same time an extension of the

compressor's stable area at this speed by 9,3 %. On the other hand, the skewed slotted casing with closed slots modification, although resulting in a greater expansion of the compressor's stable area than the circumferentially grooved casing modification, resulted in an efficiency reduction of almost 5 % at the design speed. It is therefore clear that local modifications to the stator can significantly affect the initiation of undesirable flow structures. Fabri and Reboux [5] have shown a significant effect of deep circumferential grooves on the compression, efficiency and displacement of the minimum working area boundary of an axial compressor with low aspect ratio blades, especially at high rotor speeds. The grooves were 6 mm deep and the blade height was 10 mm. Very detailed data from measurements of the transonic compressor can also be found, for example, in Tesch [6].

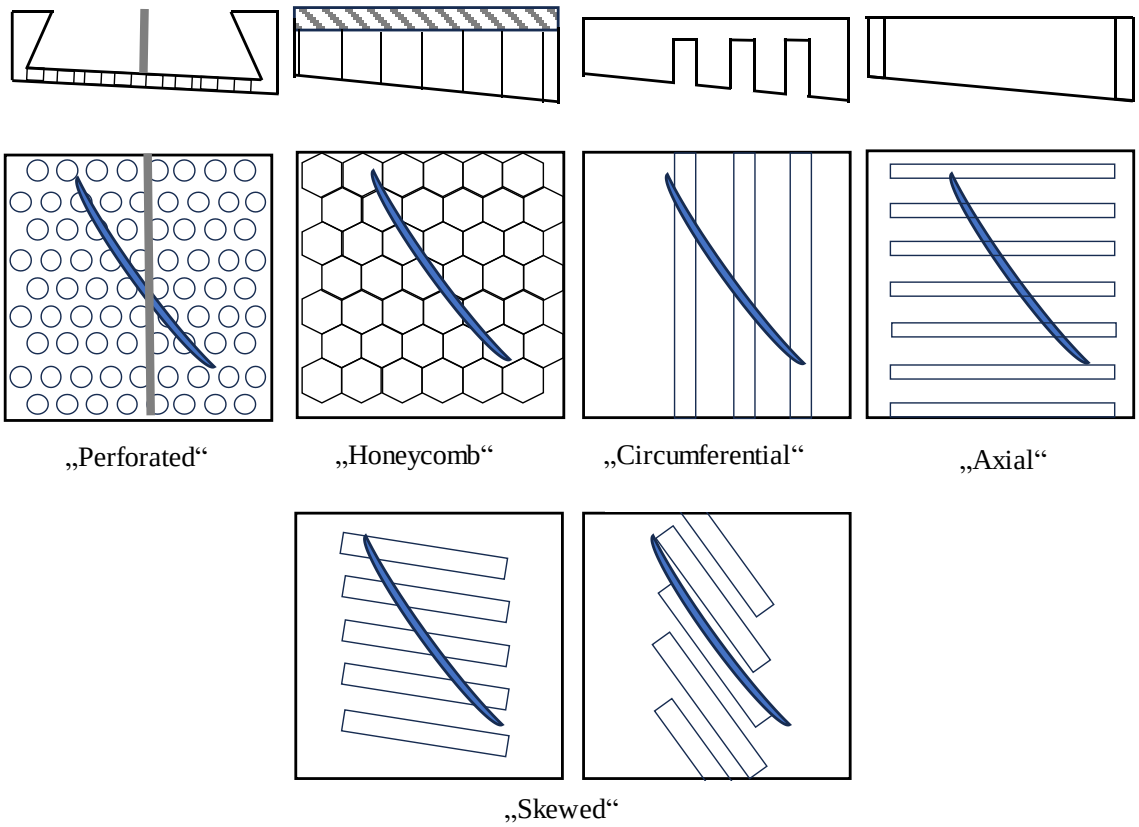

Figure 2 An overview of experimentally tested casing treatments type in the case of axial compressors. Adopted from [7]***.***

Sun et al. [7] pointed out that historically relatively fewer modifications to stator geometry have been implemented on centrifugal compressors than on axial compressors. This fact is probably a reflection of the fact, as stated for example by Khelladi et al. [8], that the aerodynamic conditions are more complex in centrifugal compressors than in axial compressors. However, In recent years increasing efficiency and operating range has become one of the main objectives in the development of centrifugal compressors for use in turbochargers. The requirement for greater flexibility of operation while maintaining the highest possible efficiency and low manufacturing costs has led to extensive research in this area. It should be noted, however, that in the case of centrifugal compressors, most modifications focus on the CT design in the impeller inducer region.

Interesting findings in terms of analysing the influence of the flow field when using circumferential grooves can also be found in the work of Bareiss et al. [9]. The modification made here consisted of creating relatively deep and narrow circumferential grooves in the stator near the trailing edge, see ***Figure 3***. The conclusions of this work show an ambiguous effect of the number of grooves on the operating parameters. As Bareiss et al. [9] mentioned, the creation of such grooves leads to an increase in friction in the shroud region, and thus to additional losses. However, an increase in efficiency has been demonstrated at some operating points. Based on this, it is evident that the grooving performed allows the emergence of a certain aerodynamic phenomena that not only compensates for these additive frictional losses, but on the contrary, even exceeds them. Bareiss et al. [9], using the CFD tool, concluded that the principle of this aerodynamic process is mainly to facilitate the transfer of fluid momentum in the circumferential direction. Because there is a vortex flow within the groove, although this is itself a dissipative process, there is no instantaneous impact between the pressure and suction sides of the blade during the flow through the TC.

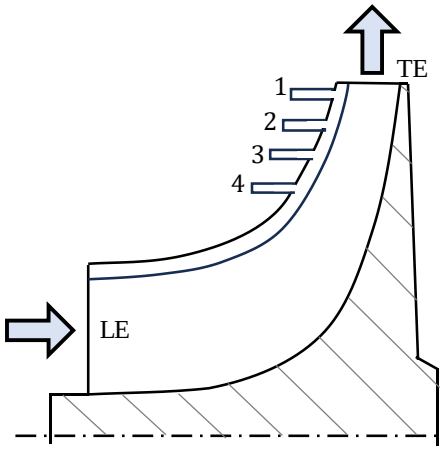

Figure 3 Casing treatment applied to a centrifugal compressor including deep circumferential grooves near trailing edge. Adopted from [9].

2.2 Mathematical background

Navier-Stokes equation in the reference frame of reference can be written as

$$\rho \frac{\mathrm{D}\vec{w}}{\mathrm{D}t} + 2\rho\vec{\omega} \times \vec{w} + \rho\vec{\omega} \times (\vec{\omega} \times \vec{x}) - \frac{\partial \sigma_{ij}}{\partial x_j} = 0, \tag{2}$$

where $\vec{w}$ is relative velocity, ρ is density, $\vec{x}$ is a position vector and σ_{ij} is Cauchy's stress tensor defined as $\sigma_{ij} = -\delta_{ij}p + \tau_{ij}$, where δ_{ij} is Kronecker's delta, p is pressure and τ_{ij} is viscous stress tensor. Multiplication the eq. (2) by $\vec{w}$ and assuming the stationary flow, that is $\partial/\partial t = 0$, the Euler pump equation including viscous stress tensor can be obtained in the form as

$$\Delta P = \dot{m}[(|u||v_u|)_{\mathrm{Out}} - (|u||v_u|)_{\mathrm{In}}] + \iint_{\mathrm{Shroud}} \tau_{ij} w_i n_j \mathrm{d}S - \iiint_{V} \tau_{ij} \frac{\partial w_i}{\partial x_j} \mathrm{d}V, \tag{3}$$

where ΔP is power transferred from the impeller to the fluid, $\dot{m}$ is mass flow, $|u|$ circumferential velocity and $|v_u|$ is circumferential velocity in stationary frame. It is worth noting the last term on the right-hand side of the eq. (3) is so-called viscous dissipation function representing the irreversible losses in a fluid. The irreversible

conversion of fluid energy into heat is therefore proportional to the product of the friction force tensor and the velocity gradient. The energy loss is defined as the volume integral of this product. The integrand of the volume integral is called as viscous dissipation density, denoted as $\dot{e} = \tau_{ij} \frac{\partial w_i}{\partial x_j}$.

2.3 Casing treatment application

Casing treatments including grooves were created in the model of a centrifugal compressor. The preliminary CFD analyses indicated a positive influence on the compression ratio and efficiency at low flow rates. Several variants of casing treatments were analysed to obtain the information regarding the prospective benefit to the operating parameters. The positive influence on efficiency was found at several operational points and it is in accordance with observation of viscous dissipation distribution $\dot{e}$ in tip clearance region as shown in ***Figure 4***. The original variant (left) including smooth stator shows higher energy losses than variant including multiple grooves (right). The middle variant includes one groove near leading edge and shows a decrease in energy losses in this region as well if compared to original variant (left). Decreasing the energy dissipation in the tip clearance region thus leads to a positive influence on efficiency. The positive impact on compression ratio is a result of increasing the outlet circumferential velocity in stationary frame v_u due to lower dissipation near shroud outlet.

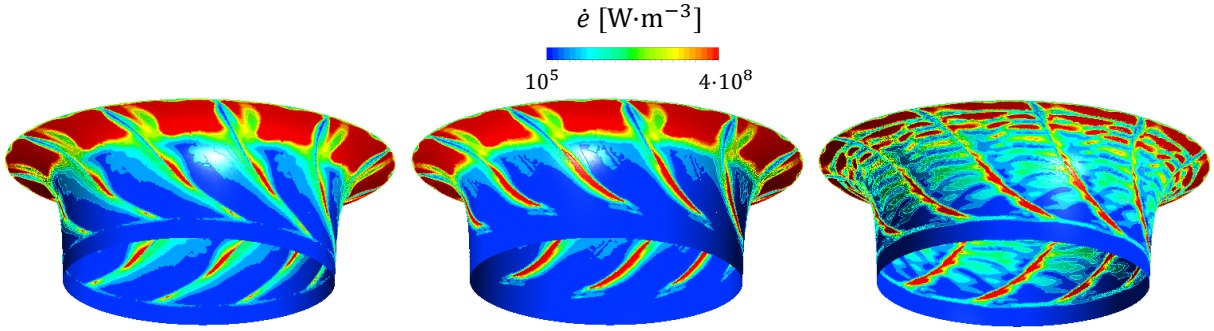

Figure 4 Distribution of viscous dissipation density (energy losses) in tip clearance region. Original on the left, one groove design in the middle and multiple grooves on the right.

4. CONCLUSION

The type of grooving performed in the work is likely correlated with the TC size, as too deep grooves led to a decrease in efficiency. Regarding the distribution and number of grooves, it seems that a higher number of grooves offers more potential to increase efficiency, which is in accordance with the research on the axial compressor mentioned above. This fact can probably lead in some way to the idea of groove interference making the generalization of the groove design for centrifugal compressors hard. This fact also confirms certain individuality of a compressor for using the grooves discussed here.

The manufacturing aspect of the proposed design is a disadvantage, as a five-axis CNC milling centre must be used to achieve the most accurate machining of the compressor stator. The further development of this research should therefore also be based on the consideration of production possibilities with a view to possible

introduction into series production. It also seems more appropriate to carry out research on the grooving under consideration on large compressors. In the case of small compressors, the problem of collision between the tool and the workpiece body can arise. In any case, stator contouring offers a considerable potential to influence the efficiency, for example for prototype production for applications requiring maximum compressor aerodynamic performance at the expense of production costs.

REFERENCES

[1] BRAEMBUSSCHE, Rene Van den. *Design and Analysis of Centrifugal Compressors*. John Wiley, 2019. ISBN 978-1-119-42410-9.

[2] GREITZER, E. M. Review—Axial Compressor Stall Phenomena. *Journal of Fluids Engineering*. 1980, **102**(2), 134-151.

[3] PRINCE, D. C., D. C. WISLER a D. E. HILVERS. A Study of Casing Treatment Stall Margin Improvement Phenomena. *ASME*. 1975, **1A**, 1-13.

[4] OSBORN, Walter M., George W. LEWIS a Laurence J. HEIDELBERG. Effect of several porous casing treatments on stall limit and on overall performance of an axial flow compressor rotor. *NASA TN D-6537*. 1971, 1-50.

[5] FABRI, Jean a Jean REBOUX. Effect of Outer Casing Treatment and Tip Clearance on Stall Margin of a Supersonic Rotating Cascade. *ASME*. 1975, **75-GT-95**, 1-7.

[6] TESCH, W. A. Evaluation of Range and Distortion Tolerance for High Mach Number Transonic Fan Stages, Task IV Stage Data and Performance Report for Casing Treatment Investigations, Volume I. *NASA CR-82867*. 1971, 1-345.

[7] SUN, Xiaofeng, Xu DONG a Dakun SUN. Recent development of casing treatments for aeroengine compressors. *Chinese Journal of Aeronautics*. 2019, **32**(1), 1-36.

[8] KHELLADI, S., S. KOUIDRI, F. BAKIR a R. REY. Predicting tonal noise from a high rotational speed centrifugal fan. *Journal of Sound and Vibration*. 2008, **313**(1-2), 113-133.

[9] BAREISS, Simon, Damian M. VOGT a Elias CHEBLI. Investigation on the Impact of Circumferential Grooves on Aerodynamic Centrifugal Compressor Performance. *Volume 2C: Turbomachinery*. American Society of Mechanical Engineers, 2015, 2015-06-15, 1-11. ISBN 978-0-7918-5665-9. Dostupné z: doi:10.1115/GT2015-42211

ACKNOWLEDGEMENT

The research leading to these results has received funding from the Specific research program at Brno University of Technology, reg. no. FSI-S-23-8235.

55. mezinárodní vědecká konference zaměřená na výzkumné a výukové metody v oblasti vozidel a jejich pohonů

září 5. - 6., 2024 – Liberec, Česká republika
Technická univerzita v Liberci
Fakulta strojní, Katedra vozidel a motorů

MODELLING TRAFFIC EMISSIONS BASED ON AN ADVANCED VEHICLE DETECTION

Michael Böhm[1], Klaudia Köbölová[2], Jakub Linda[3], Jiří Pospíšil[4]

Abstract
Air pollution from traffic emissions affects billions of people worldwide, yet measurements are very limited. Pollution concentrations in cities vary rapidly over short distances due to unevenly distributed emission sources, dilution and physico-chemical transformations. Conventional monitoring methods lack the necessary resolution to characterise exposures and locate hotspots. Detailed, specific and up-to-date data are crucial for in-depth analysis, modelling, management or planning. This paper explores and develops a widely applicable solution for real-time traffic pollutant estimation based on high-accuracy traffic dynamics data and microscopic multimodal emission models. A key aspect is the implementation of an advanced image processing method for vehicle detection and classification. Accurate vehicle trajectories together with terrain morphology are input to new micro-simulation models for the generation of exhaust and non-exhaust pollutants (CO_2, NO_X, PM).

[1] Ing. Michael Böhm, Ph.D., Institute of Automotive Engineering, Brno University of Technology, Technická 2896/2, 616 69 Brno, email: Michael.Bohm@vutbr.cz
[2] Ing. Klaudia Köbölová, Energy Institute, Brno University of Technology, Technická 2896/2, 616 69 Brno, email: Klaudia.Kobolova@vutbr.cz
[3] Ing. Jakub Linda, Energy Institute, Brno University of Technology, Technická 2896/2, 616 69 Brno, email: Jakub.Linda@vutbr.cz
[4] prof. Ing. Jiří Pospíšil, Ph.D., Energy Institute, Brno University of Technology, Technická 2896/2, 616 69 Brno, email: pospisil.j@fme.vutbr.cz

1. INTRODUCTION

Air pollution is a problem that threatens everyone and the environment. The low atmosphere is heavily polluted by heavy traffic. The most serious pollutants are particulate matter (PM10), nitrogen oxides (NO_X) and seemingly harmless carbon dioxide (CO_2) emissions. To characterise the state of the air, defining source emissions is an important first step. Transport emissions are generally calculated from emission factors multiplied by the number of cars passing. The emission factor (EF) expresses how much emissions of a particular type are produced by a particular car movement. Exhaust-related emissions, including NO_X, CO_2, SO_2 and PM10, are now a well-known and well-studied problem. Emission factors depending on the type of vehicle, driving mode and fuel used are embedded in various methodologies and standards [1-3]. However, exhaust emissions are calculated by different methods, but the procedures differ, resulting in different emission factors for similar conditions. For the characterization of EF in the Czech Republic, the methodological procedure of the Transport Research Centre [1], the communication of the Air Protection Department of the Ministry of Environment [2] and the emission inventory reports from the Czech National Institute of Transportation [3] were first examined. The advantage of the CDV methodology is the availability of EF for different transport modes and fuels. However, it cannot be used for individual cars as it is calculated as an average over the year and for total transport. In addition, cross-border sources were examined, focusing on data from the European Union. Various emission inventory databases exist (e.g. European Environment Agency [4], European Monitoring and Evaluation Programme [5], The Handbook of Emission Factors for Road Transport [6], National Atmopsheric Emissions Inventory [7]), but the EF is reported in different units, for different vehicle categories and often the calculation is generic for total transport. For these reasons, it was decided to use an internal combustion engine thermodynamics simulation software tool to determine the EF for exhaust emissions.

The second group consists of non-exhaust emissions, which are generated by mechanical processes (abrasion of brakes, tyres and road surfaces) or resuspended as settled dust due to turbulence caused by traffic. The main pollutant in non-exhaust emissions is particulate matter (PM10). This part of emissions will become progressively more dominant with the development of electric mobility. Several difficulties arise when examining particulate matter from sources other than exhaust particles. First, due to the lack of standard measurement procedures, researchers use many different sampling methodologies, leading to biased and difficult to compare results. There are many different parameters that affect the non-exhaust particles in terms of their physicochemical properties. For example, brake particle wear and emission rates depend on the driving pattern (i.e. frequency and intensity of braking) and the conditions under which braking occurs (vehicle speed, ambient temperature and chemicals available in the environment). The particles generated by tyre wear depend largely on the characteristics of the tyres tested, the road surface characteristics and also on vehicle operating conditions [8]. Resuspension of road dust depends on parameters such as traffic density, road surface properties and especially its maintenance status, local meteorology and vehicle characteristics and operation [9].

2. TRANSPORT EMISSIONS MODELLING

2.1 Gaseous emissions

The GT-Suite simulation tool was used to calculate the gaseous emissions. This allows the modelling of exhaust emissions and knock. By default, it predicts 13 combustion products (N_2, O_2, CO_2, CO, H_2O, H_2, H, O, OH, NO, N, SO_2 (if sulfur is present in the fuel(s)), and Ar (inert, argon will pass if present in the inlet)) using equilibrium chemistry. In addition, selected species can be calculated using chemical kinetics, but only for some models or if the user explicitly specifies them. This section discusses the available options.

Engine model

As a model engine for the creation of the model was used a turbocharged engine of VW manufacturer 1.4 TSI, which was installed in the car škoda octavia and was one of the best-selling engines of this vehicle. This vehicle was sold between 2012 and 2017 and the engine had to meet the EURO 5 emission standard that was current at the time.

	1.4l TSI (103 kW)
Engine volume [cm3]	1390
bore [mm]	74.5
stroke [mm]	80
Compression ratio [-]	10.5

Table 1: *engine parameters*

Emission system model

The catalyst simulation model was a detailed model in the secondary post-processing circuit. The original baseline 1.4 TSI model was combined with the TWC retrofit model by Ramanathan and Sharma, which uses the published TWC passenger car reaction mechanism. A secondary circuit is used to solve the reactions using a quasi-stable (QS) flux solver, which can reduce the computation time. Various monitors show the TWC conversion efficiency, exhaust lambda, oxygen supply, temperature before and after the TWC, and ΔT across the TWC.

Vehicle model

The dimensions of the vehicle are based on the actual Škoda Octavia, which is also produced in the configuration with the 1.4 TSI (103 kW) petrol engine described at the beginning of this chapter. The complete model consists of a detailed model of the engine (shown above), the transmission, a simplified vehicle and the controls for each element. The main control element is the Driver, which adjusts the throttle and brake pedal positions based on the current vehicle speed and power demand to ensure that the simulated vehicle speed profile replicates the desired speed profile as closely as possible.

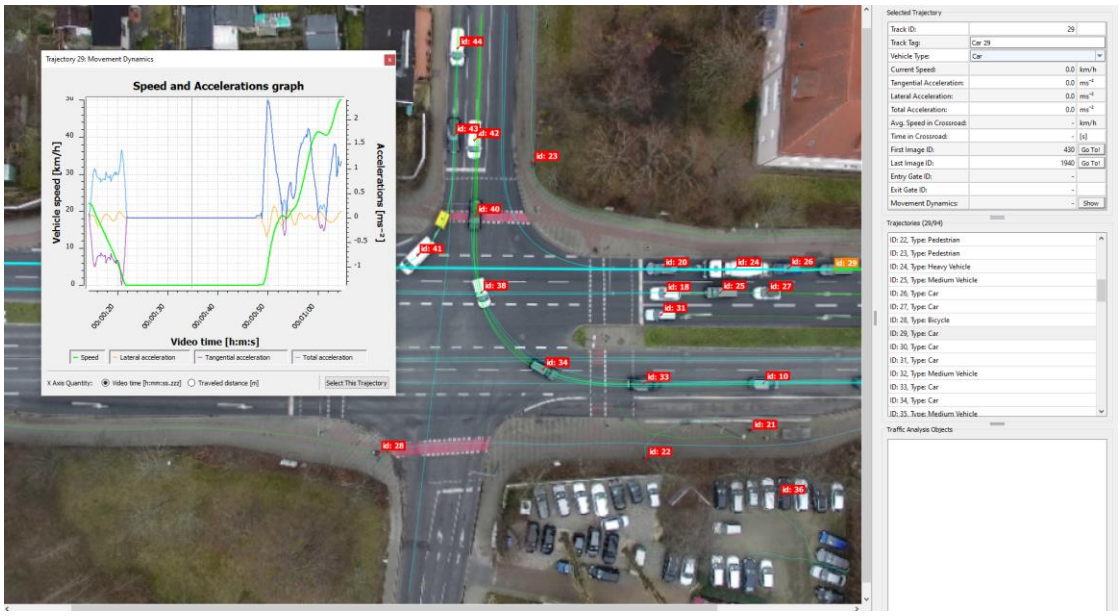

Figure 1: *Camera recording of vehicles passing through the intersection with speed and acceleration of vehicles*

2.2 PM emissions

The problems that have arisen from the search for available emission factors for particulate matter in traffic are several and can be summarized as follows:

- EF are determined for a steady flow of traffic, i.e. for a certain constant speed
- EFs are determined for a certain number of cars, they do not differentiate between car types
- EFs are set for PM in general, it is not known which types of PM sources are included (brake wear, tire wear, road wear, resuspension, exhaust)
- If EFs are determined for certain dynamic driving behavior, the exact dynamics are not known

There is a group of studies that offer a detailed view of PM formation during dynamic vehicle behavior. These studies deal with the formation of PM from various sources, such as road wear, brake wear, etc. However, they only result in the resulting concentration near the source, not emissions. An example can be the study [10], which leads to relationships for the determination of PM concentration at different levels of braking.

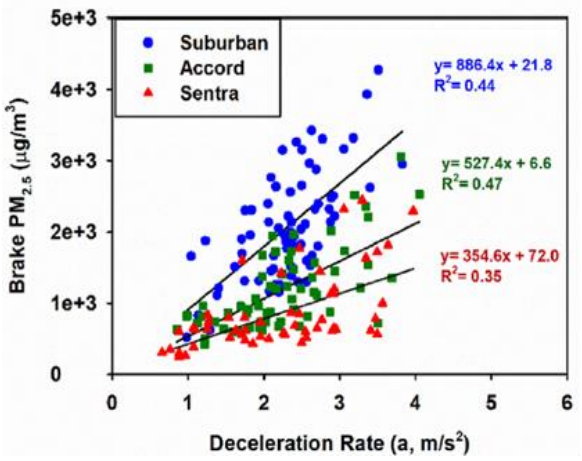

Figure 2: *Camera recording of vehicles passing through the intersection with speed and acceleration of vehicles [10]*

In the first step of the calculation, certain assumptions must be made regarding the shape of the relationship between EF and acceleration or velocity:

- Emissions of exhaust particles have a linear dependence, at zero acceleration the EF is equal to idling values, which can be estimated to be 1/20 of the EF value at maximum acceleration [11].
- Brake wear emissions have a simple linear character, while the resulting shape of the curve depends on the weight of the vehicle and the brake pads used [12].
- Emissions from tire wear depend primarily on vehicle speed, with a quadratic dependence assumed [13].
- Road abrasion emissions are assumed to be proportional to tire abrasion emissions and are 1.36 times higher than tire emissions [14]
- Emissions from resuspension also have a linear character, based on knowledge about resuspension it is assumed that resuspension occurs from a speed of up to 30 km/h [15].

2.3 CFD simulation

Flow around vehicles is a well-studied problem in CFD. However, most of the research is focused on the aerodynamic aspect of vehicles, which is negligible within the scope of the project solution, as the project is devoted to the spread of pollution. The "Ahmed body" case was chosen as the reference geometry Various vortices are formed in the area behind the vehicle, which regularly change their size and position [16]. Some of the eddies periodically separate and create a so-called drift. Some do not change their position and form so-called recirculation zones. A detailed description of the nature of the flow behind the vehicle can be found in the publication [17].

Flow in urban areas is also well explored in CFD. The geometry of cities is commonly replaced by block structures. The urban street canyon is a well-known type of urban geometry in modeling studies. It is mostly used to study the dispersion of pollutants in cities. The street canyon consists of at least two buildings of height H [m] separated by width W [m] and length B [m]. Different H/W configurations are used in the studies. Different flow regimes have been described for different H/W [18].

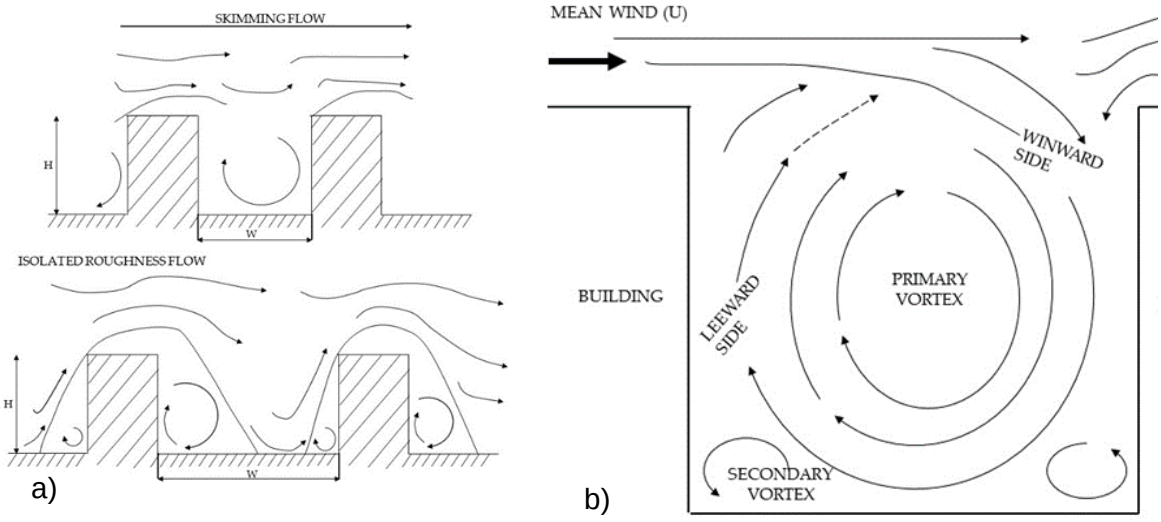

Figure 3: *a) different flow regimes for different H/W configurations, according to [25]. b) detailed description of the canyon vortex according to [28]. Element names are left in their original designations.*

3. RESULTS AND CONCLUSIONS

3.1 Gaseous emissions

It is possible to implement any vehicle speed curve into vehicle models. On the basis of the detected real courses of passage of vehicles through the intersection, it is then possible to simulate various scenarios (with stopping, fast passage, etc.).
In the next step, in the case of using simplified models (fast running model or map based model), it is also possible to directly connect the models and send the current value of the vehicle speed to the model, when the model would predict immediate emissions. It is easy to change the driving profile and possibly the body of the vehicle for a given model. More complicated is the replacement of the drive (combustion engine), when it is necessary to use the entire detailed model at the beginning, or to create simplified models.

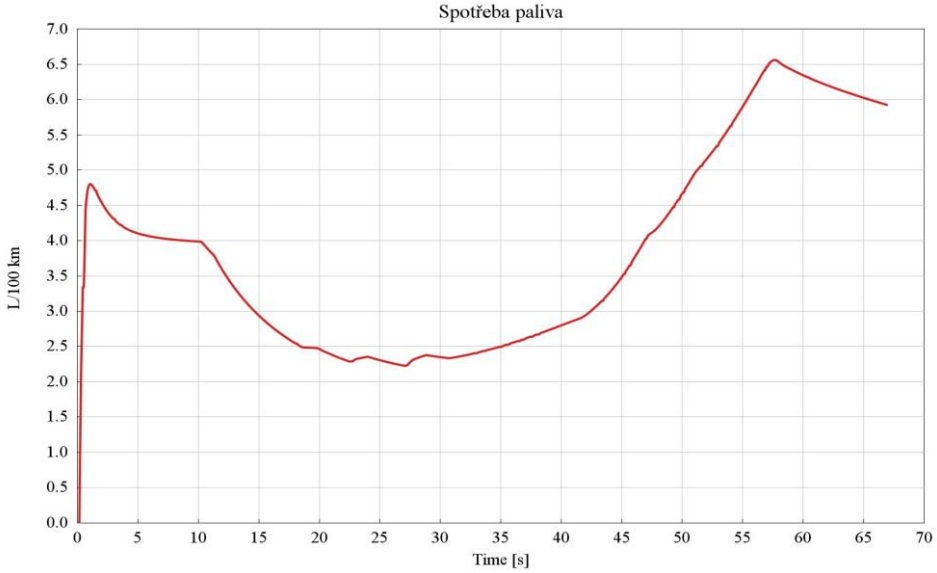

Figure 4: *Fuel consumption during the passage through the intersection*

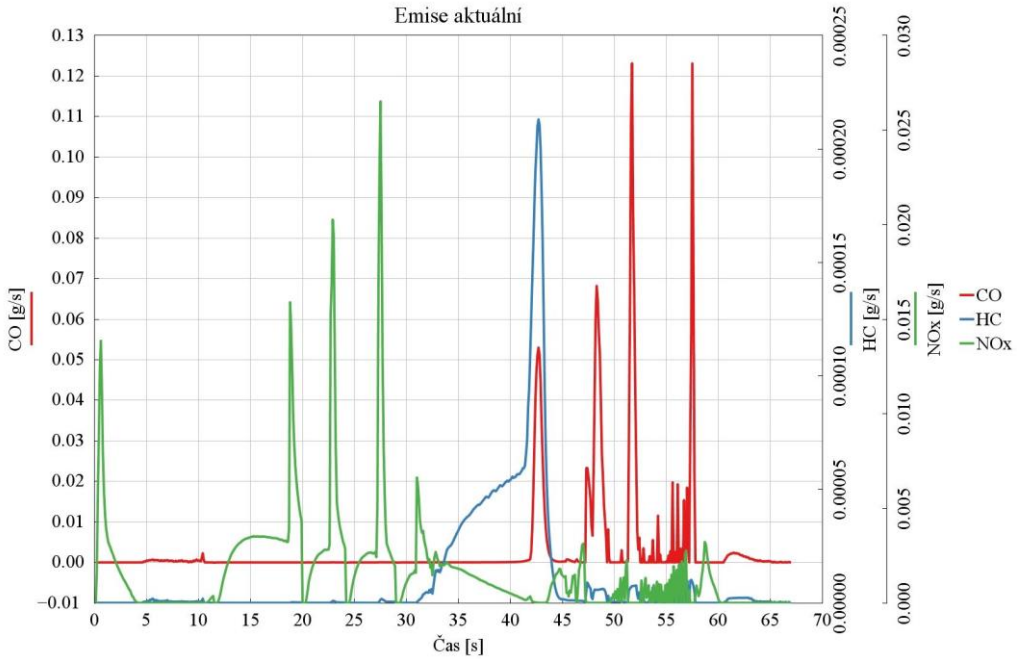

Figure 5: *Exhaust gas emissions while passing through an intersection*

3.2 PM emissions

If the expected shapes of the dependence of the emission factors are determined and the total amount of particles emitted per driving cycle is known, it is possible to recalculate the emission factors in the form of mg/s. From known driving cycle data with 1 s resolution and known emissions for a given particle type, the problem boils down to an equation with one unknown. The sum of the emissions in each time interval equals the total emissions, where the unknown is a constant in a linear or quadratic equation. In this way, the shape and slope of EF can be defined as a function of acceleration or velocity. The resulting dependencies then look like this:

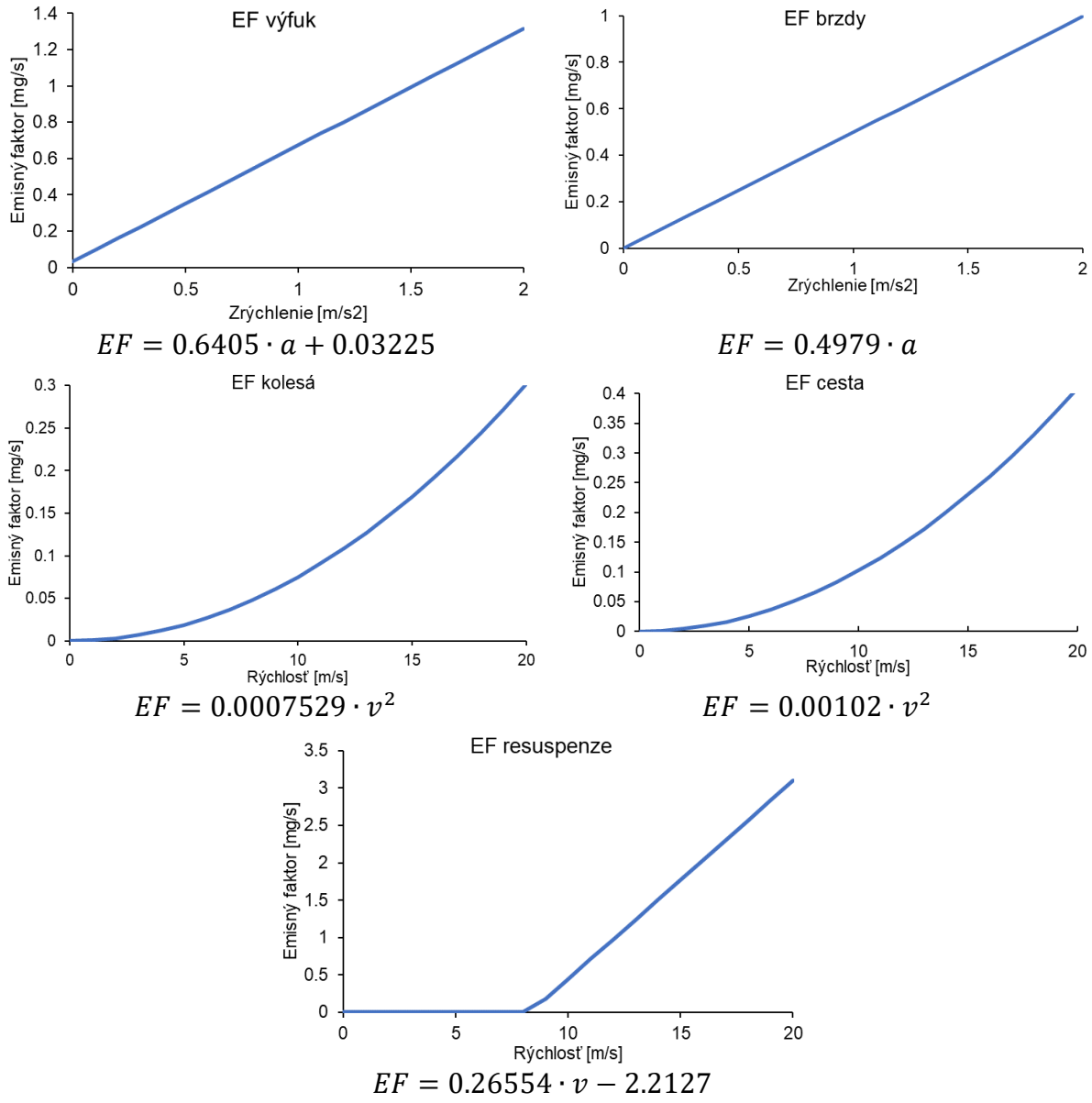

Figure 6: *Dependencies of emission factors*

3.3 CFD

The calculation was iteratively performed until the convergence criteria and other parameters, especially those related to the wall functions (y+ value), were met. After the calculation of the flow, i.e., velocity and pressure field information, solid particles were introduced into the simulations.

The particles are fed into the simulation after the current field has been calculated and are solved using a Lagrangian approach, i.e. their tracking is followed. To convert from particle trajectories to the appropriate concentration, a custom function had to be programmed into the software. The deposition and tracking results then look as follows.

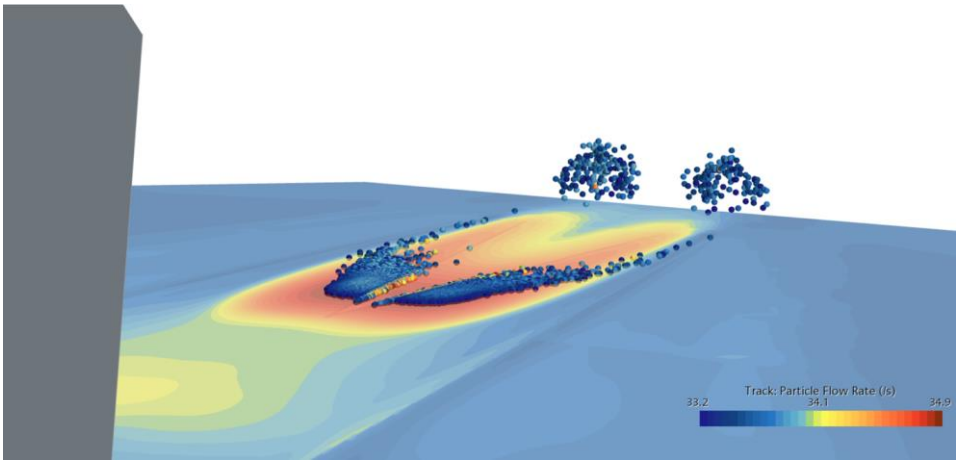

Figure 7: *Particles settling behind a moving car model*

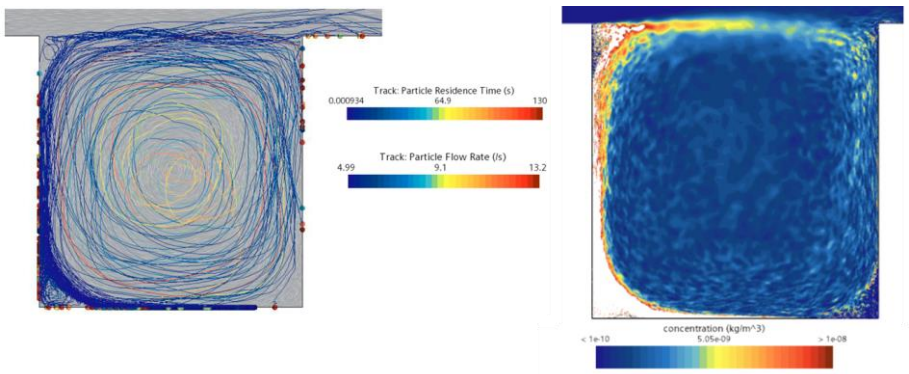

Figure 8: *Particle routing in the space between buildings and associated*

In next phase of the project, the models will be modified to account for acceleration and deceleration zones. At the same time, emission factors will be applied to the models according to the preliminary results. A reference intersection will be selected for validation.

REFERENCES

[1] Ministerstvo životního prostředí Sdělení Odboru Ochrany Ovzduší MŽP, Jímž Se Stanovují Emisní Faktory Podle § 12 Odst. 1 Písm. b) Vyhlášky č. 415/2012 Sb., o Přípustné Úrovni Znečišťování a Jejím Zjišťování a o Provedení Některých Dalších Ustanovení Zákona o Ochraně Ovzduší; 2021;

[2] Ilona Dvořáková, V.D.H.H.P.M.J.Š. Česká Zpráva o Emisní Inventuře v Roce 2020; 2020;

[3] European Environment Agency EMEP/EEA Air Pollutant Emission Inventory Guidebook 2023.
[4] European Monitoring and Evaluation Programme.
[5] The Handbook of Emission Factors for Road Transport.
[6] National Atmopsheric Emissions Inventory.
[7] Piscitello, A.; Bianco, C.; Casasso, A.; Sethi, R. Non-Exhaust Traffic Emissions: Sources, Characterization, and Mitigation Measures. Science of The Total Environment 2021, 766, 144440, doi:10.1016/j.scitotenv.2020.144440.
[8] Casotti Rienda, I.; Alves, C.A. Road Dust Resuspension: A Review. Atmos Res 2021, 261, 105740, doi:10.1016/j.atmosres.2021.105740.
[9] Oroumiyeh, F.; Zhu, Y. Brake and Tire Particles Measured from On-Road Vehicles: Effects of Vehicle Mass and Braking Intensity. Atmos Environ X 2021, 12, 100121, doi:10.1016/j.aeaoa.2021.100121.
[10] Harrison, R.M.; Jones, A.M.; Gietl, J.; Yin, J.; Green, D.C. Estimation of the Contributions of Brake Dust, Tire Wear, and Resuspension to Nonexhaust Traffic Particles Derived from Atmospheric Measurements. Environ Sci Technol 2012, 46, 6523–6529, doi:10.1021/es300894r.
[11] Grigoratos Theodoros; Martini Giorgio Non-Exhaust Traffic Related Emissions – Brake and Tyre Wear PM; Luxembourg , 2014;
[12] Kwak, J.H.; Kim, H.; Lee, J.; Lee, S. Characterization of Non-Exhaust Coarse and Fine Particles from on-Road Driving and Laboratory Measurements. Science of the Total Environment 2013, 458–460, doi:10.1016/j.scitotenv.2013.04.040.
[13] Fitz, D.R.; Bumiller, K.; Etyemezian, V.; Kuhns, H.D.; Gillies, J.A.; Nikolich, G.; James, D.E.; Langston, R.; Merle, R.S. Real-Time PM10 Emission Rates from Paved Roads by Measurement of Concentrations in the Vehicle's Wake Using on-Board Sensors Part 2. Comparison of SCAMPER, TRAKERTM, Flux Measurements, and AP-42 Silt Sampling under Controlled Conditions. Atmos Environ 2021, 256, doi:10.1016/j.atmosenv.2021.118453.
[14] Woo, S.-H.; Jang, H.; Lee, S.-B.; Lee, S. Comparison of Total PM Emissions Emitted from Electric and Internal Combustion Engine Vehicles: An Experimental Analysis. Science of The Total Environment 2022, 842, 156961, doi:10.1016/j.scitotenv.2022.156961.
[15] Banga, S.; Zunaid, Md. CFD Simulation of Flow around External Vehicle: Ahmed Body. IOSR Journal of Mechanical and Civil Engineering 2017, 12, 87–94, doi:10.9790/1684-1204038794.
[16] Alves, R.M.; Almeida, O. de Validation of Experimental and Numerical Techniques for Flow Analysis over an Ahmed Body. Int J Eng Res Appl 2017, 07, 63–71, doi:10.9790/9622-0704036371.
[17] Oke, T.R. Street Design and Urban Canopy Layer Climate. Energy Build 1988, 11, 103–113, doi:10.1016/0378-7788(88)90026-6.
[18] Yazid, A.W.M.; Sidik, N.A.C.; Salim, S.M.; Saqr, K.M. A Review on the Flow Structure and Pollutant Dispersion in Urban Street Canyons for Urban Planning Strategies. Simulation 2014, 90, 892–916, doi:10.1177/0037549714528046.

ACKNOWLEDGEMENT

The authors gratefully acknowledge funding from the Specific research on BUT FSI-S-23-8235.

55. mezinárodní vědecká konference zaměřená na výzkumné a výukové metody v oblasti vozidel a jejich pohonů

září 5. - 6., 2024 – Liberec, Česká republika
Technická univerzita v Liberci
Fakulta strojní, Katedra vozidel a motorů

SENSITIVITY ANALYSIS FOR IMPACTS OF POSSIBLE FUTURE VEHICLE FLEET DEVELOPMENT

Jan Macek[1], Josef Morkus[2]

Abstract
Data sources for alternative fleet development scenarios. Publicly available data, Technical Inspection Stations data sources and model-based vehicle feature predictions. Use of previously developed, semi-analytical and statistical tool FECET for TTW and WTW assessment of different vehicle fleet scenarios, considering types of energy carriers with impacts on energy consumption and green-house gas emissions. Examples of output data, enabling analysis of pros and cons for different powertrain types. Possible changes of fleets due to mobility modes changes, shifts between vehicle types and sizes, energy carrier use and vehicle fleet renewals. Future enhancements of FECET tool for life-cycle analysis and pollutant prediction.

1. INTRODUCTION

The political need for limiting green-house gases (GHG) emissions in Europe is widely well-known from Green Deal for Europe and Fit for 55 framework documents, because

[1] Jan Macek, Czech Technical University in Prague, Faculty of Mechanical Engineering, U 12201, Technická 4, 166 07 Praha 6, jan.macek@fs.cvut.cz
[2] Josef Morkus, Czech Technical University in Prague, Faculty of Mechanical Engineering, U 12201, Technická 4, 166 07 Praha 6, josef.morkus@fs.cvut.cz

of result of scare of climatic crisis. It has been reflected, e.g., by regulation [1]. On one hand, it limits vehicle manufacturers, considering mean emissions from vehicle fleets sold end registered in EU countries. On the other hand, the following directives, known as RED II and recently RED III, oblige the member states to accept National Climate-Energy Plans (NCEP, in Czech NKEP), focused on GHG emission reduction and the use of so-called Renewable Energy Sources (RES, OZE) – e.g., in [2].

Therefore, the methodology for surface-transport vehicle fleet development, described in previous papers of the authors – e.g., [5] or [7], has found the broad application in realistic data mining for those purposes, especially in correcting the biased conclusions of some politicians or experts from non-physics-based science domains. The Future Energy Consumption and Environment Impacts of Surface Vehicle Transport (FECET) code, combining database elaboration with simulations in MS Excel 365 (200 MB), has been substantially improved for those purposes.

The goal of the current contribution is presenting the recent development of the methodology. The top-down use is based on available data from public and non-public, but reliable resources (e.g., Technical Inspection Stations) and applications of statistics-based estimations of energy consumption and GHG emissions, as in COPERT methodology - [3] or GreenNCAP resources - [4]. The bottom-to-up checking simulation-based modelling enables predictions of not yet statistically elaborated new powertrains. Moreover, the detailed modelling of typical car class representatives, done using in-house database of powertrain simulation inputs, is able to find errors in statistics (including COPERT methodology), caused by mistakes of data providers or extrapolation by purely regression or AI-based applications outside of the range of their validity.

The available range of the current paper makes it possible to present the selected outputs and to outline the fields, in which the code can be used. Some warning results, based on the holistic view on the surface transport facts, are included, as well.

2. DATA SOURCES AND CHECKING METHODS

The public resources from the Statistical Year Books of the Czech Republic, amended in the discussions with representatives of the Czech Government, Technical Inspection Stations data (TIS or STK) pre-processed in The Center for Transport Research (CDV Brno) and manufacturers' vehicle information were among the main sources. Due to pandemic situation during the second half of 2020 and the whole years 2021 and 2022 the basic data used were limited to the period of 2017-2020 with some correction from 2023 new information, especially on electric vehicles.

The checks are based on comparison of the energy consumption and transport output performance (passenger.km or t.km) data resources from the Ministries of Industry and Trade, Transport, Environment, Finances (including Custom Office Data) and manufacturers or importers of fuels, electric energy (including electricity market operator OTE) and vehicles. The estimated standard deviations in those data are close to 10%, which is partially caused by overlaps in methodology of data classification.

Moreover, the COPERT methodology or its application for the current case is not error-free, as stated above, since it predicts, e.g., for long-haul trucks, the results below total minimum of road energy consumption, which can be found from vehicle mass including

pay-load (checked as integral number of transport performance outputs – passenger.km or t.km), driving resistance and efficiency of the powertrain using analytical method - [8]. That is why the simulation of achievable energy consumption parameters were cross-checked using both mentioned top-down and bottom-to-up methods by means of a simple vehicle model, described in the next section.

3. VEHICLE AND POWERTRAIN SIMULATIONS

For road energy consumption, it is possible to use the traction work on the wheels and the overall efficiency of the powertrain with partial efficiencies of storage and extraction of the energy carrier (fuel) from the storage tank, the efficiency of the engine or motor itself (altogether $\eta_{PM} = \eta_M \eta_{stor}$) and the efficiency of both the gearbox and the final gear (η_{trans}). Then, with the tractive force at wheels F_{wheel} and work needed for its coverage W_{wheel} it yields

$$E_{road} = \frac{1}{36 s_{tot}} \int_{s_{tot}} \frac{dW_{wheel}}{\eta_{trans} \eta_M \eta_{stor}} = \frac{1}{36 s_{tot}} \int_{s_{tot}} \frac{F_{wheel} ds_{wheel}}{\eta_{trans} \eta_{PM}} \left[kWh \square 100\ km \right] \qquad (1)$$

For variable driving modes, it is necessary to integrate over time or path, which is the basis of a weighted average for representative values of individual variables. For any efficiency in the chain ***x***, the following relation applies the relative values ***rel***, related to the rated output (brake) power ***P***, using the operation-representative power and the losses ***L***

$$\eta_x = \frac{P_x}{P_x + L_x} = \frac{P_{rel,x}}{P_{rel,x} + \frac{L_x}{P_{x,rated}}} = \frac{1}{1 + L}; \quad e.g.,\ P_{rel,M} = \frac{P_{M,brake}}{P_{M,rated}}; \quad L = L_M P_{rel,M} \qquad (2)$$

A linear regression polynomial relation then used for losses during active engine/motor performance with the exponents of nonlinear regression ***x, y*** a x_g

$$L = \left[A_O + A_5 P_{rel} + A_6 P_{rel}^{\ z} + A_3 \omega_{rel} + A_4 \omega_{rel}^{\ x} + A_1 \frac{P_{rel}}{\omega_{rel}} + A_2 \left(\frac{P_{rel}}{\omega_{rel}} \right)^y \right] \frac{\omega_{rel}^{x_g}}{P_{rel}} \qquad (3)$$

The relative angular velocity or relative speed of the engine is set close to speed optimum, expressed by relative angular speed, by implicit adjusting the overall gear ratio i_{trans}. Then, the road energy consumption E_{road} can be found from the well-known driving resistance force F_{wheel} formula with rolling (***roll***), air drag (***D***), slope (***slope***) and inertia (acceleration) terms in dependence on total vehicle mass with some kinetic energy reduction coefficients and speed. If the COPERT data are available, the mean representative vehicle speed can be found from vehicle and powertrain data, using non-linear equation solver with some additional refinements - [5]. It is possible, nevertheless, if mean operation accelerations and slopes are set. This uncertainty, caused by estimation and replacement of both kinetic and potential energy changing terms, e.g., by single equivalent slope term, is not critical for standard powertrains but it might be important if the measures for energy recuperation other than simple coasting-down are available. The estimation of it was done comparing the representative speed found by comparing operation speed estimations (e.g., 70 – 90

km/h for all cars, 30 – 40 km/h for city operated vehicles as vans or municipal transport buses, etc.). The check is provided by comparing the real driving energy recuperation possibility, found from measurements and detailed simulations of typical electrified vehicles.

These formulas have been adjusted for dual-fuel or flex-fuel use, including the changes of engine efficiency and additional mass of both engine and storage tanks. Hybrid (i.e., twin-prime-mover vehicle, HEV) or full-electric powertrains (BEV) were considered, as well with possibility of energy recuperation. Using the **relative** share of the first prime-mover P_1, and distinguishing between non-recuperable rolling and drag resistance wheel works on one hand and equivalent-slope work on the other hand, the total energy consumption respecting both prime-mover efficiencies can be described as

$$E = \left(W_{roll} + W_D + W_{slope}\right)\left(\frac{P_1}{\eta_{tot1}} + \frac{1-P_1}{\eta_{tot2}}\right) - E_{rec}$$
$$E_{rec} = \left(W_{slope,rec} - W_{roll,rec} - W_{D,rec}\right)\eta_{rec,tot} \qquad (4)$$

Available recuperable work is reduced by rolling and drag resistances during recuperation period, which can be found from the equivalent forces along the same path of recuperation. The energy recuperation efficiency is evaluated from the chain of energy harvesting (electric generator operation and battery charging) and the second use of stored energy (e-motor and discharging efficiency once again), whereas the efficiency of the primary potential and kinetic energy provision was already considered in the first term of energy consumption in the Eq. *(4)*. The total recuperation efficiency is calculated by multiplication of the described chain partial efficiencies

$$\eta_{rec,stor} = K_{rec}\eta_{trans}\eta_G\eta_{CH,rec}$$
$$\eta_{rec,DCH} = \eta_{trans}\eta_{eM}\eta_{DCH} \qquad (5)$$

in which the partial possibility of braking by recuperation is reflected by the recuperation coefficient K_{rec}<1. The same procedure with adjusted efficiencies is used also for catenary supplied electric vehicles (e.g., trolley-buses), where recuperation to grid is used.

4. FECET CALIBRATION

The energy consumption and GHG predicting tool was checked comparing the results of energy consumption simulations, multiplied by the number of CZ registered vehicles and their annual mileage according to TIS (STK) records. COPERT data were used in all cases they provide realistic representative speed with estimated equivalent slope term, important for recuperation role assessment. Simultaneously, the transport performance output was kept at levels, published in statistics of the Ministry for Transport, distributing them to vehicle classes using estimated share of them.

The results of calibration can be found in *Figure **1***, as far as energy is considered, and *Figure 2* through *Figure 3* for transport performance outputs. The accordance with other sources, as TRANSPLINEX - [5] or total Czech fuel consumption data, are very good except for some local deviations, caused by lack of data for light-duty commercial

vehicle transport (LD), transit vehicles (estimated from toll data) and some overlaps in statistics. The reduction of TJ to TWh is mentioned at horizontal grid lines in *Figure **1***.
.

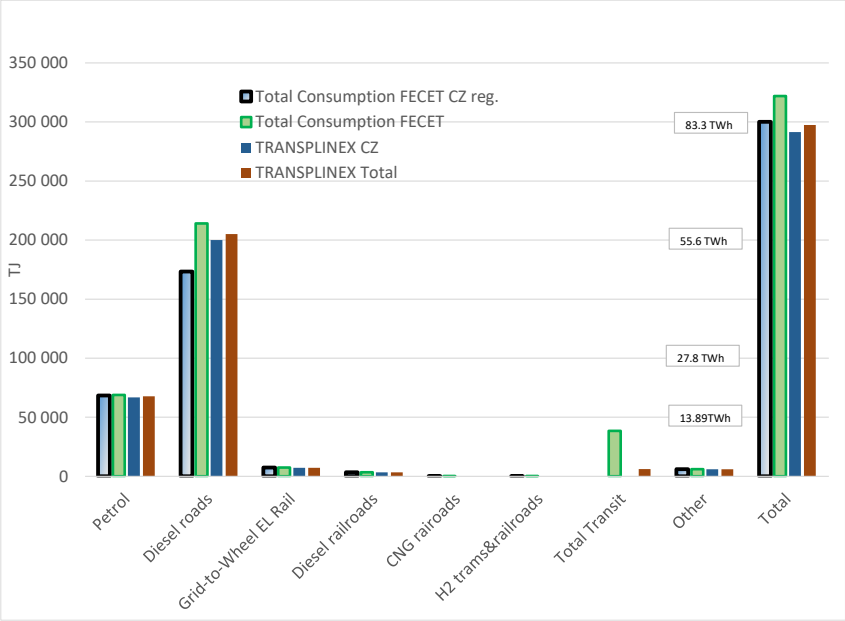

Figure 1: *Comparison of TRANSPLINEX calibration data and FECET prediction of energy for different energy carriers and domestic or transit vehicles (Czech Republic, 2020)*

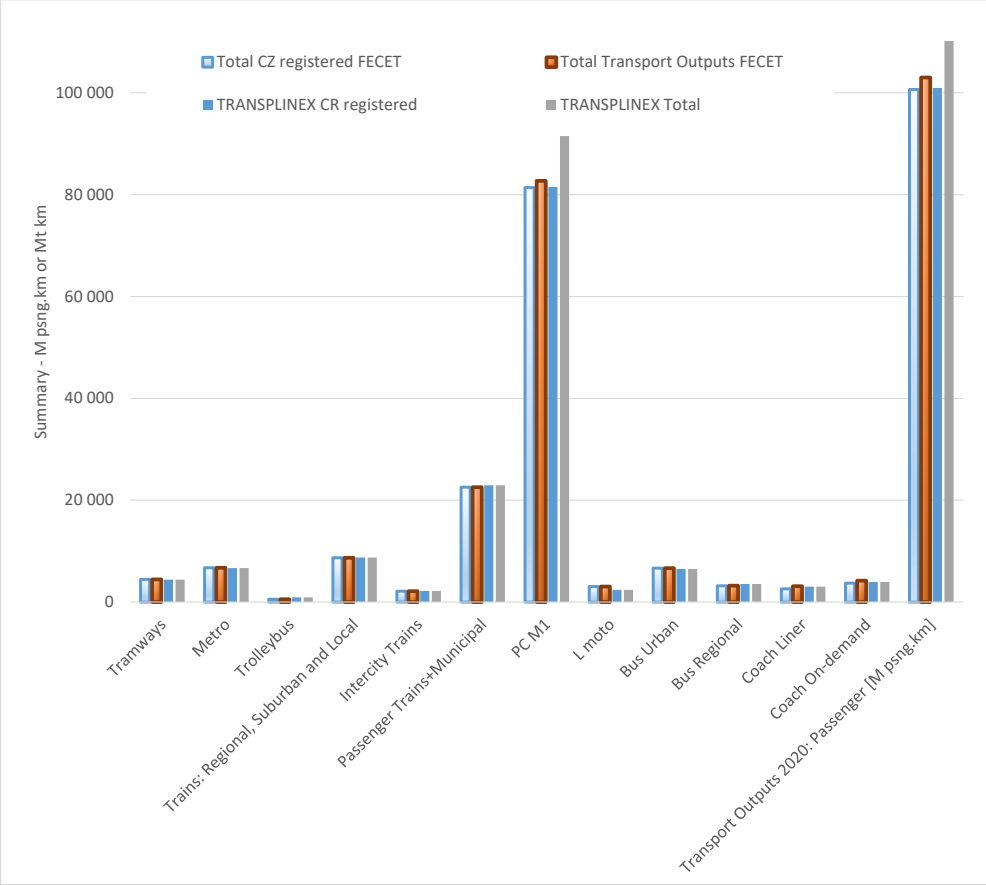

Figure 2: *Comparison of calibration data and FECET prediction of passenger transport performance for different vehicle classes (Czech Republic, 2020)*

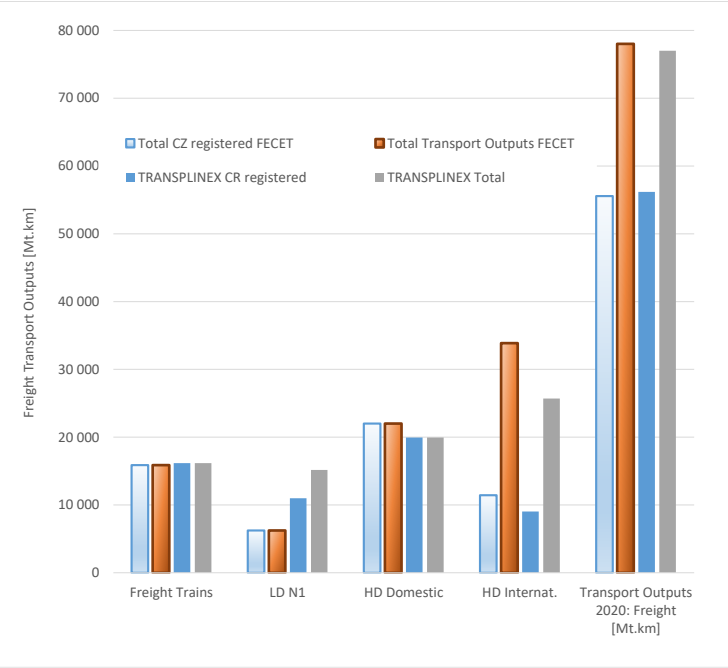

Figure 3: *Comparison of calibration data and FECET prediction of freight transport performance for different vehicle classes (Czech Republic, 2020)*

5. EXAMPLES FROM FLEET DEVELOPMENT SCENARIOS

The analysis of transport mode changes and vehicle fleet development should be started by comparison of shares of different vehicle classes on transport outputs (*Figure 4*) and total energy consumption (*Figure 5*).

The overwhelming role of individual, passenger car transport covered by fossil fuels, followed by rail transport with massive electricity use and then by diesel-oil bus transport is clear from it, as the majority of diesel-oil road freight transport, followed by electricity “fueled”, bulk rail transport. Inside individual transport, the share of light vehicles as e-bikes and motorcycles is also negligible. The problems in changes like “back to the rail” or “substitute individual by mass passenger transport” are transparent, as well. That is why the following examples will be mainly focused on individual passenger transport vehicles, i.e., cars.

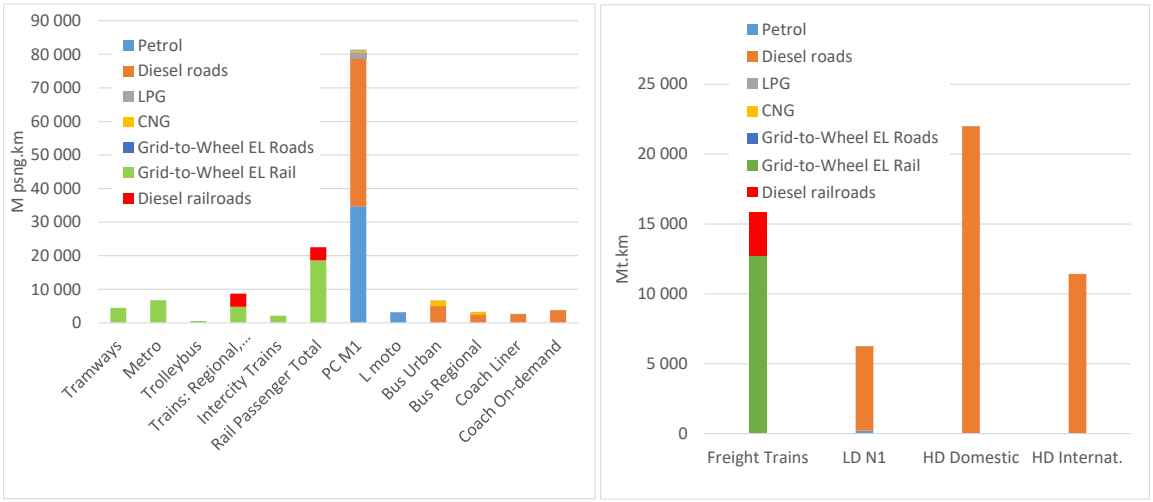

Figure 4: *FECET results of passenger (left) and freight transport performance outputs (right) for different vehicle groups and energy carriers (Czech Republic, 2020)*

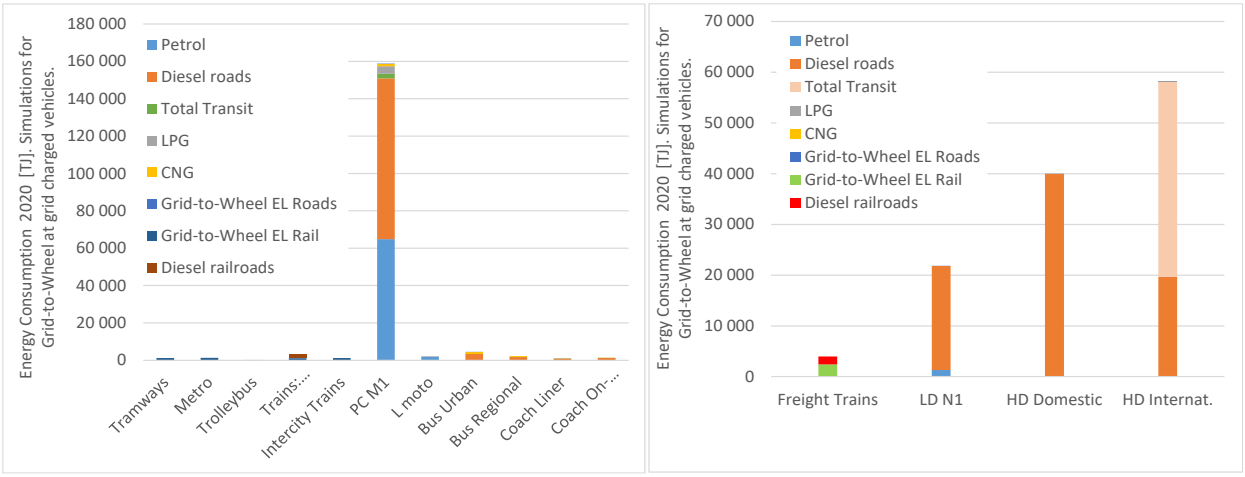

Figure 5: *FECET results of energy consumption shares for different energy carriers and vehicle groups, passenger transport at left, freight at right side (Czech Republic, 2020)*

The significant role of hydrocarbon fuels for cars is evident from *Figure 5*, which is amplified by smaller tank or grid-to wheel efficiency, if chemical energy is used instead of already produced electric energy. The efficiency itself, which is higher for diesel internal combustion engines ICE), as expected, need not to be proportionally followed by better specific energy per transport input improvement. The reason is in the curb mass of a vehicle, equipped by different prime movers and energy storage systems. The results in *Figure 6* demonstrate the really achieved ratio of ICE/BEV cars less than three for cars but less than two for long-haul freight transport. Car diesels are even less “efficient” in this sense due to their massive use in heavier cars - *Figure 6* shows weighted averages for the whole vehicle group. The use of dieses in light (L7) category of vehicles is limited to diesel minicars outside of car M1 or motorcycle L1-L4 groups.

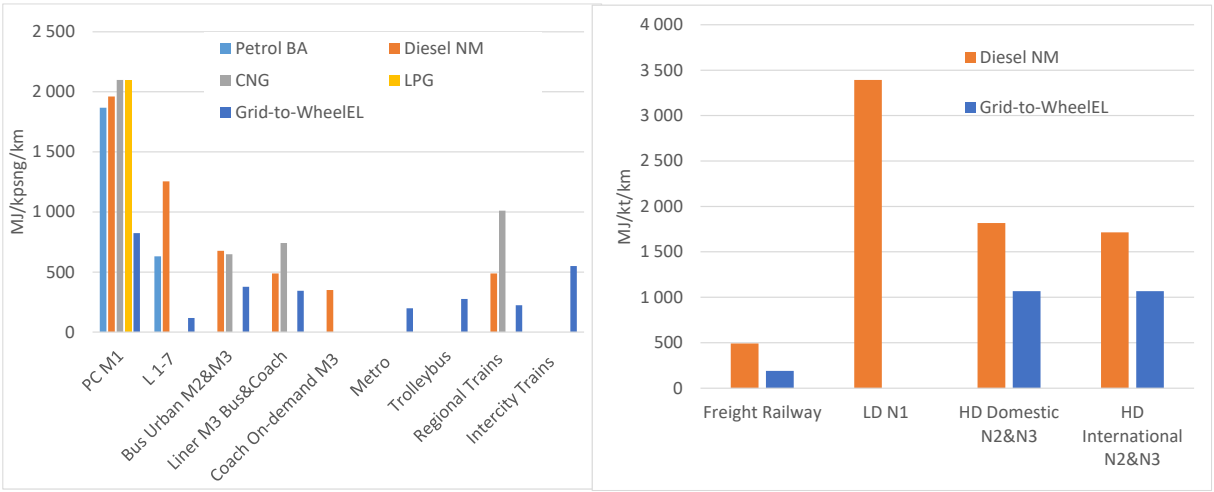

Figure 6: *FECET results of specific energy consumption per transport output for different energy carriers and vehicle groups, passenger transport at left, freight at right side with delivery vans LD and long-haul HD (Czech Republic, 2020)*

Tank-to-Wheel (TTW) or Grid-to-Wheel (GTW, incl. grid input-to-charger loss) of different powertrains including recuperation are presented in *Figure 7*. Despite recuperation, the internal losses of electric vehicles are not insignificant and the idea of just 90% e-motor efficiency need to be corrected, especially if the input for driving auxiliaries (e.g., cooling fan or HVAC) is fairly considered. The advantage of higher ICE load at heavy duty (HD) vehicles or buses creates another factor, which moves

the ICE efficiency to higher values unlike those of the unused rated power in most of cars.

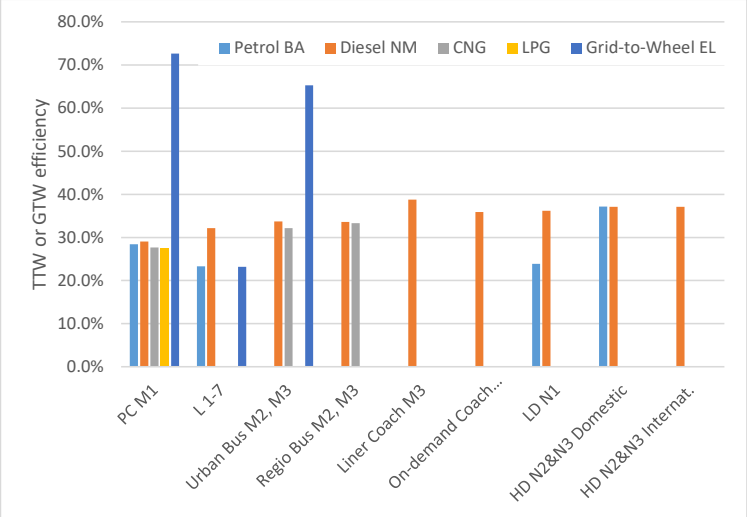

Figure 7: *FECET prediction of energy efficiency TTW or GTW for different vehicle powertrains*

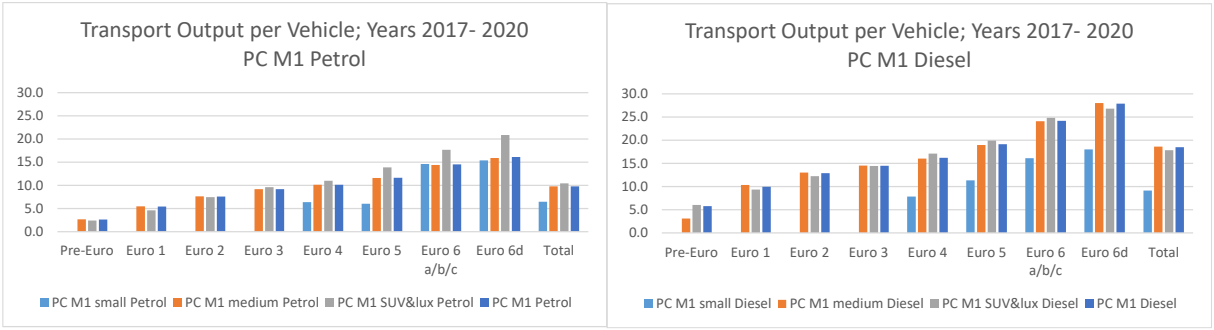

Figure 8: *Transport outputs per vehicle for different age of passenger cars*

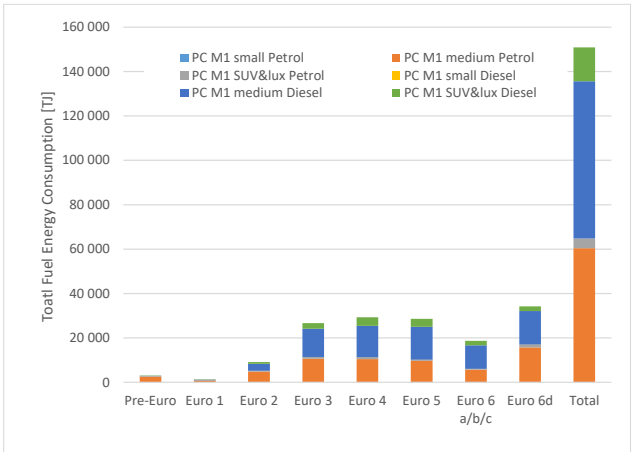

Figure 9: *Energy consumption for petrol and diesel, age and class of passenger cars*

Finally, the age of vehicles changes all parameters, although the efficiency of powertrains is not changed too from the times of Euro 4/IV. The reason is in more strict pollutants standards, shifting the operation point along Pareto margin, trade-of curve to lower efficiency. Nevertheless, the share of new vehicles considering transport

outputs per a vehicle is significant, as expected, which confirms *Figure 8*. The use of more efficient diesel-powered vehicles is more intensive. The same result is presented by energy use in *Figure 9*. Similar, even steeper trends can be found among commercial vehicles and buses.

All of energy consumption results are simply re-calculated into GHG TTW or GTW emissions and can be also amended by life-cycle analysis, as already shown in one of previous papers - [9]. Let's show just one case focused on more massive employment of electrified cars (battery BEV, plug-in PHEV or full HEV hybrids). The simplest boundary condition is to keep transport performance outputs and proportional representation of different car-size types. The speed of calculations in FECET enabled the authors to perform complicated iterative simulations using try-and-error mode.

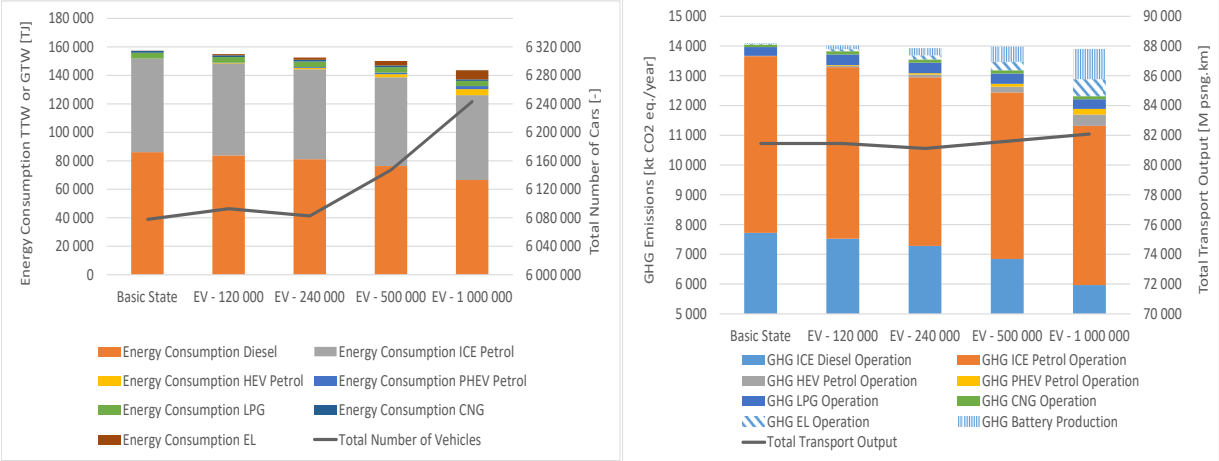

Figure 10: *Energy consumption and GHG emission changes due to more intensive employment of electrified vehicles (HEV, PHEV, BEV) keeping the proportionality in representation of different vehicle-size classes (number of EVs in axis description, basic state approx. 24 000 cars). Iterated constant transport outcomes. Time-to-sell a car 10 years.*

The number of vehicles (left side of *Figure 10*) is slightly increased, if number of electrified vehicles goes up, due to slightly different share of smaller vehicles in the new fleet. Energy consumption is slightly reduced due to more efficient use of already previously produced electric energy, if TTW for fossil or bio fuels and GTW – incl. charging losses – method is used for assessment. Electricity consumption summarizes BEV and PHEV charging, petrol consumption in PHEVs and HEVs is presented separately – almost no diesel HEVs are present in the Czech fleet. Although approx. 17% of fleet is electrified in the last case, the share of liquid fuels is still significant, gas fuel energy (LPG and CNG) being negligible.

Transport outputs were kept on the almost same level (right side of *Figure 10*) and GHG emissions were evaluated according WTW method, including fuel and electricity production. While the coefficients for hydrocarbon fuels were set according to 91[2], the emission factors for operation electricity production was 400 g CO_2 eq./kWh (lower than **net electricity consumption factor** in Germany or Czechia today), the production of accumulator cells in China with 582 g/kWh was assumed, although this official factor might be a little optimistic. The other CO_2 car production emissions are not included, although they would be slightly higher for electric vehicles. The time-of-using a battery at primary customer (before the car is sold,

mostly abroad) was assumed to 10 years, i.e., 2 years more than the warranty time for a battery. The conclusion is clear – before nuclear power stations amend the GHG emission factor in the whole Europe, there is no environmental profit from forced electrification.

3. CONCLUSION

The analytical capacity of the tool FECET, developed for prediction of energy consumption and GHG emissions, can be easily used for scenario assessments, as presented on an example. Before, the FECET has been substantially calibrated using independent sources of data from the current road and rail vehicle fleets in Czechia.

FECET allows to compare different possibilities of future fleet development with all major impacts on energy and material consumption. The market analysis must be provided by different sources. The political decisions are not yet predictable, however, but the impact study done before they are set might be useful for unbiased discussion on them.

REFERENCES

[1] Nařízení Evropského parlamentu (EU) č. 2023/851 (earlier 2019/631)
[2] SMĚRNICE EVROPSKÉHO PARLAMENTU A RADY (EU) 2018/2001 podpoře využívání energie z obnovitelných zdrojů, CELEX_32018L2001_CS_TXT
[3] COPERT Methodology. https://copert.emisia.com/copert-data/
[4] Life Cycle Assessment (LCA): How Sustainable is Your Car (greenncap.com). The Consortium Members Archive - Green NCAP: New Car Assessment Program, 2022, https://www.greenncap.com/
[5] POSPÍŠIL M., RED III - je racionální plnit náhradu GHG nebo úsporu OZE? Setkání expertní skupinyTAČR MOSUMO, VŠCHT Praha, 9.5.2024
[6] MACEK J., Simple Comparison of Solutions for GHG Reduction in Transport. Global Gamma Conference 2021, GammaTechnologies Westmont IL, p. 1-32
[7] MACEK, J., MORKUS, J., KOLÁŘ, J., Model of Surface Vehicle Fleet Energy Consumption Suitable For Climate-Energy Policy Assessment. L. Conference Of Internal Combustion Engines, Mendel University In Brno, 2019. pp. 110-123
[8] MACEK, J., MORKUS, J., Optimum Limits of Motor Vehicle Driving, XLVIIIth Conference Of Czech And Slovak Combustion Engine Research, Technical University of Liberec, 2017
[9] MORKUS J., MACEK J., How Ecological Is Your Electric Car? In: LIII. International scientific conference of the Czech and Slovak universities research dealing with R&D of ICE, 7. – 9.9. 2022, STU Bratislava, FSj, ISBN 978-80-227-5215-2, pp. 15-22

ACKNOWLEDGEMENT

This work has been supported by the projects of National Competence Center TN 0200 0054 BOVENAC and THETA TK 0401 0099_MOSUMO. The help of project colleagues, namely of Prof. Milan Pospíšil from the University of Chemistry and Technology Prague, Dr. Vojtěch Máca from the Charles University, Center of Environment and discussions in the think-tank Realistic Power Engineering and Ecology, https://realisticka.cz has been substantial, as well This support and collaborations are gratefully acknowledged.

55. mezinárodní vědecká konference zaměřená na výzkumné a výukové metody v oblasti vozidel a jejich pohonů

září 5. - 6., 2024 – Liberec, Česká republika
Technická univerzita v Liberci
Fakulta strojní, Katedra vozidel a motorů

PREDICTION OF GAS LEAKAGE THROUGH THE TURBOCHARGER SEALING SYSTEM

Pavel Novotný[1], Jiří Vacula[2], Petr Kudláček[3], František Kocman[4]

Abstract

The phenomena called compressor fouling is partly influenced by the gas leakage flow from the seal system of the turbocharger rotor. The prediction of gas flow through the sealing system depends not only on many design parameters but also on the operating conditions of the turbocharger. The paper presents experimentally validated computational model to quantify the mass flow of gases through the sealing system as a function of operating conditions. The computational model is applied to a truck engine turbocharger and the results are verified experimentally. The results show that the magnitude of gas blow-by is not only influenced by the geometrical parameters of the lubrication system, but is controlled by the thermo-mechanical loading of the turbocharger with a non-negligible influence of the radial dynamics of the rotor.

1. INTRODUCTION

The problem of environmental pollution caused by internal combustion engines (ICEs) in transport means has been perceived as serious and needs remedial actions. The most discussed issues are the reduction of fuel consumption and the associated CO_2

[1] Pavel Novotný, Brno University of Technology, Technická 2896/2, 616 69 Brno, Czech Republic, novotny.pa@fme.vutbr.cz
[2] Jiří Vacula, Brno University of Technology, Technická 2896/2, 616 69 Brno, Czech Republic, jiri.vacula@vutbr.cz
[3] Petr Kudláček, Brno University of Technology, Technická 2896/2, 616 69 Brno, Czech Republic, petr.kudlacek@vutbr.cz
[4] František Kocman, Brno University of Technology, Technická 2896/2, 616 69 Brno, Czech Republic, frantisek.kocman@vutbr.cz

production in emissions. However, ICE operation also generates the non-negligible production of particles by both diesel engines [1] and spark-ignition engines [2] and there are some negative effects of particles on efficiency of turbochargers.

During ICE operation, particles are deposited in the turbocharger (TC) compressor. Particle deposition can lead to a significant reduction in compressor efficiency. The particle deposition process, known as compressor fouling, is partly influenced by gas leakage from the sealing system of the turbocharger rotor. This leakage gas contains fine liquid oil particles, some of which are deposited on the compressor walls. A reduction in the production of these particles can be achieved by limiting gas leakage through the turbocharger sealing system.

TC is used as a standard to increase the specific performance and reduce the fuel consumption of the ICE. In recent years, research and development of TCs have focused on increasing the ranges of operating conditions for the TC, maximising efficiency (especially in transient operating conditions) or increasing reliability [3]. However, during TC operation, there is also a natural leakage of gases – the so-called gas blow-by (GBB) – this is the gas flow rate from the compressor or turbine to the central casing due to the pressure difference [4], and typically measured in litres per minute. Thus, the TC is one of the significant sources of GBB in ICEs, and with modern trends requiring higher pressure ratios, this source is increasing further. At the same time, intake air or exhaust gases entering the central housing of the compressor or turbine are considered to be contaminants of the lubricant. A high concentration of gas in a lubricant can cause many negative effects. For example, a lubricant with a high air content becomes compressible and less resistant to oxidation, and the lubricant loses its properties and eventually its service life more quickly.

If the accumulated amount of air in the central housing increases significantly, the lubricant can also leak through the seal system back into the compressor or turbine. This effect can be particularly noticeable under certain operating conditions, such as very low rotor speeds, in which there is very low pressure in the compressor outlet and no natural pressure gradient towards the central housing. Under these operating conditions, the gas returns from the central housing to the compressor or turbine, creating a so-called gas blowback flow, and this gas carries a certain amount of lubricant with it. This lubricant is subsequently partially burned, and this negative phenomenon is accompanied by the increased production of unburned hydrocarbons in ICE exhaust gases [5]. An example of an operating condition that produces the gas blowback flow associated with increased lubricant consumption (LC) has been presented by Sherrington et al. [6].

LC is a natural but undesirable effect of ICE operation. The piston group (PG) is usually the dominant source in an ICE. An investigation of the mechanisms of LC in ICEs has revealed that many studies, e.g. Thirouard and Tian [7], have declared that LC is highly dependent on the oil-dragging mechanisms in the gas blowback flow; thus, a decrease in LC can be achieved by controlling these gas blowback flows. Although not all mechanisms are the same for TCs and ICEs, it can be assumed that the mechanism of oil dragging in gas blowback flow will also be very significant for TCs. The reduction in LC is likely to be related to the control of GBB and blowback flows, and by reducing these flows, the LC can be reduced as well. This reduction is also likely to have a positive effect on the LC of the whole ICE, given that studies [8; 9] have proven the large effects of the TC on the overall LC. Excess LC is also one of the main factors that reduce TC reliability [10].

The seal system is a key design element of the TC that allows the control of GBB and therefore the LC. The seal system uses flexible seal rings located between the rotating groove on the rotor shaft and the central housing on both the compressor and turbine sides. These seal systems usually include several seal rings placed in some configurations in the central housing and with defined clearances in the rotor grooves. The seal rings are mounted with specific pretension in the central housing and define a labyrinth shape by their position within the rotor groove. The actual shape of the labyrinth is influenced by the movements of the rotors and thermal deformations due to the given operating conditions. Under certain operating conditions, contact between the seal rings and the rotor groove may occur, which may subsequently cause the axial displacement of the ring in the central housing and establish its new position. Thus, the ring is constantly being pushed away from the walls of the rotor groove. As a result, the dimensions and shape of the labyrinth vary over time.

Controlling gas leakage through the TC seal system depends on the knowledge of the mechanisms of GBB. The prediction of GBB through the seal system and the explanation of GBB mechanisms under operating conditions are the aims of the work. The prediction focuses on the effects of mechanical interactions between the seal rings, rotor grooves and central housing. Knowledge of the individual mechanisms will lead to the ability to control GBB, depending on the design parameters and operating conditions, and will enable targeted design solutions to reduce GBB and hence indirectly reduce LC and particulate matter production.

2 COMPUTATIONAL AND EXPERIMENTAL METHODS

2.1 Computational Approach

The computational model for the solution of GBB requires a balanced combination of the physical depth of description of individual processes and the efficient formulation of basic equations for their numerical solution. The approach chosen for the solution of the coupled dynamics of bodies, fluid dynamics and heat transfer used the principles of a virtual turbocharger. This nonlinear mechanical computational model was developed and experimentally verified for TC rotor dynamic simulations with floating ring journal bearings by Novotný et al. [11] and for the simulations of lubrication and dynamic simulations of a double-sided thrust bearing, according to Novotný et al. [12]. Considering the objectives of this study, this model was extended to include sealing ring dynamics, gas dynamics and a more detailed description of the thermal effects.

The assembled computational model in Multibody system ADAMS contained 30 moving rigid bodies, two moving 3D elastic bodies, four mass point bodies, 12 differential equations, 35 constraint joints, nine motion generators, four 3D contact forces, 28 force elements, 124 data elements, 416 design variables and 734 solver variables. A schema of the virtual turbocharger, including the submodules, is presented in **Figure 1**. A detailed description of the calculation models of individual systems can be found in Novotný et al. [13].

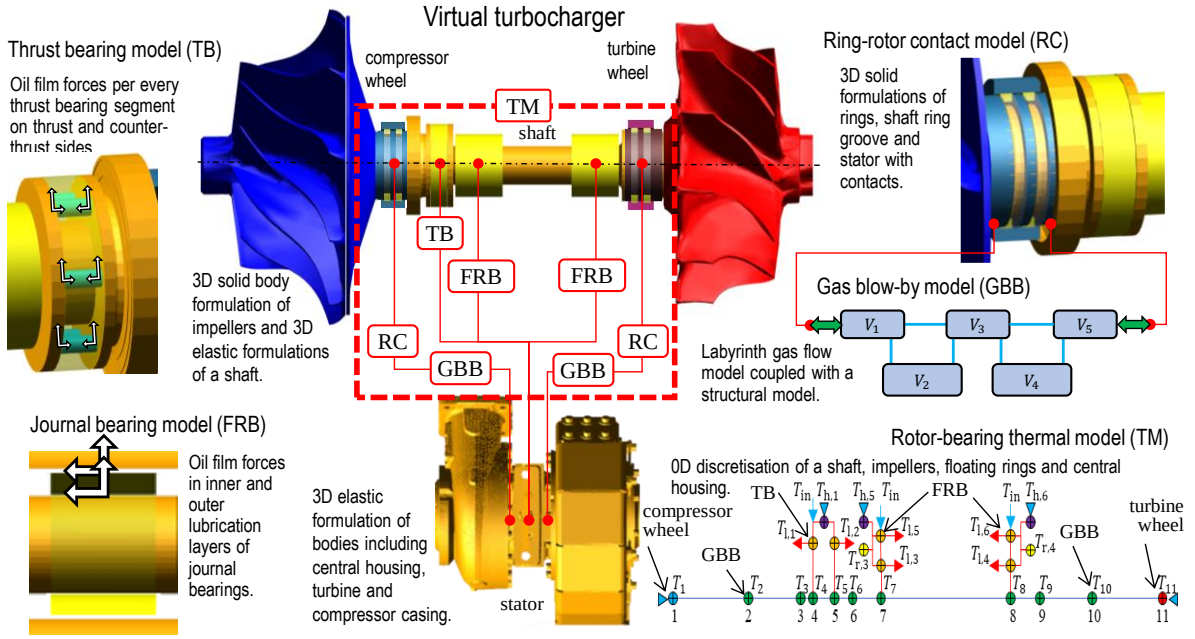

Figure 1: *Graphical representation of the virtual turbocharger, including the submodules. (a) represents the thrust bearing thermohydrodynamic model (TB) [12], resulting in oil film forces for every thrust bearing segment on the thrust and counter-thrust sides. (b) shows the seal ring–rotor contact model (RC) with 3D solid body formulations of the rings, shaft ring grooves and a stator part. (c) presents the thermohydrodynamic model of the floating ring bearing (FRB) [11] with oil film forces in the inner and outer lubrication layers. (d) is the gas blow-by model (GBB) and e) is the rotor-bearing thermal model (TM) using 0D discretisation of a shaft, impellers, floating rings and the central housing.*

2.2. Experimental Setup

The verification of the calculated quantities was carried out by means of technical experiments in the test laboratory by means of measurements of basic quantities including temperatures and gas pressures in front of and behind the impellers, displacements on the axial bearing and others. GBB values were directly measured on the test bench for the entire turbocharger.

Quantity	Sensor type	Measurement range	Measurement accuracy
Gas temperature	thermocouple	−40– 1200°C	±1.5°C for 0–333°C or ± 0.75°C for 333–1200°C, class 1, DIN EN 60584
Gas pressure	piezoresistive	0– 1500 bar	±1 % of FSO at room temp
Oil temperature	thermocouple	0– 200°C	±1.5°C, class 1, DIN EN 60584
Oil pressure	piezoresistive	0.5– 6 bar	±0.5%
Distance	eddy current	0– 500 µm	±1 µm
Gas flow rate	orifice pressure difference	1.5– 75 $dm^3 min^{-1}$	±1.5% of FSO

Table 1: *List of sensor characteristics used for technical experiments.*

The test TC was installed on an inline six-cylinder ICE with a maximum power output of 260 kW at an engine speed of 2200 min^{-1}. The sensor characteristics used to

measure the gas and oil pressures and temperatures, the minimum lubrication gap thickness of the thrust bearing and the GBB through the seal system are presented in **Table 1**Chyba! Nenalezen zdroj odkazů.. A detailed description of the technical experiment including the location of individual sensors can be found can be found in Novotný et al. [13].

3. DISCUSSION OF RESULTS

In general, the level of the GBB in the TC is mainly monitored under the operating conditions of the ICE design. In the case of this study, a continuous TC run-up along the operating line with increasing rotor speed was chosen. According to the initial assumptions, one of the major influences on the GBB was the axial movement of the rotor controlled by the thrust bearing. Therefore, the accuracy of the prediction of the axial displacement greatly affected the prediction of the GBB. A comparison of the calculated and measured minimum thicknesses of the lubrication gap of the thrust bearing is presented in **Figure 2**. The results also demonstrated the influence of the TC rotor radial vibrations, with the range of vibrations being defined by the upper and lower envelopes. The higher thickness of the lubrication gap was obtained at rotor speeds when the axial force was close to zero, i.e. the axial forces from the compressor and turbine sides were balanced.

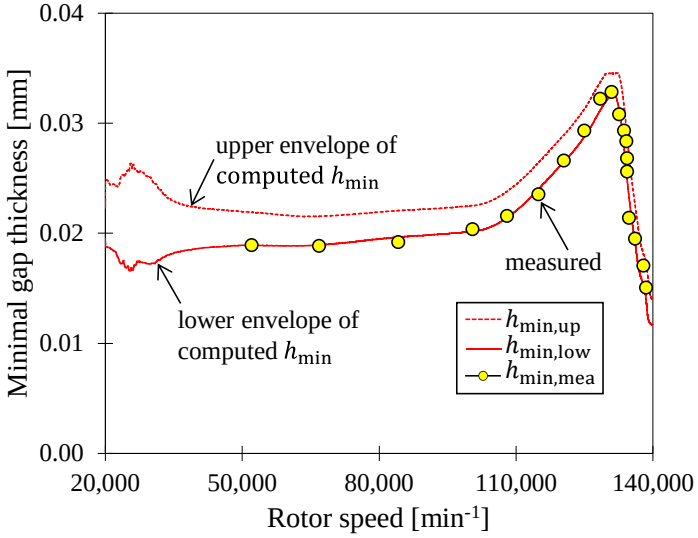

Figure 2: *Calculated minimum thickness of the lubrication gap, presented by the upper envelope ($h_{min,up}$) and lower envelope ($h_{min,low}$) and obtained from the thrust side of the thrust bearing at the edge of the work surface. The yellow points present the measured values in the form of the lower envelope of the minimum thickness of the lubrication gap thickness ($h_{min,mea}$).*

The prediction of the GBB through the TC sealing system depending on the rotor speed was the main result. **Figure 3** compares the calculated values of the GBB with experimentally determined values. **Figure 3** also shows the calculated GBB corresponding to the compressor and turbine sides of the seal system. The turbine side was dominant at low rotor speeds, but both sides gradually reached similar values at high rotor speeds. The compressor side should have started to dominate at very high speeds, but a sharp decrease in the compressor pressure ratio restricted the GBB at very high speeds.

The comparison of calculated and measured values in **Figure 3** shows some differences. These were caused by a combination of many partial phenomena that were not predicted accurately by the computational model. However, the likely main reason for the differences was the inaccurate prediction of temperatures at the location of the seal system on the turbine side.

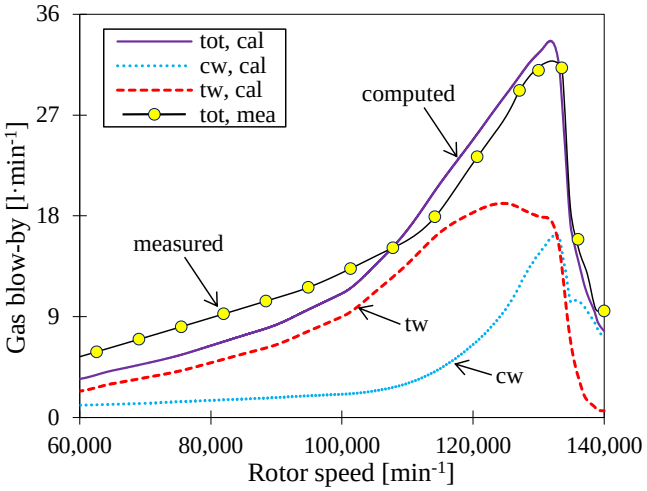

Figure 3: Comparison of the calculated (cal) and measured (mea) gas blow-by through the seal system (tot) and a separation of the calculated values into components corresponding to the compressor side (cw) and turbine side (tw). The results were presented for a continuous TC run-up along the operating line with increasing rotor speed.

4. CONCLUSION

The GBB under the typical design operating conditions of the TC is influenced by the geometric configuration of the seal system, thermodynamic conditions of the TC and movement of the rotor. The individual effects on the GBB can be summarised as follows:

- The mechanism of the GBB through the ring gap is influenced by the cross-sectional area size of the ring gap, pressure gradient and temperature in the seal system. The mechanism is always present, and the rotor movement has very little effect. If the thickness of the thin gap is limited on a given side, the ring gap mechanism dominates.
- The mechanism of the GBB through the thin gap is fundamentally affected by the movement of the rotor in the axial direction because the axial movement of the rotor can simultaneously limit the mass flow rates on one side of the seal system and increase them on the other. The radial movement of the rotor also has a certain observable effect, i.e. mainly related to the rotor tilt at a given location. A small impact on the GBB can be observed at the locations of strong rotor resonances.
- The rotor movement in the axial direction defines the geometric shape of the sealing labyrinth, and it is mainly influenced by the pressure differences on the impellers and characteristics of the thrust bearing. This effect is crucial, thus representing the factor that must always be considered for computational modelling approaches.
- The thermodynamic conditions on the impellers affected both the GBB and the axial movements of the rotor. The pressure ratios on the impellers determined

the axial load on the rotor, and the impeller temperature significantly affected the temperature distribution in the rotor and therefore in the seal system. This influence is very visible on the turbine side, where the temperatures significantly exceeded the oil inlet temperatures, and the corresponding GBB then varies in accordance with the gas properties at a given temperature, i.e. mainly the gas density.

The evaluation of the quality of GBB prediction by the computational model, including the influence of different mechanisms, required some aspects to be considered. The proposed computational model – the so-called virtual turbocharger – combined many physical processes, and each of these processes was described with some modelling inaccuracy. Thus, the solution results of the computational model included a non-negligible difference. This difference was especially visible at lower rotor speeds, wherein the values reached roughly 30%. However, this difference, although relatively large, was not important from a practical point of view, since the GBB values were small and therefore not significant for TC operation. The cause of these differences must be sought, primarily under thermal boundary conditions.

ABBREVIATIONS

cw	compressor side
FRB	floating ring bearing
GBB	gas blow-by
ICE	internal combustion engine
LC	lubricant consumption
TC	turbocharger
TB	thrust bearing
TM	rotor-bearing thermal model
tw	turbine side

REFERENCES

[1] SARVI, Arto, Carl-Johan FOGELHOLM and Ron ZEVENHOVEN. Emissions from large-scale medium-speed diesel engines: 1. Influence of engine operation mode and turbocharger. *Fuel Processing Technology*. 2008, **89**(5), 510-519. ISSN 03783820.

[2] QIAN, Yong, Zilong LI, Liang YU, Xiaole WANG and Xingcai LU. Review of the state-of-the-art of particulate matter emissions from modern gasoline fueled engines. *Applied Energy*. 2019, **238**, 1269-1298. ISSN 03062619.

[3] FENELEY, Adam, Apostolos PESIRIDIS and Amin ANDWARI. Variable Geometry Turbocharger Technologies for Exhaust Energy Recovery and Boosting-A Review. *Renewable and Sustainable Energy Reviews*. 2017, **71**, 959-975. ISSN 13640321.

[4] DHARIWAL, H.C. Control of blowby emissions and lubricating oil consumption in I.C. engines. *Energy Conversion and Management*. 1997, **38**(10-13), 1267-1274. ISSN 01968904.

[5] BRANDENBERGER, Sandro, Martin MOHR, Koni GROB and Hans NEUKOM. Contribution of unburned lubricating oil and diesel fuel to particulate emission from passenger cars. *Atmospheric Environment*. 2005, **39**(37), 6985-6994. ISSN 13522310.

[6] SHERRINGTON, Ian, Neil GRICE and John JACKSON. A Capacitance Based Transducer to Detect Oil Leakage from the Turbine End of a Turbocharger. *SAE Technical Paper*. 1993, **1993**(930191).

[7] THIROUARD, Benoist and Tian TIAN. Oil Transport in the Piston Ring Pack (Part I): Identification and Characterization of the Main Oil Transport Routes and Mechanisms. *SAE Technical Paper*. 2003, **2003**(20030345).

[8] DELVIGNE, Thierry. Oil Consumption Sources in a Modern Gasoline Engine Including Contribution of Blow-by Separator and Turbocharger: An Experimental Study Based on the Use of Radiotracers. *SAE International Journal of Fuels and Lubricants*. 2010, **3**(2), 916-924. ISSN 1946-3960.

[9] MANNI, M., M. CARRIERO and A. ROSELLI. A Study of Oil Consumption on a Diesel Engine with Independently Lubricated Turbocharger. *SAE Technical Paper*. 2002, **2002**(2002-01-2730).

[10] PLAKSIN, Aleksey, Alexander GRITSENKO and Konstantin GLEMBA. Modernization of the Turbocharger Lubrication System of an Internal Combustion Engine. *Procedia Engineering*. 2015, **129**, 857-862. ISSN 18777058.

[11] NOVOTNÝ, Pavel, Petr ŠKARA and Juraj HLINÍK. The effective computational model of the hydrodynamics journal floating ring bearing for simulations of long transient regimes of turbocharger rotor dynamics. *International Journal of Mechanical Sciences*. 2018, **148**, 611-619. ISSN 0020-7403.

[12] NOVOTNÝ, Pavel, Jozef HRABOVSKÝ, Jaroslav JURAČKA, Jiří KLÍMA and Vladimír HORT. Effective thrust bearing model for simulations of transient rotor dynamics. *International Journal of Mechanical Sciences*. 1, 2019, **2019**(157-158), 374-383.

[13] NOVOTNÝ, P., P. KUDLÁČEK and J. VACULA. Explanation of the mechanisms of unsteady gas flow through the turbocharger seal system, including thermal and structural interactions. *Propulsion and Power Research* [online]. 2023, **12**(2), 180-198. ISSN 2212540X.

[14] HE, Hong, Siyou XU, Ruiqian YAN and Jianbo JI. Study on the Seal Leakage of Turbocharger. *Fluid Machinery and Fluid Mechanics*. Berlin, Heidelberg: Springer Berlin Heidelberg, 2009, 234-237. ISBN 978-3-540-89748-4.

ACKNOWLEDGEMENT

The research leading to these results has received funding from the Specific research program at Brno University of Technology, reg. no. FSI-S-23-8235.

55. mezinárodní vědecká konference zaměřená na výzkumné a výukové metody v oblasti vozidel a jejich pohonů

září 5. - 6., 2024 – Liberec, Česká republika
Technická univerzita v Liberci
Fakulta strojní, Katedra vozidel a motorů

MOBILE HYDROGEN FILLING STATIONS

Vít Doleček[1], Petr Hatschbach[2]

Abstract
Mobile hydrogen filling stations usually do not contain any compressor to feed high-pressure tanks in the vehicles. Only source of pressurized hydrogen is initial pressure in the storage. Cooling of hydrogen is not available too. All weak points and issues of this simplified solution are described and analyzed. The paper is supplemented by the results of model case simulations.

1. INTRODUCTION

Development of hydrogen mobility is not possible without massive investment into the hydrogen infrastructure. At start, only few buses were operated in close vicinity of its home depot. Filling of buss hydrogen bottles was manual process with pressure limited to half (35 MPa) of automotive standard (70 MPa). Nowadays, there are only two fully automatized vehicle filling stations in Czech Republic enabling first unlimited usage of hydrogen cars. At least around Litvinov or Prague. Nevertheless, other public hydrogen

[1] Vít Doleček, Czech Technical University in Prague, Technická 4, 166 07, Praha 6, v.dolecek@fs.cvut.cz
[2] Petr Hatschbach, Czech Technical University in Prague, Technická 4, 166 07, Praha 6, petr.hatschbach@fs.cvut.cz

filling stations are under construction. In addition to high hydrogen vehicle prices together with relatively high hydrogen price development of hydrogen mobility is very slow in comparison to other alternative powertrains such as battery electric vehicles.
Hydrogen filling stations works with highly pressurized hydrogen and that is why its operation is subject of strict ISO regulations [1], [2], [3]. ISO standards involve hydrogen cooling and station to vehicle communication for fast and safe hydrogen filling without risk of overheating of composite pressure tanks. Because of all these aspects, a fully automatic hydrogen filling station is a very complicated (see Figure 1) and expensive piece of equipment which together with the small number of vehicles in operation are the reasons for the poor development of the infrastructure. This closed circle seems to coming to an end in the form of small hydrogen producers. These producers, usually owners of solar parks, want to store energy in the form of hydrogen for later use. What will probably not solve the hydrogen mobility in large scale may help the development of hydrogen vehicles usage. Increased count of hydrogen vehicles in future could create hydrogen infrastructure more viable.

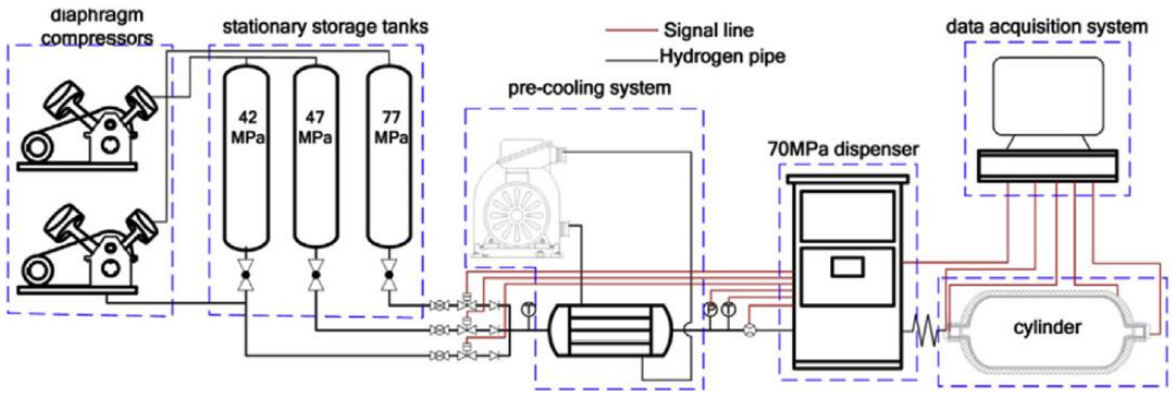

Figure 1*: Schematic diagram of hydrogen filling station example.*

Small hydrogen producers need to solve issue with hydrogen transport into the location of consumption without large investments into something very much close to what we understand as public hydrogen infrastructure. Mobile hydrogen storage created for instance with container filled with pressurized tanks is suitable and low prize solution (see Figure 2). Container might consist also necessary equipment for efficient and safe dispose of hydrogen. Lower hydrogen pressure level and requirement for simplicity and autonomy does not allow to use any compressor and cooling system. The only source of energy for hydrogen filling is the pressure difference between hydrogen mobile storage and filled vehicles.
Hydrogen mobile filling stations need to solve issue with heating of vehicle pressure tanks. Energy requirement for hydrogen compression and pressure limit for high pressure gas transport set the maximum reasonable hydrogen pressure level for mobile storage. Vehicle target pressure was set to 35 MPa and mobile storage will work with maximum pressure of full storage only a bit higher (around 50 MPa). Small pressure difference create issue how to effectively discharge as much hydrogen as possible and no to carry hydrogen back and forth. These two issues are addressed in this paper.

Figure 2: *Example of mobile hydrogen storage.*

2. PHYSICAL PROPERTIES OF GASEOUS HYDROGEN

In the gaseous state, hydrogen occurs as a diatomic molecule H_2. It is a colourless, flammable gas burning with a nearly invisible, ultraviolet or blue flame with a very high calorific value (per unit mass). Some important physical properties are presented in Table 1.

Chemical Symbol	H_2
Standard atomic weight	1.00794
Melting Point	14.025 K (−259.125 °C)
Boiling point at NTP (20°C & 1 atm)	20.268 K (−252.882 °C)
Critical temperature & pressure	33.25 K, 1.307 MPa
Density at NTP (20°C & 1 atm)	0.008375 kg/m^3
Flame temperature in air	2045 °C
Higher heating value at 25°C	141.80 MJ.kg^{-1}
Lower heating value at 25°C	119.96 MJ.kg^{-1}

Table 1: *Physical properties of gaseous hydrogen.*

2.1 Real gas state equations

Under normal conditions (e.g. temperature 20 °C and pressure 1 atm =101 325 Pa), an ideal gas model can be used for thermodynamic calculations. The ideal gas is assumed to be perfectly compressible and without internal friction. The ideal gas law may be written as:

$$pV_m = RT \quad \text{or} \quad pv = rT \tag{1}$$

where:

p ... pressure [Pa]

T ... temperature [K]

ρ ... density [kg.m^{-3}]

$v = \frac{1}{\rho}$ ... specific volume [m^3 kg^{-1}]

$V_m = M/\rho$ ... molar volume [m^3.mol^{-1}]

M ... molar mass [kg.mol^{-1}] – for hydrogen H_2 = 0,00201588 kg.mol^{-1}
R = 8,31446261815324 J.K^{-1}.mol^{-1} ... molar (universal) gas constant
r ... specific gas constant [J.K^{-1}.kg^{-1}] – for hydrogen H_2 = 4116,07 J.K^{-1}.kg^{-1}

2.1.1 Redlich–Kwong equation

But in the case of increasing pressures and/or decreasing temperatures, deviations from the ideal gas model increase and the ideal gas law cannot be used. When transferring hydrogen between storage tanks, it is necessary to consider hydrogen as a real gas due to very high storage pressures and large pressure and temperature changes.
Based on the theories of corresponding states principles, many equations have been developed to describe the properties of real gases. The most commonly used real-gas state equation is the Redlich–Kwong equation:

$$p = \frac{RT}{V_m - b} - \frac{a}{\sqrt{T}\, V_m\, (V_m + b)} \tag{2}$$

where:

$$a = \frac{1}{9(\sqrt[3]{2} - 1)} \frac{R^2\, T_c^{\,2.5}}{P_c} = 0.42748\, \frac{R^2\, T_c^{\,2.5}}{P_c},$$
$$b = \frac{\sqrt[3]{2} - 1}{3}\, \frac{R\, T_c}{P_c} = 0.08664\, \frac{R\, T_c}{P_c},$$

and where:

T_c ... critical temperature- for hydrogen T_c = 33.5 K
P_c ... critical pressure – for hydrogen P_c = 1.307 MPa

so, for hydrogen the constants *a* and *b* are:

a = 0.144373094
b = 1.83971.10^{-05}

However, the practical application of the Redlich–Kwong equation is complicated by its complex structure containing the volume as a cubic nonlinear term. The calculation usually requires iterative solutions.

2.1.2 Compressibility factor approach

Another option for describing the behaviour of hydrogen as a real gas is to use a compressibility factor *Z* which expresses to what extent the behaviour of the real gas deviates from the description by the ideal gas law:

$$Z = \frac{pv}{rT} \tag{3}$$

Chen et al. [4] proposed relatively simple real gas model where an approximation function for the compressibility factor is used in the form:

$$Z = \left(1 + \frac{\alpha p}{T}\right) \tag{4}$$

Where for hydrogen is a coefficient α = 1,9155.10^{-6} K.Pa^{-1} and is valid in pressure range to 100 MPa and temperature range 253 K to 393 K.
The model gives very good agreement with NIST data (relative error to 1,1 %, which is better than the Redlich–Kwong equation).

2.2 Joule–Thomson effect

Joule–Thomson effect is related to the description of real gas temperature changes during a throttling. For most gases, throttling as an isoenthalpic process results in a decrease in temperature, which is used, for example, in gas liquefaction. For hydrogen (and helium and neon) the opposite is true. For hydrogen, the inversion temperature below which the gas temperature is reduced during adiabatic expansion is very low (202 K = -71°C at atmospheric pressure).

Joule–Thomson effect is expressed by the Joule–Thomson coefficient given by the ratio of the change in temperature *T* to the change in pressure *p* at constant enthalpy *i*:

$$k_{JT} = \left(\frac{\delta T}{\delta p}\right)_i \quad (5)$$

An important parameter is the so-called inversion temperature – the temperature at which the Joule–Thomson coefficient is zero.
If the temperature of the throttled gas is **lower** than the inverse temperature, the Joule–Thomson coefficient is **greater** than zero and the gas is **cooled** by throttling.
If the temperature of the throttled gas is **above** the inversion temperature, the Joule–Thomson coefficient is **less** than zero and the gas is **heated** by the throttling.

Thus, for hydrogen, the Joule–Thomson coefficient at temperatures above 202 K (-71°C). At normal ambient temperature it will therefore be negative and as the gas expands during the throttling process the gas temperature will rise. This phenomenon will occur, for example, when filling the tanks of a vehicle from the cylinders of hydrogen storage tanks or when rapidly filling other tanks from a large, hard source of compressed hydrogen. However, the low absolute value of the Joule-Thomson coefficient (approx. 0.03 K/bar at 300 K) means that in practice the temperature increase will be relatively small and often negligible.

2.3 Temperature change during rapid filling

During the distribution of the compressed hydrogen, the hydrogen will be transferred from one tank to another. This can be often a rapid process in which the pressure and temperature of hydrogen will change rapidly. The rapid change in temperature can be limiting and must not exceed the limits allowed for hydrogen storage components, particularly pressure cylinders.
From a thermodynamic point of view, a combination of three phenomena occurs during rapid hydrogen flow:

a) Compression of the gas in the filled container and expansion of the gas in the discharged container.
b) If the filling takes place rapidly, it can be roughly considered as an adiabatic process, which will increase the temperature of the gas in the filled reservoir and decrease the temperature in the discharged reservoir.
c) During filling, the hydrogen expands from the higher pressure in the discharged container to the lower pressure in the filled container by passing through the throttling valve, which, due to the negative value of the Joule-Thomson coefficient for hydrogen at normal temperatures, results in an increase in the temperature of the hydrogen.
d) The kinetic energy of the fast-flowing gas is converted into internal energy of the gas in the filled tank, which also results in a temperature rise.

e) The calculations show that the first phenomenon, adiabatic compression of the gas in the filled tank, has the greatest influence on the increase of the temperature of the gas in the tank and is crucial in controlling the process of gas distribution.

3. HYDROGEN STORAGE IN PRESSURE TANKS

Low hydrogen density demands very high pressure to store maximum possible amount. To provide storage gravimetric density similar to gasoline tank or battery pack high pressure up to 70 MPa is used. Other type of storing technology involving extreme cooling was not considered because of its very high energy demand.

3.1 Hydrogen high pressure tank construction

Several constructions types are used to store technological gases. Different technology is used in dependence on the pressure inside tank – see Table 2. Due to hydrogen molecular size, high-density polymer liner is used inside the tank as a sealant – see Figure 3.

Type	Materials	Typical pressure (MPa)	Gravimetric density (weight %)
I	All-metal construction	30	1.7
II	Mostly metal, composite overwrap in the hoop direction	20	2.1
III	Metal liner, full composite overwrap	70	4.2
IV	All-composite construction	70	5.7

Table 2: *Pressure tank materials according to their type.*

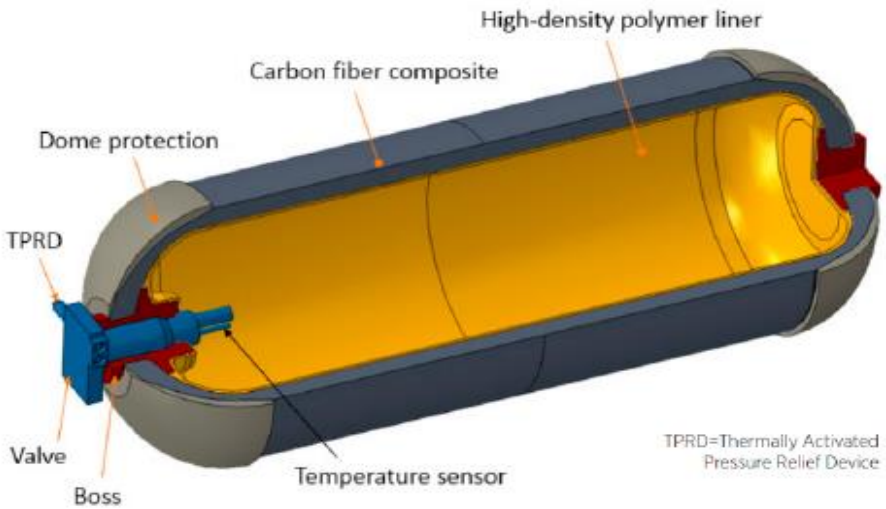

Figure 3: *Example of type IV composite pressure tank construction.*

Only pressure tank construction type 3 and 4 are used for hydrogen transportation. Type 3 tanks are widely used for pressures of 35 MPa and in recent years also for 70 MPa. The metal liner of type 3 is usually made of aluminum, which, unlike the plastic

liner of type 4, has a higher thermal conductivity and specific heat capacity. It can dissipate more heat generated during the filling of the tank. Nevertheless, thanks to much better higher gravimetric density of the tank, hydrogen vehicles use type 4 fully composite tanks. Type 4 cylinders are also mostly applied in hydrogen distribution and in mobile hydrogen filling stations.

3.2 Hydrogen temperature rise during filling

Hydrogen thermodynamic properties described in chapter 2 are natural source of heat generated during rapid tank filling. Joule-Thompson effect at throttling valve heats hydrogen only by several Kelvins. Hydrogen compression inside the pressurized tank is much stronger source of heat (see Figure 4) and can potentially be a source of tank damage if the temperature of the composite tank wall exceeds approximately 85°C.

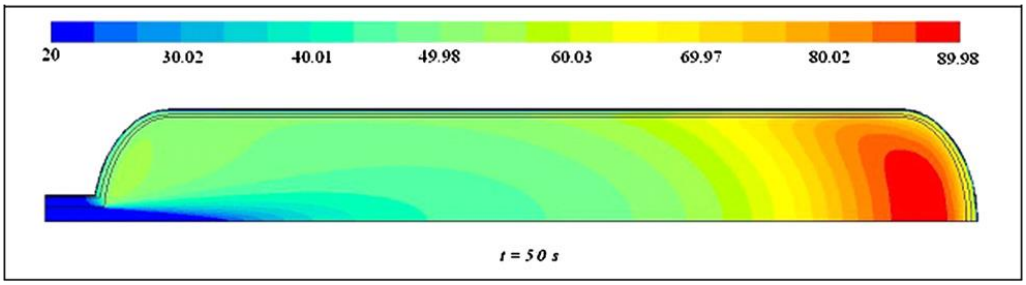

Figure 4: *Temperature distribution after 50 s of filling of the hydrogen tank [5].*

Appropriate adjustment of the flow inlet direction to the tank ensures mixing of hydrogen charge and homogenization of temperature inside the tank (see Figure 5). This approach improves uniform heating of the tanks and provide increase of heat transfer to the walls (up to 800 $W.m^{-2}K$) for better heat dissipation and faster tank filling.

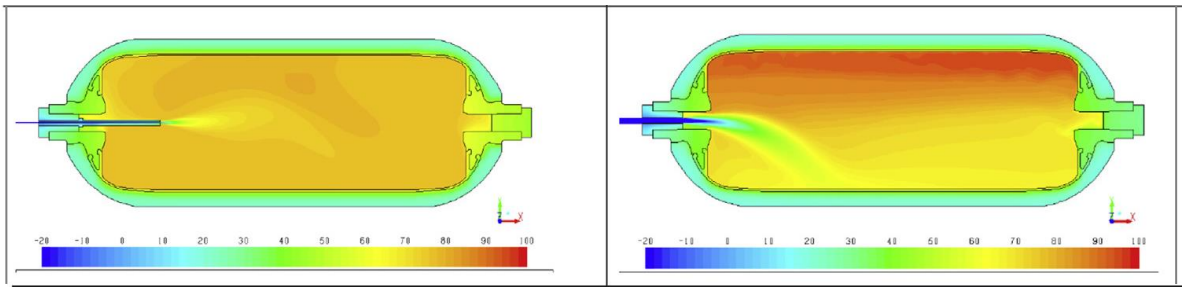

Figure 5: *Temperature distribution in hydrogen tank with two variants of flow inlet direction [6].*

Despite these measures, it is necessary to maintain a lower filling rate or not to fill the tanks to pressures higher than 35 MPa. For the case of a mobile filling station, a combination of both is considered.

4. MOBILE HYDROGEN STORAGE

Mobile hydrogen storage combines a set of pressure tanks, a dispensing equipment and simple control computer for monitoring and controlling of filling. Everything is built into the container for easy transportation. The whole capacity of the storage is divided into several sections. This configuration enables cascade filling. Mobile hydrogen storage does not contain any compressor nor refrigeration equipment and tank filling

is ensured only by sufficient gas overpressure. Without cascade filling configuration would storage empty only to vehicle target pressure (plus some pressure difference which is considered approximately 1 MPa). At this pressure, the amount of hydrogen in “empty” storage is still significant.
The cascade storage arrangement improves the efficiency of the storage utilization. Sections with pressure lower than target can be used in the beginning phase of filling when vehicle tank pressure is low enough. Equipment required for this type of arrangement is pressure monitoring of each section and a solenoid valves for automatic section switching. Increased complexity of control system is well compensated by an increased hydrogen amount filled into cars. The only question is how many sections is needed and how to divide the total count of pressure tanks into sections.

4.1 Hydrogen vehicle filling simulation

Engineering simulation tools help to understand possible issues of newly developed machines and accelerate new product design. GT-SUITE from Gamma Technologies [7] is well established pack of simulations tools used in automotive industry. Thanks to great versatility of the software, it has already been used for many unusual applications with excellent results. Redlich-Kwong equation of state is possible to use to capture Joule-Thompson effect. Nevertheless, the best results for simulation of hydrogen flow at very high pressures are achieved with REFPROP tool from NILS [8] which is also built-in, mainly for refrigerant circuits simulations.

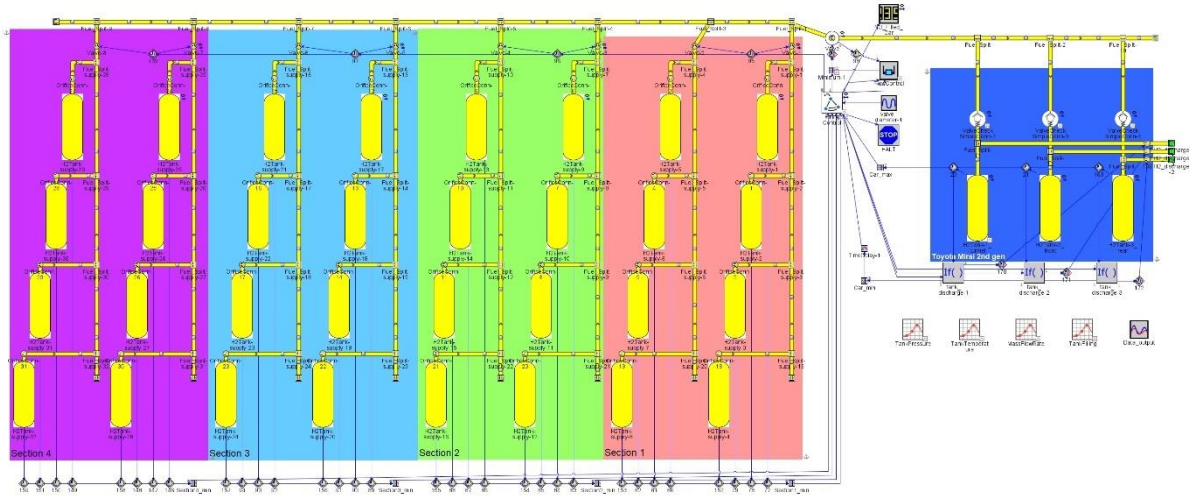

Figure 6: *Hydrogen mobile storage simulation model created in GT-SUITE. Different colours represent storage division into sections.*

The simple simulation model of mobile hydrogen storage example was created (see Figure 6) consisting of 32 pressure tanks of total internal volume 10656 litres. Model also contains hydrogen pressure tanks representing vehicle – Toyota Mirai which is typical hydrogen vehicle. The heat transfer to the tank walls was calibrated using results in papers [5] and [6]. Hydrogen initial pressure in the storage was 50 MPa and vehicle target pressure was 35 MPa.
The simulation model was used for validation of sequential filling concept and for simulation of vehicle composite tanks heat up during filling. Simulation results provided estimation of hydrogen mass flow rate limit for safe filling with respect to constraint given by composite material of vehicle pressure tank walls. Example of results for case

of hydrogen temperature 15°C in Figure 7 show that mass flow rate limit is approximately 9 $g.s^{-1}$ with filling time of approximately 6 minutes.

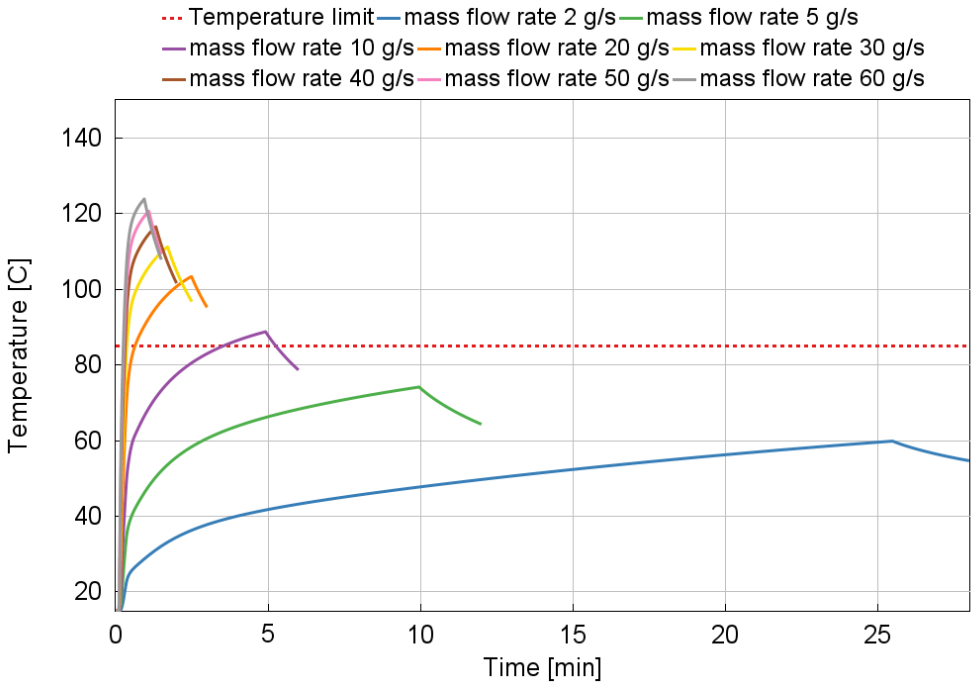

Figure 7: *Vehicle composite tank temperature during filling in dependence on hydrogen mass flow rate with hydrogen initial temperature 15°C.*

4.2 Arrangement of hydrogen storage into sections

Simulation time of the transient 1-D simulation of hydrogen storage emptying was quite long. From this reason simple model of thermodynamic state in individual pressure tanks was programmed in MS Excel using same REFPROP plug-in for calculation of hydrogen properties. This allowed simple and fast evaluation of several configuration of storage division into sections. Results of two storage configuration are displayed in Figure 8. In case of undivided storage with only one section, only 22% of its capacity can be used. Division of storage to 4 sections improves this usage to 55% and division to 8 sections to 65%. Count of filled vehicles can be improved from 88 (4 sections) to 107 (8 sections). Further small improvement can be achieved by uneven division into sections. This benefit can be achieved with a relatively small increase of system complexity and costs.

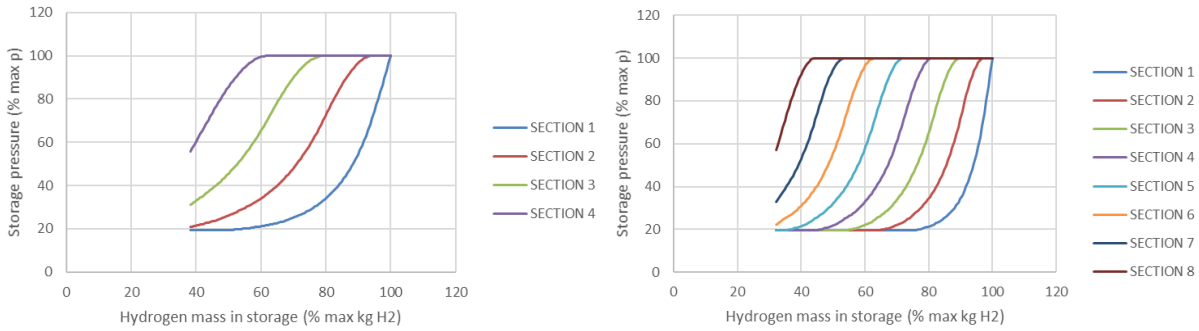

Figure 8: *Hydrogen pressure in dependence on stored mass in the storage for division into 4 sections (left) and division into 8 sections (right).*

5. CONCLUSION

A hydrogen mobile filling station is a relatively simple tool for hydrogen transport from the point of production to consumers, which can help to develop hydrogen mobility. Using a simulation tool, the preliminary design of a mobile filling station was analysed and improved. The filling rate has been optimized regarding the heating of the pressure tanks. Hydrogen supply utilization was improved by sequential filling with help of division of the storage into sections with smaller count of pressure tanks.

6. REFERENCES

[1] SAE J2600 Compressed Hydrogen Surface Vehicle Fuelling Connection Devices, (2015). https://saemobilus.sae.org/content/J2600_201510/ (accessed June 28, 2024).

[2] SAE J2799 Hydrogen Surface Vehicle to Station Communications Hardware and Software, (2019). https://saemobilus.sae.org/content/J2799_201912/ (accessed June 28, 2024).

[3] SAE J2601 Fuelling Protocols for Light Duty Gaseous Hydrogen Surface Vehicles, (2020). https://doi.org/https://doi.org/10.4271/J2601_202005 (accessed June 28, 2024).

[4] H. Chen, J. Zheng, P. Xu, L. Li, Y. Liu, H. Bie, Study on real-gas equations of high pressure hydrogen, Int J Hydrogen Energy. 35 (2010) 3100–3104. https://doi.org/10.1016/j.ijhydene.2009.08.029 (accessed June 28, 2024).

[5] Zhao L., Liu Y., Yang J., Zhao Y., Zheng J., Bie H., Liu X., Numerical simulation of temperature rise within hydrogen vehicle cylinder during refuelling, International Journal of Hydrogen Energy, 35 (2010) 8092-8100. https://doi.org/10.1016/j.ijhydene.2010.01.027 (accessed June 28, 2024).

[6] Bourgeois T., Brachmann T., Barth F., Ammouri F., Baraldi D., Melideo D., Acosta-Iborra B., Zaepffel D., Saury D., Lemonnier D., Optimization of hydrogen vehicle refuelling requirements, International Journal of Hydrogen Energy, 42 (2017) 13789-13809. https://doi.org/10.1016/j.ijhydene.2017.01.16 (accessed June 28, 2024).

[7] GT-SUITE v2024, Gamma Technologies, https://www.gtisoft.com/

[8] REFPROP tool, National Institute of Standards and Technology (NIST), U.S. Department of Commerce, https://www.nist.gov/srd/refprop (accessed June 28, 2024).

7. ACKNOWLEDGEMENT

This work has been realized using the support of Technological Agency, Czech Republic, programme National Competence Centres, project # TN02000054 Josef Bozek National Center of Competence for Surface Vehicles. This support is gratefully acknowledged.

55. mezinárodní vědecká konference zaměřená na výzkumné a výukové metody v oblasti vozidel a jejich pohonů

září 5. - 6., 2024 – Liberec, Česká republika
Technická univerzita v Liberci
Fakulta strojní, Katedra vozidel a motorů

ANALYSIS OF THE EFFECTS OF SYNTHESIS GASES ON THE PARAMETERS OF COMBUSTION ENGINE

Andrej Chríbik[1], Lukáš Luknár[2], Matúš Margetin[3], Roland Jančo[4]

Abstract
Synthesis gases produced from municipal waste or plastic waste pose a great alternative source of energy, as they are not only reducing dependency on the fossil fuels, but also diversify energy sector and reduce the amount of a landfilled waste. This is directly related to the recent initiatives and legislation that consists in the greening of transport. Our work focuses on the research of the effects of selected medium-energy synthesis gases on the internal and external parameters of a turbocharged internal combustion engine in the operation engine speed 1 500 min^{-1}.

[1] Andrej Chríbik, Faculty of mechanical engineering STU in Bratislava, Námestie slobody 17, 811 06 Bratislava 1, andrej.chríbik@stuba.sk
[2] Lukáš Luknár, Faculty of mechanical engineering STU in Bratislava, Námestie slobody 17, 811 06 Bratislava 1, lukas.luknar@stuba.sk
[3] Matúš Margetin, Faculty of mechanical engineering STU in Bratislava, Námestie slobody 17, 811 06 Bratislava 1, matus.margetin@stuba.sk
[4] Roland Jančo, Faculty of mechanical engineering STU in Bratislava, Námestie slobody 17, 811 06 Bratislava 1, roland.janco@stuba.sk

The examined synthesis gases are classified as medium-energy fuels with a lower mass heating value in the range from 9 to 18 MJ.kg^{-1}. From the point of view of the internal performance parameters, the decrease in the mean indicated pressure was from 8 % to 16 % compared to the operation on natural gas.

1. INTRODUCTION

Social development, improvement of living standards and gradual deterioration of the environment have shown that it is a necessity to deal with the issue of waste recovery. Currently, it is necessary to make the greatest possible effort to create and establish various innovative methods and techniques suitable for primary and secondary processing of municipal waste, but also waste as such. These steps are stipulated in methodological and professional manuals of individual states, but also of the European Union. In addition, wastes, their creation, and their management are also treated legislatively. Several ecological plans have been based on long-term analyses [7]. According to the norms of the European Union, states are limited, e.g. by the action plan of the European Union for circular economy. Despite all legislative interventions and despite the influence of non-governmental organizations or activists, the generated municipal waste in the countries of the European Union is yearly increasing, as shown in the graph in Figure 1, [1-5].

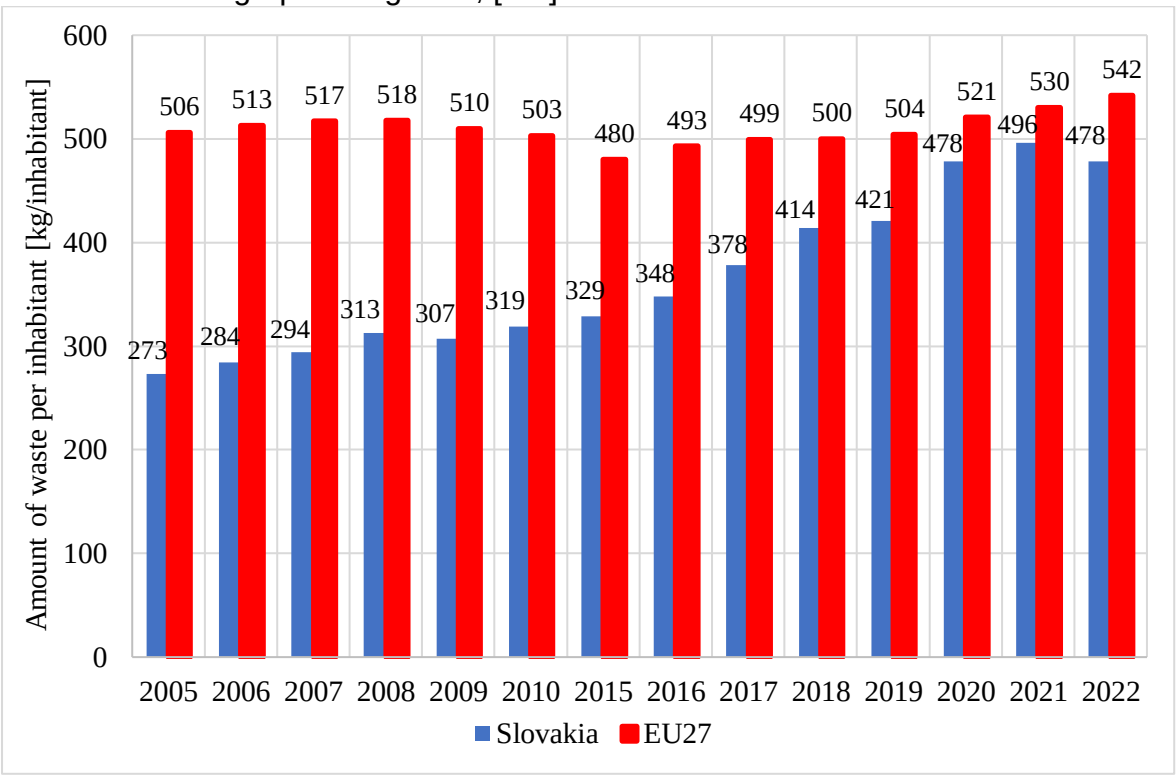

Figure 1: The amount of municipal waste produced per inhabitant per year for Slovakia and the European Union

In 2022, an average of 542 kg of municipal waste per inhabitant was produced in the EU 27 states, i.e. 12 kg of waste more than in 2021. In Slovakia, a slight decrease was recorded in this indicator, specifically by 18 kg per inhabitant. However, all these data contribute to the fact that this issue is becoming more topical [3].

One of the ways to reduce the amount of landfill waste is recycling. However, not every part of municipal waste can be recycled or its recycling is profitable. In addition to recycling, however, some other processes and technologies are used to process municipal waste, which is energetically and economically more advantageous and also globally ensures a reduction of the amount of landfilled waste, [5]. These processes can be divided into two groups: waste-to-fuel processes and waste-to-energy processes. The second mentioned are ways of burning waste that lead to production of electricity and heat. Conversely, fuel recovery methods use gasification and pyrolysis methods to chemically break down the complex organic molecules of municipal waste into simple molecules of predominantly saturated hydrocarbons and carbon oxides. The products - gases obtained in this way - are often referred to as synthesis gases. In the production process itself, the gases have to be cleaned and subsequently, they can be used for chemical production (including the production of synthetic fuels) or direct use in cogeneration units, [6-9].

This paper investigates the effect of different gaseous fuels on the operation of a partially turbocharged (compression ratio 1.25) Lombardini LGW 702 reciprocating internal combustion engine with an electrically driven AISIN AMR 300 compressor. The fuels were chosen to mimic synthesis gases obtained from municipal waste and plastic gasification so that they could help in setting the correct boundary conditions for the optimal synthesis gas composition. The properties of the selected synthetic gases are listed in the following table (Table 1), where the properties of the reference fluid, which was natural gas, are also listed. Natural gas had the following composition: methane 93.7% vol., ethane 3.7% vol., higher hydrocarbons 1.3% vol., inert gases 1.3% vol..

Parameter	Unit	Natural Gas	SG1	SG2	SG3	SG4	SG5
CH_4	[% vol.]	93.7	15	40	20	15	5
H_2	[% vol.]	0.0	20	20	25	20	35
CO	[% vol.]	0.0	30	10	20	25	35
CO_2	[% vol.]	0.6	35	25	35	35	20
N_2	[% vol.]	0.7	0	5	0	5	5
LHV	[MJ.kg^{-1}]	48.370	9.522	18.054	11.228	8.991	10.404
LHV	[MJ.m^{-3}]	34.657	10.536	16.530	11.538	9.948	9.306
A/F ratio	[kg.kg^{-1}]	16.77	2.84	5.93	3.47	2.71	2.87
Fuel in Air	[% vol.]	9.1	27.6	18.1	25.2	28.6	31.9
M	[g.mol^{-1}]	17.2	26.6	22.0	24.7	26.6	21.5
$\rho_{NTP\ fuel}$	[kg.m^{-3}]	0.716	1.107	0.916	1.028	1.107	0.984
$\rho_{NTP\ mixture}$	[kg.m^{-3}]		1.177	1.152	1.160	1.176	1.105
$LHV_{mixture}$	[MJ.m^{-3}]	3.147	2.911	2.992	2.905	2.843	2.965

Table 1: *Physical and chemical properties of natural gas and synthesis gas (LHV – lower heating value of fuel, A/F – air to fuel ratio, M – molar mass, $\rho_{NTP\ fuel}$ – density of fuel at NTP, $LHV_{mixture}$ - volumetric heating value of stoichiometric mixture, NTP = 20 °C, 101 325 Pa)*

From a basic comparison of the volumetric heating value of the mixture, which has the largest share of performance parameters and is also a determining parameter for preliminary estimation of performance parameters, it follows that the highest performance parameters can be expected for SG2 gas (2,992 kJ.m^{-3}).

On the contrary, the worst parameters are expected for the gas with the designation SG4, which has the lowest heating value of the stoichiometric mixture (2,843 kJ.m^{-3}). The synthesis gas SG5 has the largest proportion of hydrogen in the mixture which situation can lead to a reduced pre-ignition angle compared to operation on natural gas due to faster fuel burnout and also increased fuel consumption due to a higher proportion of fuel (31.9% vol.) in the stoichiometric mixture. Hydrogen also has harms the stability of combustion (occurrence of abnormal phenomena - detonation combustion, ignition of the mixture in the intake pipes).

2. EXPERIMENTAL PART

The experimental measurements were carried out on the supercharged spark-ignition combustion engine LGW 702 from the Lombardini Company, which in its modified version has been used for many years as an experimental engine for the application of alternative gaseous fuels at the Institute of Automotive Engineering and Design. The supercharging of the internal combustion engine was carried out using a mechanically driven compressor AISIN AMR 300, which was driven utilizing a controllable asynchronous motor. The internal combustion engine is part of the micro-cogeneration unit, the parameters of which are described in more detail, e.g. in [10, 11].

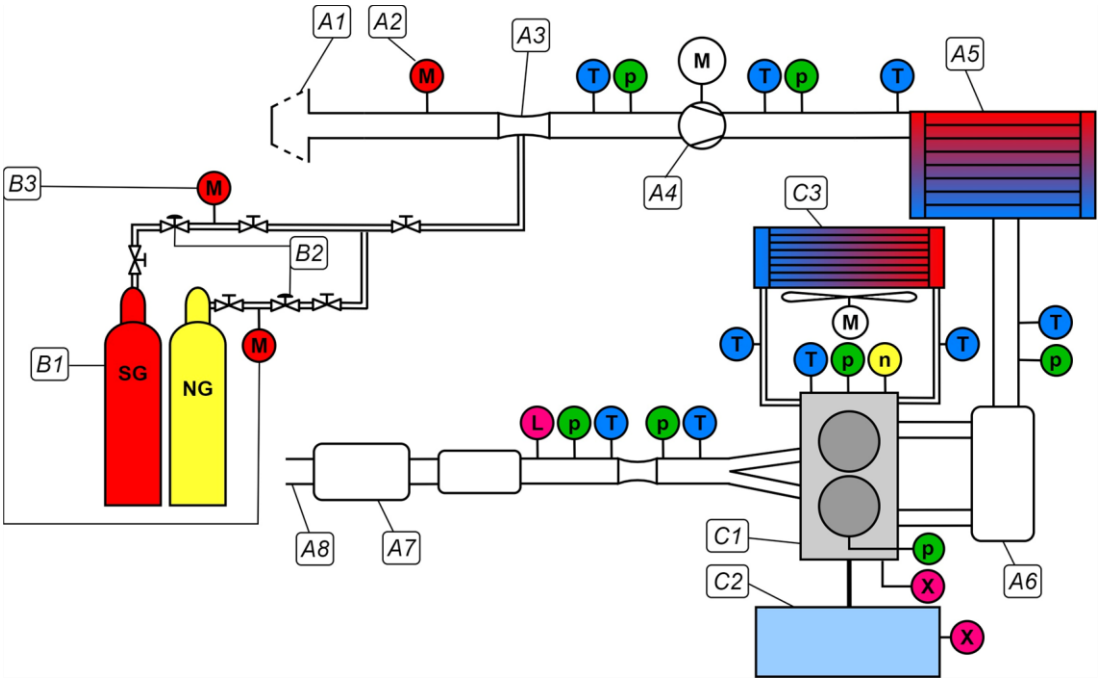

Figure 1: *The basic scheme of the supercharged internal combustion engine Lombardini LGW 702K (A1 –* air filter*, A2 – mass air flow sensor (MAF), A3 - mixer with diffuser, A4 – mechanical compressor AISIN AMR 300, A5 – water intercooler of the compressed mixture, A6 – collection container, A7 – silencer, A8 – exhaust tip for discharging exhaust gases, B1 - pressure bottle with syngas or natural gas, B2 – pressure regulators, B3 – fuel mass flow and volumetric fuel consumption sensors, C1 – internal combustion engine Lombardini LGW 702K, C2 – dynamometer AVL P80, C3 – engine cooler, T – temperature sensor, p – pressure sensor, M – electric motor, n – engine speed, L – broadband lambda probe).*

The diagram of the combustion engine together with the AVL dynamometer is shown in the figure below (Figure 2). The internal combustion engine was equipped with pressure sensors from Kistler. A piezoelectric pressure sensor was integrated in the pressure spark plugs (6118CC-4CQ02-4-1), which sensed the dynamic course of pressure in the cylinder. To reduce this pressure to absolute values, a pressure correction method was used based on sensing the absolute pressure in the intake manifold using a 4075A10 piezo-resistive sensor. The current position of the crankshaft was sensed using the 2613B1 encoder. The start of ignition angle was varied using the IMF Soft programmable control unit and was recorded on the data bus using an opto-coupler connected in parallel with the Bosch P65-T combined ignition coil.

All measured data were post-processed using a program created in the Matlab environment. From the measured pressure curves in the cylinder, the course of fuel combustion in the combustion chamber is evaluated using a single-zone-zero-dimensional thermodynamic model. This model, based on the use of the law of conservation of energy, will be used for combustion analysis only when the system is closed (i.e. both the intake and exhaust valves are closed). The course of the gradual release of heat from the fuel was determined based on the Rassweiler-Withrow method. The required start and end of combustion angle for combustion analysis are determined from the entropy change during the supply and realise of heat [12].

In addition to the above-mentioned analysis, an evaluation of the mean indicated pressure and a statistical analysis of the parameters for the evaluation of the uniformity of the engine operation, which are represented by the so-called coefficient of variation (COV). The coefficient of variation is calculated as the ratio of the standard deviation to the arithmetic mean of the investigated parameter:

$$COV = \frac{\sqrt{\frac{1}{n-1}\sum_{i=1}^{n} x_i - \bar{x}}}{\bar{x}}.100 \qquad [\%] \quad (1)$$

where n is the total number of consecutive cycles, xi is the *i*-th value of the investigated parameter in the given cycle and $\bar{x}$ is the average value of the investigated parameter from the given number of cycles. Cycle variability has a significant impact on the overall life of the combustion engine as well as on its performance parameters. During one working mode of the engine, approximately 195 consecutive cycles were recorded at an operating speed of 1500 min^{-1}.

2.1 Analysis of the course of pressure in the combustion chamber

From the analysis of the performance parameters it follows that among the synthesis gases, the highest torque (54.1 N.m) is at the operating speed of 1,500 min^{-1} and a filling of 1.25 when burning synthesis gas SG2. Conversely, the lowest torque (50.1 N.m) is when operating on SG1 and SG3. The highest volumetric fuel consumption (161 $l.min^{-1}$) is when operating on SG5 synthesis gas, and on the contrary, the lowest (91 $l.min^{-1}$) is when operating on SG2 gas, which is fully in line with the expected results based on the analysis of volume percentage of the fuel in the stoichiometric mixture.

The following figure (Figure 3) shows the IMEP values depending on the angle at which 50% of the fuel weight is burned. The graph was created from a gradual change in the start of ignition angle from 36°CA BTDC to approximately 10°CA BTDC, depending on the gas composition when there is still the possibility of regular engine operation without misfiring. The highest average values of IMEP (1.245 MPa) are achieved when burning the reference fuel, which is natural gas. This value corresponds to the angle α_{50MFB} 6.4° CA ATDC.

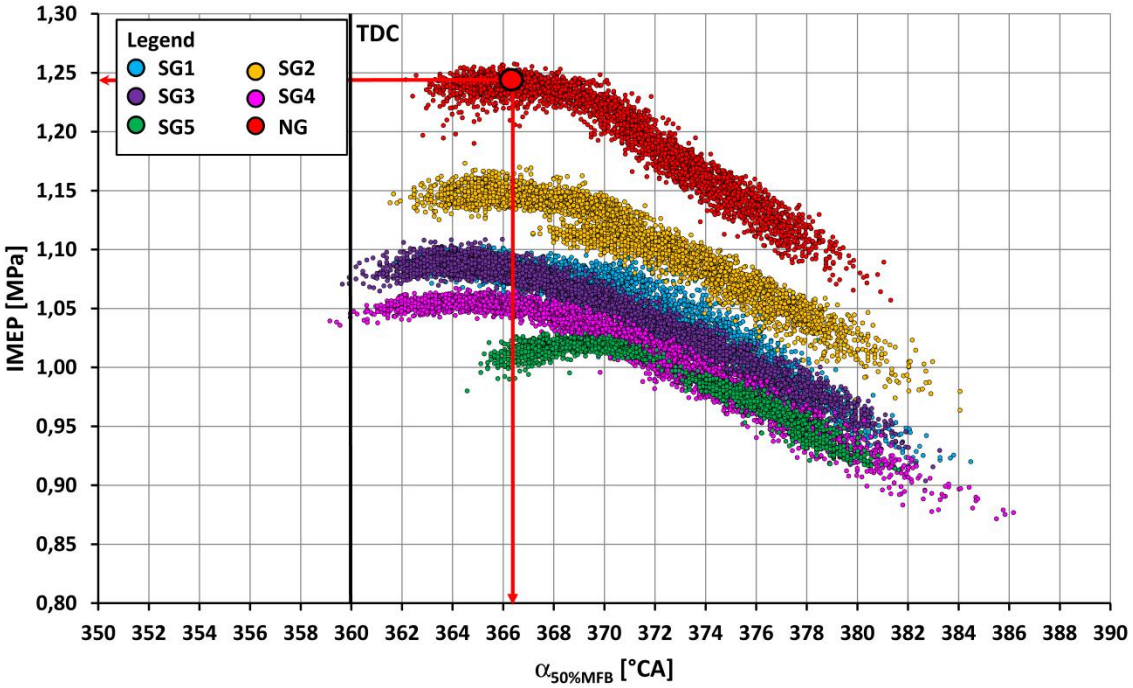

Figure 2: *Course of the mean indicated pressure (IMEP) depending on the angle when 50% of the fuel mass is burned for natural gas and synthesis gases, with a marking of max. IMEP values for natural gas (optimal start of ignition (SOI) angle 26°CA BTDC). Conditions: speed 1500 min^{-1}, full load, the stoichiometric ratio of the mixture, the proportional compression on the compressor 1.25*

When burning synthesis gas SG2, the largest value of IMEP (1.149 MPa) is reached at approximately 6.1 °CA ATDC, when 50% of the fuel is burned. The volumetric heating value of the stoichiometric gas mixture SG2 (2,992 MJ.m^{-3}) is also the highest among the investigated gases. On the contrary, the lowest value of IMEP (1.042 MPa) has the synthesis gas SG5, which also has the largest angle (8.7 °CA ATDC), when 50% of the fuel has been burned. This gas also contains the largest proportion of hydrogen (35% by volume). The coefficient of variation (COV) of the IMEP for natural gas was 0.65% at the optimal starting pre-ignition angle. The highest value among synthesis gases (even at the optimal start of the ignition angle) was when burning synthesis gas SG1 (0.70%), which can also be seen in the dispersion of values in the previous graph. Conversely, SG5 gas has the lowest value (0.46%).

The following developed p – α diagram shows the course of the average pressure curve (created from 195 consecutive cycles) in the combustion chamber of the engine in the region of the top dead centre at the time of combustion. Pressure curves for selected synthesis gases and methane are shown, always for the optimal start of ignition angle, which is different depending on the fuel composition.

The highest maximum pressure (5. 75 MPa) is reached when natural gas is burned. The lowest value of the maximum pressure (4.52 MPa) is achieved when burning SG1 gas. The position of the maximum pressure had a narrow interval for all gases (from 6.6 to 9.9 °CA ATDC). The coefficient of variation of the maximum pressure was 6.9% for natural gas. Among the synthesis gases, SG3 gas had the lowest value (5.0%) and SG5 gas had the highest value (5.3%).

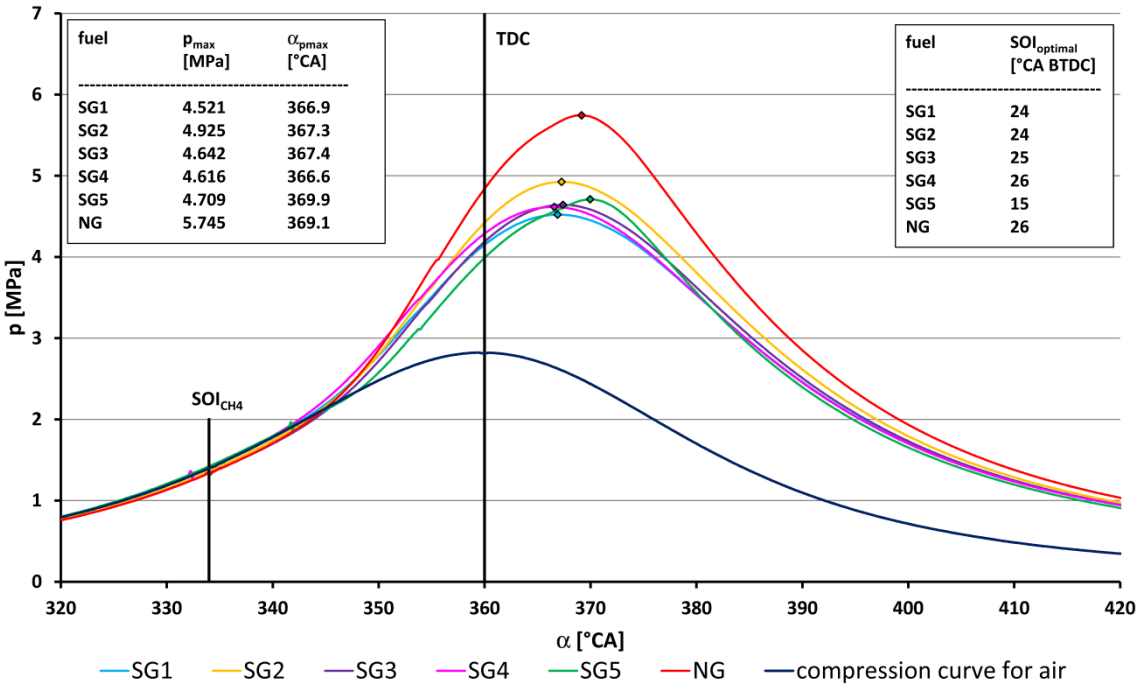

Figure 3: *Course of pressure in the cylinder of the internal combustion engine when operating on natural gas and synthesis gases, Conditions: speed 1500 min^{-1}, full load, the stoichiometric ratio of mixture, the optimal start of ignition angle for each fuel, the proportional compression on the compressor 1.25*

Another parameter affecting the life and operation of the engine is the parameter of the maximum pressure rise rate per degree of rotation of the crankshaft. This value when burning natural gas is 0.238 MPa/1°CA. The highest value (0.239 MPa/1°CA) was recorded for gas labelled SG5, which is again related to the relatively highest proportion of hydrogen (35% vol.). On the contrary, the lowest value (approx. 0.199 MPa/1°CA) was when burning gas marked as SG1 and SG2.

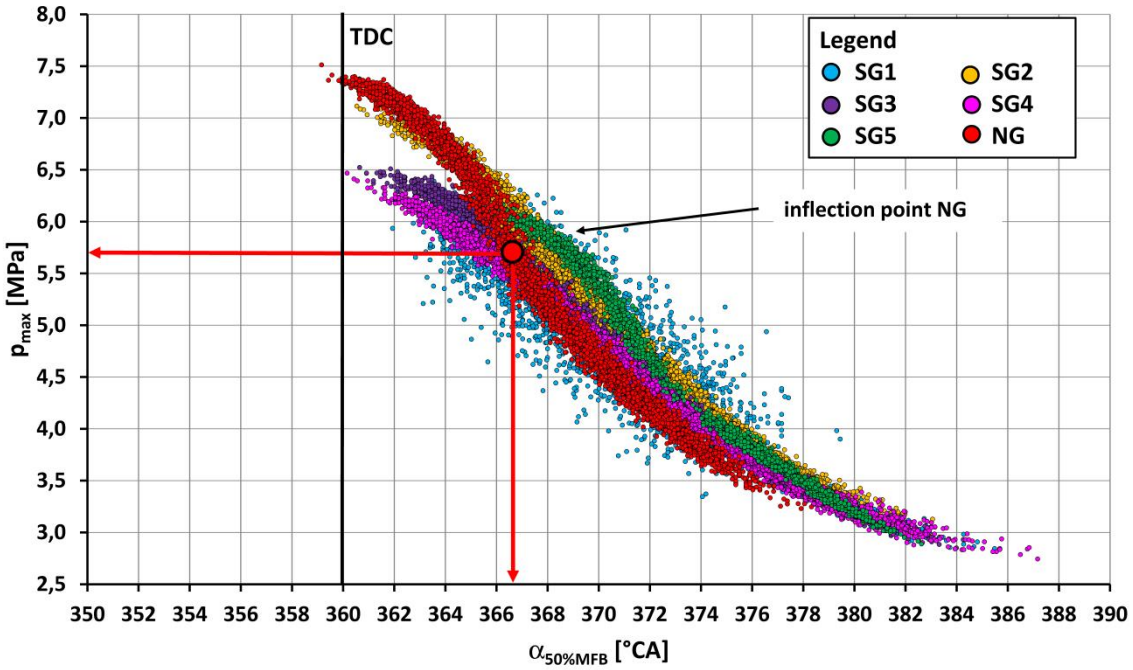

Figure 4: *Course of the maximum pressure depending on the angle when 50% of the fuel for natural gas and synthesis gases is burned. Conditions: speed 1500 min^{-1}, full load, the stoichiometric ratio of the mixture, the proportional compression on the compressor 1.25*

The prevising figure (Figure 5) shows the course of the maximum pressure for each cycle depending on the angle at which 50% of the mass of the fuel is burned. The graph was created similarly to the IMEP graph as a set of data (195 cycles for each operating point – start of ignition) with the start of ignitions from approx. 10°CA BTDC to 36°CA BTDC with 1°CA step. As can be seen from the course, by increasing the start of ignition value, the value of the maximum pressure for natural gas stabilizes at the level of 7.4 MPa, and approximately at the place (angle α_{50MFB}) of the maximum mean indicated pressure is also the place of the inflection point in the course of the maximum pressure, which can also be seen in Figure 5. The position of the inflection point corresponds to a pressure value of 5.7 MPa and an angle of α_{50MFB} 6.2 °CA ATDC. The lowest value of maximum pressure (5.9 MPa) is when burning SG1 gas. All synthesis gases had approximate inflection points at the α_{50MFB} angle when the highest performance parameters (max. IMEP) are also achieved at this angle, and thus the optimal value of the start of ignition angle also corresponds to this condition.

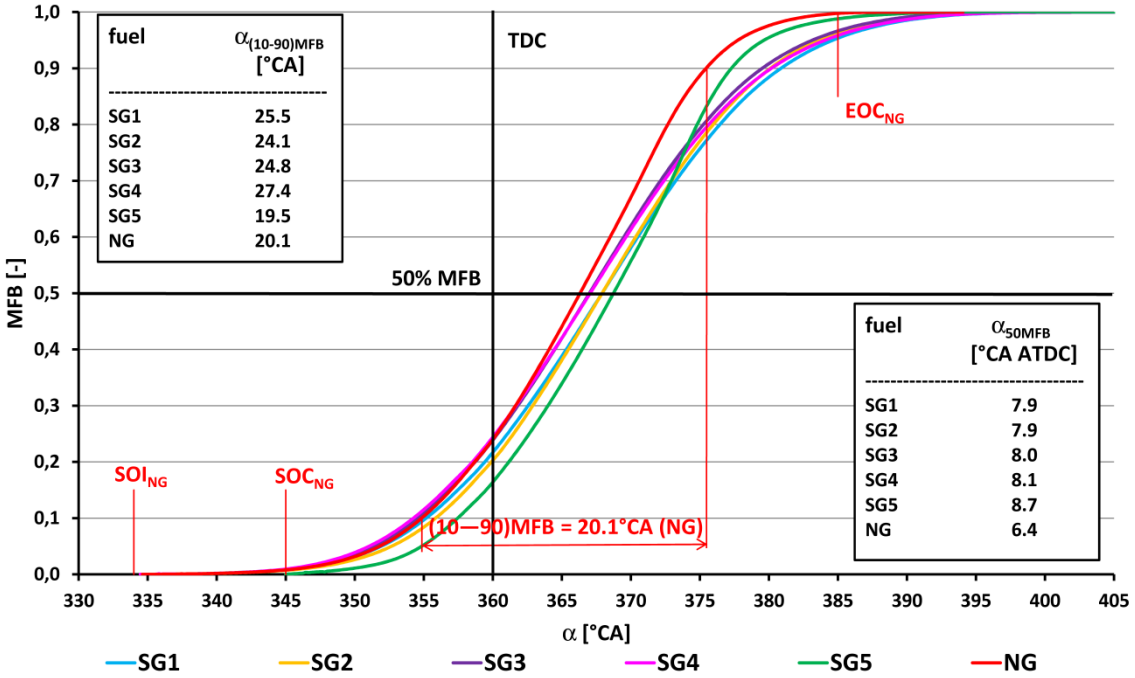

Figure 5: *Course of burning out of fuel as dependent on the crankshaft angle for natural gas and synthesis gases (SOI – Start of Ignition, SOC – Start of Combustion, EOC – End of Combustion) Conditions: speed 1500 min^{-1}, full load, the stoichiometric ratio of the mixture, the proportional compression on the compressor 1.25*

The prevising figure (Figure 6) shows the mass fraction of burned fuel depending on the angle of rotation of the crankshaft for selected compositions of the synthesis gas mixture compared to natural gas.

From the analysis of the course of fuel burning, it follows that the time between the start of the ignition (SOI) and the moment of the start of visible combustion (SOC) is approximately 11.1 °CA. The time between SOI and 5 wt. % natural gas burning is approximately 15.9 °CA. The main combustion time of (10-90) %MFB for natural gas lasts 20.1 °CA. The total burning time (from SOC to EOC) for methane has a value of approx. 40 °CA. Synthesis gases have different main combustion times, mainly depending on the presence of hydrogen in the mixture. The higher the proportion of hydrogen in the mixture, the shorter the combustion time and the ignition delay. For this reason, synthesis gas SG5 also has the shortest combustion time (19.5 °CA). On the contrary, the longest main combustion time (27.4 °CA) is given to gas marked SG4. The time between the SOI and the moment when 5% of the fuel is burned is again the shortest (9.8 °CA) when burning synthesis gas SG5 and, conversely, the longest (17.0 °CA) when burning SG4 gas. By increasing the amount of burned fuel, the differences in the individual phases between the fuels also increase. The coefficient of variation of position (COV) generally increases with the increasing proportion of fuel burned. For natural gas, these values are as follows: $COV_{\alpha 10\%MFB}$ = 0.19%, $COV_{\alpha 50\%MFB}$ = 0.36%, $COV_{\alpha 90\%MFB}$ = 0.57%. When burning syngas, the highest values in the entire range are for syngas labelled SG4 ($COV_{\alpha 10\%MFB}$ = 0.20%, $COV_{\alpha 50\%MFB}$ = 0.34%, $COV_{\alpha 90\%MFB}$ = 0.69%). Synthesis gas labelled SG5 has the lowest values ($COV_{\alpha 10\%MFB}$ = 0.12%, $COV_{\alpha 50\%MFB}$ = 0.21%, $COV_{\alpha 90\%MFB}$ = 0.41%).

3. CONCLUSION

The transformation of municipal waste into synthesis fuel using gasification is of irreplaceable importance both in reducing the production of carbon dioxide released into the atmosphere and also in partially saving classic resources and replacing them with renewable ones, since in the current situation there may be a problem with a lack of resources. The above-mentioned synthesis gases can be with advantage effectively used in stationary cogeneration units because of their low heating value and also high hourly consumption. The influence of fuel composition on the internal parameters of the supercharged combustion engine (proportional compression of the mixture 1.25) at the operating speed of the cogeneration unit of 1,500 min^{-1} is summarized in the following points:

- the optimal start of ignition angle had to be changed from the value of 15°CA BTDC for synthesis gas SG5 (limit of stable ICE operation) to the value of 26°CA BTDC for synthesis gas SG4;
- the mean indicated pressure of the combustion engine cycle is reduced at least (by 8%) for the SG2 synthesis gas (1.149 MPa) compared to natural gas (1.245 MPa). The greatest drop in performance parameters (by 16%) compared to natural gas is for the synthesis gas marked SG5, which also has the lowest volume heating value (9.306 $MJ.m^{-3}$) out of the studied synthesis gases;
- from among synthesis gases, the maximum pressure value was at its highest (4.93 MPa) when SG2 gas was burned. SG1 gas had the lowest value (4.52 MPa). Variations of maximum pressure were the highest (5.3%) when operating on SG5 synthesis gas, and on the contrary, the lowest value was recorded when operating on SG3 gas (5.0%);
- the highest pressure rise rate (0.239 MPa/1°CA) was measured when operating on synthesis gas SG5, which had the highest proportion of hydrogen (35% vol.). The lowest pressure rise rate value (0.199 MPa/1°CA) was measured when operating on synthesis gases SG1 and SG2;
- from the analysis of the course of fuel combustion, it follows that the longest main combustion time (i.e. 10-90MFB) characterizes the synthesis gas SG4 and has the value of 27.4 °CA. On the contrary, SG5 gas (19.5 °CA) has the shortest burning period. The combustion start time (SOI-5%MFB) was the shortest (9.8 °CA) for the operating synthesis gas SG5 and, conversely, it was the longest (17.0 °CA) for the synthesis gas SG14. The coefficients of variation of the course of fuel burning out were average, the lowest was for the synthesis gas SG5 and the highest for the synthesis gas SG4.

The results give some ideas on how to set up waste gasification technologies to gain the optimum power and the best economic output from cogeneration units.

REFERENCES

[1] Slovensko [online]. [cit. 2024-01-11]. From https://www.slovensko.sk/sk/agendy/agenda/_komunalny-odpad

[2] Odpady – portál [online]. [cit. 2024-01-11]. From https://www.odpady-portal.sk/Dokument/102076/co-su-to-vlastne-komunalne-odpady.aspx

[3] Televízia TA3 [online]. [cit. 2024-01-11]. From https://www.ta3.com/clanok/251625/produkcia-odpadu-rastie-slovak-vyhodil-minuly-rok-v-priemere-497-kilogramov-smeti

[4] Európsky parlament [online]. [cit. 2024-01-11]. From https://www.europarl.europa.eu/news/sk/headlines/society/20210128STO96607/ako-chce-eu-do-roku-2050-dosiahnut-obehove-hospodarstvo

[5] Finreport [online]. [cit. 2024-01-11]. From https://www.finreport.sk/ekonomika/denne-vytvorime-1-3-kilogramu-odpadu-na-osobu-sme-skladkova-velmoc/

[6] Sensoneo [online]. [cit. 2024-01-11]. From https://sensoneo.com/global-waste-index/

[7] Ministerstvo životného prostredia [online]. [cit. 2024-01-11]. From https://www.minzp.sk/files/sekcia-enviromentalneho-hodnotenia-riadenia/odpady-a-obaly/registre-a-zoznamy/ppvo-sr-19-25.pdf

[8] Ministerstvo životného prostredia [online]. [cit. 2024-01-11]. From https://www.minzp.sk/files/iep/publikacia_zelensie-slovensko-sj_web.pdf

[9] Štatistický úrad Slovenskej republiky [online]. [cit. 2024-01-11]. From https://datacube.statistics.sk/#!/view/sk/VBD_SK_WIN/zp1005rs/v_zp1005rs_00_00_00_sk

[10] CHRÍBIK A., POLÓNI M., LACH J., and RAGAN B.: Utilization of Synthesis gases in the combustion engine, KOKA2015, 2015, pp. 229-238. ISBN 978-80-227-4429-9

[11] CHRÍBIK A., POLÓNI M., LACH J., RAGAN B.: The effect of adding hydrogen on the performance and the cyclic variability of a spark ignition engine powered by natural gas. In Acta Polytechnica. Vol. 54, No. 1 (2014), s. 10-14. ISSN 1210-2709

[12] CHRÍBIK, Andrej - POLÓNI, Marián - MAGDOLEN, Ľuboš - MINÁRIK, Matej. Medium-energy synthesis gases from waste as an energy source for an internal combustion engine. In Applied Sciences. Vol. 12, issued 1 (2022), s. 1 - 22, art. no. 98. ISSN 2076-3417

ACKNOWLEDGMENT

This work was supported by the Slovak Research and Development Agency under Contract No. APVV-20-0046, APVV-20-0428, and was also supported by the Scientific Grant Agency under Contract No. VEGA 1/0666/24.

55. mezinárodní vědecká konference zaměřená na výzkumné a výukové metody v oblasti vozidel a jejich pohonů

září 5. - 6., 2024 – Liberec, Česká republika
Technická univerzita v Liberci
Fakulta strojní, Katedra vozidel a motorů

MULTI-MODE DEDICATED HYBRID TRANSMISSION APPLICATION FOR HEAVY-DUTY TRUCK

Rastislav Toman[1], Mikuláš Adámek[2]

Abstract
Dedicated Hybrid Transmissions (DHT) represent a "HEV-tailored" approach to a more common powertrain hybridization option of using parallel hybrid electric vehicle (HEV) topologies. However, within the heavy-duty trucks, the powertrain electrification progresses more slowly in general. Some DHTs are used in passenger vehicles with the objective of reducing the overall fleet CO_2 emissions, but not to the same extent in heavy-duty trucks. The objective of this paper is to evaluate a multi-mode HEV with a DHT and two electric machines with optional series or parallel operation, combined with a 5.9-litre six-cylinder diesel internal combustion engine. All of this is done in eight vehicle driving cycles that replicate different use cases for such vehicles. The energy management control strategy is optimal in nature, and it determines the power split in various modes of operation. It is based on Pontryagin's Minimum Principle and programmed in-house using Python 3.9.0.

[1] Rastislav Toman, Faculty of Mechanical Engineering, Czech Technical University in Prague, Technická 4, Prague 6, Rastislav.Toman@cvut.cz
[2] Mikuláš Adámek, Faculty of Mechanical Engineering, Czech Technical University in Prague, Technická 4, Prague 6, Mikulas.Adamek@cvut.cz

1. INTRODUCTION

The hybridization end electrification of vehicle fleets is moving rather slowly in heavy-duty applications. In our past studies [1, 2] we have evaluated different options for 7.5-tonne truck, ranging from cheap hybrid electric vehicle (HEV) parallel topology to plug-in HEV variants, and finally to battery electric vehicle (BEV) variants. All of these were combined with classical shifting transmission: 6-speed for HEV and PHEV, 2-speed for BEV.

Here, we want to follow-up loosely on these studies, combining the truck with multi-mode dedicated hybrid transmission (DHT), which we have also studied and optimized in [3] for passenger vehicles.

DHT powertrains aim to improve on mechanical efficiencies and lower the overall powertrain complexity compared to “classical” HEV options with shifting transmissions and parallel topologies. This is possible, because the DHT solutions are not designed as some “ad-on” to the ICEV powertrain, but as a “HEV-tailored” solution. Generally, DHTs operate the ICE only in best efficiency regions, in combination with high braking energy recuperation capabilities, and E-Mode in low vehicle speeds.

We use the Pontryagin’s minimisation strategy (PMP) as an energy management strategy, as we have done also in the abovementioned studies [1, 2, 3]. Our PMP implementation forms a part of broader in-house simulation, optimization, and benchmarking environment, based on Python 3.9.0.

1.1 Goals of the paper

The goals of our paper are following:

- First, to present two different multi-mode DHT options for the heavy-duty truck applications.
- Second, to study the charge-sustaining operation (CS) fuel consumption in different vehicle driving cycles.
- Finally, to evaluate the sensitivities of DHT powertrains on vehicle load mass, and selected energy management strategy parameter.

2. MULTI-MODE DHT

The studied multi-mode DHT solution is originally from Schaeffler and was first presented in 2019 [4]. This DHT (Figure 1) uses two electric motors: generator EM1, and traction motor EM2; together with an ICE, C0 friction clutch, and fixed gear ratios. Gear 1 is internal, to match the different speed ranges of the ICE and EM1 (and EM2); and gears 2 and 3 set the EM2 RPM range to maximum design vehicle speed.

This DHT layout allows for three base operation modes (Table 1):

- E-Mode with EM2 providing the only traction power necessary for the vehicle, either in motor or generator mode (there is a possibility of additional E-Boost using EM1).
- P-Mode, when ICE and EM2 provide the traction power, with the possibility of ICE load-point-shifting (LPS).

- S-Mode, when EM2 provides the traction power, and ICE charges the battery through EM1.

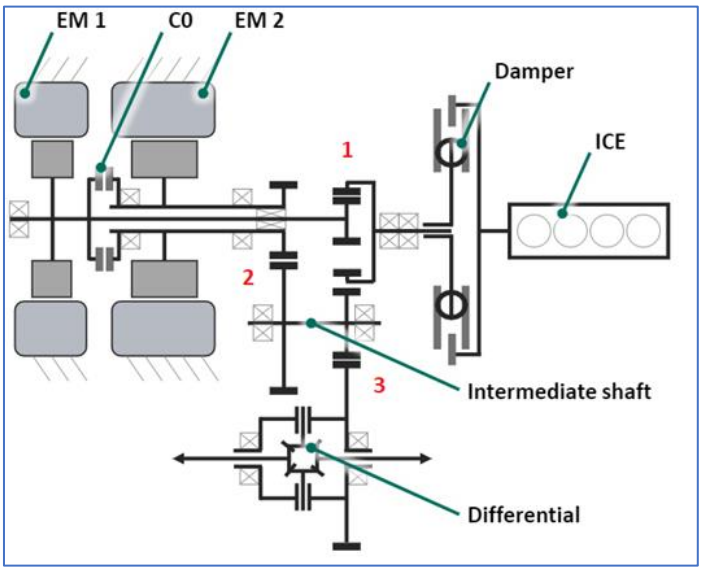

Figure 1: DHT layout

Vehicle always starts at either E-Mode or S-Mode, depending on the battery SOC; P-Mode is available only from certain vehicle speed, depending on gear ratios. Generally, ICE in P-Mode operates as in 4^{th}-5^{th} gear with conventional transmission.

Exact gear ratios for the DHT versions used in this study will be introduced in the following chapter.

	C0	ICE	EM1	EM2
E-Mode	Open	Off	Off	Mot/Gen
P-Mode	Closed	Mot	Off	Mot/Gen
S-Mode	Open	Mot	Gen	Mot/Gen

Table 1: *DHT operation modes*

3. VEHICLE DATA AND PARAMETERS

We have prepared two different DHT versions, that use the same ICE and high voltage battery, but different generator (EM1) and traction motor (EM2). Differences in EMs require also different gear ratios for these two DHT versions.

	DHT-V1	DHT-V2
Vehicle frontal area [m^2]	6.1	
Drag coefficient [-]	0.6	
Tire rolling resistance factor [-]	0.015	
Dynamic tire rolling radius [m]	0.4	
Vehicle mass (no load) [kg]	3594	3600

Table 2: *Main vehicle parameters*

Main vehicle parameters (summed-up in Table 2) are from IVECO EuroCargo 7.5-ton variant. Base vehicle mass is 3500 kg; here, to get the vehicle masses for our DHT versions, we add masses of EM1, EM2, HV-Battery, and DHT; and subtract the base transmission's mass (ZF 6AS1000). A small difference in mass between DHT versions is a result of different EM masses.

Both DHT variants are combined with 5.9 L inline 6-cylinder turbocharged diesel ICE (5.9 L TDI).

High voltage battery system is based on Samsung SDI lithium-ion prismatic cells with nominal voltage of 3.7 V and capacity of 37 Ah. These cells are configured into 104s1p system (104 cells in series), giving us total voltage of around 400 V, and energy capacity of 15.6 kWh (at 90 % SOC).

Electric motors for *DHT-V1* are production motors GKN AF-130 (EM1), and GKN AF-230 (EM2). For *DHT-V2* we used high-speed EM from Bosch as EM1 and scaled the GKN AF-230 to 13000 RPM and 420 kW (EM2). Peak parameters of the ICE and all motors are in Table 3 (peak EM efficiencies include power electronics).

	Torque [Nm]	Power [kW]	Speed [RPM]	BSFC [g/kWh]	Efficiency [%]
5.9 L TDI	869	181	2250	206.7	-
DHT-V1 EM1	335	130	8000	-	92.9
DHT-V1 EM2	670	260	8000	-	92.9
DHT-V2 EM1	200	140	15500	-	93.5
DHT-V2 EM2	670	420	13000	-	92.9

Table 3: *ICE and EMs' parameters*

EMs for *DHT-V1* were chosen to give us "cheap" version of the multi-mode transmissions, since both are in production for long time. On the other side, the EMs for *DHT-V2* both represent high-speed traction machines and would cost more.

	DHT-V1	DHT-V2
i_1 [-]	0.280	0.180
i_2 [-]	2.930	3.930
i_3 [-]	3.830	4.450
$i_{ICE-tot}$ [-]	3.142	3.148
i_{EM-tot} [-]	11.222	17.489

Table 4: *DHT gear ratios*

Table 4 contains the gear ratios for *DHT-V1* and *DHT-V2*, both prepared with a goal of achieving vehicle top speed of around 120 km/h (similar to ICEV variant). Both variants lead to a minimum ICE operating speed around 40 km/h.

Higher maximum speed of EMs for *DHT-V2* allows for higher i_2 and i_3 gear ratios, and give higher maximum traction forces in E-Mode (Figure 2) – however, to match the ICE speed with vehicle speed, the i_1 must be lower compared to *DHT-V1*.

In an extreme case, when a truck with *DHT-V1* would need higher traction force, the *DHT-V1* powertrain could use the additional E-Boost.

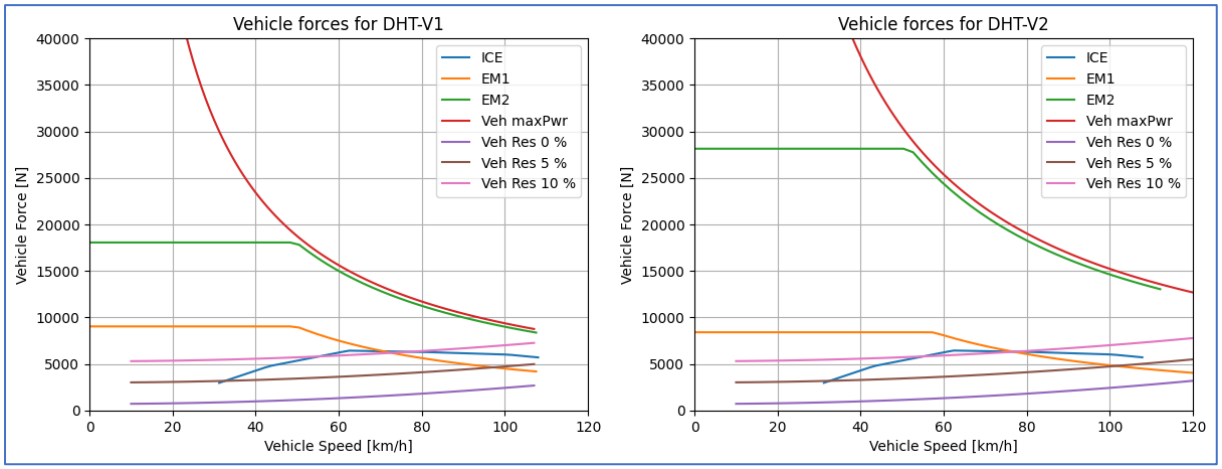

Figure 2: Vehicle forces diagrams

Figure 3 (EM1 characteristics are recalculated to ICE characteristic) then shows the combined characteristics of ICE and EM1, together with S-Mode operation line of best combined charge efficiency.

Peak combined efficiencies of both DHT versions in S-Mode are similar. The one for *DHT-V1* achieves slightly broader range of high values, but the one for *DHT-V2* achieves higher peak value.

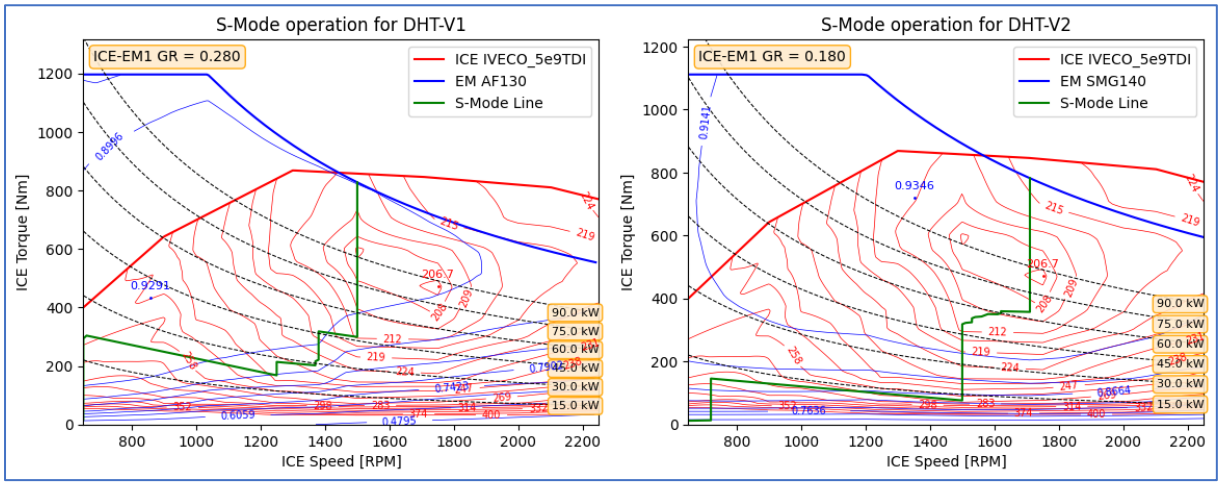

Figure 3: S-Mode operation

4. VEHICLE DRIVING CYCLES

Simulation sensitivities were carried out using eight vehicle driving cycles, all suitable for medium duty to heavy-duty vehicles.

Table 5 shows the main parameters of these eight vehicle driving cycles, Figure 7 in the Annex then shows the speed profiles.

The low-speed vehicle driving cycles *VehC1* and *VehC5*, should highlight the DHT powertrains' strengths, and high-speed cycles *VehC3* and *VehC9* their weaknesses.

Vehicle Driving Cycle	Time		Distance	Vehicle Speed	
	Total	Idle		Max.	Avg.
	[s]	[s]	[km]	[km/h]	[km/h]
VehC1	1740	442	10.87	58.26	30.14
VehC3	3604	970	41.92	95.43	57.27
VehC4	1877	361	17.77	91.25	42.17
VehC5	598	227	1.90	44.58	18.35
VehC6	3853	702	32.92	99.30	37.60
VehC7	1700	397	10.75	70.49	29.68
VehC8	1372	262	11.99	91.25	38.85
VehC9	765	6	16.51	96.40	78.19

Table 5: *Vehicle driving cycles' parameters*

4. SIMULATION MODEL

Our simulation model combines a quasi-static approach with the already mentioned PMP energy management strategy. Both were presented in more detail in [3].

ICE and EM are modelled using steady-state maps (efficiency maps for EM, and BSFC map for ICE), that are dependent on rotational speed and torque demand. HV-battery quantities are calculated with an equivalent battery model with SOC and operation mode (charge and discharge) dependent internal resistance maps, and open circuit voltage maps.

PMP optimal energy management strategy determines the optimal power-split between ICE and EM2 in P-Mode, together with optimal charging strategy if S-Mode is necessary. The switch from E-Mode or S-Mode to P-Mode is determined by EV_{Lim} parameter, that must be higher than the abovementioned minimum ICE operating speed, which is around 40 km/h for our DHT variants. In the main study EV_{Lim} value is then 45 km/h.

Equation (1) shows the Hamiltonian formulation with two control variables PDL_{ICE} (ICE pedal position in P-Mode) and Pwr_{EM1} (charge power requirement in S-Mode), equivalence factor p and battery SOC ξ.

$$\begin{aligned} H(\xi(t), PDL_{ICE}(t), Pwr_{EM1}(t), p, t) \\ = \dot{m}_{ff}(PDL_{ICE}(t), Pwr_{EM1}(t), t) \\ + p\left[\dot{\xi}(\xi(t), PDL_{ICE}(t), Pwr_{EM1}(t), t)\right] \end{aligned} \quad \textbf{(1)}$$

5. SIMULATION RESULTS

Simulation results are divided into three parts:

- Main comparisons of DHT variants with *PHEV-15* and *ICEV* results from [2] as a baseline.
- Vehicle load sensitivity, comparing base load of 1100 kg and 2300 kg load results.
- Energy management strategy settings sensitivity, comparing EV_{Lim} value of 45 km/h strategy, with S-Mode only strategy (EV_{Lim} value of 120 km/h).

For each setting of vehicle driving cycle, DHT version, vehicle load, and EV_{Lim} parameter, we have optimised the value of equivalence factor p from equation (1) to achieve the same SOC at the start and end of the vehicle driving cycle (CS mode).

Base vehicle mass of *PHEV-15* variant is 3730 kg, and of *ICEV* 3500 kg.

5.1 Main comparisons

Figure 4 shows the results for the main comparison, using vehicle load of 1100 kg. Generally, both DHT versions achieve very similar results in CS mode compared to *PHEV-15* variant with 6-speed transmission.

These results show, that DHTs perform better especially in low-speed vehicle driving cycles *VehC1* and *VehC5*, as expected. However, also in medium and high-speed vehicle driving cycles is the performance very good.

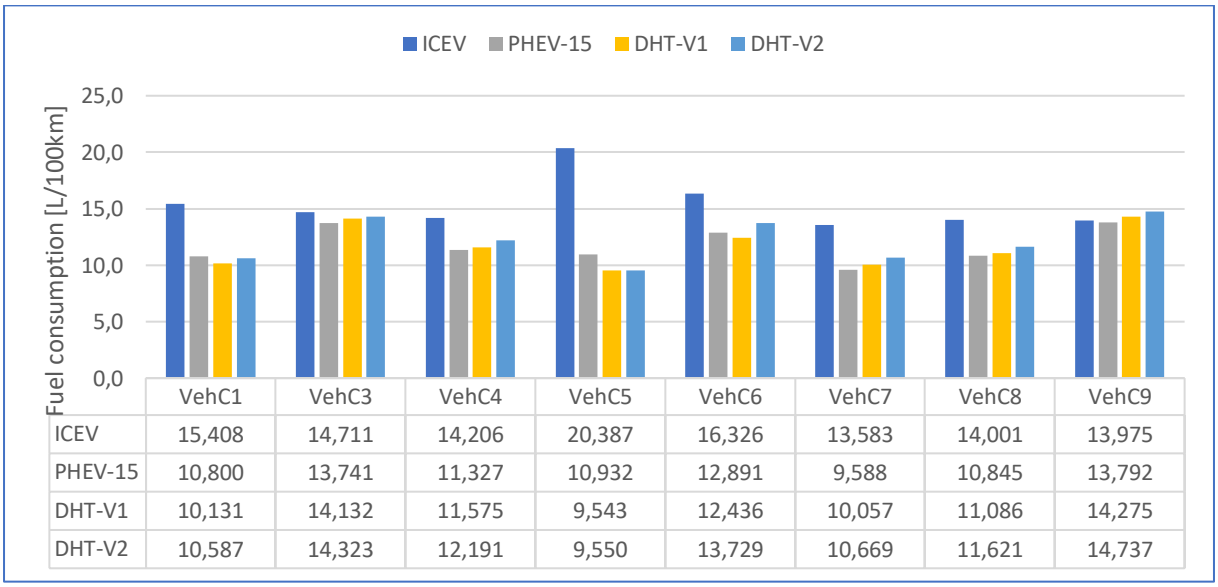

	VehC1	VehC3	VehC4	VehC5	VehC6	VehC7	VehC8	VehC9
ICEV	15,408	14,711	14,206	20,387	16,326	13,583	14,001	13,975
PHEV-15	10,800	13,741	11,327	10,932	12,891	9,588	10,845	13,792
DHT-V1	10,131	14,132	11,575	9,543	12,436	10,057	11,086	14,275
DHT-V2	10,587	14,323	12,191	9,550	13,729	10,669	11,621	14,737

Figure 4: Main comparison results

Comparison between *DHT-V1* and *DHT-V2* shows, that a cheaper *DHT-V1* generally outperforms the *DHT-V2*. This is due to the size of traction motor EM2, which for *DHT-V1* operates closer to its optimum efficiency, and also the combination of ICE and EM2 in P-Mode that also lead to better charging efficiencies available in P-Mode LPS.

Finally, it is interesting to note, that high ICE efficiency in very broad range of operating points leads to the ICE-only operation instead of LPS in P-Mode. Energy management strategy tends to recharge the HV-battery first by recuperated energy from braking, then by P-Mode charge, and only if there is no other option using the S-Mode.

5.2 Vehicle load sensitivity

Vehicle load sensitivity in Figure 5 shows the results for 2300 kg vehicle load.

DHT versions are less sensitivity to vehicle load compared to *PHEV-15*. For example, the *DHT-V1* version in *VehC4* driving cycle, achieves better FC than *PHEV-15*. Then, for both low-speed vehicle driving cycles *VehC1* and *VehC5*, is the fuel consumption benefit of DHTs higher, compared to 1100 kg load in Figure 4.

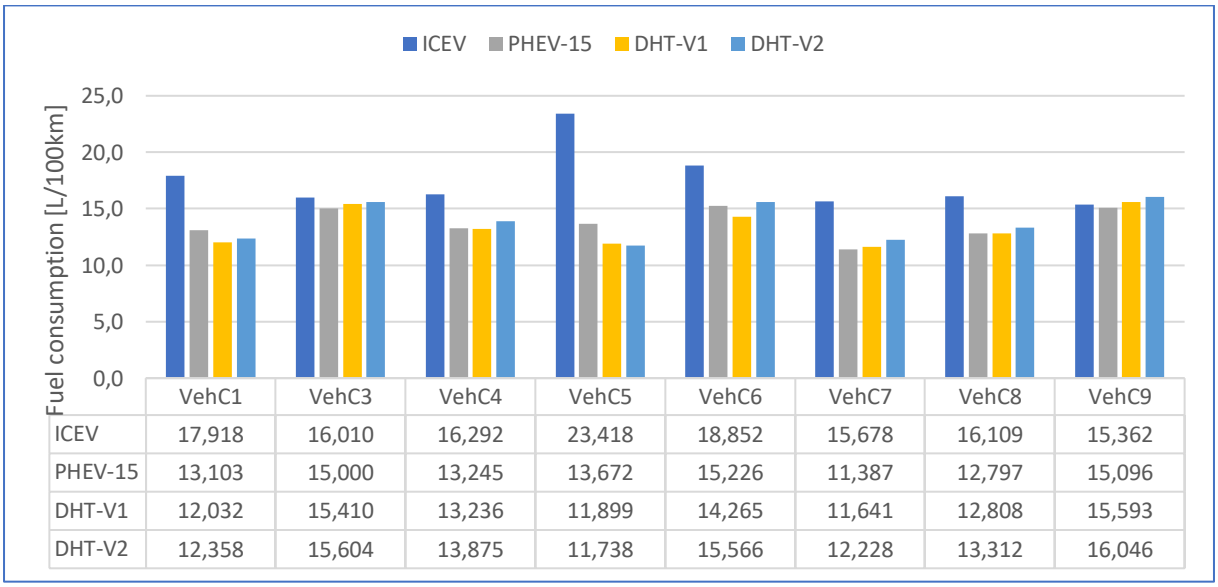

	VehC1	VehC3	VehC4	VehC5	VehC6	VehC7	VehC8	VehC9
ICEV	17,918	16,010	16,292	23,418	18,852	15,678	16,109	15,362
PHEV-15	13,103	15,000	13,245	13,672	15,226	11,387	12,797	15,096
DHT-V1	12,032	15,410	13,236	11,899	14,265	11,641	12,808	15,593
DHT-V2	12,358	15,604	13,875	11,738	15,566	12,228	13,312	16,046

Figure 5: Vehicle load sensitivity

5.3 Energy management strategy settings sensitivity

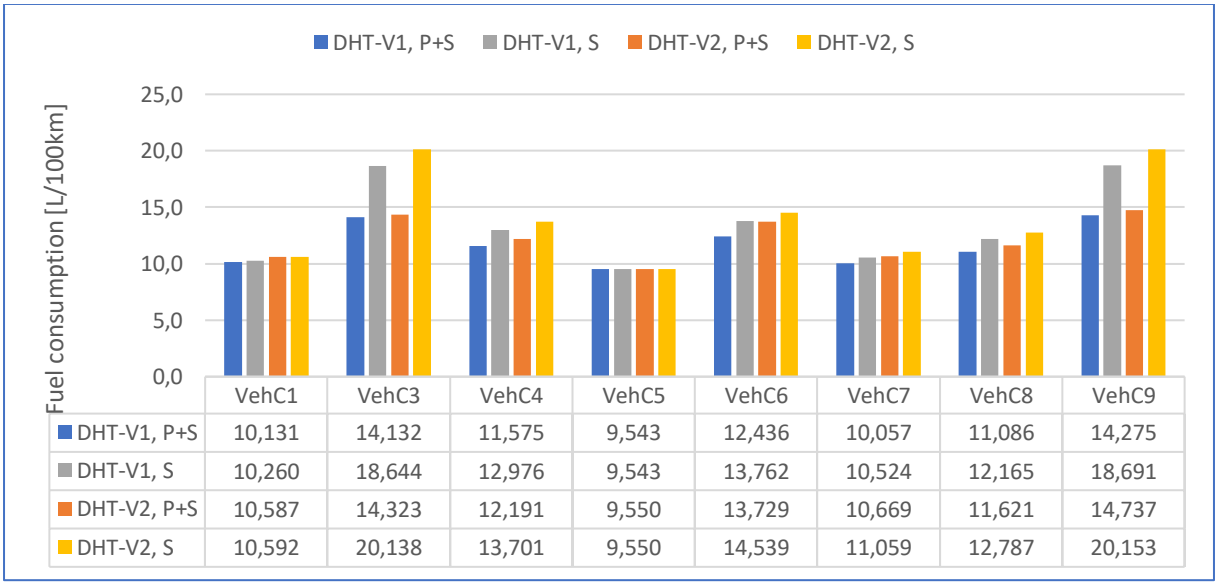

	VehC1	VehC3	VehC4	VehC5	VehC6	VehC7	VehC8	VehC9
DHT-V1, P+S	10,131	14,132	11,575	9,543	12,436	10,057	11,086	14,275
DHT-V1, S	10,260	18,644	12,976	9,543	13,762	10,524	12,165	18,691
DHT-V2, P+S	10,587	14,323	12,191	9,550	13,729	10,669	11,621	14,737
DHT-V2, S	10,592	20,138	13,701	9,550	14,539	11,059	12,787	20,153

Figure 6: Energy management strategy settings results

Finally, third sensitivity compares two “extreme” possible settings of energy management strategy EV_{Lim} parameter (Figure 6). First option of EV_{Lim} 45 km/h is the design baseline, where ICE starts its operation at around 940 RPM. This means, energy management strategy can use the P-Mode charging as well as the S-Mode charging (hence “P+S” in Figure 6). The second option of EV_{Lim} 120 km/h means the vehicle powertrain works as a series HEV: battery can only be charged using recuperation energy or S-Mode charging when necessary (hence “S” in Figure 6).

Vehicle driving cycles with low overall speeds, that must use S-Mode charging show very low sensitivity on EV_{Lim} parameter (*VehC1* and *VehC5*, followed by *VehC7*). On the other side are the high-speed vehicle driving cycles *VehC3* and *VehC9*. For these, the forced S-Mode charging results in FC penalty of more than 25 %.

The general trend from main result in chapter 5.1 is preserved: *DHT-V1* performs better than *DHT-V2*.

6. CONCLUSION

We have prepared two different versions of a DHT powertrain, combining different EMs with 5.9 L TDI ICE, 15.6 kWh 400 V HV-battery, and 7.5-tonne heavy-duty truck. *DHT-V1* represents a cheaper option with lower speed – lower power EMs, that are readily available on the market. *DHT-V2* then combines high speed EMs, with traction motor EM2 achieving also high power.

Both versions were tested on a set of eight vehicle driving cycles with different maximum and average speeds, and lengths. Main tests were extended by two sensitivities: one on vehicle load, and the other on energy management strategy parameter. All results were then compared to a set of older results for the same heavy-duty truck combined with 6-speed shifting transmission and plug-in HEV parallel topology (*PHEV-15*).

DHT versions’ performance in all cycles is very similar to *PHEV-15*: DHTs perform better in low-speed vehicle driving cycles, *PHEV-15* in medium to high-speed cycles. *DHT-V1* always achieve better fuel efficiency than *DHT-V2*. This leads us to a conclusion, that in a multi-mode DHT powertrain of this type it is important to match EM and ICE characteristics in both P-Mode and S-Mode, to achieve best fuel efficiency.

Regarding the vehicle loads, DHT variants are slightly less sensitive to higher loads compared to *PHEV-15*. Second sensitivity showed that energy management strategy E-Mode limit parameter that determines the switch from E-Mode or S-Mode (series operation mode) to P-Mode (parallel operation mode) can lead up to more than 25 % fuel consumption penalty for high-speed vehicle driving cycles, where P-Mode charging is more efficient than S-Mode.

To conclude, our study showed promising results for DHT powertrain use in heavy-duty application. A thorough optimization study including EM parameters, together with DHT gear ratios could lead to further improvements in fuel consumptions for all test cases.

REFERENCES

[1] Toman, R., Parallel HEV Topologies for Heavy-Duty Truck, Proceedings of KOKA 2022 Conference, p. 223-233, ISBN 978-80-227-5215-2

[2] Toman, R., Adámek, M., Complex Evaluation of Heavy-Duty Truck Hybridization and Electrification Options, Strojnícky časopis – Journal of Mechanical Engineering, Vol 72 (2022), No. 3, 97-112, DOI: 10.2478/scjme-2022-0044

[3] Toman, R., Heřmanová, J., Adámek, M., Denk, P., Soukup, J., Evaluation Study of a Multi-Mode HEV with a Dedicated Hybrid Transmission, Proceedings of the FISITA 2021 World Congress, Prague, 13–17 September 2021, 10.46720/F2020-ADM-108

[4] Lauinger, Ch., Reitz, D., Bayoux, L., Adrian, M., Ciesek, M. (2019). Hybrid Transmissions of the Future, Proceedings of 18th International CTI Symposium Automotive Drivetrains

ACKNOWLEDGEMENT

This work was realized using support of:

- Technological Agency, Czech Republic, programme National Competence Centres II, project # TN02000054 Božek Vehicle Engineering National Center of Competence (BOVENAC).
- The Grant Agency of the Czech Technical University in Prague, grant No. SGS24/090/OHK2/2T/12.

This support is gratefully acknowledged.

ANNEX

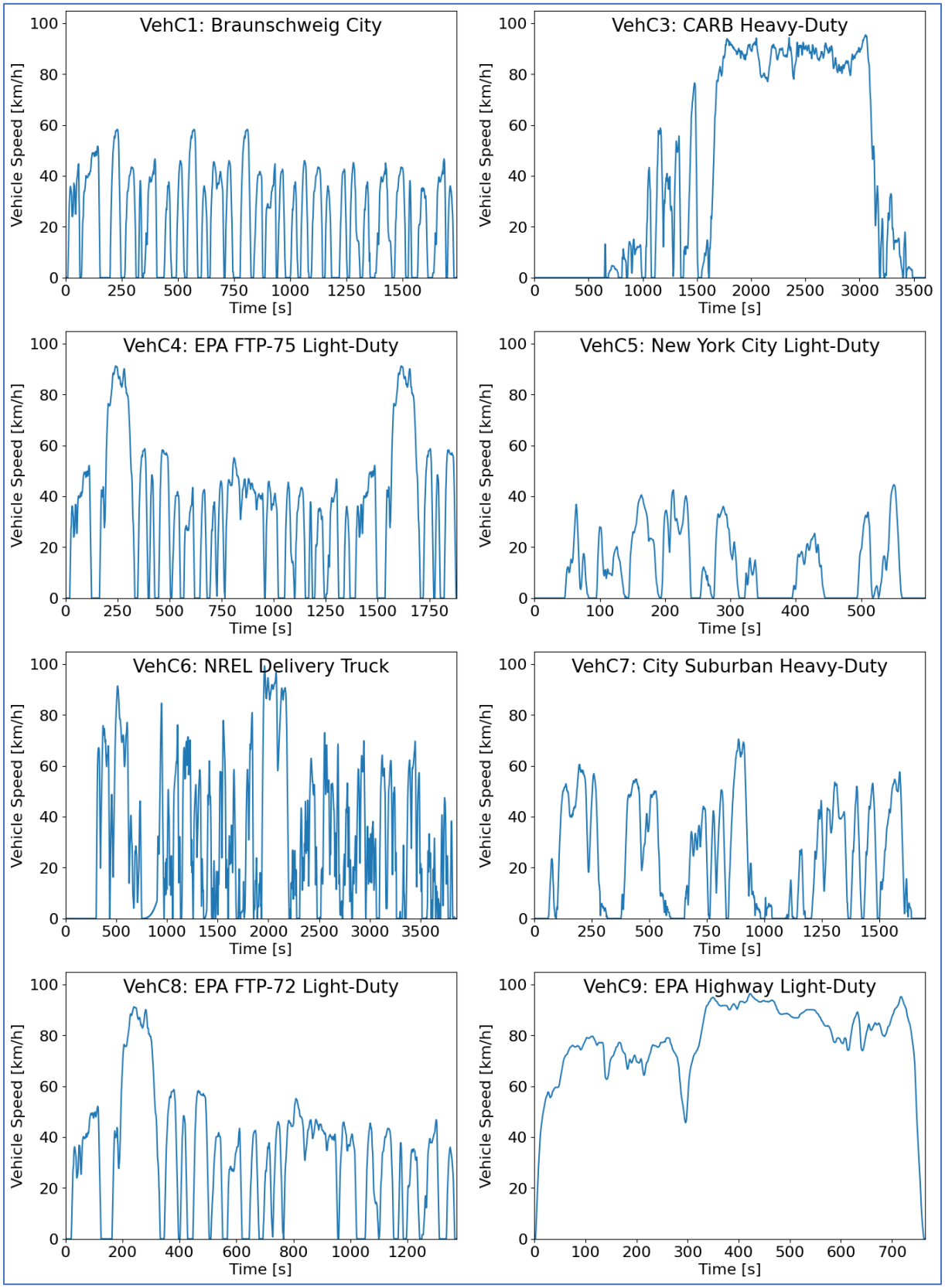

Figure 7: Vehicle driving cycles

55. mezinárodní vědecká konference zaměřená na výzkumné a výukové metody v oblasti vozidel a jejich pohonů

září 5. - 6., 2024 – Liberec, Česká republika
Technická univerzita v Liberci
Fakulta strojní, Katedra vozidel a motorů

HYDROGEN - THE FUEL OF THE FUTURE, OR THE STUDY OF BIOHYDROGEN PRODUCTION FROM WASTE WHEY BY ANAEROBIC BACTERIA FOR ITS SUBSEQUENT USE AS A FUEL FOR THE AUTOMOTIVE INDUSTRY

Matěj Poulíček[1], Viktorie Alexandra Pacasová[2], Josef Štětina[3], Stanislav Obruča[4]

[1] Ing. Matěj Poulíček, Institute of Automotive Engineering, Brno University of Technology Technická 2896/2 Brno, Matej.Poulicek@vut.cz
[2] Ing. Viktorie-Alexandra Pacasová, Institute of Food Science and Biotechnology, Brno University of Technology, Purkyňova 464/118 Brno, Viktorie-Alexandra.Pacasova@vut.cz
[3] prof. Ing. Josef Štětina, Ph.D. Institute of Automotive Engineering, Brno University of Technology Technická 2896/2 Brno, josef.stetina@vutbr.cz
[4] prof. Ing. Stanislav Obruča, Ph.D. Institute of Food Science and Biotechnology, Brno University of Technology, Purkyňova 464/118 Brno, obruca@fch.vut.cz

Abstract
With the growing impact of industry on climate change, interest in alternative energy sources has increased. One renewable source is hydrogen, producible via anaerobic bacteria like Clostridium. This study models a single-cylinder spark ignition engine using biohydrogen from these bacteria, optimizing the mixing ratio, ignition advance, and other factors to enhance power, torque, and combustion efficiency. Additionally, a dual compression ignition engine model will be developed where the biohydrogen serves as a secondary fuel to diesel. Results from both engine models will be compared to evaluate the biohydrogen's efficacy in spark ignition and compression ignition engines.

1. INTRODUCTION

The combustion of hydrogen in internal combustion engines is one of the alternatives for powering vehicles to reduce emissions. Hydrogen has many unique physical properties, including low molar mass, high diffusion coefficient, high thermal conductivity and low viscosity. Therefore, hydrogen can be used as an energy carrier that can be conveniently produced using electricity from renewable sources, biomass and fossil fuels. [1]
Biohydrogen, produced by anaerobic bacteria such as *Clostridium butyricum* and *Clostridium tyrobutyricum*, represents a promising source of renewable energy with significant potential for reducing greenhouse gas emissions and efficient use of waste materials. Hydrogen combustion produces only water vapour, without emissions, which contributes to improving air quality and combating climate change. Hydrogen can be produced from waste materials from the food industry, such as whey from the dairy industry, thereby promoting a circular economy and reducing the environmental burden associated with the disposal of these wastes. Its high energy density (122 MJ/kg) makes hydrogen a powerful energy carrier suitable for a variety of transport and energy applications.
Compared to hydrogen fuel cells, internal combustion engine technology is economically less expensive to produce and can use a variety of fuel types, including those with lower purity. Hydrogen as a fuel offers several advantages over conventional fuels, such as short quenching distance, high flame spread rate in mixtures and, most importantly, a wide range of air-fuel ratios, which allows efficient combustion of very lean mixtures, as shown in TABLE 1.
Internal combustion engines are primarily divided into spark ignition (SI-ICE) and compression ignition (CI-ICE) engines. When comparing various parameters, hydrogen enriched engines show several differences in combustion characteristics for both types of engines.
In spark ignition engines, hydrogen can be burned as a secondary fuel or even as a primary fuel without much difficulty. It can be supplied indirectly to the intake air in the intake manifold or directly into the combustion chamber. The ignition of the air mixture is initiated by a spark plug.
In a diesel engine, ignition of the mixture is achieved by the timely release of fuel into the heated air in the combustion chamber. Due to the specific properties of hydrogen, such as its high auto-ignition temperature, low ignition energy and high flame propagation speed, the use of hydrogen alone in a diesel engine is economically and technically complicated. However, this ignition complication can be solved by using hydrogen as a secondary fuel with which the intake air is enriched and this mixture is

then ignited by the diesel fuel injected into the combustion chamber during the compression stroke.
The main disadvantage of hydrogen combustion is the risk of flame backflow into the intake manifold. This is due to the small quenching distance of the hydrogen, which allows the hydrogen flame to pass through the narrow space between the valve and the valve seat. If a mixture of hydrogen and air is then present in the intake manifold between points, the flame will propagate through the intake manifold and the resulting temperature and pressure can damage sensitive intake tract components such as the mass air flow sensor the ignition, intake air pressure sensor or fuel injectors.
In this project, hydrogen is produced using anaerobic bacteria *Clostridium butyricum* CCM 8499 and *Clostridium tyrobutyricum* CCM 8498, enabling us to utilize food industry waste as a carbon source for biohydrogen production. However, the gas mixture produced by these bacteria contains not only biohydrogen, but also other gases (e.g. CO_2), which can affect the final mixing ratio for combustion in internal combustion engines.

Property	Hydrogen (H_2)	Gasoline (C_6-C_{12})	Methanol (CH_3OH)	Methane (CH_4)
Energy density of stoichiometric mixture with air [kJ/dm3]	3,23	3,84	3,56	3,31
Energy density at STP [MJ/N m3]	11	32000	15700	35
LHV specific energy [MJ/kg]	120	42-44	20	48
Molecular diffusion coefficient [cm2/s]	0,61	0,05	0,13	0,16
Octane [RON]	>130	92-98	106	120
Auto-ignition temperature [°C]	571	220	470	632
Minimum ignition energy [mJ]	0,02	0,24	0,21	0,29
Maximum flame speed [m/s]	2,8	0,37-0,43	0,45	0,37-0,43
Explosion limits - volume in air [%]	18,2-58,9	1,4-3	6,7-36	5,7-14
Flammability limits - volume in air [%]	4,1-74	1,4-7,6	6-36,5	5,3-15
Lean limit equivalence ratio in air	0,1	0,58	0,57	0,5

Table 1: *Properties of common fuels [1]*

2. BODY OF PAPER

2.1 Production of biohydrogen

2.1.1 Used microorganisms

The bacteria used in this project to produce biohydrogen are *Clostridium butyricum* CCM 8499 and *Clostridium tyrobutyricum* CCM 8498, under patent certificate No. 305 450, deposited in the Czech Collection of Microorganisms (CCM).

2.1.2 Media

The bacteria *Clostridium butyricum* CCM 8499 and *Clostridium tyrobutyricum* CCM 8498 are cultured in Reinforced Clostridial Medium (RCM) with different carbon sources such as glucose (RCM) or lactose (RCM*):

	RCM	RCM*
Yeast Extract	3 g	3 g
Lab-Lemco powder	10 g	10 g
Bacteriological peptone	10 g	10 g
Starch	1 g	1 g
NaCl	5 g	5 g
Sodium acetate	3 g	3 g
Glucose	5 g	X
Lactose	X	5 g
Destilled water	1000 ml	1000 ml

Table 2: *Composition of RCM and RCM* media used for the cultivation of Clostridium butyricum CCM 8499 and Clostridium tyrobutyricum CCM 8498*

2.1.3 Cultivation of microorganisms

The entire cultivation process will be carried out in an inert chamber filled with nitrogen (N_2) and containing oxygen (O_2) up to 2% of the total chamber volume. The bacteria will be first cultivated at first in 50 ml tubes containing 20 ml of RCM or RCM* medium at 37 °C for 24-48 h. The inocula prepared in this way will be subsequently inoculated into 50 ml tubes containing 20 ml of production medium (again RCM or RCM* medium). 0,6-1 ml of inoculum will be inoculated into the production medium. The culture of the production cultures will be carried out again at 37 °C for 24-72 h. During cultivation, the gas mixture produced by the bacteria will be collected and subsequently analysed using the Hiden QGA system ('quantitative gas analysis') to determine the hydrogen content produced.

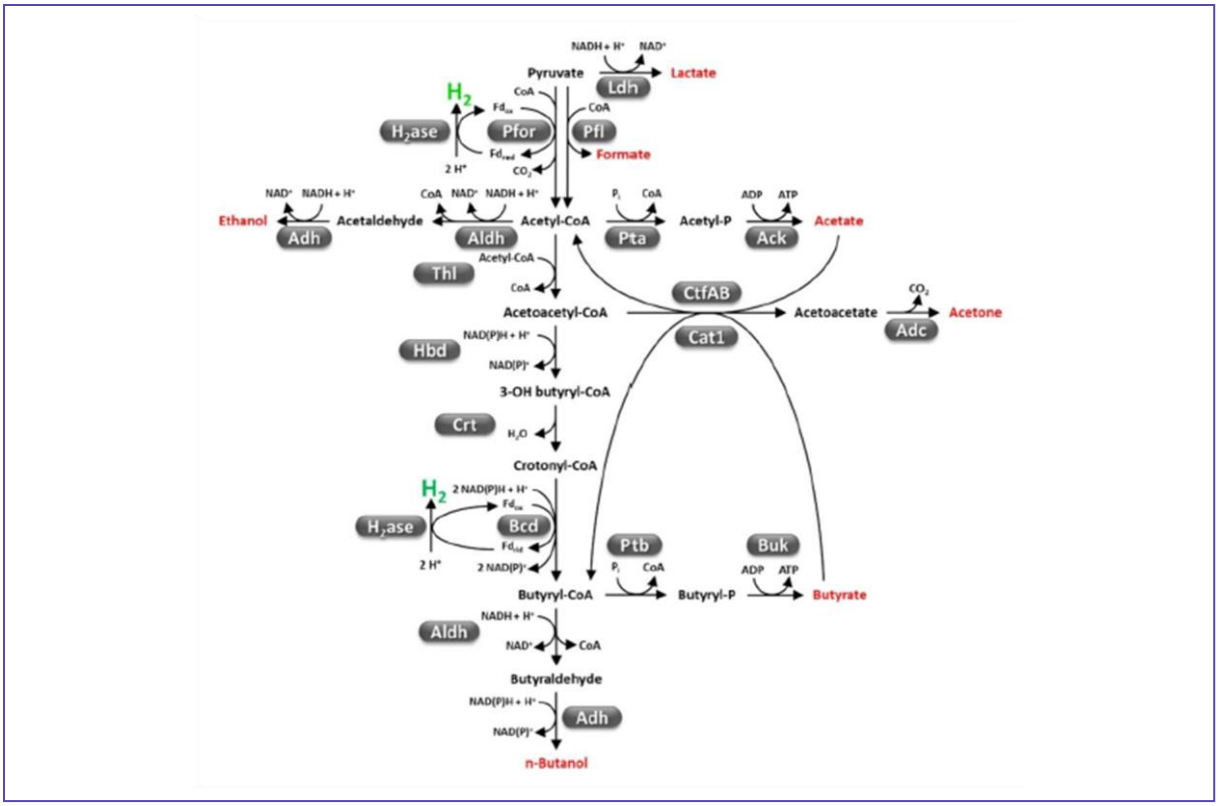

Figure 1: *Metabolic pathway connected to hydrogen production in genus Clostridium*

2.2 Hydrogen usage internal combustion engines

2.2.1 Hydrogen as a primary fuel for spark ignition internal combustion engines

Hydrogen is a suitable primary fuel for powering spark ignition internal combustion engines. Due to the absence of carbon in the fuel mixture, the formation of carbon dioxide and carbon monoxide is minimised. Exhaust gases consist mostly of water vapour and may contain small amounts of carbon oxide emissions due to the combustion of engine oil [2] [3] When combusting lean mixtures (with excess air), the high temperature in the combustion chamber results in NO_X emissions, which can be reduced by exhaust gas recirculation (EGR) or by a selective catalytic reduction catalyst (SCR) using an aqueous AdBlue solution.

The principle of function H2 SI-ICE

Hydrogen is released indirectly - into the intake air stream in the intake manifold, with which it is drawn into the engine cylinder and burned. The mixture is ignited in a similar way to conventional spark-ignition engines by the spark plug. Experimental work has shown that hydrogen-fuelled spark-ignition engines can operate at up to 30 % power without airflow control, allowing a reduction in throttling losses in the low-load range. [3]

2.2.2 Hydrogen as a secondary fuel for spark ignition internal combustion engines (SI-ICE)

When burning conventional fuels in spark-ignition internal combustion engines - gasoline, LPG, CNG, it is necessary to maintain a relatively precise mixing ratio between fuel and air. The value of the mixing ratio directly affects the combustion

characteristics of the mixture burned. If the mixing ratio is inappropriate, important combustion parameters of the mixture are affected, which can have a negative impact on the output power, efficiency, durability and also on the specific effective fuel consumption. In certain cases of inappropriate air to fuel ratio, detonative combustion may also occur during combustion. The addition of hydrogen as a secondary fuel to the combustion mixture can also achieve more beneficial characteristics than combustion of the primary fuel alone. Additivation can extend the mixing ratio range of lean mixtures, increase the burning rate, but also reduce the formation of emissions of unburned hydrocarbons HC and carbon oxides, in particular carbon dioxide CO_2 and carbon monoxide CO. By increasing the burning rate, higher thermal efficiency can be achieved. Enrichment of the mixture in spark-ignition engines appears to be particularly advantageous in part-load conditions, where it is possible to burn very lean mixtures and reduce the losses due to throttling of the intake air. Typical efficiency gains are around 5-30 %. [2] The advantage of these systems is the possibility of operating on multiple fuels. The vehicle is not dependent on only one fuel source.

The principle of function H2 enriched dual fuel SI-ICE

Hydrogen is released into the intake air stream via injectors in the intake manifold and is drawn into the cylinder where it is burned with the primary convection fuel. The primary fuel can be in both liquid and gaseous form and can be released either indirectly into the intake manifold or directly into the engine cylinder. If the primary fuel, as well as the secondary fuel (hydrogen), is released into the intake manifold in a gaseous state - (e.g. LPG systems, CNG, biomethane, etc.), then the two fuels can be premixed in a certain ratio and released together into the intake manifold, which can reduce the amount of some fuel system components. The mixture is then compressed in the cylinder and ignited by the spark plug. Due to the variable combustion characteristics of the mixture depending on its composition, it is necessary to adjust the ignition timing in order to optimise engine operation and avoid negative effects. [7]

Knock resistence

Resistance to knock (detonation combustion) is a very important parameter of fuels for spark-ignition internal combustion engines. However, the knock resistance - the so-called octane number of the fuel - cannot be simply specified in the case of hydrogen combustion as for convection fuels, as there are some irregularities under different combustion conditions. This is due to the high flame propagation velocity and low ignition energy, which causes a sharp pressure to increase in the combustion chamber, which can be similar to actual detonation combustion, including the typical acoustic effect. These characteristics have led to the claim that octane number is not a suitable parameter for hydrogen combustion. A measure, referred to as the methane number, has been developed for resistance to gaseous fuel knock. [4] However, this designation has subsequently been criticised due to the relatively unusual combustion properties of methane and hydrogen. [5] Resistance to detonation combustion shows a different behaviour in the case of enrichment with mixtures of hydrogen and carbon monoxide, compared to enrichment with pure hydrogen. [6] Overall, hydrogen enriched blends at concentrations below 20% by volume showed similar resistance to detonation combustion as the primary fuel at the same mixture ratio diluted with EGR gases. Running on a highly diluted mixture with EGR gases and a parallel extremely lean H_2 fuel can increase the resistance to detonation combustion, which can increase

the compression ratio or boost pressure, leading to a significant increase in engine efficiency. [3]

2.2.3 Hydrogen as a primary fuel for compression ignition ICE

Due to the specific properties of hydrogen, its use as a primary fuel for compression ignition engines with current technologies is not suitable. Complications arise in particular from the poor controllability of ignition timing, low ignition energy and consequently high flame propagation velocity.

2.2.4 Hydrogen as a secondary fuel for dual compression ignition ICE

Diesel engines, compared to petrol engines, usually operate with a significant excess of air and their performance and emission parameters are regulated mainly by the timing and the amount of primary fuel injected into the combustion chamber. When the intake air is enriched with hydrogen, the primary fuel can be partially replaced to achieve positive results.

The principle of function H2 enriched dual fuel CI-ICE

The hydrogen is released into the intake manifold where it is sucked into the engine cylinder in various proportions together with air. [7] [8] During the compression stroke, this mixture is compressed, which significantly increases its temperature. In the area around the top dead center, primary fuel with lower flash point is injected, known as pilot injection. The tiny droplets of primary fuel ignite after a short time delay due to heat, igniting the hydrogen-air mixture.

Effect of the AFR (air-fuel ratio) of the intake mixture

The concentration of hydrogen in the intake air can cause different enrichment effects. The mixture of hydrogen and air is divided into two categories based on mixture flammability. [7] [8]

Lean mixture below the flammability limit

If the mixture of the inlet gas is too lean of hydrogen and is below the so-called ignition limit, then the flame does not spread throughout the combustion chamber and combustion occurs only in the diffusion combustion areas. When this occurs, the hydrogen is burned in a relatively short interval and the combustion of the tiny droplets of primary fuel is affected. The hydrogen-air mixture, which does not directly interact with the burning droplets, ignites when the temperature and pressure in the combustion chamber reach critical auto-ignition values. This effect causes a further increase of temperature, a decrease of oxygen concentration and an increase of water concentration, which affects the duration of the diffusion flame surrounding the primary fuel droplets.

Mixture within flammability limits

If the hydrogen concentration in the inlet mixture is within the flammability limits, then it is likely that the flame will spread throughout the combustion chamber after the primary fuel has ignited. This will increase the concentration of steam water in the combustion chamber, increase the temperature and pressure, affecting the diffusion flame in the closeness of the primary fuel droplets. [5]) [7] [9] [10] [11]

2.3 GT–SUITE simulations

Due to the unknown composition of the generated gas, it has not been yet decided how this gas will be further used. There are two possible strategies that will be chosen based on the results of the quantitative gas analysis. If hydrogen is present in a minority in the mixture, the individual gas components will need to be separated to increase the hydrogen concentration. Alternatively, if the proportion of impurities in the mixture is low, it may be more economical to inject the hydrogen mixture directly into the engine together with the other gases produced by fermentation. The final decision will depend on the presence of specific gases in the mixture. Some gases, such as CO_2, are inert and will remain unchanged when passing through the internal combustion engine, while other components may oxidise to CO_2 or be potentially harmful to the engine and its components.
For the purpose of this project, a model of the Tatra 928 T3D compression ignition V8 engine was created in GT-Suite software, based on a real engine. This model was optimised to achieve the performance parameters declared by the manufacturer. In order to reduce the length of the individual simulations, the model was reduced to a single-cylinder variant, which was enhanced with a hydrogen injector placed in the intake manifold, just ahead of the intake valve. Refer to Figure 2.

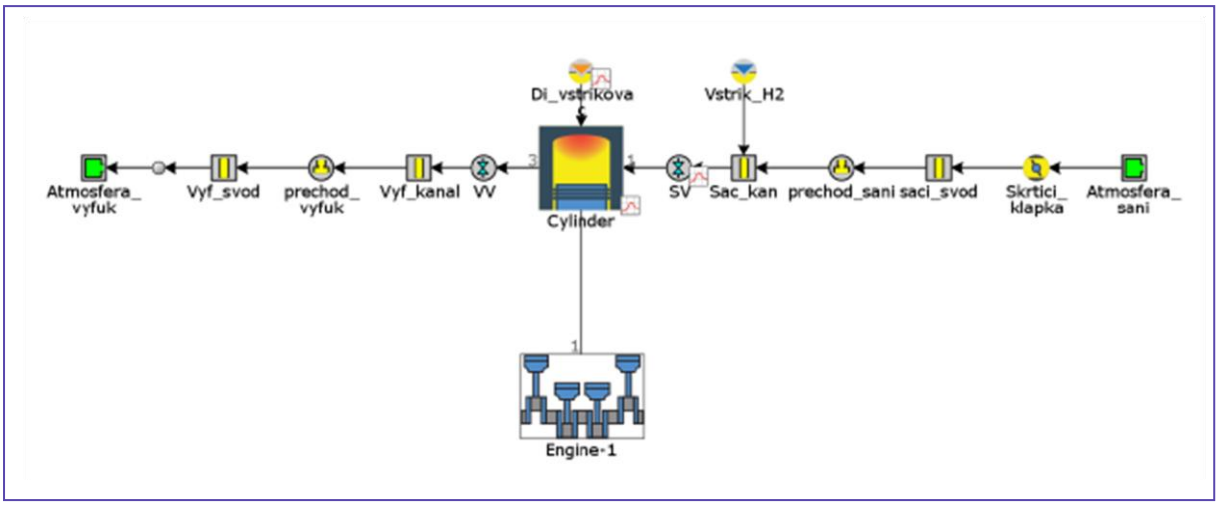

Figure 2: *Reduced dual fuel CI-ICE model in GT-Suite*

The performed simulation will provide important information about the engine behaviour when combusting the generated gas with different mixture compositions and determine the optimal conditions for its use in an internal combustion engine. Based on the results of this simulation and the quantitative analysis of the gas, it will be possible to decide whether further separation of the gas or its direct use in a compression ignition or spark ignition variant of the engine is necessary.

3. CONCLUSION

This project focuses on the potential for the use of biohydrogen, produced by fermentation of food waste using specific bacteria of the genus *Clostridium*, in internal combustion engines. Although the production of biohydrogen is not yet complete and the exact composition of the generated gas has not yet been determined, the results so far indicate promising possibilities for its application.
In the introductory parts of the article, the technology of biohydrogen production was described, which represents an environmentally friendly method of converting food waste into a valuable energy source. This process has the potential not only to reduce greenhouse gas emissions but also to make efficient use of waste materials from the food industry.
The main part of the study focused on the possibilities of using biohydrogen in internal combustion engines, culminating in a chapter on simulations carried out in GT-Suite. First, a model of a real Tatra T3D 928 engine was created and optimized according to the manufacturer's parameters. The model was then reduced to a single cylinder variant for more efficient simulation purposes and a sequential hydrogen injector was integrated into the intake manifold.
The results suggest that the optimal strategy for biohydrogen utilization will depend on the proportion of hydrogen and the presence of other gases in the mixture. Two possible strategies include either separation of the individual components to increase the hydrogen concentration or direct use of the gas mixture in the case of low impurity content. A final decision can only be made once the quantitative gas analysis has been completed.
This research contributes to the understanding of the potential of biohydrogen as an alternative fuel and provides a basis for further experimental work. Future steps will include the completion of the quantitative gas analysis, more accurate simulations and experimental validation of the results, allowing the full potential of biohydrogen to be exploited for internal combustion engines and to contribute to sustainable development and energy self-sufficiency.

REFERENCES

[1] SHERIF, S.A.; GOSWAMI, D. Yogi; STEFANAKOS, Elias K. a STEINFELD, Ido. Handbook of Hydrogen Energy. 20140124. CRC Press, 2014. ISBN 9781420054477.

[2] VERHELST, S; VERSTRAETEN, S a SIEREN, R. A comprehensive overview of hydrogen engine design features. online. Proceedings of the Institution of Mechanical Engineers Part D-Journal of Automobile Engineering. 2007, č. 2218, s. 911-920. Dostupné z: https://www.researchgate.net/publication/245391477_A_comprehensive_overview_of_hydrogen_engine_design_features. [cit. 2024-01-02].

[3] JAMAL, Y a WYSZYNSKI, M. L. On-board generation of hydrogen-rich gaseous fuels—a review. International Journal of Hydrogen Energy. 1994, roč. 19, č. 7, s. 57-570.

[4] SAIKALY, K; ROUSSEA, S; RAHMOUN, C; LE CORRE, O a TRUFFET, L. Safe operating conditions determination for stationary SI gas engines. online. Fuel Processing Technology. 2008, roč. 28, č. 11, s. 1169-1179. Dostupné

z: https://www.sciencedirect.com/science/article/abs/pii/S0378382008001148. [cit. 2024-01-06].
[5] LIU, Z a KARIM, G.A. Knock characteristics of dual-fuel engines fuelled with hydrogen fuel. online. International Journal of Hydrogen Energy. 1995, roč. 20, č. 1, s. 919-924. Dostupné z: https://www.sciencedirect.com/science/article/pii/0360319995000237. [cit. 2024-1-06].
[6] LI, H; KARIM, G.A. a SOHRABI, A. Knock and Combustion Characteristics of CH4, CO, H2 and Their Binary Mixtures. online. SAE Technical Paper. 2003. Dostupné z: https://www.researchgate.net/publication/285955554_Knock_and_Combustion_Characteristics_of_CH4_CO_H2_and_Their_Binary_Mixtures. [cit. 2024-01-06].
[7] HEYWOOD, J. B. Internal Combustion Engine Fundamentals. McGraw Hill. New York, 1988.
[8] SARAVANAN, N. a NAGARAJAN, G. An experimental investigation of hydrogen-enriched air induction in a diesel engine system. online. International Journal of Hydrogen Energy. 2008, roč. 33, č. 6, s. 1769-1775. Dostupné z: https://www.sciencedirect.com/science/article/pii/S0360319908000025. [cit. 2024-01-07].
[9] MCTAGGART-COWAN, G.P.; JONES, H.L.; ROGAK, Steven; BUSHE, W.K. a HILL, P.G. Direct-Injected Hydrogen-Methane Mixtures in a Heavy-Duty Compression Ignition Engine. online. In SAE 2006 World Congress. 2006. Dostupné z: https://www.researchgate.net/publication/289928825_Direct-Injected_Hydrogen-Methane_Mixtures_in_a_Heavy Duty_Compression_Ignition_Engine. [cit. 2024-01-07].
[10] SARAVANAN, N a NAGARAJAN, G. An experimental investigation on optimized manifold injection in a direct-injection diesel engine with various hydrogen flowrates. online. Proceedings of the Institution of Mechanical Engineers, Part D: Journal of Automobile Engineering. 2007, roč. 221, č. 12, s. 1575-1584. ISSN 0954-4070. Dostupné z: https://doi.org/10.1243/09544070JAUTO609. [cit. 2024-4-15].
[11] PATRO, T. Burning rate assessment of hydrogen-enriched fuel combustion in diesel engines. online. International Journal of Hydrogen Energy. 1994, roč. 19, č. 13, s. 275-284. ISSN 03603199. Dostupné z: https://doi.org/10.1016/0360-199(94)90098-1. [cit. 2024-04-15].
[12] MASOOD, M; ISHRAT, M a REDDY, A. Computational combustion and emission analysis of hydrogen–diesel blends with experimental verification. online. International Journal of Hydrogen Energy. 2007, roč. 32, č. 13, s. 2539-2547. ISSN 03603199. Dostupné z: https://doi.org/10.1016/j.ijhydene.2006.11.008. [cit. 2024-04-15].

ACKNOWLEDGEMENT

This work is supported by a junior interfaculty project between the Faculty of Chemistry and the Faculty of Mechanical Engineering. Project ID BD162403002.

55. mezinárodní vědecká konference zaměřená na výzkumné a výukové metody v oblasti vozidel a jejich pohonů

září 5. - 6., 2024 – Liberec, Česká republika
Technická univerzita v Liberci
Fakulta strojní, Katedra vozidel a motorů

APPLICATION OF ELECTRICALLY ASSISTED TURBOCHARGING FOR THE CASE OF LARGE-BORE GAS SI ICE

Oldrich Vitek[1], Jan Macek[2], Bohumil Mares[3], Jiri Klima[4], Martin Vacek[5]

Abstract
The paper deals with application of electrically assisted turbocharging (HP e-Turbo, e-Booster without downstream intercooling) for the case of 2-stage turbocharged large-bore gas SI ICE. The main focus is put on steady state operation under different load levels while varying NO_x level (according to TA Luft norm) – different sensitivity studies were performed. Transient performance is also considered. Detailed analysis of data was carried out – main advantages and disadvantages of considered turbocharging configurations were drawn while comparing these with standard configuration(s).

[1] Oldrich Vitek, CTU in Prague, Technicka 4, Prague, Oldrich.Vitek@fs.cvut.cz
[2] Jan Macek, CTU in Prague, Technicka 4, Prague, Jan.Macek@fs.cvut.cz
[3] Bohumil Mares, CTU in Prague, Technicka 4, Prague, Bohumil.Mares@fs.cvut.cz
[4] Jiri Klima, PBS Turbo, Vlkovska 279, Velka Bites, Jiri.Klima@pbsturbo.eu
[5] Martin Vacek, PBS Turbo, Vlkovska 279, Velka Bites, Martin.Vacek@pbsturbo.eu

1. INTRODUCTION

Large-bore spark-ignited internal combustion engines became very popular in last couple of decades due to very high efficiency and low pollutant formation. This is achieved by strong Miller cycle (early IVC) in combination with high air excess – both these measures require very efficient boost group which has to be able to provide high boost pressure. This is usually achieved by application of 2-stage boost group. It is well-known that such engine layout leads to complex design and complex engine control. It is also known that 2-stage boost group configuration has very high potential in terms of achievable BMEP, BSFC, transient response and low pollutant level (NO_x) – c.f. [2], [3], [4], [5] and [6]. However, it is expected that future NO_x limits will become much stricter while engine load will increase as well to further improve engine efficiency. Moreover, additional fuel sources may become important: hydrogen, biogas, ammonia, methanol or possibly low energy content gas mixtures (containing a lot of CO_2). All that will lead to increased requirements with respect to boosting systems. And not only steady-state operation will be of main importance – engine transient response is expected to become even more important (e.g., due to 'intermittent' nature of renewable energy sources).

Transient operation of large-bore ICEs is usually not that critical (when compared with automotive ICE applications). In the case of large-bore gas SI ICEs, which are typically used for power and heat generation (i.e., it is a co-generation unit), this is the case in majority of their applications. However, there are cases when the phenomenon might become important – example could be 'island operation' of such a unit which has to react quicky with respect of fast load changes at constant engine speed.

The presented work is a part of the research within the TA CR program of National Competence Centres (TN02: NCK2). Results (shown in the paper) are based on a long-term cooperation between PBS Turbo and Czech Technical University in Prague as a lot of experience & knowledge was transformed from previous research projects between those 2 subjects.

Main paper goal is to study the effect/influence of electrically assisted boosting systems for the case of large-bore highly turbocharged gas SI ICE while focusing mainly on steady-state operation. Additional goals are the following:

- To test different solutions: e-turbo and e-booster without downstream intercooling.
- To evaluate transient performance of selected variants.
- To perform sensitivity studies of selected parameters.

2. MATHEMATICAL MODEL

Engine model was built in 0-D/1-D SW tool [1] while using previous experience with similar engines [2], [3], [4], [5] and [6]. As the presented work is closely related to the previously published papers [5] and [6], the engine model is in principle the same – however, it was extended/modified to allow for engine transient calculations (this mainly concerns ICE control and some details, e.g., fully transient heat transfer model) and application of e-boosting technologies (e-turbo, e-booster). Main engine parameters are summarized in Table 1. The most important model features are the following. Simplified FE (Finite Element) model is used to calculate combustion chamber temperatures while Woschni formula (c.f. [7]) is applied to estimate the heat

transfer coefficient between the in-cylinder gas and the walls (boundary condition for FE model). All necessary model constants were estimated by the authors – they are based on authors' experience with similar engines in the class of large-bore turbocharged gas IS ICE. Mechanical efficiency was calculated using default GT-Power formula (based on Chen-Flynn model [8]). Concerning combustion model, no experimental data were available. Simple Vibe function model was applied using the experience from a similar engine (c.f. [2], [3], [4]). The combustion duration is constant regardless of engine load, air excess and considered fuel composition – it was verified (by means of detailed sensitivity study) that this assumption has minor influence on optimization of boost group (among others) under steady state operation. Moreover, it is also supported by other literature sources (e.g., [10]) dealing with gas SI ICE equipped with scavenged pre-chamber. Knocking was not considered – however, minimum air excess (depending on engine load) was estimated for CH_4 fuel to avoid this phenomenon. NO_x formation is calculated by means of multi-zone combustion model while using Zeldovich kinetic mechanism [9] – the model constants were carried over from other model(s) of similar engines (e.g., [2], [3], [4]). Moreover, all the previous work (concerning highly turbocharged gas SI ICEs) suggests that such a model (after certain calibration) provides very reasonable values in terms of NO_x formation. That is why the authors are confident that this is the case even under very high load (BMEP above 35 bars).

Parameter	Unit	Value
Bore-to-Stroke Ratio	[-]	0.784
Compression Ratio	[-]	14.0
Engine Speed	[rpm]	1500
Charging		2-stage turbocharged
Combustion concept		Scavenged pre-chamber
Fuel		CNG
Configuration		V20
No. of Intake Valves		2
No. of Exhaust Valves		2
BMEP	[bar]	20-36

Table 1: *Main engine parameters*

Standard turbomachinery maps were provided by turbocharger manufacturer (PBS Turbo) including available ranges of swallowing capacity for each compressor/turbine. Each turbocharger stage has its own intercooler. The total efficiency of the two-stage boost group is above 70%. Inertia of each turbocharger was known as it is important even for steady-state calculations – it is critical for transient ones. Finally, mechanical losses (mainly caused by bearings) were provided as a function of shaft speed for each turbocharger while considering both sliding bearing and ball bearing.

The Figure 1 shows the control layout of the engine. It is a bit simpler when compared with previous work [2], [3], [4] – as one of the conclusions was that EGR technology is less effective for such kind of ICE (it is better to get more air and/or use stronger Miller cycle), hence there are only 3 main control circuits: BMEP, air excess and compressor surge. Regarding the BMEP control logic, there are 6 possibilities (intake throttling, 2 versions of waste-gating, compressor blow-by, e-boosting and VGT), however the VGT

was disregarded after some considerations (high cost with relatively low benefit). Air excess is controlled in such a way that prescribed level of NO_x (recalculated according to TA Luft norm) at exhaust gases is achieved. Dealing with compressor surge, the standard approach was applied by means of by-passing certain amount of compressed cooled air/mixture back to LP compressor inlet.

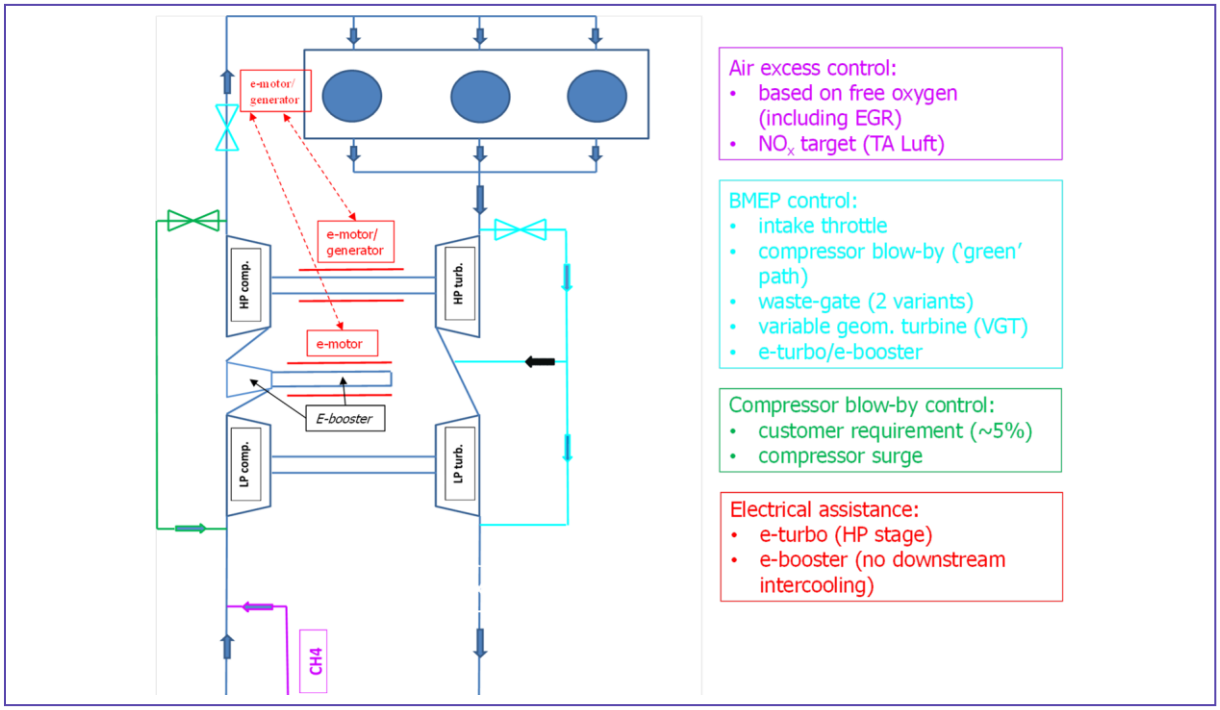

Figure 1: *Engine layout including main control circuits*

The electrically assisted boosting variants are based on concepts/approaches of e-turbo and e-booster – the e-turbo represents a classical turbocharger equipped with e-motor, which can work as e-generator as well – it can be called as electrically assisted turbocharger and, in this paper, only HP stage is considered as e-turbo. Other possibility is the e-booster which is an additional compressor powered by e-motor. The position/location of e-booster (in the boost systems) can be varied – after discussion with PBS Turbo, it was decided to position it between LP and HP stage while no intercooler is applied downstream of e-booster (hence it increases HP compressor inlet temperature). The reason behind this decision is the fact that intercoolers are large, heavy and expensive devices while the e-booster is supposed to help only 'slightly' in terms of boost pressure level (the majority of compression work is expected to be performed by the 2-stage turbocharger group) to avoid a major redesign of a boost system layout.
There are additional control circuits to adjust intercooler properties (pressure loss, cooling efficiency) to achieve target values – in other words, using the 'right' inter-cooler size/design for each engine operating conditions (which may vary significantly in terms of BMEP, air excess, fuel composition). Similar approach was used for low-pressure exhaust manifold to get reasonable pressure losses.

3. COMPUTED CASES

The presented data are focused on steady-state performance of the target engine (c.f. Table 1) under different operating conditions – this usually concerns engine load and NO_x level (defined by German norm TA Luft). Each operating point is fully optimized by means of genetic algorithm while varying 9 parameters (combustion phasing (1), sizes of all turbomachinery (4), timing of intake/exhaust valve opening/closing events (4)) to minimize BSFC while satisfying many constrains. Each point in the graphs (e.g. Figure 2) corresponds to a different engine (due to different valve timing events) with different turbochargers. The base/standard variant for comparison is based on the classical throttle control (no electrical assistance), which was presented (among others) in [5] – this variant is usually labelled as 'cont_THROTTLE' in the figures while the e-turbo uses 'cont_eTurbo' and e-booster is labelled 'cont_e-BOOSTER'.
The following effects are presented in the paper:

- Influence of NO_x level for the case of e-turbo application while being compared with the base variant.
- Effect of e-turbo for varying load with fixed ICE design parameters.
- Potential of e-booster application without downstream cooling.
- Transient response.

4. DISCUSSION OF RESULTS

This section presents selected results, which were obtained during TA CR NCK II project BOVENAC, while focusing on electrically assisted turbocharging for the case of 2-stage turbocharged large-bore gas SI ICE (it should be stressed that the engine is operated under constant NO_x level, which is a significant difference when compared with automotive applications). As it is mentioned in the previous section, 2 different approaches of electrically assisted turbocharging are considered: e-turbo (at HP stage) and e-booster (between LP and HP stage, without intercooling). Due to limited scope of the paper, only the most important aspects are commented.

4.1 Influence of NO_x Level for the Case of E-Turbo Application

The large-bore gas engines are usually operated at constant NO_x level to satisfy certain requirements. Typically, the German norm called TA Luft is applied and its base level is labelled as 'TA_Luft=100%'. However, the norm is relatively old, hence more strict NO_x level are required – e.g., 'TA_Luft=20%' represents a case when NO_x level is 5-times lower when compared with the base value. The comparison of a standard engine control (using throttle) with e-turbo while varying NO_x level (from 100% down to 5% of base TA Luft) is presented in Figure 2 while showing BSFC and air excess for fully optimized engine setting. It should be stressed that each point (in the Figure 2) is optimized independently, hence each point represents a different engine.

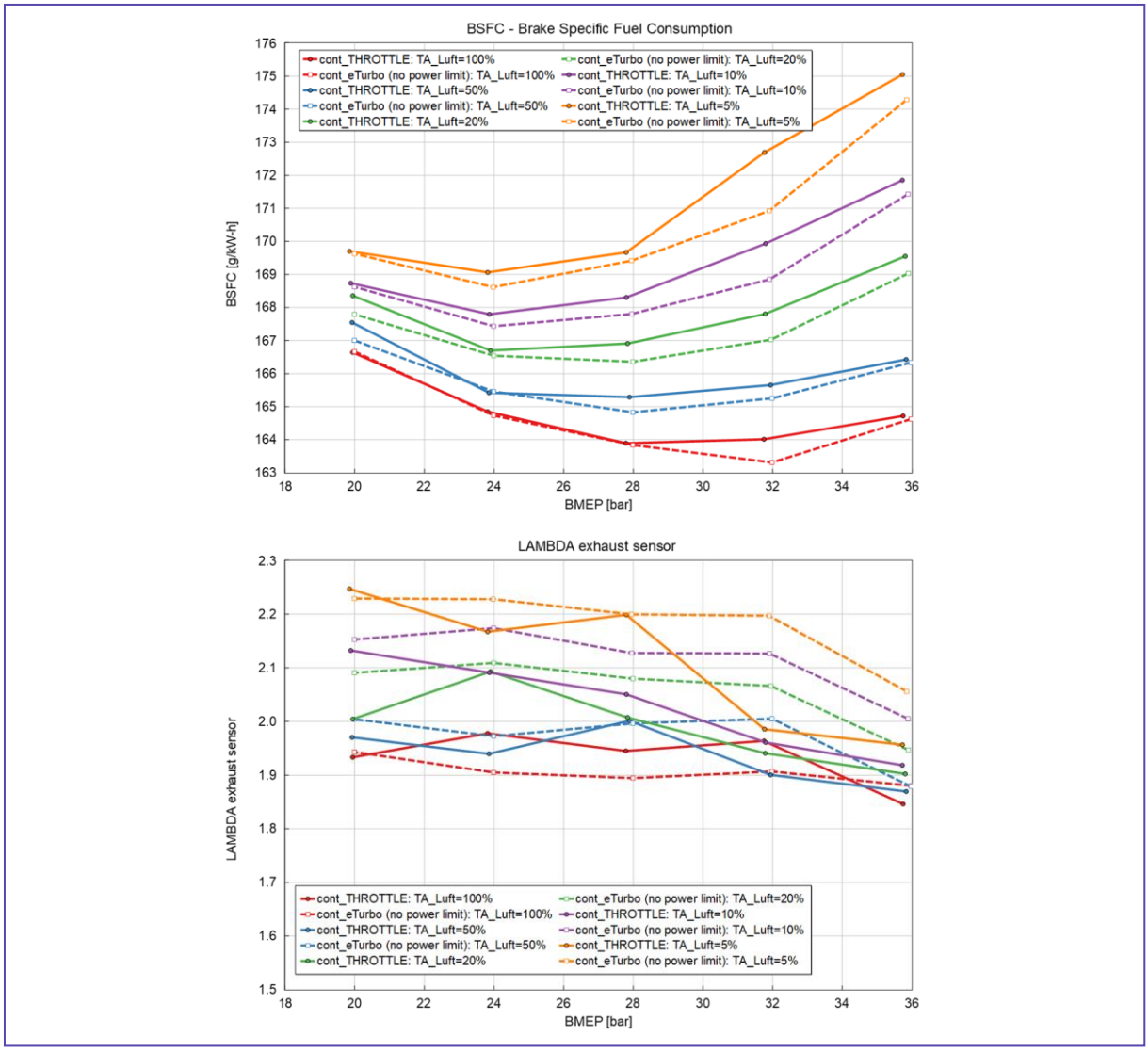

Figure 2: *Comparison of base variant (throttle; continuous line) with e-turbo (dashed line) under different engine loads (BMEP) and different NO_x levels (defined by TA Luft multiplier) – engine fuel consumption (top sub-figure) and engine air excess (bottom sub-figure)*

When comparing BSFC (top subfigure in Figure 2), the application of e-turbo makes sense only under high engine load or low NO_x level while the potential (to improve BSFC) is typically between 0.5-1.0 g/kW/h. The trend is logical: the higher the required boost pressure, the higher the potential of e-turbo application. Under relatively low load (typically below 24 bar of BMEP), there is usually no BSFC improvement. When load is increased, the BSFC improvement increases as well while the best e-turbo performance is at BMEP of 32 bar. Additional increase of engine load does not yield the expected BSFC improvement – on the contrary, the BSFC curves get closer, thus suggesting that required boost pressure is too high and it could be achieved only at cost of additional BSFC penalty. The BSFC diagram confirms that the best engine efficiency can be achieve for BMEP between 24 and 32 bars, hence confirming again that pure focus on ICE downsizing is not the best solution – engine rightsizing is the right solution. Moreover, the diagram shows that the lower the NO_x level (hence, the higher the boost pressure), the lower the optimal BMEP level. This trend was expected

as the 2-stage boost group has its optimal performance within certain pressure levels (6-8 bars of boost pressure) – when operated below/above these values, engine gas exchange requires more piston work, thus leading to increased BSFC.

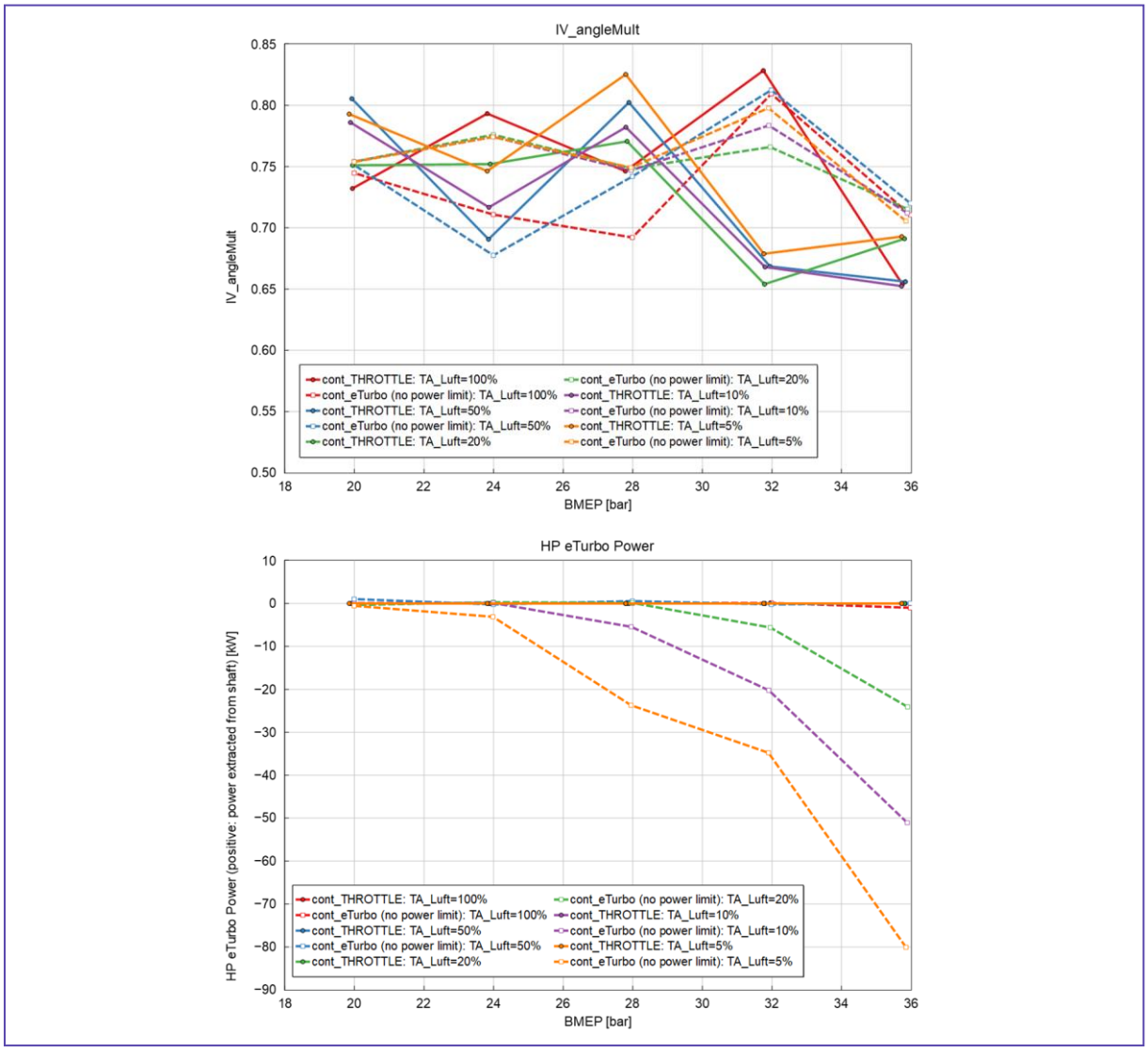

Figure 3: *Comparison of base variant (throttle; continuous line) with e-turbo (dashed line) under different engine loads (BMEP) and different NO_x levels (defined by TA Luft multiplier) – intake valve width multiplier (top sub-figure) and HP turbine electrical power assistance (bottom sub-figure)*

The optimal value of air excess is plotted in bottom subfigure of Figure 2. The e-turbo variants usually operate under higher air excess as they can achieve slightly higher boost pressure more effectively (when compared with the base variant). This allows for more optimal combustion phasing and weaker Miller (top subfigure in Figure 3) cycle to satisfy required NO_x level. All that helps BSFC, as it is described above. All the optimizations were unrestricted in terms of electrical assistance power – the optimal value is plotted in bottom subfigure of the Figure 3. All the optimal values are below 100 kW, which is a reasonable value (this was discussed with the experts in PBS Turbo).

Concerning boost group performance, the e-turbo variant has usually slightly larger HP compressor and slightly smaller LP compressor while the same applies to turbine sizes

– this leads to lower HP stage speed and higher LP stage speed. Exhaust valve size becomes a limiting factor (especially for the base variant) under high mass-flow rate conditions.

4.2 Effect of E-Turbo for Varying Load with Fixed ICE Design Parameters

The previous sub-section (4.1) deals with thermodynamic potential of e-turbo (comparing with the base variant) under different load and NO_x level, hence each point in the diagrams represents different engine setting (i.e., different valve opening/closing events, different turbochargers, different combustion phasing). This sub-section (4.2) shows comparison of e-turbo vs. base variant while using fixed engine setting (which was optimized for BMEP of 24 bar for each variant under constant NO_x level of TA Luft=100%) – this means that the whole curve represents a particular engine (operated under different conditions). Moreover, the effect of limited e-turbo power is presented as well while considering 20, 50 and 100 kW as max. allowed electrical power to assist the e-turbo. All that is shown in Figure 4.

As presented in the previous section, there is almost no difference in terms of BSFC between the base variant and the e-turbo one at nominal BMEP (of 24 bars). However, if higher engine power is required, the e-turbo could provide higher boost pressure (when compared with the base variant), hence higher power/BMEP – but it is not massively higher, moreover there is surprisingly small effect when comparing different max. power levels of electrical assistance. The main reason behind that is the LP compressor performance – the operating points are out of optimal efficiency region and close to the stall/choke line. And it is clear from the figure that higher BMEP/power output is achieved with significantly higher BSFC.

When decreasing engine load, the e-turbo is slightly more efficient (top subfigure in Figure 4) – the BSFC improvement potential is usually below 0.5 g/kW/h. This is mainly caused by the possibility to recuperate small amount of HP turbine power (bottom subfigure in Figure 4), which is more effective/efficient when compared with throttling control. However, this is not a general trend/observation – there are cases where there is almost no difference (between e-turbo and the base variant). Finally, when using waste-gating of HP stage only, the efficiency is very similar to what could be achieve with e-turbo. Obviously, the e-turbo variant is much faster during a transient load change, which is discussed below in the subsection 4.4.

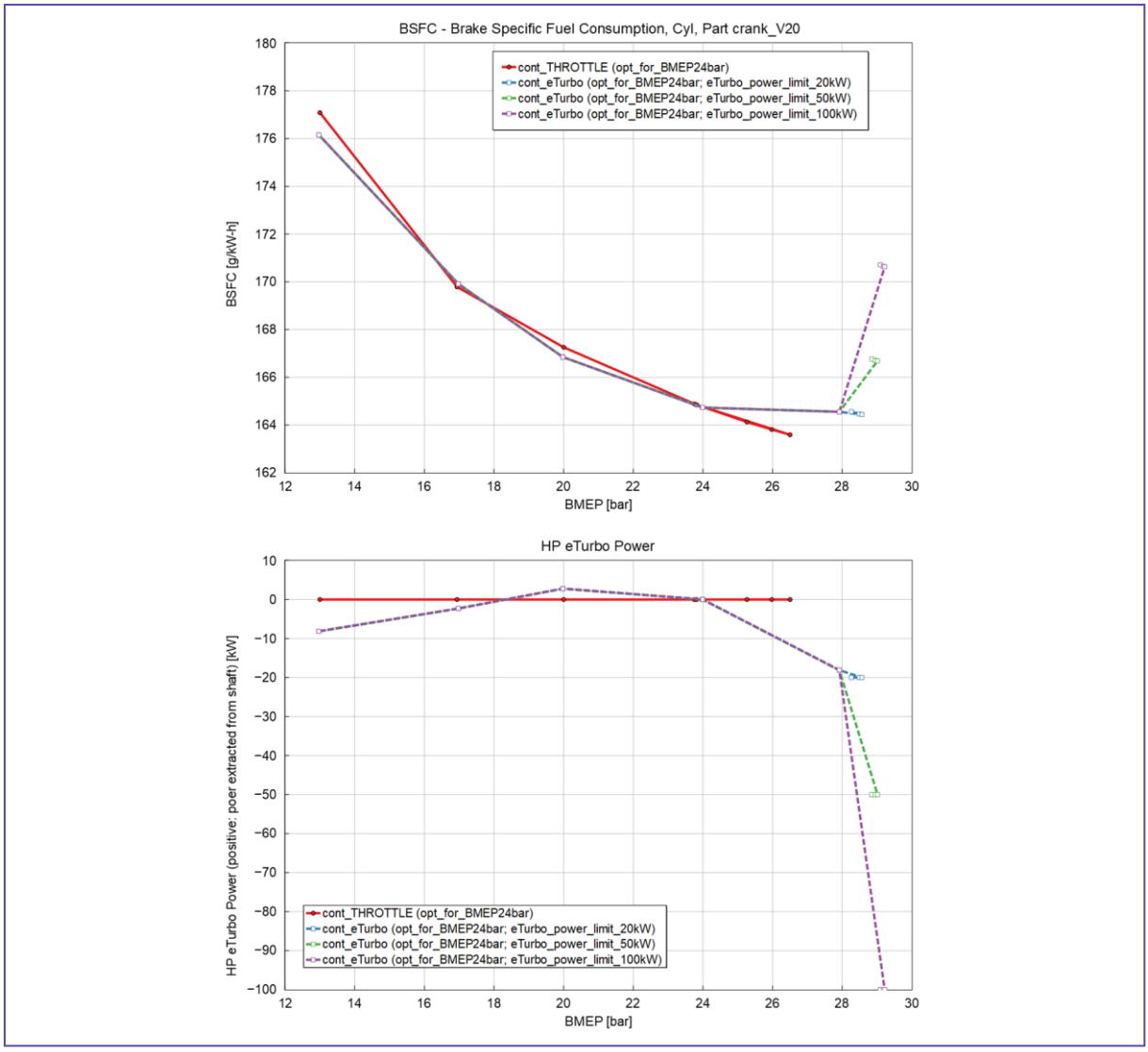

Figure 4: *Comparison of base variant (throttle; continuous line) with e-turbo (dashed line) under different engine loads (BMEP) with fixed engine setting while considering different power limits of electrical assistance – engine fuel consumption (top sub-figure) and HP turbine electrical power assistance (bottom sub-figure)*

4.3 Potential of E-Booster Application without Downstream Cooling

This section is focused on potential of e-booster application on the target engine. The e-booster is supposed to be located between LP and HP turbochargers and no intercooling (directly downstream of the e-booster) is considered – the reasons behind that are based on the packaging and price considerations. As the qualitative trends of important parameters are similar to those presented in section 4.1, only the selected diagrams are shown in the following text while considering the base variant, the e-turbo one and the e-booster one – c.f. Figure 5.

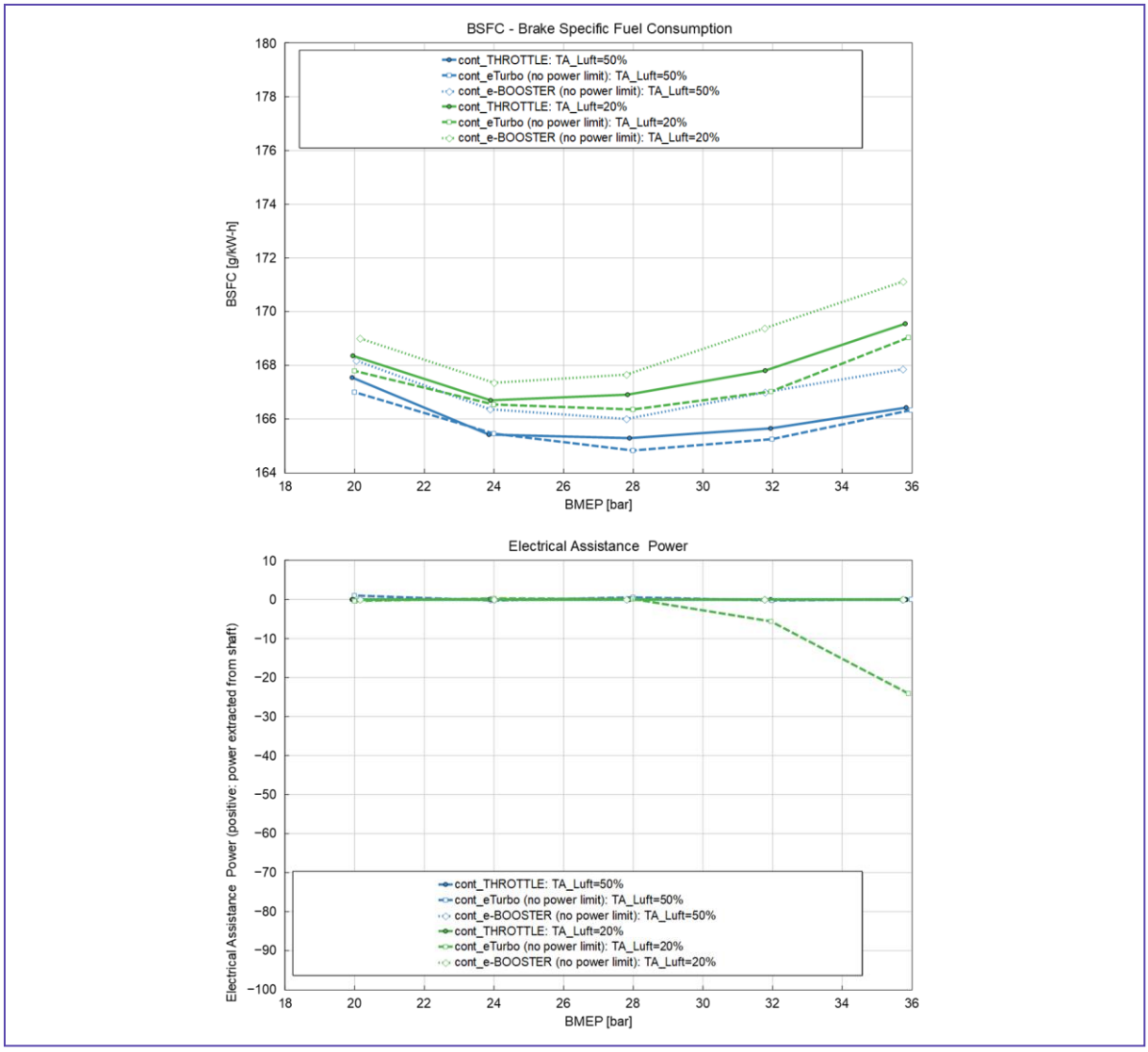

Figure 5: *Comparison of base variant (throttle; continuous line) with e-turbo (dashed line) and with e-booster (dotted line) under different engine loads (BMEP) and different NO_x levels (defined by TA Luft multiplier) – engine fuel consumption (top sub-figure) and electrical assistance power (bottom sub-figure)*

The main conclusion from Figure 5 is that application of the e-booster does not bring any BSFC improvement (c.f. top subfigure in Figure 5) – on the contrary, the BSFC is always higher regardless of engine load or NO_x level while comparing with either the base variant or e-turbo one. This is caused by 2 main factors – additional pressure loss in the intake pipe system and no intercooling (downstream of e-booster), which increases HP compressor power requirement. These 2 factors create such a significant disadvantage that the optimized solutions try to avoid the e-booster engagement as much as possible. Hence, the main benefit of e-booster application is related to improved transient performance when compared with the base variant – c.f. subsection 4.4.

4.4 Transient Response

Transient performance of the target engine is discussed in this subsection. As presented above in the previous sub-sections, the steady-state operation of the engine has relatively small potential (if any) in terms of engine efficiency improvement. This is in-line with previous research of the authors while focusing on automotive application(s) – c.f. [11]. However, the situation is different when transient performance is considered – c.f. Figure 6 and Figure 7 where the base variant is compared with e-turbo while considering 3 limits of electrical power assistance (20, 50 and 100 kW).

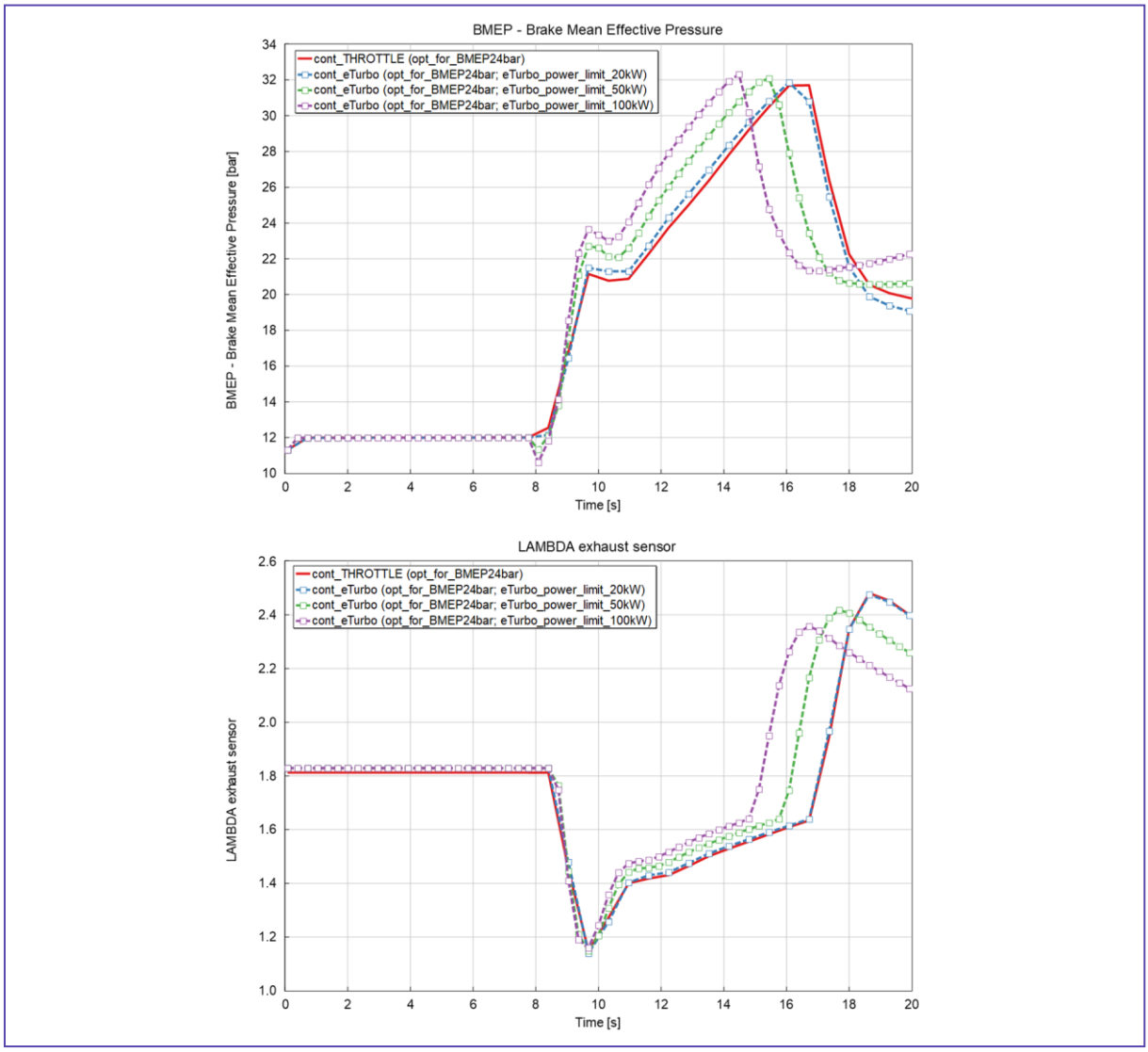

Figure 6: *Comparison of base variant (throttle; continuous line) with e-turbo (dashed line) during transient load change (at constant engine speed) with fixed engine setting (optimized for BMEP of 24 bars and TA Luft of 100%) while considering different power limits of electrical assistance – BMEP (top sub-figure) and air excess (bottom sub-figure)*

The transient is defined as engine load change from 12 bars of BMEP to 32 bars – c.f. top subfigure in Figure 6 (the same definition is used in [6]), the load change starts at time of 8 seconds. When considering only 20 kW of electrical assistance, the transient duration is only very slightly faster when compared with the base variant (without any electrical assistance). However, when using 50 or 100 kW, the load change is clearly

faster (1 and 2 seconds, respectively), thus showing clear benefit, which could be critical for specific applications. Other important parameters are shown in Figure 6 and Figure 7 – the effect of electrical assistance is most visible on HP turbocharger speed (top subfigure in Figure 7).

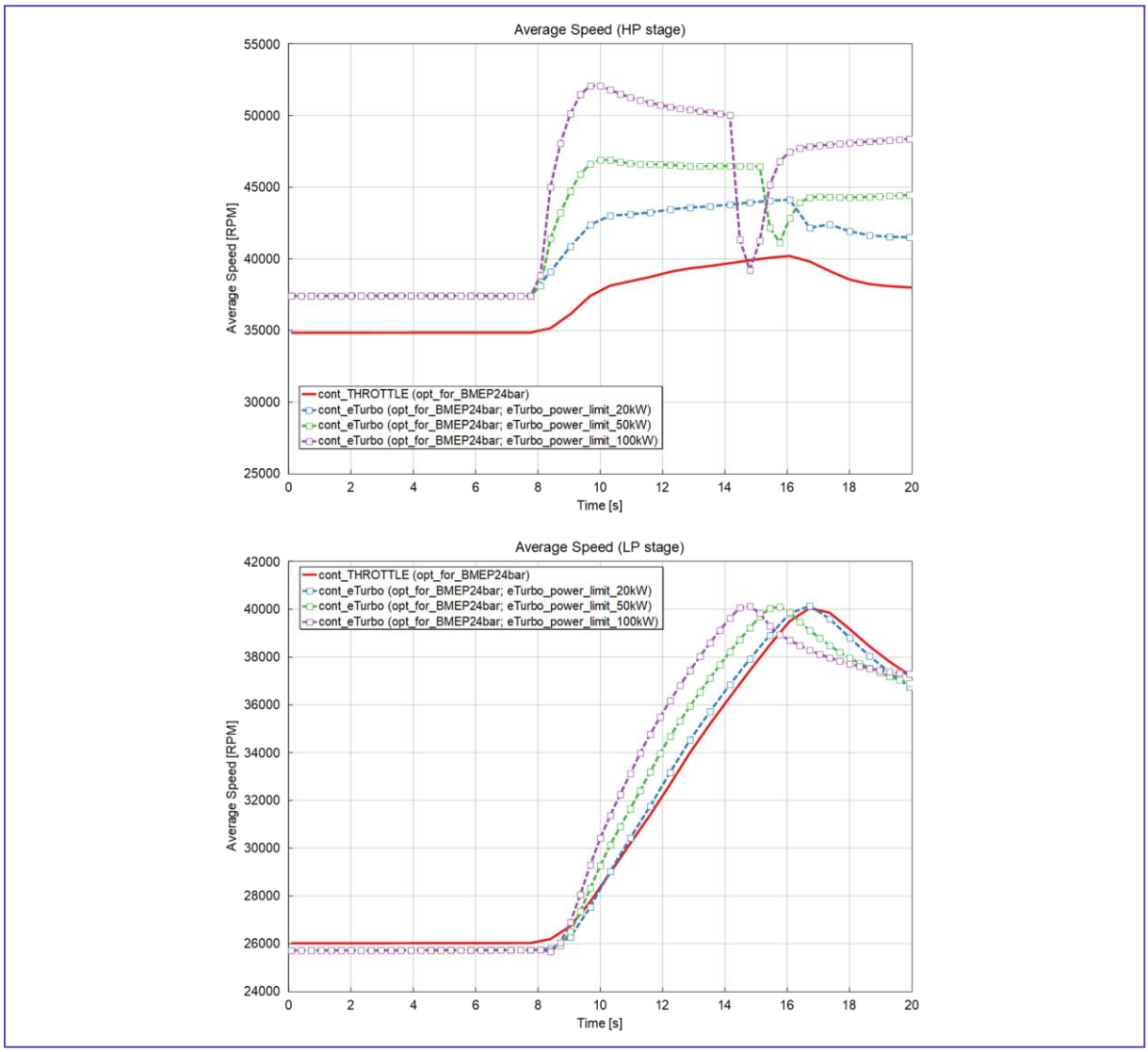

Figure 7: *Comparison of base variant (throttle; continuous line) with e-turbo (dashed line) during transient load change (at constant engine speed) with fixed engine setting (optimized for BMEP of 24 bars and TA Luft of 100%) while considering different power limits of electrical assistance – HP turbocharger speed (top sub-figure) and LP turbocharger speed (bottom sub-figure)*

Comparison of e-booster with e-turbo and the base variant is presented in Figure 8 (engine setting is optimized for different conditions when compared with Figure 6 and Figure 7 – Figure 8 corresponds to optimized setting for TA Luft=20% while Figure 6 and Figure 7 for TA Luft=100%). The e-booster variant is clearly faster than the base one (by 2 seconds), however it is slower than the e-turbo one (by 1 second). The reasons behind the fact that e-turbo is faster than e-booster are (again) additional pressure loss of intake pipe system and increased HP compressor inlet temperature – HP turbocharger speed (bottom subfigure in Figure 8) is actually very similar (in terms

of its time increase) to the base variant, thus confirming that increase of boost pressure (hence, BMEP) is primarily driven by e-booster.

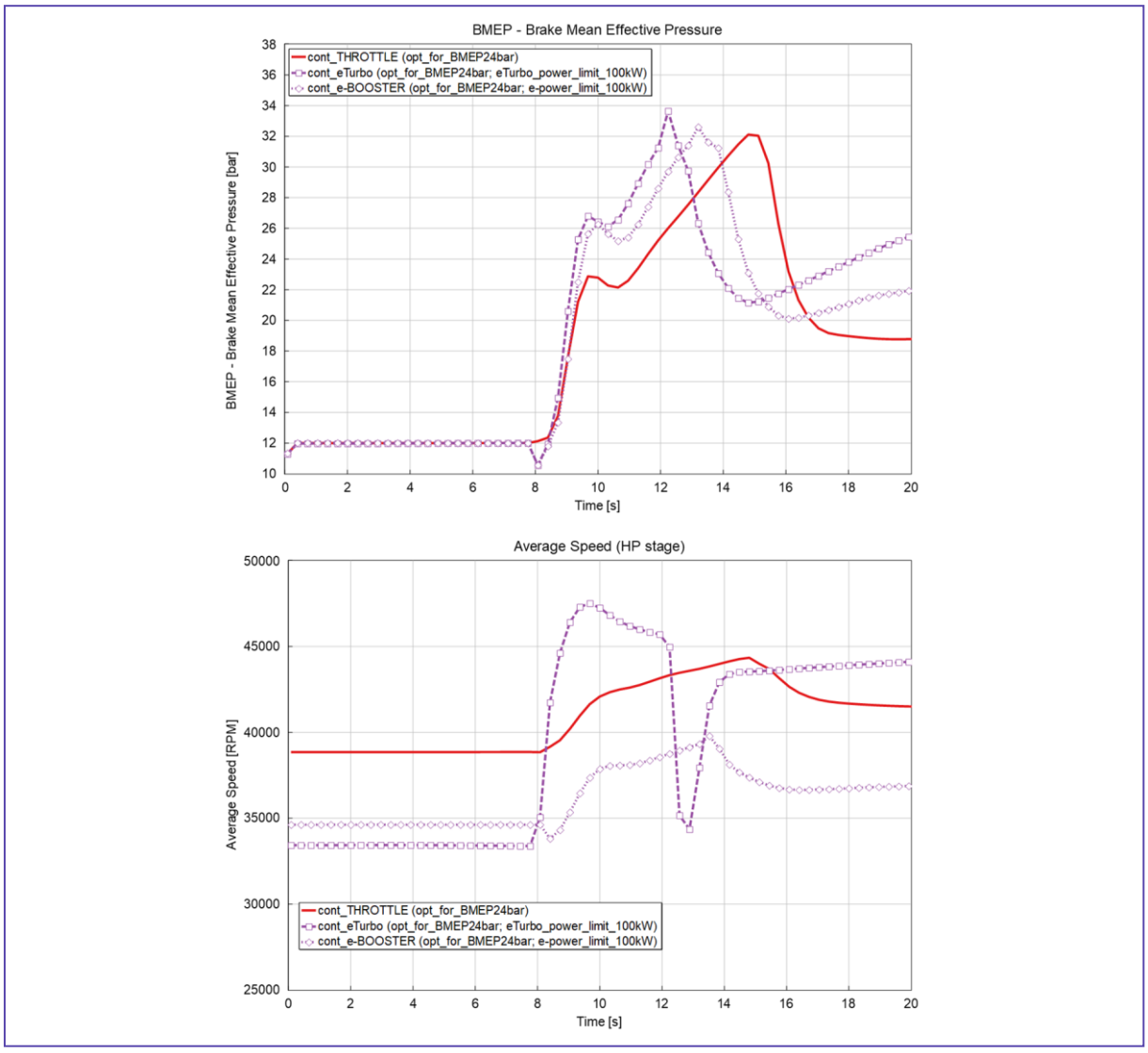

Figure 8: *Comparison of base variant (throttle; continuous line) with e-turbo (dashed line) during transient load change (at constant engine speed) with fixed engine setting (optimized for BMEP of 24 bars and TA Luft of 20%) while considering different power limits of electrical assistance – BMEP (top sub-figure) and HP turbocharger speed (bottom sub-figure)*

5. CONCLUSION

The paper deals with application of electrically assisted turbocharging for the case of 2-stage turbocharged large-bore gas SI ICE operated under constant engine speed, varying load and constant NO_x level (defined by TA Luft norm) – the results were obtained by means of 0-D/1-D CFD calculations/optimizations. Dealing with electrical assistance of the boost group, 2 options were considered – electrically assisted HP turbocharger and e-booster (without downstream intercooling) located between HP and LP turbocharger. Both steady-state operation and transient one were considered.

The presented research work is based on previous experience (c.f. [2], [3], [4], [5] and [6]) and it could be considered as its extension in the field of electrically assisted turbocharging.
The main conclusion is that there is a limited potential to improve engine efficiency (i.e., decrease BSFC) under steady state operation when compared with the base variant (throttling is used to control BMEP) – this could be achieved for e-turbo only as selected e-booster configuration has 2 clear disadvantages (additional pressure loss in the intake pipe system and increased HP compressor inlet temperature). Moreover, the potential BSFC decrease is typically small (below 0.5 g/kW/h) and it could be achieved under very high boost pressure operation only.
On the other hand, transient performance is clearly faster even if the power of electrical assistance is limited to low values (below 100 kW) – this is the main advantage of considered solutions of electrically assisted turbocharging. Under suitable conditions, there are other 'small' benefits – low BMEP operation could be improved in terms of BSFC and if needed, max. engine BMEP could be increased, however it should be stressed that these improvements are relatively small. The e-turbo variant is more efficient when compared with the e-booster solution – on the other hand, e-turbo is much more expensive while e-booster could be used/applied as 'add-on' to existing installations and being activated only when needed.
The final conclusion is that electrically assisted turbocharging enables to optimize the boost group purely for steady state operation, which could yield small BSFC benefits, while transient operation is significantly faster (when compared with the 'classical' solution without any assistance). This statement is in-line with [11], which is focused on automotive application(s).

REFERENCES

[1] GT-Power User's Manual, *GT-Suite version v2022*. Gamma Technologies Inc., 2022.

[2] Vitek, O., Macek, J. *Steady State Performance of Large Bore Engine,* In: Proceedings of KoKa 2014*, ISBN 978-80-7375-801-1*.

[3] Vitek, O., Macek, J. *Transient Performance of Large Bore Engine*, In: Proceedings of KoKa 2015, ISBN 978-80-227-4424-9.

[4] Vitek, O., Macek, J. *Engine Performance Comparison of 2-stage Boost Group with Single-stage One*, In: Proceedings of KoKa 2016, ISBN 978-80-214-5379-1.

[5] Vitek, O., Macek, J., Klima, J., Vacek, M. *Two-stage Turbocharged Large-Bore Gas SI ICE – Operation under Different NOx Level Conditions*, In: Proceedings of KoKa 2020, ISBN 978-80-01-06744-4.

[6] Vitek, O., Macek, J., Mares, B., Klima, J., Vacek, M. *Two-stage Turbocharged Large-bore SI ICE – Transient Operation under Different Conditions*, In: Proceedings of KoKa 2023, ISBN 978-80-214-6164-2.

[7] Woschni, G. An *Universally Applicable Equation for the Instantaneous Heat Transfer Coefficient in the Internal Combustion Engine*. SAE Transactions, Vol. 76:3065, 1967.

[8] Chen, S, Flynn, P. *Development of a Single Cylinder Compression Ignition Research Engine*. SAE Technical Paper Series. Paper 650733.

[9] Zeldovich, Y. B. *The Oxidation of Nitrogen in Combustion and Explosions*. In: Acta Physicochim, USSR, 21:557–628, 1946.

[10] Wimmer, A., Pirker, G., Zelenka, J., Chmela, F., Zurlo, J., and Trapp, C. *The Potential of Exhaust Gas Recirculation in Large Gas Engines*. Proceedings: Conseil International Des Machines A Combustion (CIMAC) Congress 2013, Shanghai, May 2013. Paper No.: 271.
[11] Vitek O., Macek J. *Thermodynamic Potential of Electrical Turbocharging for the Case of Small Passenger Car ICE under Steady Operation*. SAE Technical Paper 2017-01-0526, ISSN: 01487191, DOI: 10.4271/2017-01-0526

LIST OF ABBREVIATIONS

BMEP	brake mean effective pressure
EGR	exhaust gas recirculation
FE	finite element
HP	high pressure
ICE	internal combustion engine
IVC	intake valve closing
LP	low pressure
NO_x	nitride oxides (NO, NO_2, N_2O)
SI	spark ignition/ignited
TA CR	technology Agency of the Czech Republic
TA Luft	German norm to define and to limit NO_x level in exhaust gases
TDC	top dead centre
VGT	variable geometry turbine

ACKNOWLEDGEMENT

This research has been realized using the support of Technological Agency, Czech Republic, Technological Agency, Czech Republic, programme National Competence Centres II, project # TN02000054 Božek Vehicle Engineering National Center of Competence (BOVENAC).

55. mezinárodní vědecká konference zaměřená na výzkumné a výukové metody v oblasti vozidel a jejich pohonů

září 5. - 6., 2024 – Liberec, Česká republika
Technická univerzita v Liberci
Fakulta strojní, Katedra vozidel a motorů

OPTIMALIZACE RÁMOVÝCH KONSTRUKCÍ ZA POUŽITÍ PROGRAMU MODEFRONTIER

Tomáš Pánek[1], Michal Vašíček[2], Gabriela Achtenová[3]

Abstrakt
Cílem této práce je optimalizovat konstrukci rámu s využitím sofistikovaného softwarového nástroje ModeFrontier. ModeFrontier je integrační platforma pro více cílovou optimalizaci, která umožňuje efektivní kombinaci různých inženýrských simulací a optimalizačních algoritmů. Proces optimalizace zahrnuje definování geometrických parametrů rámu, mechanických vlastností materiálů a zatížení, kterým bude rám vystaven. Pomocí parametrických studií a automatizovaných iterací ModeFrontier umožňuje najít optimální konfiguraci rámu, která minimalizuje hmotnost a maximalizuje pevnost a tuhost. Výsledky této optimalizace ukazují na značné zlepšení mechanických vlastností rámu při zachování nebo snížení jeho hmotnosti, což přináší významné úspory materiálů a nákladů. Práce rovněž demonstruje výhody využití ModeFrontier pro komplexní inženýrské problémy a jeho schopnost integrovat různé simulační nástroje a optimalizační techniky do jednoho procesu.
Klíčová slova: optimalizace, rám, hmotnost, tuhost, životnost

[1] Ing. Tomáš Pánek, ČVUT Praha, Technická 4, Praha, tomas.panek@fs.cvut.cz
[2] Ing. Michal Vašíček, Ph.D., ČVUT Praha, Technická 4, Praha, michal.vasicek@cvut.cz
[3] doc. Dr. Ing. Gabriela Achtenová, ČVUT Praha, Technická 4, Praha, gabriela.achtenova@fs.cvut.cz

1. ÚVOD

Tento článek se zabývá tvorbou nástroje pro parametrizaci nosníků a následnou optimalizaci rámových konstrukcí pomocí 1D elementů, které ve 3D prostoru substituují 2D, nebo 3D geometrii nosníků.

Samotná optimalizace je tvořena v numerickém programu ModeFrontier za využití jeho optimalizačních a statistických nástrojů.

Cílem této metodiky je časová a finanční úspora při tvorbě rámových konstrukcí. Tohoto je dosaženo zejména absencí prvotní 3D geometrie. Díky využití numerického programu dochází ke zrychlení výpočetního času. To má za následek zlevnění celého procesu díky možnosti nižšího počtu pracovníků a možnosti výpočtu bez použití výpočetního serveru.

Vzhledem ke stále se zvyšujícím nárokům trhu a tlaku na udržitelnost, úspory a zachování konkurenceschopnosti, je toto téma velmi poplatné dnešní době.

2. METODOLOGIE

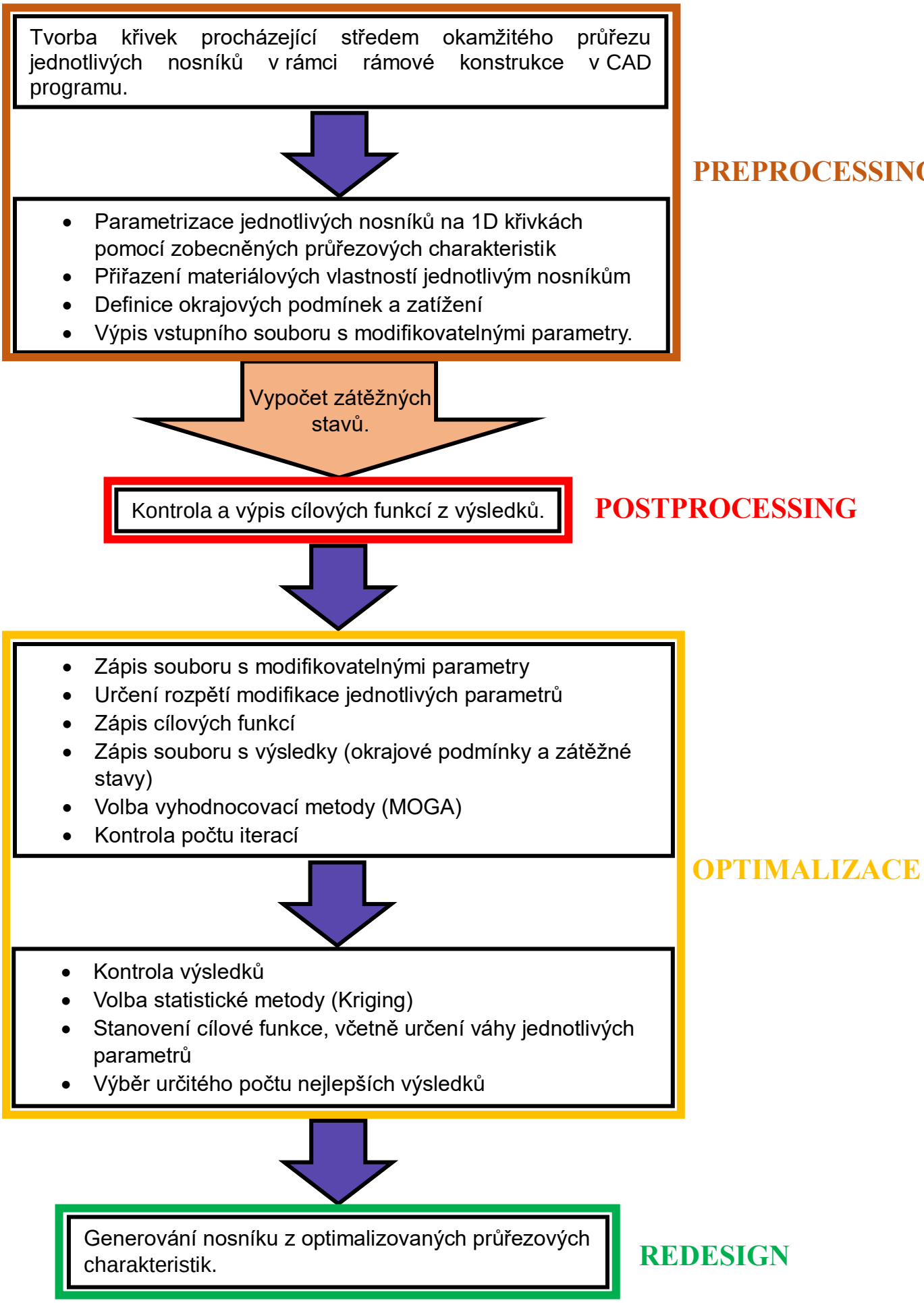

2.1. Preprocessing

2.1.1. Stavba modelu

Proces začíná stavbou křivkového modelu z 1D křivek ve 3D prostoru. Může jít o spojování uzlových bodů v nějakém omezeném zástavbovém prostoru, či se používá již stávající konstrukce a dochází pouze k vytažení křivek ze středů okamžitých průřezů nosníků. [1] [2]

Při tvorbě modelu je nezbytné, aby CAD program, ve kterém je model tvořen, podporoval beziérové modelování, tedy B-Spline. Použití T-Spline je problematické pro další zpracování v MKP programu. [1] [2]

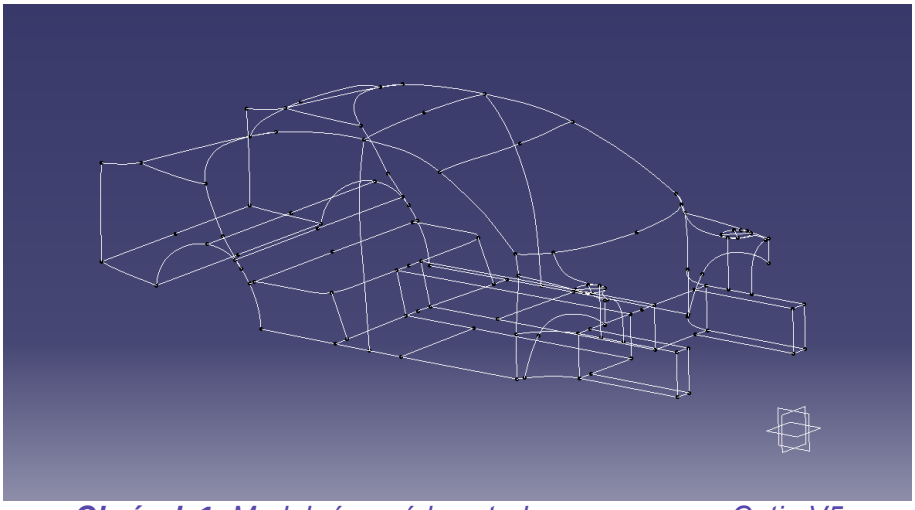

***Obrázek 1**: Model rámové konstrukce v programu Catia V5*

2.1.2. Parametrizace modelu

V prostředí Abaqusu CAE jsou jednotlivým křivkám přiřazeny zobecněné průřezové charakteristiky, které odpovídají základnímu stavu průřezu nosníku. Tyto zobecněné průřezové charakteristiky jsou dále parametry, které je možno v určitých mezích upravovat tak, aby byl zachován profil, ale došlo k jeho modifikaci v závislosti na zatížení. [1] [3] [4]

Dále jsou nosníky pokryty 1D elementy. Zde je vhodné volit větší hustotu sítě, aby bylo získáno dostatečné množství uzlových bodů pro cílové funkce. Výsledkem je parametrický model, který je připraven pro optimalizaci. [1] [3]

2.1.3. Okrajové podmínky a zátěžné stavy

Aby bylo možné sledovat chování rámové konstrukce, je zapotřebí dodat modelu okrajové podmínky a zátěžné stavy. Co se okrajových podmínek a zátěžných stavů týče, primárním cílem je optimalizace na tuhost a životnost, nicméně je v omezené míře možné pozorovat také plasticitu, a to jak u statických, tak dynamických výpočtů. V případě 1D element se toto omezení vztahuje výhradně na osový tah a tlak. [1] [3]

Co se týče cílových funkcí, nástroj je vyvíjen primárně na použití pro kontrolu posuvů, jejichž minimalizací v určitých bodech může dojít ke zvýšení tuhosti konstrukce, optimalizace hmotnosti a kontroly napětí. [1] [3] [4] [5]

Takto připravený model je pomocí datasetu *.inp* v programu Abaqus CAE exportován do textové podoby a dále řešen řešičem Abaqus, zpravidla jako úloha lineární statiky. [1] [3]

2.2. Výpočet zátěžných stavů

Prostřednictvím řešiče dojde na základě zátěžných stavů ke spočítání modelu. V případě zkušebního výpočtu se jednalo o lineární statiku řešenou implicitní metodou. [1] [3]

Co se týče samotných zátěžných stavů a okrajových podmínek, tak pro daný model bylo zvoleno zatěžování jak ohybem, tak krutem. [1] [3] [4] [5]

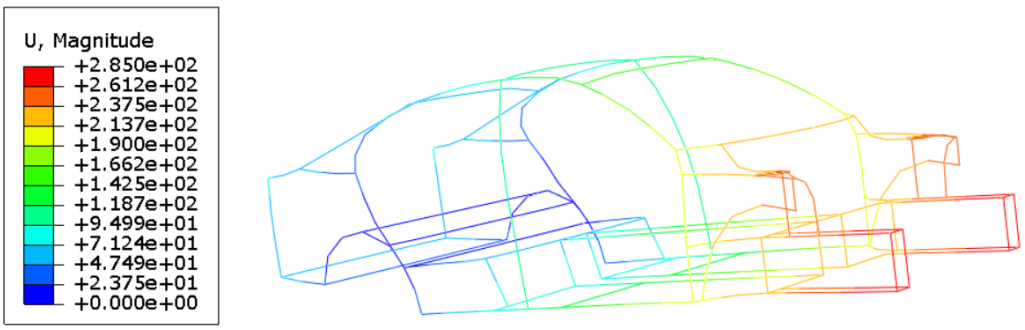

***Obrázek 2**: Zatěžování ohybem s vyobrazením výslednic posuvů*

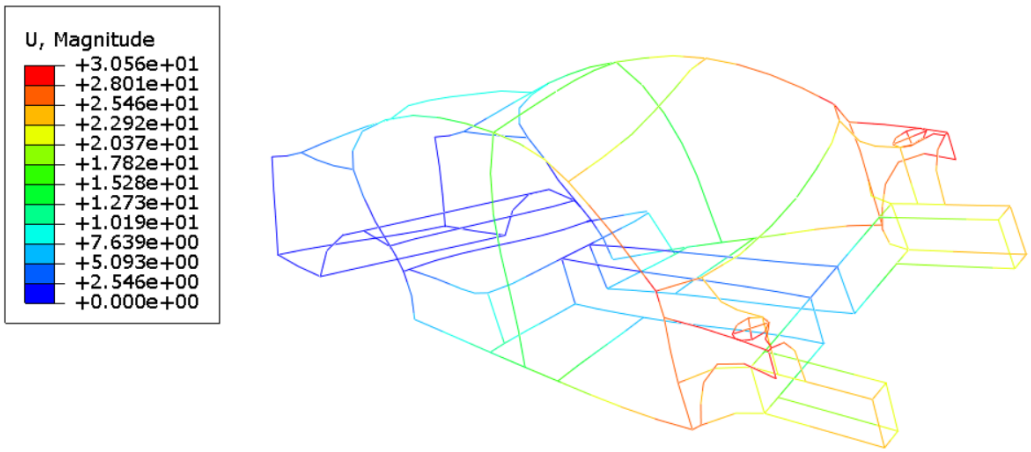

***Obrázek 3**: Zatěžování krutem s vyobrazením výslednic posuvů*

2.3. Postprocessing

V rámci postprocessingu dochází ke kontrole vypočtených dat, okrajových podmínek a zátěžných stavů. Je také vhodné zkontrolovat celistvost modelu, jelikož kolize a nespojitost je v programu Abaqus CAE velmi těžko rozeznatelná v rámci preprocessingu. K tomuto úkonu je možné využít preprocessing ANSA, který nabízí širokou škálu kontrol a úprav modelu. [1] [3]

V tomto kroku je nezbytné vypsat cílové funkce, na které bude optimalizace zaměřena. [1] [3]

2.4. Optimalizace

Optimalizace je prováděna za účelem zlepšení cílových vlastností konstrukce, konkrétně zvýšení její tuhost, pevnosti, optimalizace kritických frekvencí a životnosti. ModeFrontier je pokročilý optimalizační numerický software, který umožňuje integraci s výsledky z řešiče Abaqus, se kterými je schopen provádět parametrické studie. [1]

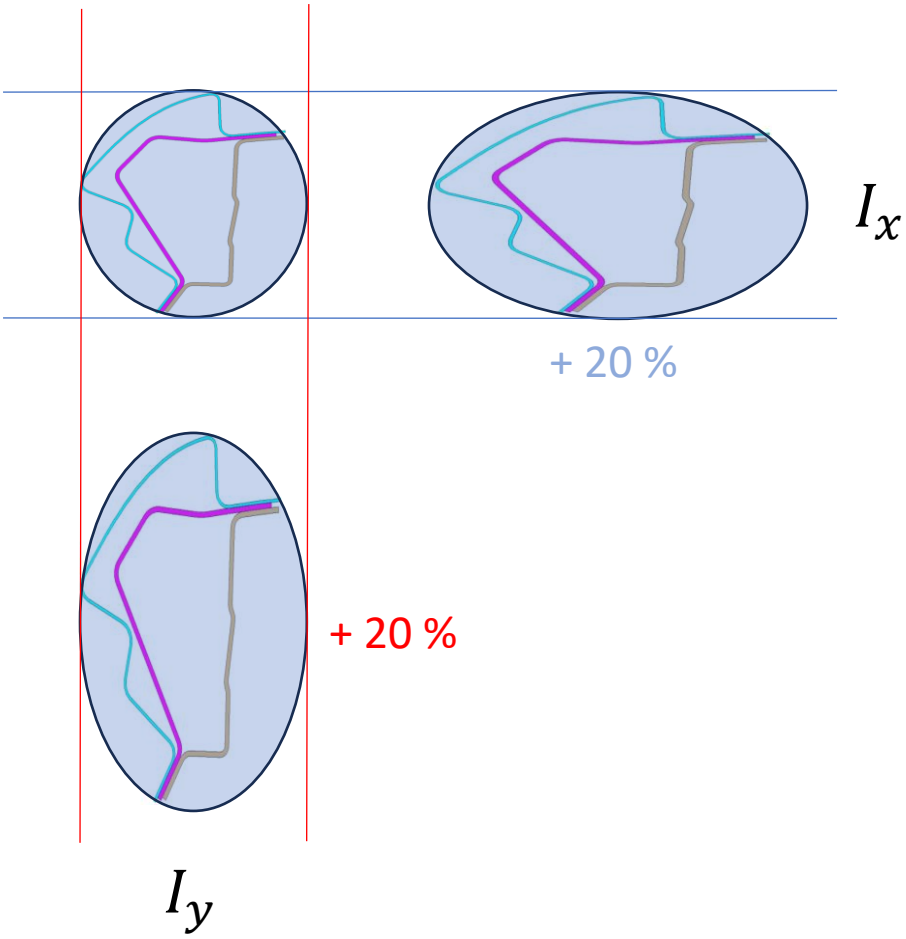

***Obrázek 4**: Schéma vyobrazující modifikaci průřezové charakteristiky nosníku*

2.4.1. Definování cílů a omezení

Prvním krokem je definování cílové funkce optimalizace, například minimalizace posuvu v některém uzlu konstrukce za účelem zvýšení její tuhosti. Dále jsou stanovena omezení, která zahrnují oblast, ve které se mohou pohybovat jednotlivé zobecněné průřezové charakteristiky, tedy setrvačné momenty vůči osám *x*, *y* a *z*, deviační moment *J* a okamžitý průřez nosníku *A*. [1]

2.4.2. Vytvoření optimalizačního diagramu

V ModeFrontieru je vytvořen optimalizační diagram, který zahrnuje generování různých variant modelu se zaměřením na cílovou funkci. [1]

2.4.3. Spuštění optimalizace

ModeFrontier nabízí řadu vyhodnocovacích metod, které mohou uživatelé využít k analýze a optimalizaci svých modelů. Jednou z hlavních je Multi-Objective Optimization, která provádí optimalizaci několik cílových funkcí současně. Často je tak

řešeno metodou Pareto front, které pomáhají identifikovat nejlepší kompromisní řešení. [1]

Nástroj v rámci Multi-Objective Optimization užitý pro tvorbu práce, na kterou odkazuje tento článek je Multi-Objective Genetic Algorithm (MOGA). V rámci tohoto nástroje jsou výsledky řešeny pomocí již zmíněných Pareto front a dále pak vyhodnocovány na cílovou funkci pomocí pokročilé statistické metody Kriging. [1]

2.4.4. Vyhodnocení výsledků

Po dokončení optimalizačního procesu jsou výsledky analyzovány a nejvhodnější konfigurace je vybrána. Tato konfigurace by měla vykazovat zvýšenou tuhost a minimalizovaný posuv v kritickém bodě. [1]

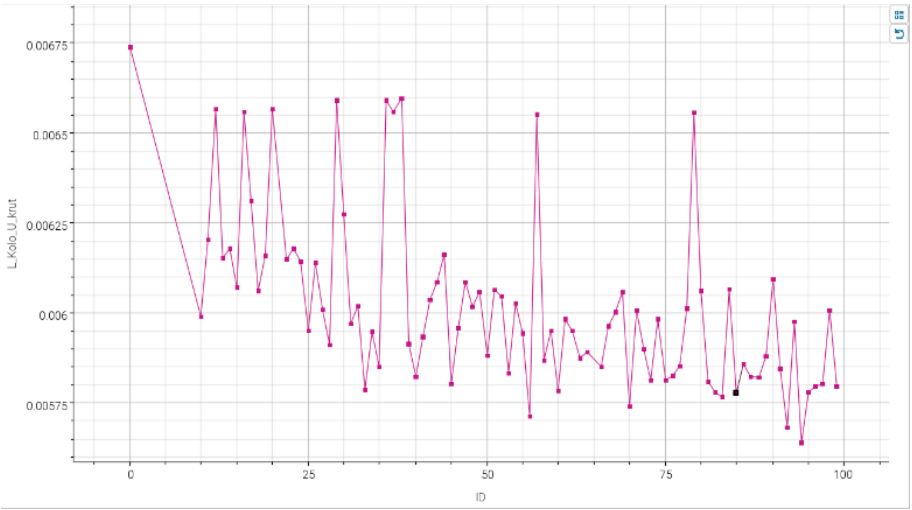

***Obrázek 5**: Optimalizace posuvů v uzlu L_Kolo při zátěžování krutem na 100 iteračních kroků*

2.5. Redesign

Na základě nejlepších statistických výsledků bude z nových zobecněných souřadnic generována optimalizovaná průřezová charakteristika. Tyto data mohou být poté nahrány do CAD programu kde bude na základě již připravené křivky vytvořen skořepinový nosník. [1] [5]

Tato technika je poplatná zejména při kalkulaci plasticity, kde při napětích, blížících se mezi kluzu na 1D elementech může docházet k přetvoření, které není možné posuzovat na 1D elementu. Substituce skořepinovým 2D elementem toto umožňuje. Vznikne tak kombinovaný model 1D a 2D element, který je schopný v před vývojové fázi ušetřit velké množství výpočetního stavu a celý proces tak výrazně zlevnit. [1] [2] [4] [5]

3. ZÁVĚR

3.1. Přínosy optimalizace

Optimalizace 1D elementů v 3D prostoru přináší několik klíčových výhod.

- **Zvýšená tuhost konstrukce**: Optimalizací průřezových charakteristik lze dosáhnout výrazného zvýšení tuhosti konstrukce, což vede k lepšímu výkonu a odolnosti vůči zatížení.
- **Snížené posuvy**: Minimalizace posuvů v kritických bodech zlepšuje stabilitu a spolehlivost konstrukce.
- **Efektivní využití materiálu**: Optimalizace umožňuje efektivní využití materiálu tím, že se zaměřuje na klíčové oblasti konstrukce, kde je zvýšená tuhost nejvíce potřebná.

3.2. Výhody kombinace 1D a 2D element

Mezi výhody této optimalizační techniky se řadí především výrazná časová úspora v před vývojové fázi rámové konstrukce. Velmi malá náročnost na výpočetní techniku, díky využití numerického programu.

Od této metody si slibuji také výrazné snížení úspor, a to jak na poli vývoje, tak následné výroby při maximálním možném využití materiálu.

ZDROJE

[1] PÁNEK, Tomáš. *VÝVOJ NÁSTROJE PRO POSOUZENÍ MECHANICKÝCH PARAMETRŮ TYPICKÝCH STAVEBNÍCH PRVKŮ KAROSERIE*. Diplomová práce. Technická 4 160 00 Praha 6: České vysoké učení technické v Praze, 2022.

[2] MIHL, Viktor. *VÝVOJ NÁSTROJE PRO AUTOMATIZOVANOU TVORBU CAD GEOMETRIE PROFILŮ*. Bakalářská práce. Technická 4 160 00 Praha 6: České vysoké učení technické v Praze, 2022.

[3] *Abaqus 2016 DOCUMENTATION*. Online. Dostupné z: http://130.149.89.49:2080/v2016/index.html. [cit. 2024-07-11].

[4] *VAŠÍČEK, Michal. Vehicle Concept, Structure, Safety. 2017. Dostupné také z: https://studium.fs.cvut.cz/studium/u12120/E211112_VCS/VCS\%20-\%20Safety\%202017.pdf*

[5] *SHI, Lei. Lightweight Design for BEV Body Using Modular-based: Multi-material Space Frame (M3-SF) Technology [online]. 26.4.2017, 2-30 [cit. 2022-06-22]. Dostupné z: https://www.lbcg.com/media/downloads/events/625/galm17-lei-shi.11599.pdf*

PODĚKOVÁNÍ

Tato práce byla podpořena grantem Studentské grantové soutěže ČVUT SGS24/089/OHK2/2T/12.

Tento výzkum byl realizován za podpory Technologické agentury České republiky, programu Národního kompetenční centra II, projekt # TN02000054 Božek Vehicle Engineering National Center of Competence (BOVENAC).

55. mezinárodní vědecká konference zaměřená na výzkumné a výukové metody v oblasti vozidel a jejich pohonů

září 5. - 6., 2024 – Liberec, Česká republika
Technická univerzita v Liberci
Fakulta strojní, Katedra vozidel a motorů

IMPACT OF FROST & ICE ON FANS FOR LIGHT DUTY VEHICLE EQUIPPED WITH HEAT PUMP

Andrej Repa[1], Petr Opravil [2]

Abstract
The transition from passenger cars with internal combustion engines to electric cars brings a lot of new questions. One of them is the frost (ice) creation on the cooling components and their impact on the function of the cooling fan, thus on the function of the entire cooling module.
This work discusses the possibilities of formation of frost (ice) as: when, where, and in what quantity can occur. It deals with the possibility of release and subsequent interaction with the rotating parts of the cooling system (fan of rotor). It evaluates the possibility of mechanical damage of the individual parts and the impact of potential damage on the function of the entire module functions.

[1] Andrej Repa, Hanon Systems Autopal Services s.r.o., Závodní 1007, 687 25 HLUK, Czech Republic, arepa@hanonsystems.com
[2] Petr Opravil, Hanon Systems Autopal Services s.r.o., Závodní 1007, 687 25 HLUK, Czech Republic, popravil@hanonsystems.com

1. INTRODUCTION

The last decade has seen a push towards Battery Electric Vehicles (BEV's), that is bringing some new technologies not usually used before for passenger cars. One of them is Heat Pump.
Need of this principle (heat pump) is driven by "loss of energy" coming from combustion, used to heat cabin and bring to passengers comfortable and safe environment. This missing energy must be replaced. In case of BEV it is directly electrical energy from main battery that significantly decrease car range [1]. Heat Pump is a good solution that can help to eliminate these losses by transferring (using) energy contained in outside air to the cabin air and at the end safe energy for main battery for vehicle range [2].

2. PRINCIPLES DESCRIPTION

Based on above mentioned we can divide system into two groups:

1. Cars with only Air Conditioning
2. Cars with Air Conditioning + Heat Pump

System in AC mode is transferring energy (heat) from cabin to outside, and in HP mode is transferring energy from outside (air) into the cabin.

Both principles are described in (*figure 1*).

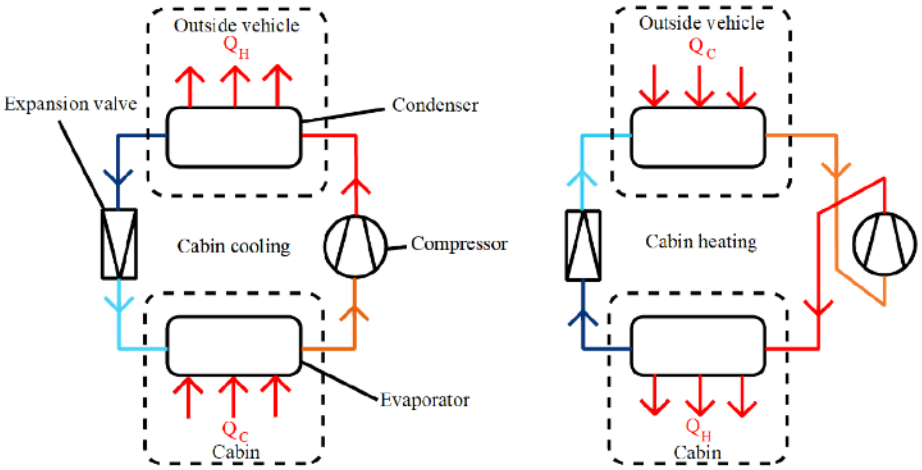

***Figure 1**: Air Conditioner and Heat Pump principle [3].*

AC as HP modes are using in principle same components, just work in the opposite cycle.
Both typically consist of condenser, expansion valve, evaporator and compressor, where condenser is placed in front cooling module and evaporator in cabin area, as visible in (*figure 2*), (condenser placed in front cooling module in HP mode fulfills the function of an evaporator).
Also conditions of usage are different:
AC mode is not used when outside temperature is less than 15 °C, and contrary to that HP mode is not used above outside temperature 15 °C, because of usage in others ranges does not make sense (from energy point of view).
In modern cars both modes can be switched at any time.

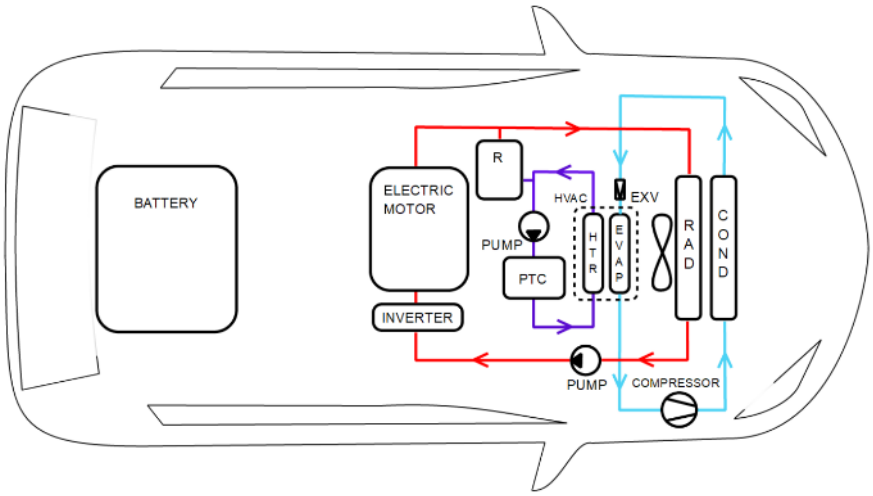

***Figure 2**: AC and HP components position in the car [3].*

Typical working temperatures of condenser in AC mode are from +50°C to +155°C (depends on refrigerant, outside temperature etc., measured on the outer surface), temperature at evaporator can drop down to minus temperatures.
Contrary condenser (in evaporation state) in HP mode can operate at -40 °C to +15°C, (measured on the outer surface).

From the above follows that frost does not occur in AC mode in front cooling module on the condenser. Frost can occur only on evaporator, what is not scope of this article, because evaporator is not a part of front cooling module, where the FAN-DRIVE is placed.
In HP mode the situation is totally different. Frost on the condenser (as a part on front module) occurs periodically.
The periodicity comes from the need to preserve the functionality of the HP mode, where frost degrades this required functionality with its insulating ability. This results in the need to melt the ice. This process must therefore be repeated periodically.
Because this situation is new is necessary to pay more attention to this problem.

3. FRONT MODULE CONCEPTS

Since heat pumps have not yet been massively deployed, system architecture are not yet standardized. Therefore, it is necessary to evaluate different variants from the point of view of freezing.

Variant a) Condenser placed between two radiators (*Figure 3*). In this case no ice particle larger than biggest gap in the radiator (that is placed at right side from condenser) can interact FAN. Gap is driven by FIN high (FH) and by FIN density (FPD) (*Figure 4*).
Typical examples used on the market for LTR are FH 4.5 or 5.5 mm and FPD 70 to 80, for HTR are FH 4.5 or 6 mm and FPD 80 to 100

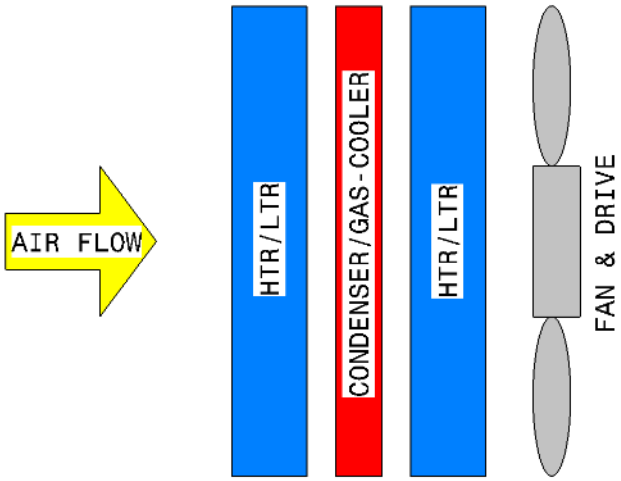

***Figure 3**: Front module configuration a)*

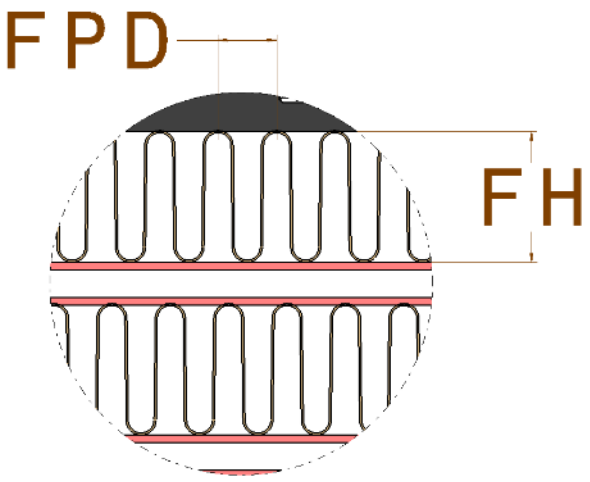

***Figure 4**: FIN definition*

Variant b) Radiator placed between two condensers (*Figure 5*). In this case no ice particle larger than biggest gap in radiator (HTR or LTR) can interact FAN from left condenser. Gap is driven by FIN high (FH) and by FIN density (FPD) as for variant a).
But any particle created on right condenser will directly interact with FAN-DRIVE.

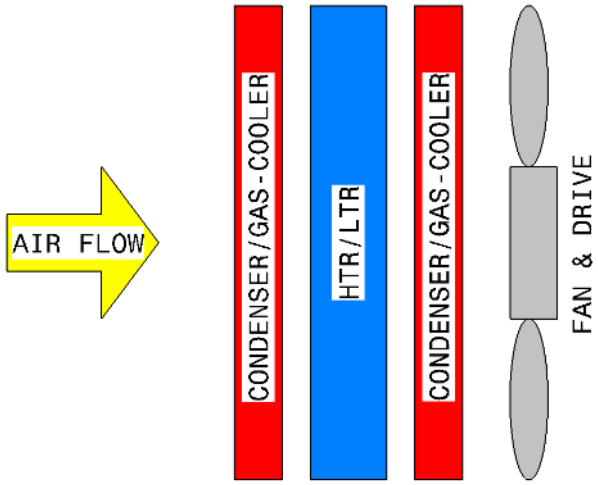

***Figure 5**: Front module configuration b)*

Variant c) Condenser placed between radiator and FAN-DRIVE (*Figure 6*). In this case any particle created on condenser will directly interact with FAN-DRIVE.

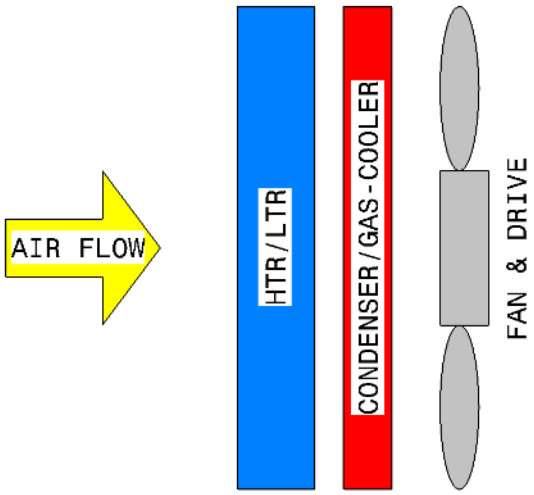

***Figure 6**: Front module configuration c)*

When the condenser is the last next to the FAN-DRIVE particles size can be defined as:

- Particles driven by FIN height (FH) and FIN density (FPD) (*figure 7*).
  Typical examples used on the market for GAS-COOLER are FH 6.5 mm and FPD 100. For condenser are FH 5.5 to 7 mm and FPD 80 to 105.

- Particles created out of the FIN area (extremely can achieve size of condenser or GAS-COOLER, but this case is not probable because of mostly vertical orientation) (*Figure 8*).

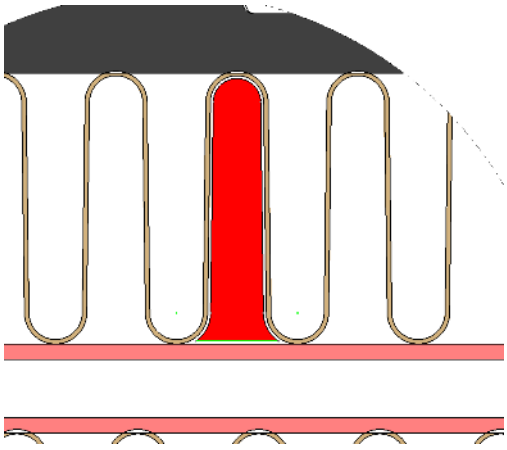

***Figure 7**: Fin area particle – red one*

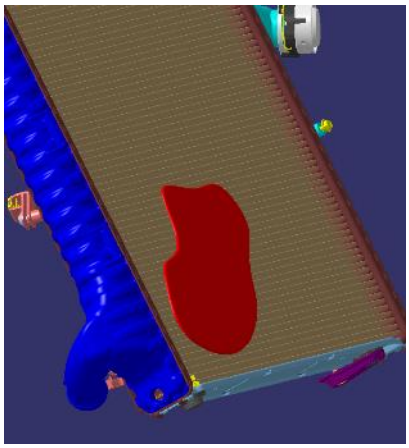

***Figure 8**: OUT of Fin area particle*

4. ICE OR FROST

1. ICE (glaze) - From the nature of the use of the vehicle, we can assume that the formation of ice as glaze occurs only by the joining of small water particles contained in the air upon hitting the cold surface of the condenser and their subsequent accumulation. Therefore, it can be assumed that the formation of larger particles of the ice will occur on the side away from the FAN, but these particles are blocked by the body of the condenser and will not reach the FAN blades.
   We do not expect the emergence of any part of an ice on the side of FAN.

2. FROST (like snow) – frost occurs due to the precipitation of atmospheric moisture on the cold surface of the condenser and the subsequent growth of water crystals on this surface.
   It happens more or less evenly over the entire surface, independent of gravity. Of course, air flow affects this, so that the frost grows against the direction of the flow (in the presence of fog), means on the side away from the FAN, which is not any problem.

Also it is possible to assume that the density and hardness of the frost is much less that of the ice therefore our next investigation will focus on the ice.

The speed of formation, or the amount of frost (ice) can be interpreted with the Mollier's HX diagram (Figure 9).

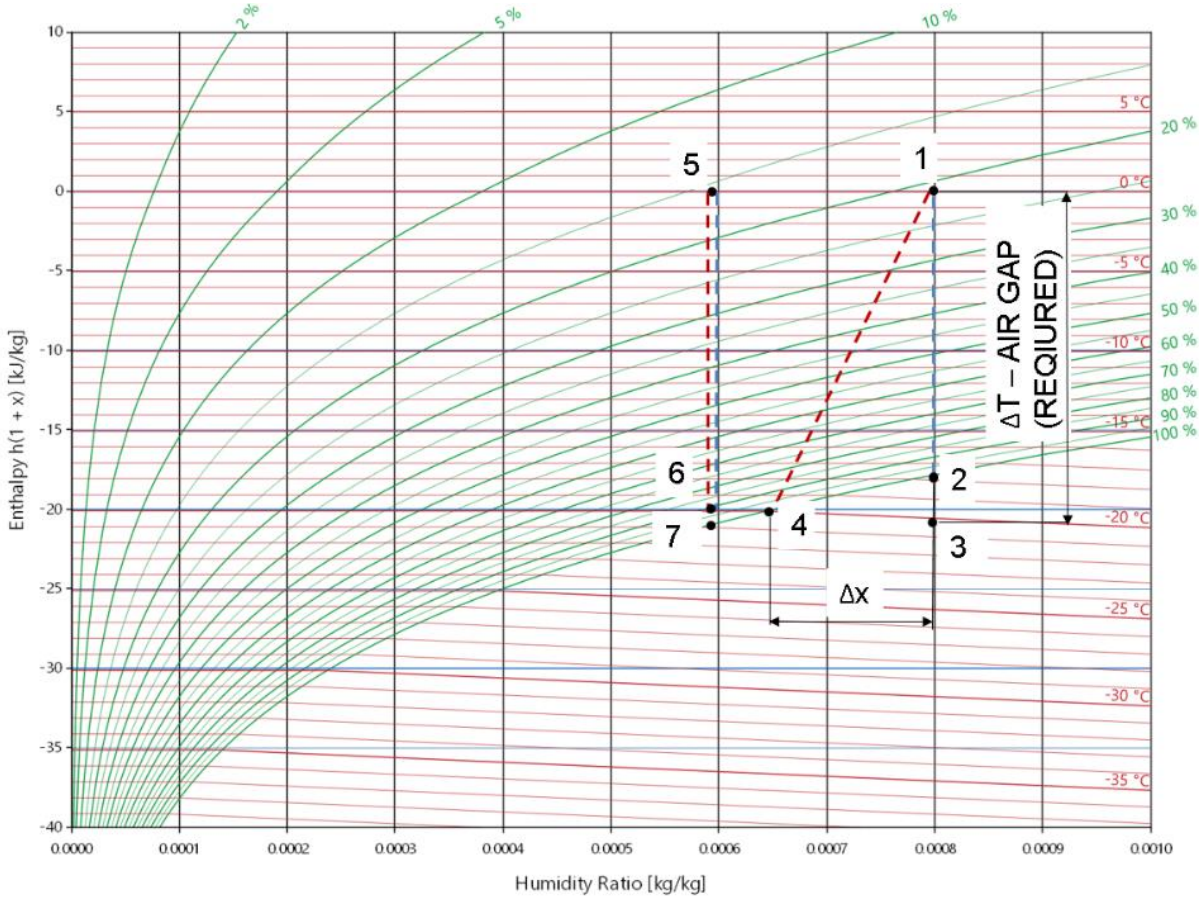

***Figure 9**: Mollier's HX diagram*

It is clear that need of energy for heating cabin grow up by decreasing of outside temperature. That push HP system to work at condensation limit of the outside air, representing in HX diagram by 100% relative humidity line. If system exceeds this limit above freezing point (of the water) nothing bad happened, but if the limit is exceeded under freezing point frost formation occurs. What causes the system to malfunction. Of course, there is an effort to avoid this situation, unfortunately it doesn't always happen.
Important for function of HP system is also the minimum air gap 5°C that cover system losses. Air gap is difference of air temperature and the condenser outer wall temperature.

5. TEST PROCEDURE

Because exact specification from customer has not yet been provided, how to test the given effect, it is appropriate to test an extreme case.
Appears from the description above this:

- Heat exchanger with FPD 70, FH 5.55
- FIN fully filled by ice
- Horizontal position of the heat exchanger
- Fan on the bottom

The test has been conducted in a temperature chamber capable of supplying coolant to at least -15°C in two steps, once without and once with FAN. Net will be placed under the assembly to catch any remaining hard particles.

Test A (without FAN):

- freezing
  - Coolant inlet temperature -15°C
  - Flow rate 14 l/min
  - Freezing time 30 min
  - Temperature in the chamber without control due to handling the sample (pouring water on the cooler, recording, etc.)
- heating
  - Coolant inlet temperature +50°C
  - Flow rate 20 l/min
  - Heating time 5 min

Test B (with FAN):

- freezing
  - Coolant inlet temperature -15°C
  - Flow rate 14 l/min
  - Freezing time 30 min
  - Temperature in the chamber without control due to handling the sample (pouring water on the cooler, recording, etc.)
- heating
  - Coolant inlet temperature +50°C
  - Flow rate 20 l/min
  - Heating time 5 min

Tracking parameters.

- Particles caught on the net
- Damage to the fan blades
- FAN functionality

5. TEST RESULTS

Test A (without FAN):

- New heat exchanger (fully functional, not affected by any other test).

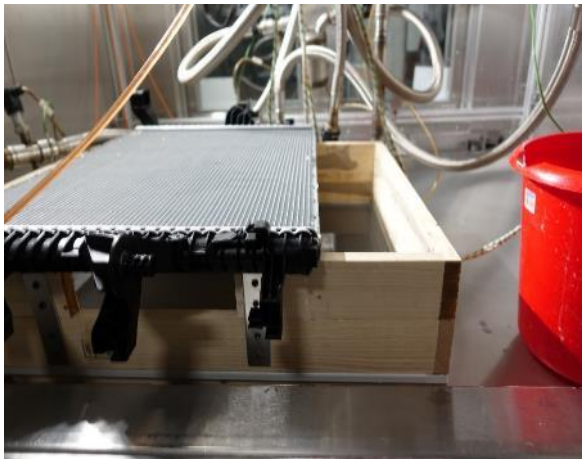

***Figure 10**: New test sample*

- Cooler full of ice (water filled by hand in some steps in freezing phase)

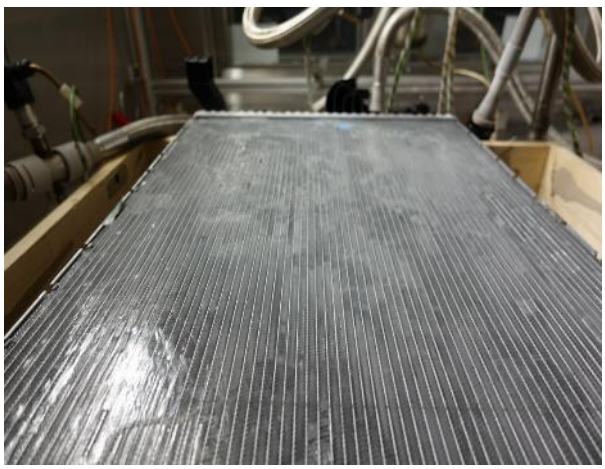

***Figure 11**: Filled heat exchanger top side*

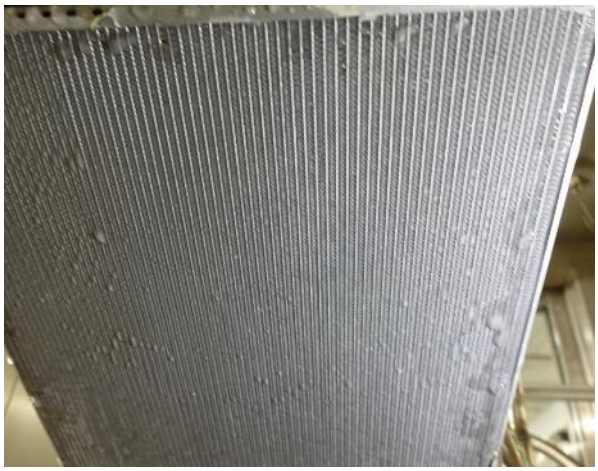

***Figure 12**: Filled heat exchanger bottom side*

- Particles caught on the net (there are visible some particles not larger than 15 mm).

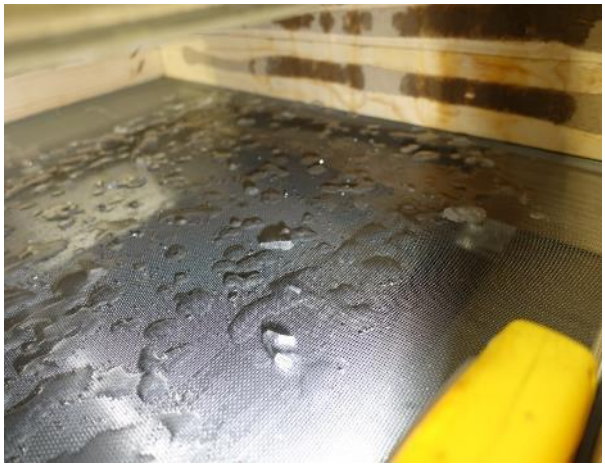

***Figure 13**: Particles caught on net*

***Figure 14**: Particles caught on net*

Test B (with FAN):

- New heat exchanger (fully function able, not affected by any other test).

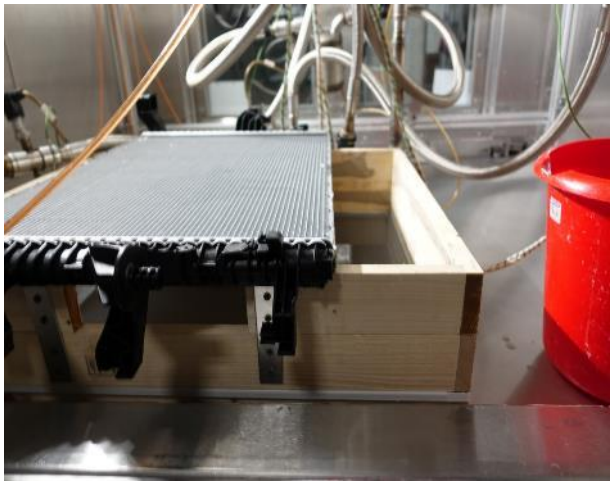

***Figure 15**: New test sample*

- Heat exchanger full of ice with and without icicles

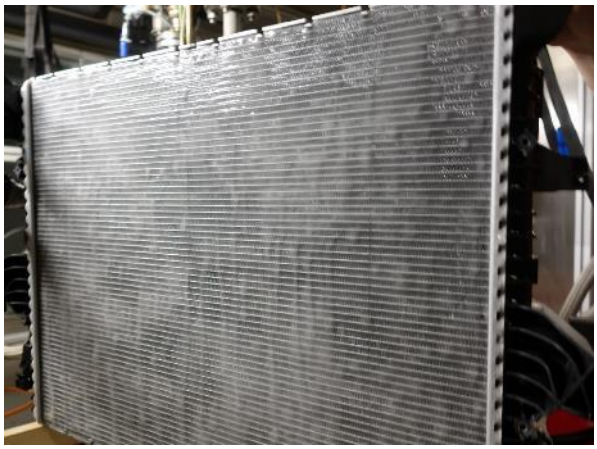

***Figure 17**: Filled heat exchanger bottom side*

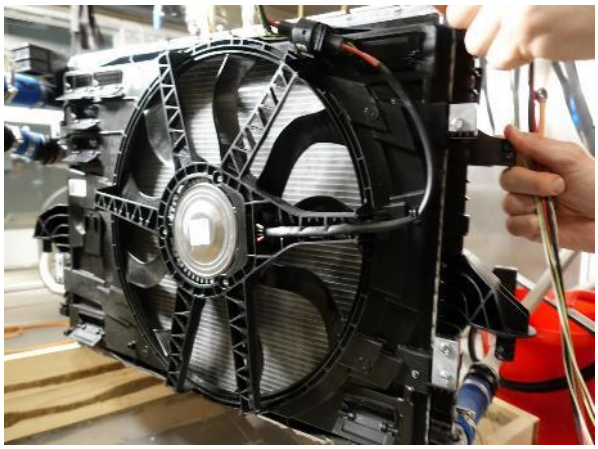

***Figure 18**: Filled heat exchanger with FAN*

***Figure 19**: Filled heat exchanger bottom side with icicles*

- New FAN-DRIVE used for testing. Fully functional sample taken from serial production.

***Figure 20**: New FAN before test*

***Figure 21**: New FAN before test another blade*

- Particles caught on the net
  - It was not possible to record because rotating fan is dangerous (must be safely closed in box) and at the end of test all of the hard particles can be ever found are melted.

- FAN after test. No damage visible.

***Figure 22**: FAN after test*

***Figure 23**: FAN after test another blade*

3. CONCLUSION

The choice to divide the test into two (with fan and without fan) proved correct, as the test with fan did not show any ice particles caught on the mesh, which is not the case with the test without fan, in which some amount was captured after all.
It logically follows from this that during the test with the fan, contact between the fan blades and ice particles must have been occurred, which was also heard during the test.
Despite this, there was no visible damage of the fan blades or loss of drive functionality, however long term test can lead to any significant wear.

In conclusion, it can be said that the formation of frost and ice on the components of the front module does not pose a great risk to the correct functionality of the FAN-DRIVE under the conditions described above.

Of course, it is advisable to wait for specifications from customers in case of unexpected anomalies and subsequent verification.

In addition, it is advisable to focus on the other emerging problems in the future, such as:

- What impact would long term test on FAN-DRIVE has
- Investigate when, what kind of and in which volume frost (ice) can occur
- What is the difference between mechanical properties of the ice (frost) and material of the FAN in all possible conditions?
- Can frost occur also on the FAN-DRIVE?

REFERENCES

[1] GEOTAB. (2022, July 13th). Temperature Tool for EV Range. https://www.geotab.com/fleet-management-solutions/ev-temperature-tool/

[2] GRAAF M., Recirculation in cold climate: challenges & opportunities [Conference presentation], 2nd Annual Automotive Thermal Management Conference, Munich, 2019, p. 25

[3] DOLEŽAL D. THERMAL MANAGMENT OF EV, BEV, PHEV AND FCEV VEHICLES, BRNO UNIVERSITY OF TECHNOLOGY, FACULTY OF MECHANICAL ENGINEERING, INSTITUTE OF AUTOMOTIVE ENGINEERING. 2023.

55. mezinárodní vědecká konference zaměřená na výzkumné a výukové metody v oblasti vozidel a jejich pohonů

září 5. - 6., 2024 – Liberec, Česká republika
Technická univerzita v Liberci
Fakulta strojní, Katedra vozidel a motorů

NÁVRH SPALOVACÍHO MOTORU V DASY

Jindřich Hořenín[1], Oldřich Vítek[2], Jan Macek[3]

Abstract

Příspěvek ukazuje využití DASY při návrhu spalovacího motoru. S použitím parametrických 3D modelů je proveden návrh a porovnání 5 motorů o výkonu 110 kW s velkým rozpětím středního efektivního tlaku, při zachování stejné střední pístové rychlosti 15,8 m/s v návrhovém bodě a omezením maximálního spalovacího tlaku na 10 MPa.

1. ÚVOD

Na ústavu automobilů, spalovacích motorů a kolejových vozidel na FS ČVUT v Praze je vyvíjen sytém pro návrh poháněcí soustavy vozidla „Design Assistance SYstem“ DASY. Tento systém vývojáři umožní s minimálními časovými a finančními náklady prozkoumat různé kombinace poháněcích soustav a díky propojení parametrického návrhu se simulačními systémy nalézt pro dané vozidlo nejvhodnější poháněcí soustavu. Parametrický model umožňuje on-line optimalizaci konstrukce poháněcí soustavy s ohledem na zvolené parametry, zejména spotřebu energie a množství

[1] Jindřich Hořenín, FS ČVUT, Technická 4 Praha 6, jindrich.horenin@fs.cvut.cz
[2] Oldřich Vítek, FS ČVUT, Technická 4 Praha 6, oldrich.vitek@fs.cvut.cz
[3] Jan Macek, FS ČVUT, Technická 4 Praha 6, jan.macek@fs.cvut.cz

škodlivých emisí, bezpečnostní rezervy, hmotnost poháněcí soustavy a zástavbové rozměry pro požadované vozidlo. Během návrhu tohoto systému jsou jednotlivé sekce testovány na příkladech. Jeden z těchto testů je popsán v tomto příspěvku.

2. NÁVRH SPALOVACÍHO MOTORU

Procedura návrhu zážehového spalovacího motoru byla otestována na příkladu návrhu motoru o výkonu 110 kW. Aby byla ověřena všestranná funkčnost systému, byly porovnány motory s velkým rozpětím středního efektivního tlaku, při zachování stejné střední pístové rychlosti 15,8 m/s v návrhovém bodě a omezením maximálního spalovacího tlaku na 10 MPa. Parametry porovnávaných motorů jsou patrné z *Tab. 1*. Hlavní výsledky porovnávaných motorů jsou shrnuty v *Tab 6*.

TYP MOTORU	označení	4V 2,5 L	4V 1,5 L	3V 1,5 L	3V 1,2 L	3V 1,0 L	jednotky
počet válců	i	4	4	3	3	3	
průměr pístu	D	90,0	74,5	82,0	76,6	73,3	mm
zdvih pístu	Z	98,0	85,9	94,6	86,7	79,0	mm
poměr zdvih vrtáni	Ɛ=Z/D	1,09	1,15	1,15	1,13	1,08	
kompresní poměr	Ɛ	12,5	10,5	10,5	10,5	10,5	
zdvihový objem motoru	V_{zm}	2,49	1,50	1,50	1,20	1,00	dm^3
otáčky při max. výkonu	n_m	4850	5250	5000	5450	6000	1/min
střední efektivní tlak	p_e	1,086	1,69	1,77	2,03	2,21	MPa
přeplňování		NE	ANO				
střední pístová rychlost	c_s	15,8					m/s
vstřik paliva		přímý vstřik paliva do válce					
počet plnicích ventilů		2 (VVA) millerův princip					
počet výfukových ventilů		2 (VVA)					

Tab. 1 *Parametry porovnávaných motorů*

Pro návrh motorů byla využita procedura vytvořená v DASY. Na základě vstupních dat byly vypočteny všechny nezbytné parametry pro tvorbu 3D modelu motoru v CREO Parametric a výpočet termodynamiky daného motoru pomocí modelu 1 válcového motoru vytvořeného v GT-Power. Regenerace 3D parametrického modelu na rozměry požadovaného motoru trvá řádově 30 minut a výpočet termodynamiky, který probíhá paralelně řádově 15 minut. Takže během 30 minut je k dispozici základní 3D model motoru, jehož součástí jsou již nadefinované mechanismy a součásti se všemi okrajovými podmínkami pro tepelné a silové analýzy.

2.1. 1D model motoru v GT-Power

Simulační model spalovacího motoru byl vytvořen v simulačním softwaru GT-Suite [1], který umožňuje simulaci celého termodynamického cyklu motoru, s využitím předchozích zkušeností s podobnými motory. Základní jednoválcový zážehový čtyřdobý motor umožňuje simulovat tří a čtyřválcové motory od atmosférických verzí až po vysoce přeplňované. Model motoru je parametricky modifikovatelný. Geometrie motoru a požadované výkonnostní parametry jsou do modelu importovány vstupním souborem, který je navázaný na 3D CAD model viz *Tab. 1*.

- **Motor**

Jednoválcový čtyřdobý zážehový motor. Hlava motoru je 4 ventilová s přímým vstřikem paliva do válce. Motor pracuje v otáčkovém módu, kde otáčky motoru jsou zadány uživatelem, a točivý moment motoru je počítán. Model motoru využívá silný stupeň millerizace. Model je založen na předpokladu, že díky silné millerizaci nedochází ke klepání motoru. Mechanická účinnost motoru je odhadována. Na základě zkušeností je spalování modelováno prediktivním modelem spalování s velmi turbulentním a rychlým hořením, délka hoření je okolo 20° otočení klikového hřídele. Dle zkušeností je pro časování spalování, definována poloha bodu 50 % vyvinu tepla. Aplikovaný model hoření je schopen správně predikovat vývin tepla (spalování) při změně otáček, zatížení, přebytku vzduchu, plnicího tlaku nebo časování ventilů. Sdílení tepla do stěn spalovacího prostoru je simulováno Woschniho modelem (viz [2]). Teploty stěn jsou počítány zjednodušenou konečně prvkovou úlohou, která dle zkušeností kvalitativně dobře reaguje na změny geometrie, zatížení motoru a střední pístovou rychlost motoru.

- **Výfukový systém**

Ve výfukovém systému jsou simulovány výfukové sekce jako by se jednalo o víceválcový motor. Tyto sekce umožňují simulovat pulzace na turbíně turbodmychadla. Modelu je přiřazeno turbodmychadlo, které zaručí požadovaný tlak v plnicím systému motoru a nastaví odpovídající protitlak ve výfukovém systému modelu motoru. Celková účinnost turbodmychadla je odhadnuta zhruba okolo 46% s tím, že jde dnes o obvyklou hodnotu pro moderní zážehové motory v uvažovaném rozsahu velikostí válcové jednotky.

- **Plnicí systém motoru**

Plnicí systém začíná tlakovou okrajovou podmínkou, na kterou navazuje vzduchový filtr. V sacím systému je chladič plnicího vzduchu. Vlastnosti plnicích kanálů jsou zadány bezrozměrnými charakteristikami, které byly ověřeny testy na aerodynamické zkušební trati. Model motoru využívá plnicí kanály s vysokým stupněm rozvíření ve směru kolmém na osu válce – Tumble. Vysoká míra rozvíření náplně válce zaručuje vysokou rychlost spalování.

Aby byla zajištěna objektivita porovnání různých variant motorů, musí být tyto motory navrženy se srovnatelnou bezpečností, proto byl proveden výpočet klikového mechanismu těchto motorů.

Analýzou klikového mechanismu jsou získány průběhy silových účinků v kontaktních místech klikového mechanismu.

2.2. Kontrola klikového mechanismu

Kontrola klikového mechanismu začíná kontrolou tepelného a strukturálního zatížení pístu, protože změna hmotnosti pístu ovlivní silové zatížení všech následných dílů klikového mechanismu.

Byly testovány 4 různé geometrie pístů. Základní geometrie pístu provedení A dle *Obr. 1*, provedení B *Obr. 2* základní geometrie je totožná s provedením A, ale má zesílené dno pístu, tato obvyklá konstrukční úprava vede ke zvýšení součinitele bezpečnosti, ale zároveň se výrazně zvyšuje hmotnost pístu. Provedení C *Obr. 3*, *Obr. 6* a D *Obr. 4*, *Obr. 5* mají odlehčený nálitek pro pístní čep a dno pístu vyztužené žebry, která zároveň zvětšují teplosměnnou plochu spodní části pístu a tím zlepšují odvod tepla. Touto konstrukcí bylo dosaženo snížení hmotnosti oproti provedení A, a zároveň zvýšení součinitele bezpečnosti. Výsledky simulací jsou shrnuty v *Tab. 2*. Referenční bezpečnost je stanovena na základě vyhodnocení namáhání daného dílu při daných otáčkách. Z průběhu zatížení je zjištěno maximální a minimální zatížení.

Z těchto zatížení je vyjádřena bezpečnost v Haighově diagramu pro daný materiál. Nejedná se o únavovou bezpečnost, provedené výpočty zatížení součástí jsou provedeny kvazistaticky, ve výpočtu jsou zahrnuty setrvačné síly, ale není uvažována dynamika, pro stanovení únavové bezpečnosti není ve stádiu úvodního návrhu k dispozici zatěžovací spektrum jednotlivých součástí.

	TYP MOTORU	označení	4V 2,5 L	4V 1,5 L	3V 1,5 L	3V 1,2 L	3V 1,0 L	jednotky
	PRŮMĚR PÍSTU	D	90,0	74,5	82,0	76,6	73,3	mm
	ZDVIH PÍSTU	Z	98,0	85,9	94,6	86,7	79,0	mm
	MAXIMÁLNÍ SPALOVACÍ TLAK	p_{max}	8,05	9,85	9,90	10,00	10,00	MPa
	SOUČINITEL PŘESTUPU TEPLA DO PÍSTU	α	551	705	752	828	889	W/(m^2·K)
	STŘEDNÍ TEPLOTA PLYNŮ NA PÍST	T_c	1 580	1 529	1 457	1 390	1 353	K
ZATÍŽENÍ PÍSTU	MAXIMÁLNÍ TEPLOTA NA PÍSTU	A	301	310	318	311	317	°C
		B	298	308	315	309	311	°C
		C	285	306	310	306	308	°C
		D	272	304	305	301	303	°C
	TEPLOTNÍ ZATÍŽENÍ	A	95	105	115	107,4	109	MPa
		B	90	101	110	105	107	MPa
		C	87	97	108	99	102	MPa
		D	81	92	101	89,1	90	MPa
	TLAKOVÉ ZATÍŽENÍ	A	105	108	119	128	126	MPa
		B	87	92	98	105	103	MPa
		C	102	105	111	122	120	MPa
		D	96	98	107	119	117	MPa
	ZATÍŽENÍ SOUČTOVÉ TEPLOTNÍ + TLAKOVÉ	A	165	192	201	198	205	MPa
		B	160	178	185	176	184	MPa
		C	142	156	162	157	162	MPa
		D	126	135	141	138	139	MPa
	REFERENČNÍ BEZPEČNOST	A	1,21	0,82	0,8	0,8	0,76	-
		B	1,25	0,9	0,89	0,94	0,88	-
		C	1,41	1,1	1,08	1,08	1,05	-
		D	1,59	1,31	1,28	1,24	1,24	-
	HMOTNOST PÍSTU	A	403,1	236,8	304,7	249,6	227,9	g
		B	418,2	251,5	320,0	264,7	238,6	g
		C	406,5	235,2	308,0	251,0	218,1	g
		D	411,2	236,5	311,1	255,7	225,8	g

***Tab. 2** Výsledky simulací zatížení pístů*

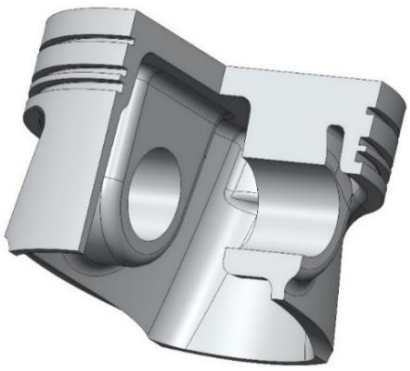

Obr. 1 *Píst provedení A*

Obr. 2 *Píst provedení B*

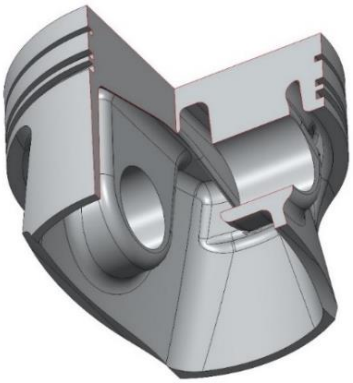

Obr. 3 *Píst provedení C*

Obr. 4 *Píst provedení D*

Obr. 5 *Píst provedení D*

Obr. 6 *Píst provedení C*

Obr 7 *Ojnice provedení A*

Obr. 8 *Ojnice provedení B*

	TYP MOTORU	označení	4V 2,5 L	4V 1,5 L	3V 1,5 L	3V 1,2 L	3V 1,0 L	jednotky
OJNICE A	POČET VÁLCŮ	i	4	4	3	3	3	
	PRŮMĚR PÍSTU	D	90,0	74,5	82,0	76,6	73,3	mm
	ZDVIH PÍSTU	Z	98,0	85,9	94,6	86,7	79,0	mm
	MAXIMÁLNÍ SPALOVACÍ TLAK	p_{max}	8,05	9,85	9,90	10,00	10,00	MPa
	MATERIÁL		C70S6	42CrMo4	42CrMo4	42CrMo4	42CrMo4	
	TLAKOVÉ ZATÍŽENÍ	NAPĚTÍ	270	365	350	390	410	MPa
		DEFORMACE	0,120	0,154	0,168	0,166	0,155	mm
	TAHOVÉ ZATÍŽENÍ	NAPĚTÍ	378	332	371	357	365	MPa
		DEFORMACE	0,092	0,062	0,084	0,079	0,075	mm
	HMOTNOST		651,0	412,9	516,7	444,4	400,2	g
	REFERENČNÍ BEZPEČNOST		1,48	1,69	1,51	1,47	1,39	-
OJNICE B	MATERIÁL		C70S6	42CrMo4	42CrMo4	42CrMo4	42CrMo4	
	TLAKOVÉ ZATÍŽENÍ	NAPĚTÍ	250	350	343	370	390	MPa
		DEFORMACE	0,096	0,144	0,152	0,153	0,150	mm
	TAHOVÉ ZATÍŽENÍ	NAPĚTÍ	207	149	208	193	198	MPa
		DEFORMACE	0,061	0,039	0,058	0,050	0,481	mm
	HMOTNOST		661,0	410,8	524,3	442,1	400,5	g
	REFERENČNÍ BEZPEČNOST		2,24	2,2	2,24	2,08	1,97	-
PÍSTNÍ ČEP	TLAKOVÉ ZATÍŽENÍ	NAPĚTÍ	264	455	453	399	410	MPa
		DEFORMACE	0,057	0,076	0,089	0,070	0,067	mm
	TAHOVÉ ZATÍŽENÍ	NAPĚTÍ	91	65	102	208	65	MPa
		DEFORMACE	0,022	0,012	0,022	0,041	0,016	mm
	HMOTNOST		124,6	75,4	92,6	78,7	89,4	g
	REFERENČNÍ BEZPEČNOST		2,77	1,57	1,57	1,8	1,66	-
KLIKOVÝ HŘÍDEL	MATERIÁL		GJS-900-2	42CrMo4	42CrMo4	42CrMo4	42CrMo4	-
	ZATÍŽENÍ NA 1 ČEPU	NAPĚTÍ	138	138	218	195	195	MPa
		DEFORMACE	0,045	0,075	0,264	0,218	0,218	mm
	MAXIMÁLNĚ ZATÍŽENÉ MÍSTO	POZICE	MJ_2B	MJ_4B	MJ_2A	MJ_2A	MJ_2A	-
		NAPĚTÍ	142	185	231	207	207	MPa
		DEFORMACE	0,149	0,230	0,264	0,258	0,258	mm
	HMOTNOST		20,31	11,00	12,26	9,49	8,11	kg
	REFERENČNÍ BEZPEČNOST		3,5	4,16	3,33	3,72	3,72	-

Tab. 3 *Výsledky simulací zatížení pístních čepů, ojnic a klikových hřídelů*

Kontrola dílů klikového mechanismu pokračuje provedením strukturálních simulací pístních čepů a ojnic. Výsledky těchto simulací jsou shrnuty v *Tab. 3*. Byly provedeny simulace se 2 typy ojnic. Konstrukce těchto ojnic se lišila provedením horního oka ojnice, které bylo pro provedení B zesíleno. Konstrukce ojnic je zřejmá z *Obr 7* a *Obr. 8*. Poté je klikový mechanismus složen z navržených dílů a je provedena simulace pohybu klikového mechanismu, z které jsou získány průběhy zátěžných sil v jednotlivých uzlech klikového mechanismu. Těmito silovými účinky jsou zatíženy klikové hřídele.

Porovnáním průběhu zatížení hlavních čepů čtyřválcového přeplňovaného motoru na *Obr. 9* a tříválcového přeplňovaného motoru *Obr. 10*, je zřejmě patrný výrazný vliv velikosti sil od působení spalovacích tlaků na zatížení klikového hřídele. Při stejných spalovacích tlacích jsou síly u tříválcového motoru vyšší což má vliv nejen na velikost napětí, ale i na polohu nejvíce zatíženého čepu klikového hřídele. Přehled zatížení a bezpečností je uveden v *Tab. 3*.

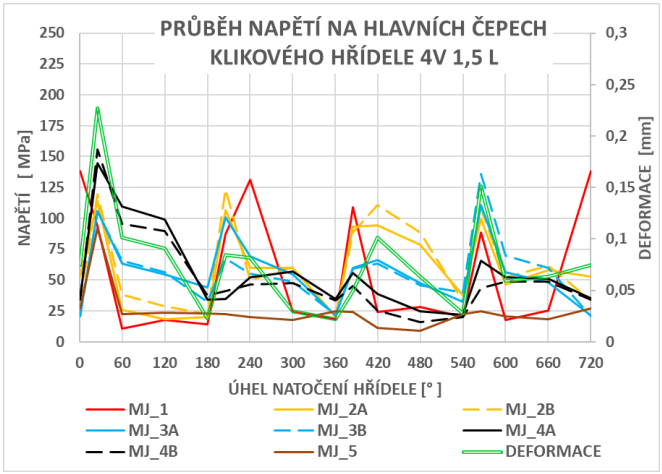

Obr. 9 *Průběhy napětí na hlavních čepech klikového hřídele čtyřválcového přeplňovaného motoru*

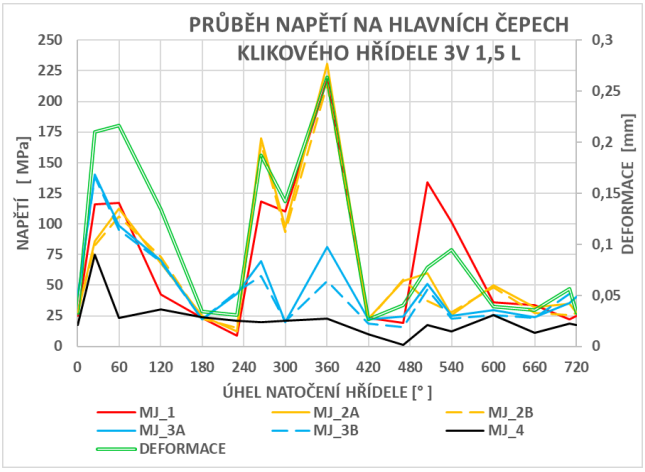

Obr. 10 *Průběhy napětí na hlavních čepech klikového hřídele tříválcového přeplňovaného motoru*

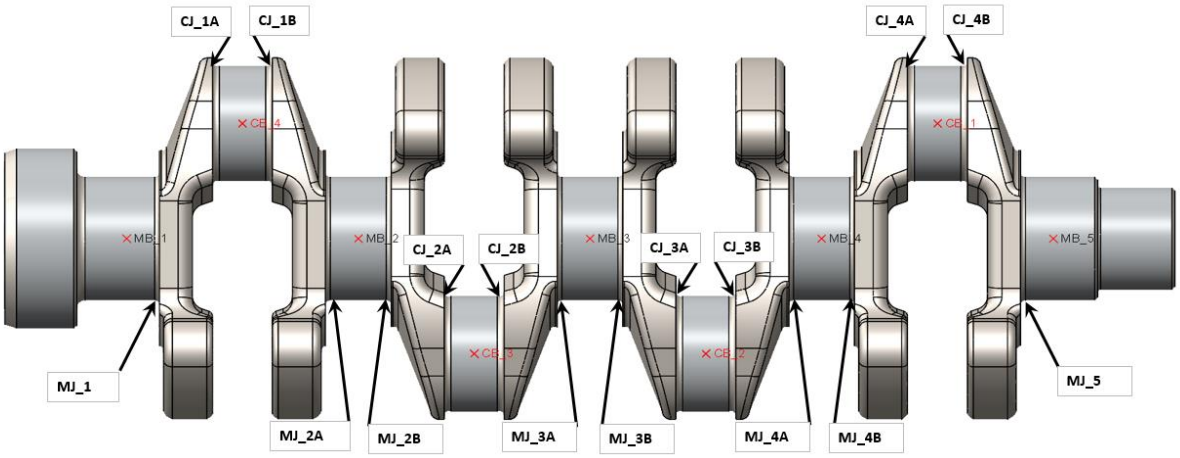

Obr. 11 *Systém značení měřených veličin na klikové hřídeli čtyřválcových motorů*

Po stanovení rozměrů klikového mechanismu jsou známy rozteče válců a lze tudíž pokračovat v návrhu hlavy válců. Pro konstrukci hlavy je nejdůležitější stanovit typ rozvodového mechanismu a geometrii plnicích a výfukových kanálů. Pro návrh plnicích kanálů je připraven parametrický model, který obsahuje definice okrajových podmínek a výpočetní sítě.

2.3. Návrh geometrie plnicích kanálů hlavy válce

Byly porovnány různé geometrie tvarování plnicích kanálů.
Popis jednotlivých provedení:
A - základní provedení plnicích kanálů dle parametrického modelu.
B – zvětšení průřezu kanálu v místě ohybu
C- změna bokorysu osy kanálu kanály jsou ve vířivější poloze
D- změna půdorysu os kanálů – vytvoření dvou samostatných rovnoběžných kanálů
E- změna půdorysu os kanálů – vytvoření dvou samostatných kanálů s rozevřením 10°
F- změna půdorysu os kanálů – vytvoření dvou samostatných kanálů s rozevřením 5°
G- kombinace varianty C a D

varianta	A	B	C	D	E	F	G	
průtok kanálem	360	359	337	376,9	377,3	377,8	357,7	[kg/h]

Tab 4 Porovnání průtoků plnicími kanály při otevření ventilu 10 mm

Vliv změny geometrie na průtokové vlastnosti je na *Obr 12* a v *Tab 4*. Z tohoto diagramu a tabulky je zřejmé, že provedení A, B, G jsou téměř totožná, a provedení D, E, F jsou také téměř totožná a přinesla zlepšení průtoku plnicími kanály. Varianta C vykázala zhoršení průtokových vlastností, ale je předpoklad, že bude dosahovat většího rozvíření náplně ve válci. Varianta G vzniklá kombinací variant C a D má předpoklady na intenzivní vír ve válci jako varianta C ale nedojde ke zhoršení průtokových vlastností. Varianta G je nejvhodnější variantou u těchto motorů, protože zajistí intenzivní víření v motoru, které je potřebné pro rychlý průběh hoření.

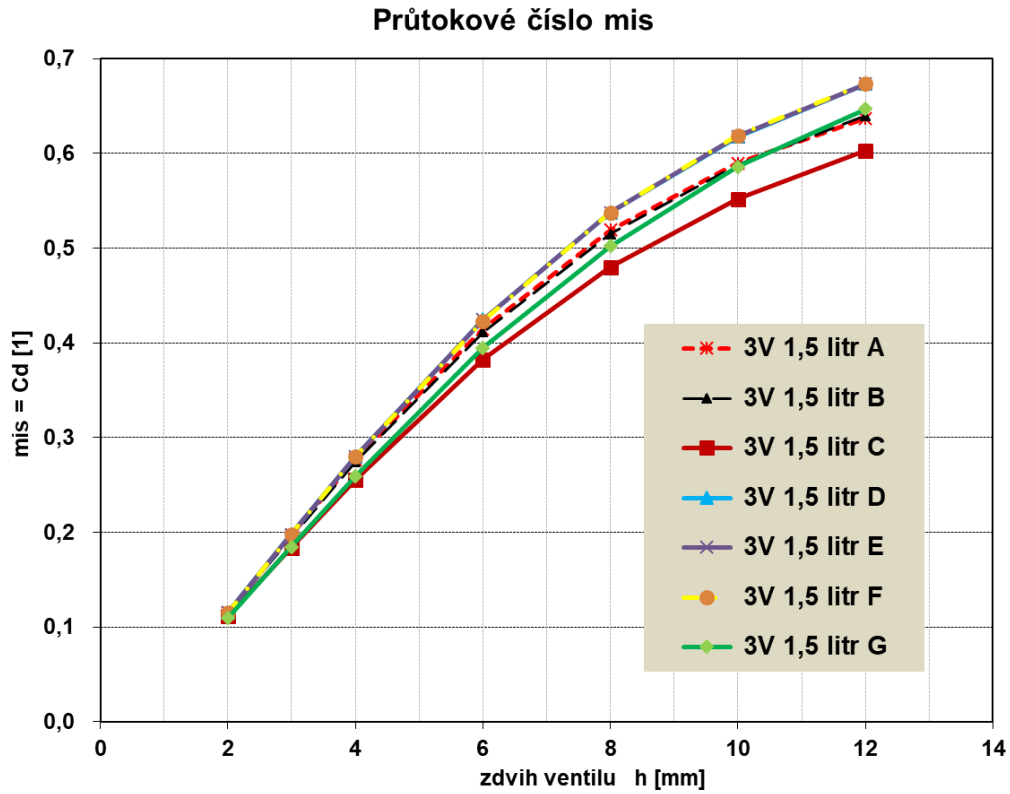

Obr 12 Porovnání průtokových vlastností plnicích kanálů při změně geometrie

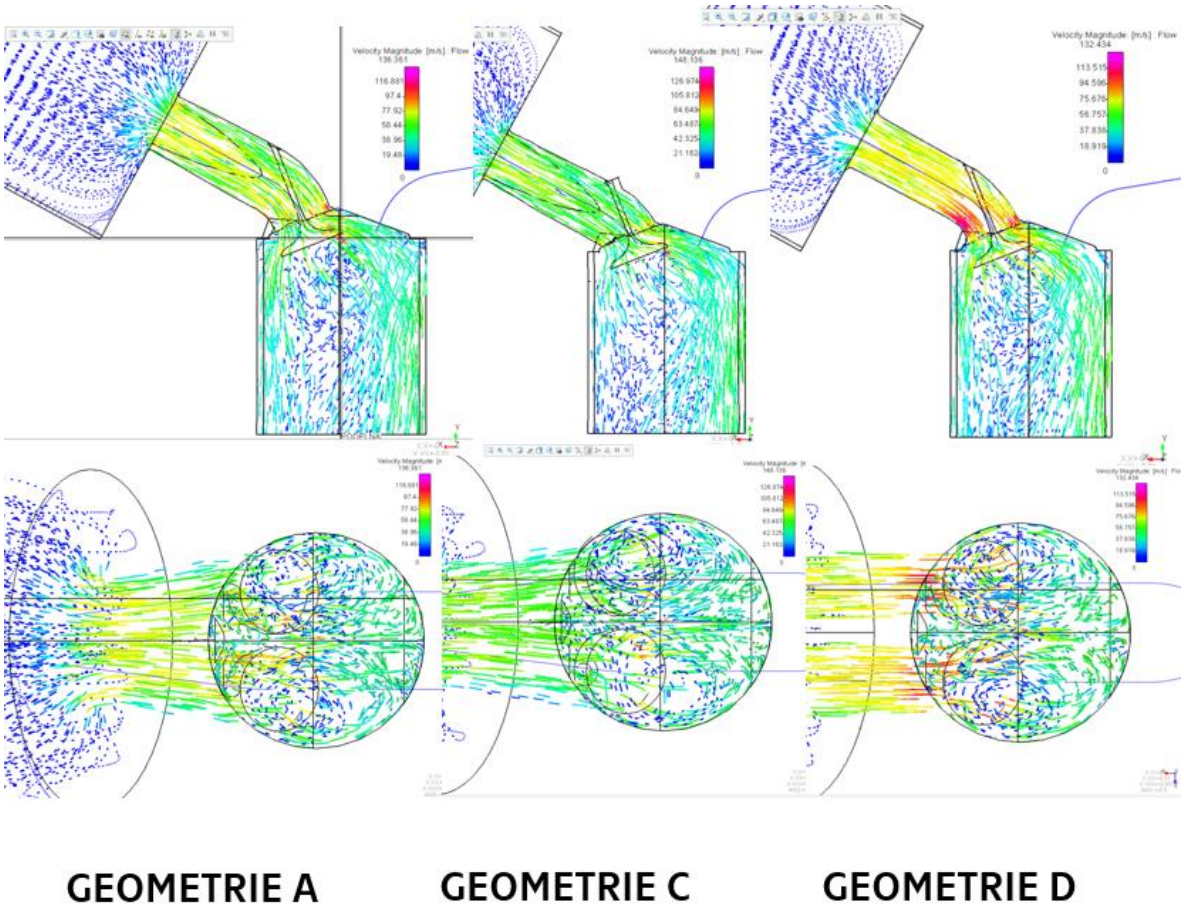

Obr 13 Různá provedení plnicích kanálů

2.4. Návrh chladicího prostoru

Pro kontrolu rozložení rychlostí v chladicím systému motoru byl využit parametrický 3D model chlazení motoru. Tento parametrický model je ovládán stejným vstupním souborem, který je využit pro tvorbu 3D modelu sestavy motoru. Simulací proudění lze navrhnout chladicí prostor s vyrovnanými rychlostmi proudění. Výstupem ze simulací jsou tlakové ztráty v jednotlivých částech systému i celková tlaková ztráta v chladicím systému, která slouží pro návrh chladicího čerpadla a stanovení ztrátového výkonu chladicího čerpadla. Díky využití parametrického modelu, který obsahuje všechny definice pro provedení simulací, trvá výpočet proudění v chladicím prostoru řádově jednu hodinu. Model se pouze pře-regeneruje na požadované velikosti a spustí se nadefinovaná simulace. Přehled průtoků, tlakových ztrát a výkonů potřebných pro pohon vodního čerpadla je v tabulce Tab 5. V této tabulce jsou zároveň uvedeny

průtoky olejovým systémem a výkony potřebné pro pohon olejových čerpadel vypočtených systémem.

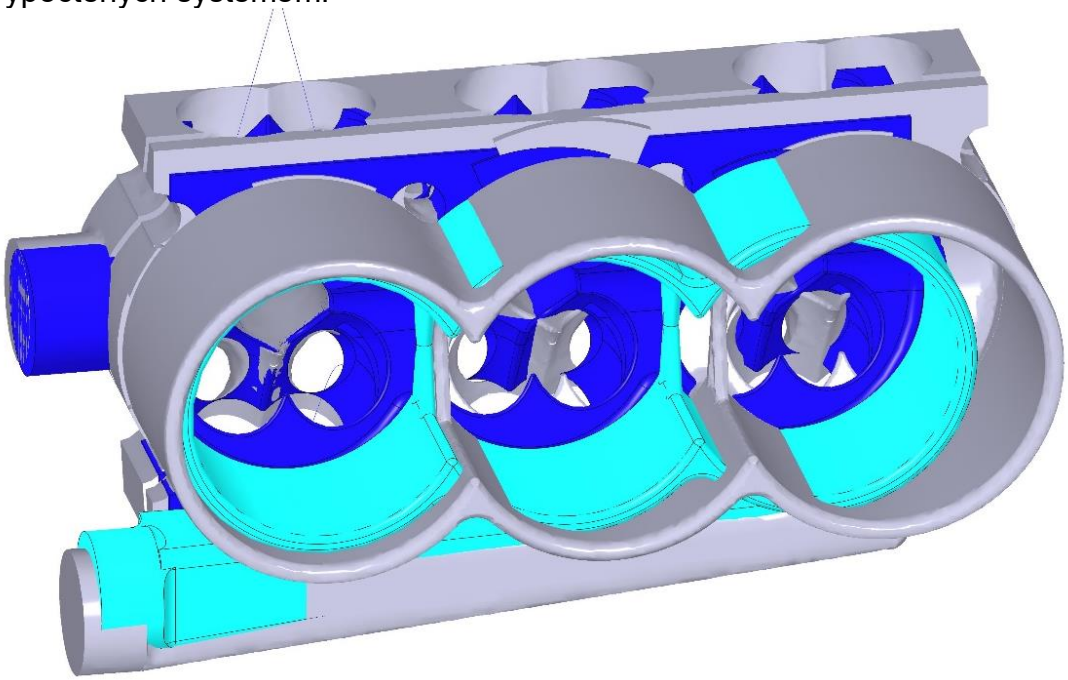

Obr 14 *Porovnání velikosti chladicího prostoru největšího a nejmenšího tříválcového motoru*

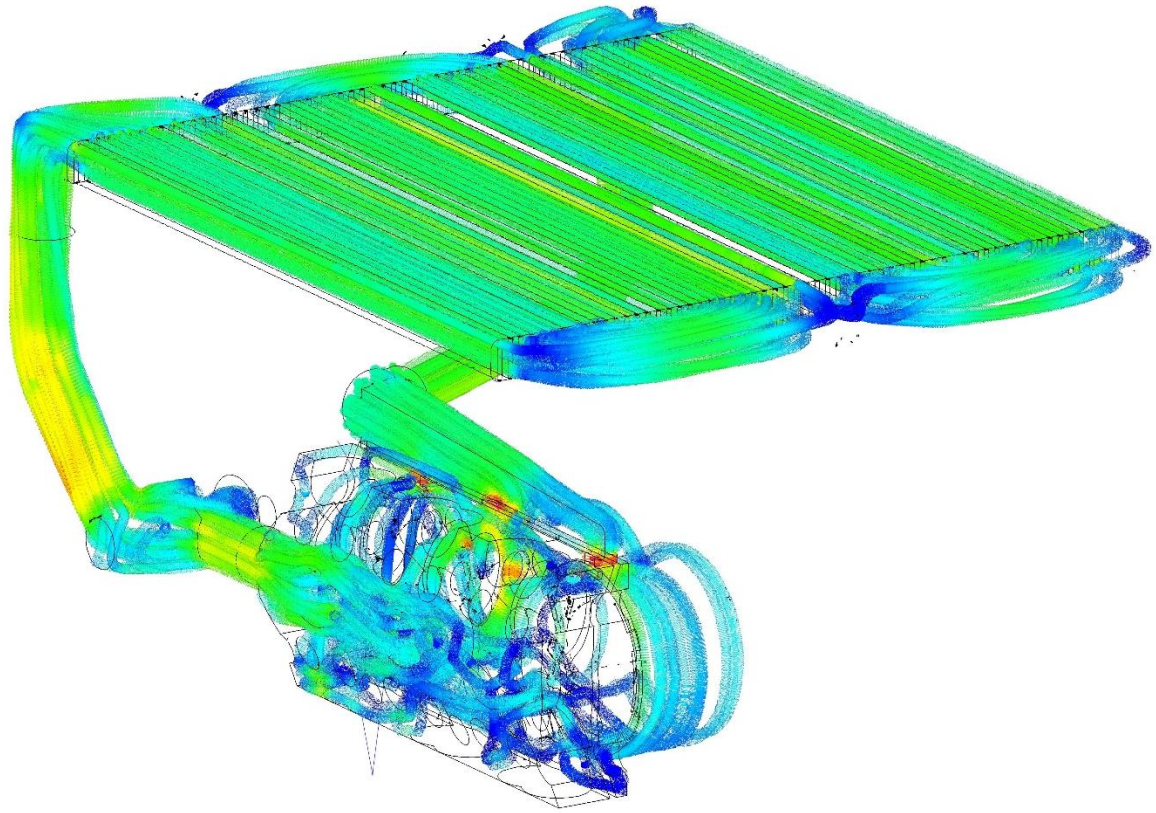

Obr 15 *Rozložení rychlostí v chladicím prostoru tříválcového motoru*

	TYP MOTORU	označení	4V 2,5 L	4V 1,5 L	3V 1,5 L	3V 1,2 L	3V 1,0 L	jednotky
ZADÁNÍ	počet válců	i	4	4	3	3	3	
	průměr pístu	D	90,0	74,5	82,0	76,6	73,3	mm
	zdvih pístu	Z	98,0	85,9	94,6	86,7	79,0	mm
	střední efektivní tlak	p_e	1,09	1,58	1,76	2,02	2,20	MPa
GT POWER	efektivní výkon motoru	P_e	109,4	109,0	110,0	110,0	110,0	kW
	chladicí výkon	P_{ch}	44,4	41,6	39,3	38,3	36,3	kW
	průtok vody	Q_{ch}	6,5	6,09	5,76	5,61	5,32	m^3/h
CREO	tlaková ztráta v chlazení	Δp_{ch}	43,66	43,80	44,30	45,20	46,20	kPa
	příkon vodního čerpadla	P_{Cch}	87,6	82,3	78,8	78,3	75,9	W
	průtok oleje ložisky	Q_{ol}	1,462	1,191	0,981	0,9577	0,983	m^3/h
	průtok oleje motorem	Q_{ol}	1,9006	1,9056	1,6677	1,6281	1,6711	m^3/h
	příkon olejového čerpadla	P_{Col}	35,2	35,3	30,9	30,1	30,9	W

Tab 5 Přehled průtoků a ztrátových výkonů chladicího a mazacího systému.

3. ZÁVĚR

Touto studií byly vytvořeny geometrie motorů, které splňují základní konstrukční podmínky a byly vybrány různá provedení dílů a materiálů těchto dílů, tak aby tyto díly měly srovnatelnou bezpečnost. Z vytvořených 3D modelů motorů lze získat všechna nezbytná data pro provádění podrobných simulací.

	TYP MOTORU	označení	4V 2,5 L	4V 1,5 L	3V 1,5 L	3V 1,2 L	3V 1,0 L	jednotky
ZADÁNÍ	počet válců	i	4	4	3	3	3	
	průměr pístu	D	90,0	74,5	82,0	76,6	73,3	mm
	zdvih pístu	Z	98,0	85,9	94,6	86,7	79,0	mm
	střední efektivní tlak	p_e	1,09	1,58	1,76	2,02	2,20	MPa
GT POWER	měrná spotřeba	m_e	227,4	232,7	232,7	238,2	241,1	g/(kW·h)
	efektivní výkon motoru	P_e	109,4	109,0	110,0	110,0	110,0	kW
	celková účinnost	η_c	37,82	36,97	36,96	36,11	35,68	%
CREO	délka motoru	L	556	487	430	412	399	mm
	výška motoru	V	651	592	627	594	575	mm
	šířka motoru	S	435	491	510	499	498	mm
	hmotnost motoru	H	95,9	76,2	77,2	69	65,3	kg

Tab 6 Hlavní parametry porovnávaných motorů

Z porovnání hlavních parametrů uvedených v *Tab 6*, je zřejmé, že nejvyšší účinnosti a nejmenší měrné spotřeby dosahuje nepřeplňovaný čtyřválcový motor o objemu 2,5 litru. Tento motor bude zároveň výrobně nejlevnější, protože nemá turbodmychadlo a z důvodu nízkých spalovacích tlaků může využít litý klikový hřídel, který je levnější a jeho výroba je energeticky méně náročná. Ojnice tohoto motoru je rovněž zvolená z levnějšího materiálu než u ostatních motorů. Tento motor je ale nejrozměrnější a nejtěžší z posuzovaných motorů. Tento motor je vhodný pro použití v hybridní hnací jednotce, protože nehrozí poškození turbodmychadla při vypnutí motoru po vysokém zatížení motoru. Naopak nejmenší a nejlehčí je nejvíce přeplňovaný tříválcový motor

a objemu 1 litr. Tento motor má nejmenší účinnost a největší měrnou spotřebu paliva. Toto ukazuje, že snaha o návrh co nejmenšího motoru s vysokým přeplněním nemusí být nejvýhodnější cestou ke snížení spotřeby motoru.
Kompromisem mezi těmito dvěma extrémy se zdá být tříválcový motor o objemu 1,2 litru, který má jen nepatrně větší rozměry a hmotnost než 1 litrový motor, a zároveň má nejlepší účinnost a nejnižší spotřebu z přeplňovaných motorů.
Z porovnání tříválcového a čtyřválcového motoru o objemu 1,5 litru je zřejmé, že oba motory mají stejnou spotřebu a účinnost. Tříválcový motor má ale výrazně více zatížené díly klikového mechanismu. Tento motor má menší zástavbovou délku, naopak jeho výška, šířka a hmotnost je větší než u čtyřválcového motoru. Cena tříválcového motoru bude nižší než čtyřválcového, protože je složen z menšího počtu drahých dílů klikového a rozvodového mechanismu, ale přibydou díly vyvažovacího mechanismu.
Takováto studie vyžaduje řádově 1 měsíc práce při využití navrženého systému DASY. 3D model motoru a všech dílů včetně okrajových podmínek, definicí výpočetních sítí a měřicích bodů je vygenerován řádově za 30 minut, takže největší čas je potřeba pouze na simulace zatížení jednotlivých součástí a vyhodnocení získaných výsledků a případné korekce pro dosažení požadované bezpečnosti. Výsledky jsou snadno porovnatelné, protože tím, že parametrické modely obsahují všechny definice okrajových podmínek i měřicích bodů, je zajištěné identické značení těchto bodů a tím jejich snadné porovnání a vyloučení chyb. Bez využití tohoto systému, by tato studie vyžadovala více jak roční práci.

POUŽITÁ LITERATURA

[1] GT-Power User's Manual, GT-Suite version v2022. Gamma Technologies Inc., 2022.
[2] Woschni, G. "An Universally Applicable Equation for the Instantaneous Heat Transfer Coefficient in the Internal Combustion Engine". SAE Transactions, Vol. 76:3065, 1967.
[3] Chen, S, Flynn, P. "Development of a Single Cylinder Compression Ignition Research Engine". SAE Technical Paper Series. Paper 650733.

PODĚKOVÁNÍ

Tento výzkum byl realizován za podpory Technologické agentury České republiky, program Národní centra kompetence II, projekt č. TN02000054 Národní centrum kompetence Božek Vehicle Engineering (BOVENAC).

55. mezinárodní vědecká konference zaměřená na výzkumné a výukové metody v oblasti vozidel a jejich pohonů

září 5. - 6., 2024 – Liberec, Česká republika
Technická univerzita v Liberci
Fakulta strojní, Katedra vozidel a motorů

ALTERNATIVE ARCHITECTURE OF BEV COOLING

Aleš Horák[1], Milan Kolomazník[2], Jiří Ordelt[3]

Abstract
The focus of this paper is to alternative ways of BEV thermal management. It presents potential of plastic HEXs as alternative to well known aluminum based HEXs. Thin hollow fibers show very good thermal performance and offers ability to form unusual shapes of HEXs. Dielectric oil and immersion cooling may become alternative to standard BEV thermal systems. The direct and indirect immersion cooling systems are described with (dis-)advantages.

[1] Ing. e.t. Ing. Aleś Horák, Ph.D., Hanon Systems Autopal Services s.r.o., Závodní 1007, 687 25 HLUK (CZ), ahorak@hanonsystems.com
[2] Ing. Milan Kolomazník , Hanon Systems Autopal Services s.r.o., Závodní 1007, 687 25 HLUK (CZ), mkoloma1@hanonsystems.com
[3] Ing. Jiří Ordelt, Hanon Systems Autopal Services s.r.o., Závodní 1007, 687 25 HLUK (CZ), jordelt@hanonsystems.com

1. INTRODUCTION

Battery Electric Vehicles (BEV) are supposed to gain massive market share to Combustion Engine Vehicles. The main challenges for BEVs are mainly battery capacity, fast charging and thermal management including optimal cooling & heating. Nowadays most of battery cells and battery packs are cooled by aluminium Heat Exchangers (HEX) using glycol-based coolant. Waste heat is transferred by conduction though mechanical contact between batteries and HEXs. Alternative option with same principle may be using plastic HEX with lower weight and lower electric conductivity. On the other hand, application of immersion cooling for battery thermal management using specific dielectric oil may lead to significant improvement. Two possible architectures of oil immersion cooling were studied. Direct immersion cooling with only one cooling loop, where dielectric oil is cooled by air in Oil Low Temperature Radiator (O-LTR). Another option may be an indirect immersion cooling with two cooling loops. One loop using glycol-based coolant with air to coolant LTR. Second loop is using dielectric oil and oil-to-coolant HEX inside the oil pan close to batteries. This paper presents results of investigations in those fields.

2. BODY OF PAPER

2.1 Standard way of battery cooling in BEV

Battery Thermal Management System is a crucial component in Battery Electric Vehicles (BEV). It regulates the temperature of the vehicle's battery, influencing and optimizing the performance, safety, efficiency, and lifespan of the vehicles. The travel distance out of one battery charge significantly depends on the ambient temperature. For example, at an ambient temperature of -7 °C compared to 23 °C, the travel distance provided by one battery charge can fall as low as 60%. Heating the cold electric drive components and the vehicle interior from low temperatures increases this negative effect even further. Fast charging requires the battery cell temperature to be held in a tight window at 40 °C, as the battery charges particularly fast in this condition at low losses [1].

There are various basic methods, including forced-air cooling, liquid cooling, phase change material (PCM), heat pipe (HP), thermoelectric cooling (TEC), etc. Some BEV systems include both coolant and refrigerant circuits with heat pump systems. Every method has its unique application condition and characteristic, advantages and disadvantages.

Liquid cooling is emerging as the dominant technology, particularly as the use of integrated thermal management systems for the whole vehicle become more common. These systems incorporate heating as well as cooling, and move heat around to control the temperatures of many components as well as the battery and cabin. The liquid coolant goes through tubes, cold plates, or other components that surround the cells and carry heat to another location, such as a coolant Low Temperature Radiators. As an example, a typical cylindrical cell in the 21700 format, has a power dissipation of around 5% when operating at low load, but can exceed that figure considerably at higher loads [2]. A 100 kWh battery pack could generate around 5 kW of heat, so only an efficient liquid-cooling system can remove that much from the cells quickly enough to keep them at a stable temperature in their optimum range [2].

Typically, those heat exchanges such as tubes, cold plates and LTRs are aluminium, manufactured using Controlled Atmosphere Brazing (CAB) or Vacuum Aluminium Brazing (VAB). Aluminium as material for heat exchangers provides excellent thermo-physical properties and CAB brazing allows mass production keeping automotive quality standards. On the other hand, brazing flux, that is essential for oxidic layer destruction during brazing, is adding Al, F, K ions and therefore potentially increasing electric conductivity and bringing risk of short circuit.

Figure 1: *Aluminium "wavy channel" heat exchanger for cylindrical battery cells [6]*

Figure 2: *Aluminium "cold plate" heat exchanger for battery packs [6]*

2.2 Alternative proposals for battery cooling

Despite the fact of low heat conductivity, a plastic HEX may be a reasonable alternative to metallic HEX. Plastic materials bring significantly lower weight (e.g. 2 720 kg/m3 Aluminium density vs. 1 120 kg/m3 density of Polypropylene) and much lower electric conductivity, which is essential for battery cooling and safety. But the main advantage of plastic HEXs is ability to form them to very unique geometrical shapes, that cannot be produced from metallic materials. In addition, the invention of Hollow Fiber (HF) [3] with outer diameter in range of 0.4 to 1.3mm with wall thickness about 10% of outer diameter allows construction of plastic HEX with heat rejection similar to aluminium HEX. Results of investigation in field of HF HEX, supported by the Technological Agency of Czech Republic (grant code TH04010031), were presented by Hanon [4]. Application of Reaction Injection Molding (RIM) with polypropylene HF allows production of compact, robust HEX with effective heat transfer between battery cells and inner cooling media based on ethylene-glycol mixture with water (see Fig. 3). Plastic materials such as polypropylene and polyamids are extrudable and may be formed into multi-port tubes. The shape of inner tube ports can be optimized to support maximal heat exchange to batteries and keep homogenous temperature gradient

along the HEX length (see Fig. 4). The polypropylene HF and RIM technology may be used to form plastic “cold plate” HEX (see Fig. 5). The polymeric HF can be designed and manufacture in such way they fill some available volume of the shell or tank. This volume may not be of regular shape and may not suit standard metallic HEX, but it can be equipped with thousands of HF side by side or in very chaotic structures to enhance heat exchange. Two examples of oil to coolant HEXs are shown on Fig. 6 and 7.

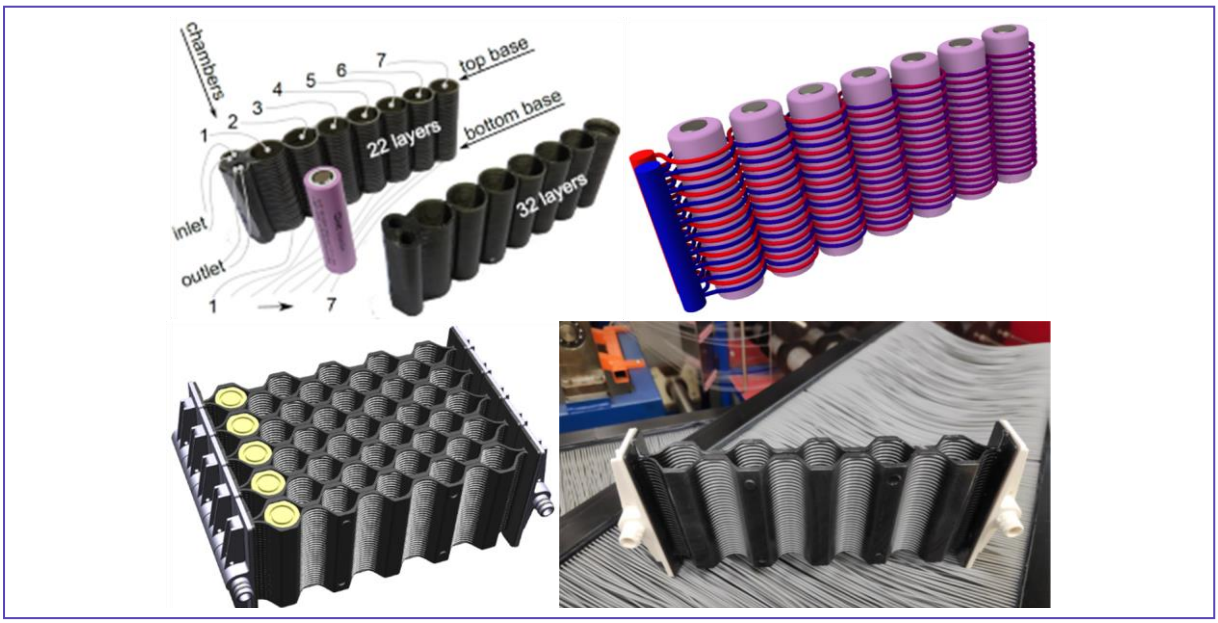

Figure 3: *Hollow fiber RIM plastic heat exchanger for cylindrical cells [5]*

Figure 4: *Extruded plastic heat exchanger for cylindrical cells [6]*

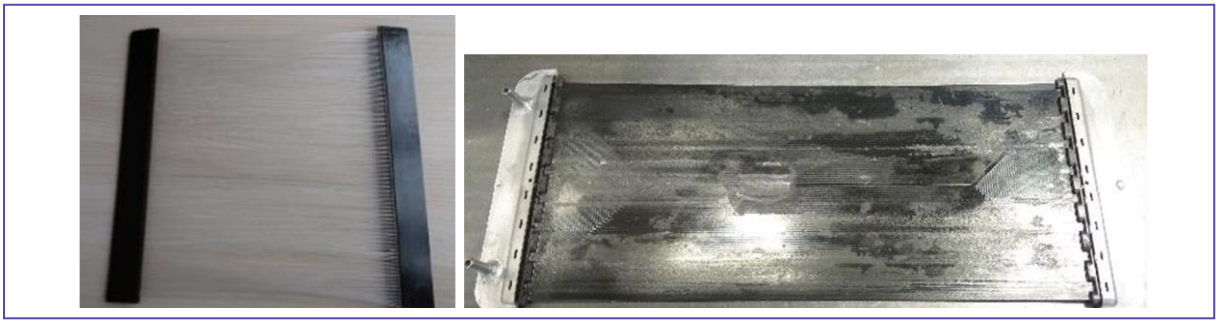

Figure 5: *Hollow fiber RIM plastic heat exchanger for battery packs, “cold plate” [5]*

Figure 6: *Oil to coolant heat exchanger with polyamid hollow fibers [4], [7]*

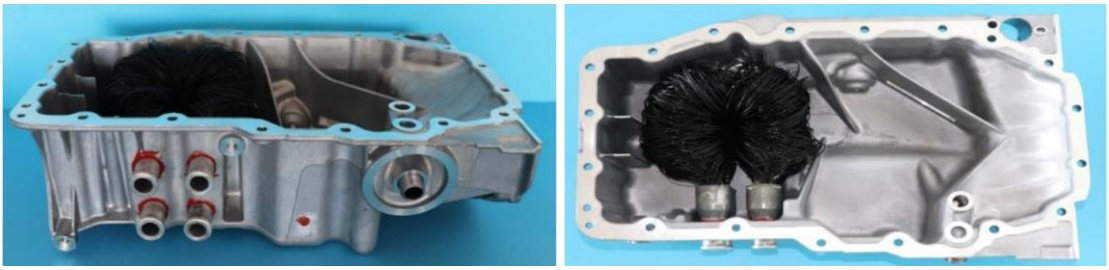

Figure 7: *Hollow Fiber plastic oil heat exchanger for immersion cooling [5]*

2.3 OIL IMMERSION COOLING FOR BEV

A complete battery pack can be immersed into special dielectric oil. This may bring various advantages to BEV application including improved thermal management and higher safety. Battery cell is completely washed by dielectric oil and therefore it is being cooled in more uniform way all around the complete surface. While the standard HEXs are cooling usually only one surface of the battery cell (e.g. cylinder wall or cylinder bottom) and the gap between HEX must be filled by special paste with high thermal conductivity. The paste application is costly and there might be degradation in properties or contact during the lifetime. Dielectric oil can be forced to flow around all battery cells and keep uniform temperature field within battery pack. The mass of the oil can better absorb temperature peaks during for example fast charging and with lack of oxygen inside the oil pan it can prevent critical events.

Two possible architectures of oil immersion cooling are possible and were investigated by Hanon Systems – Direct and Indirect immersion cooling systems. Direct immersion cooling (see Fig. 8) is system with only one cooling loop, where dielectric oil is cooled directly by in Oil Low Temperature Radiator (O-LTR). Oil is driven by oil pump into oil pan, where battery pack is kept closed. The oil flow inside the oil pan keeps the cells at optimal thermal conditions. The O-LTR is situated in front side of the vehicle as part of the cooling module and it is cooled down by air flow at ambient temperature. The position in cooling module and architecture of cooling module affects air mass flow and air temperature, which are essential parameters for optimal O-LTR performance. For example, adding R744 Gascooler or any other HEX in front of the O-LTR may heat up cooling air and add additional flow resistance for cooling air negatively affecting heat transfer from dielectric oil to ambient air.

Indirect immersion cooling system contains two cooling loops (see Fig. 9). One loop is using glycol-based coolant, while the second loop is using dielectric oil. Glycol loop contains LTR, hoses and coolant driven by coolant pump. The LTR is air-to-coolant

HEX very similar to existing radiators commonly used in BEVs. The glycol loop includes another HEX that is common with oil loop. This coolant-to-oil HEX transfers heat between both circuits. The related oil flows inside the closed oil pan is responsible for keeping batteries inside the optimal parameters.

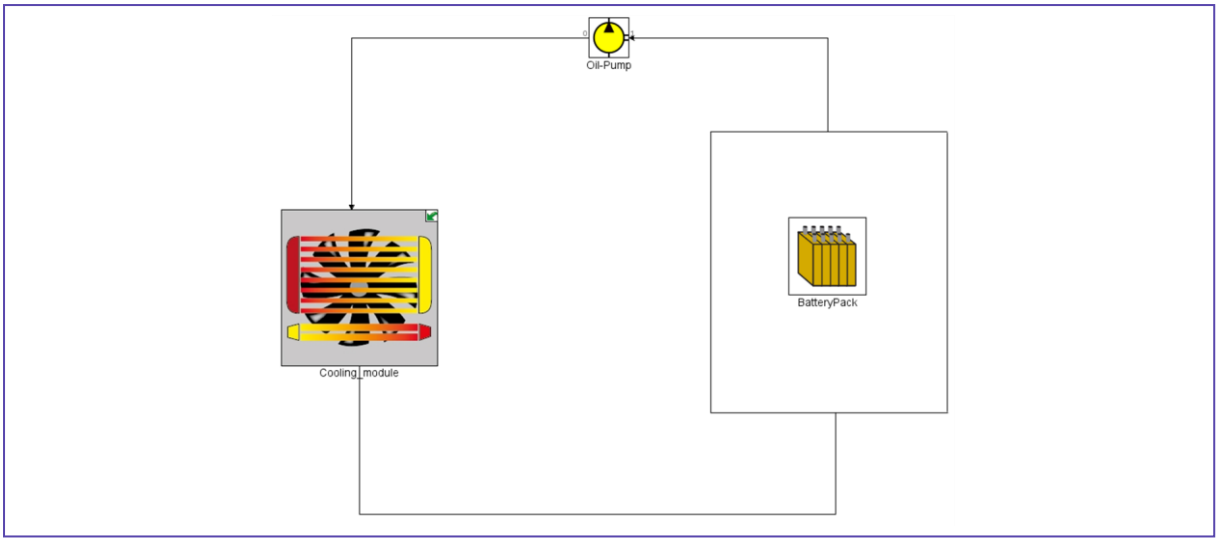

Figure 8: *Schematics of Direct immersion cooling system [6]*

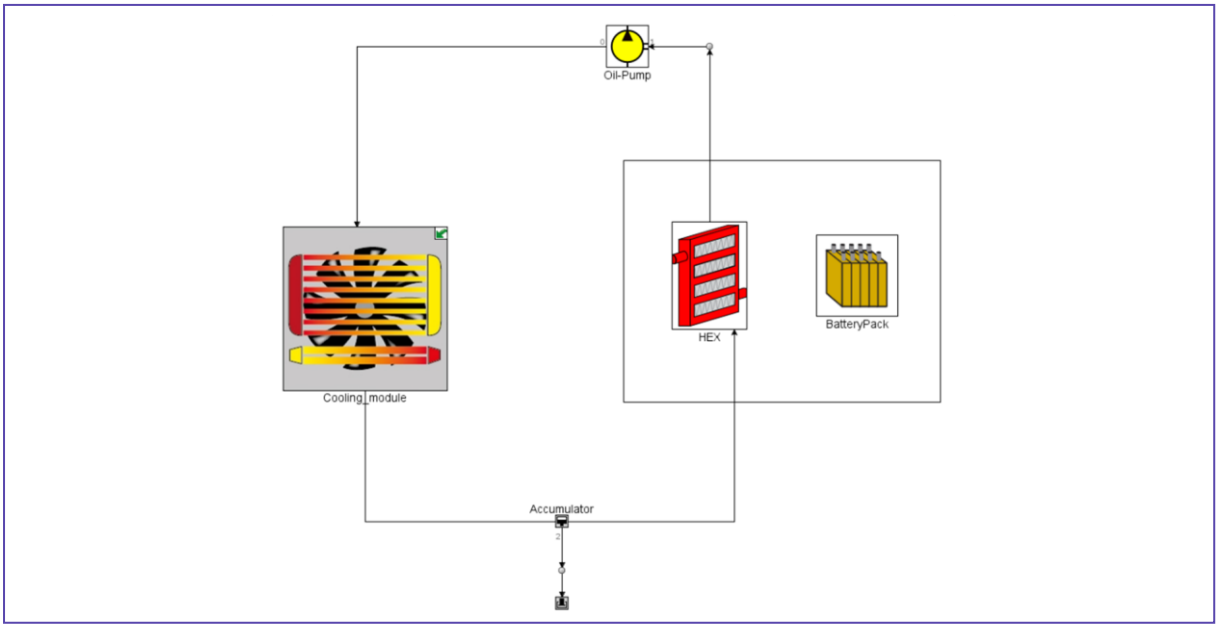

Figure 9: *Schematics of Indirect immersion cooling system [6]*

On the other hand, the immersion cooling does have some significant disadvantages. Thermal system with such us layout is much more complex and does need unique or additional sub-components. It adds extra weight to car body with large oil pan for battery pack and weight of additional fluid including dielectric oil (50 – 200 L per application). It would affect service and maintenance of BEV during lifetime.
The architecture of immersion cooling systems, both direct or indirect, needs new HEX and as the concept is very fresh, the design concept of HEXs is very fluid. Hanon Systems considers well known aluminium HEXs optimized to immersion cooling as

well as more revolutionary HEXs from plastic materials (chapter 2.2). Aluminium tube and fin design seem to be applicable for O-LTRs. This design (air-to-oil HEX) shows best ratio between thermal performance and pressure drop. The simulated and measured data [6] show reduction in thermal performance compared to similar tests with coolant and increase of the inner pressure drop. Those observations are valid for large portfolio of radiator tubes (18,5 – 36,4 mm tube depth). Both parameters, lower heat rejection and higher oil pressure drop, will negatively affect system performance of direct immersion cooling and therefore complete system have to be balanced including power of oil pump.

Figure 10: *Aluminium brazed O-LTR for direct immersion cooling at calorimeter during performance & pressure drop test [6]*

Indirect immersion cooling system consists of two circuit. One circuit with coolant is conventional as all the components are well known. The focus is therefore with coolant-to-oil HEX as this is new and it is key to make immersion cooling effective. The essential part of this cooler is available package space. For optimal function cooler should be placed inside the oil pan very close to batteries or ideally it shall create complete envelope around the battery pack. Of course, the cooler can be placed outside the oil pan and supply oil pan & batteries with heat transfer media flow, but such arrangement will be less effective due to additional pressure drop and mainly not optimal heat treatment of every single battery cell (larger temperature gradient between cells).

Figure 11*: Aluminium brazed tube-fin heat exchanger for indirect immersion cooling, full size of approx. 1200 x 1600 mm, 10,8mm thickness [6]*

The heavy batteries in BEVs are mostly located under vehicle floor to keep centre of gravity as low as possible. The oil pan with batteries is expected to be in similar position. For such arrangement and for application with high capacity of batteries a solution using several large and thin aluminium tube-and-fin radiators is very effective [6]. To optimize heat rejection of 2-4x radiators in size of approx. 1 200 x 400 mm and keep temperature gradient on the batteries within ± 1 K it is essential to evaluate combination of parallel and counter flow configurations. For some of the applications only one radiator of extreme size (active core of 1 200 x 1 600 x 10,8 mm) may work the best considering optimal heat rejection, lowest pressure drop and battery cell cooling uniformity (see pictures 11 & 12).

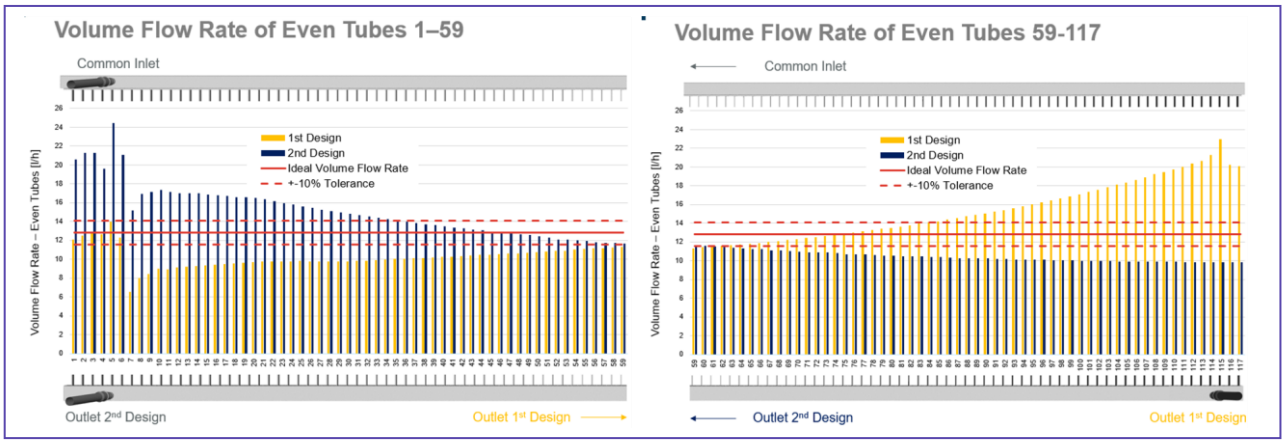

***Figure 12**: Flow simulation, tube-fin heat exchanger, full size of approx. 1200 x 1600 mm, 10,8mm thickness [6]*

2.4 COOLING LIQUIDS

For optimal design of any HEX and evaluation though measurement at calorimeter a cooling liquid is essential. Most applicable thermo-physical properties are reviewed and compared in Table 1 and Figure 13 & 14 for pure water, glycol-based coolant, typical transmission oil and two examples of newly developed dielectric oil for BEV cooling.

Liquid	Density [kg/m^3]	Heat capacity [kJ/kg.K]	Thermal conductivity [W/m.K]	Kinematic viscosity [mm2/s]	Dynamic viscosity [mPa.s]
Water (100%)	998,1	4,190	0,5950	1,00	4,30
Water-glycol (50 / 50 %)	1 068,6	3,310	0,4156	1,00	4,60
Oil for transmission	858,5	1,892	0,1356	73,82	63,37
Dielectric oil I.	805,0	2,180	0,1430	19,40	15,60
Dielectric oil II.	794,9	2,030	0,1396	9,28	7,38

***Table 1:** Table of thermo-physical properties for cooling liquids at 20°C [8], [9], [10], [11]*

Usually the pure water is supreme media for heat exchangers, but in technical practise a mixture with glycol is mostly used. Typically oils for lubrication performs significantly worse [12]. Lower density and reduced Heat capacity lead to 20-40 % reduction of heat rejection. The main impact on the cooling system is due to excessive pressure drop as

the viscosity of lubricant is extremely high mainly at low temperatures. The high pressure drop is reducing effectiveness of the pump and lowers down the volume flow to cooler, which leads to additional degradation of heat rejection. Dielectric oils are bringing not only lower electric conductivity, but improved thermo-physical properties. Those liquids stand in between standard lubricants and glycol-based coolants. Improved Heat capacity (approx. +15%) and reduced viscosity (approx.. minus 75-88%) makes immersion cooling systems much more thermal effective.

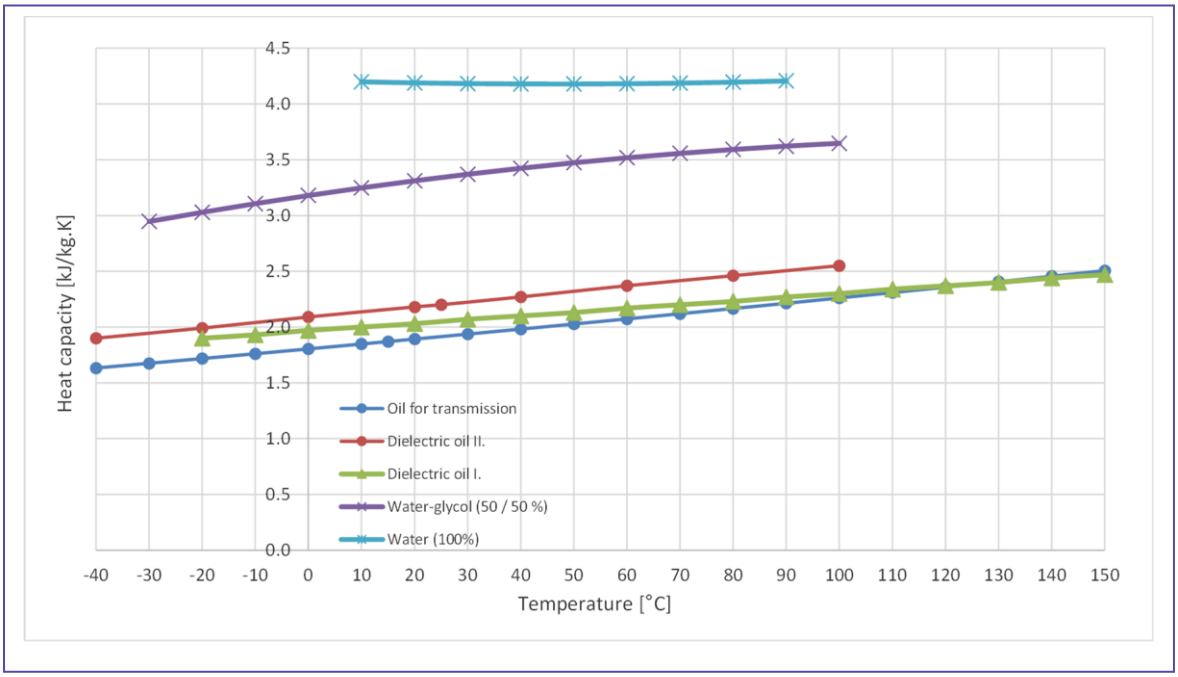

Figure 13: *Graph for Heat capacity per temperature for cooling liquids [8], [9], [10], [11]*

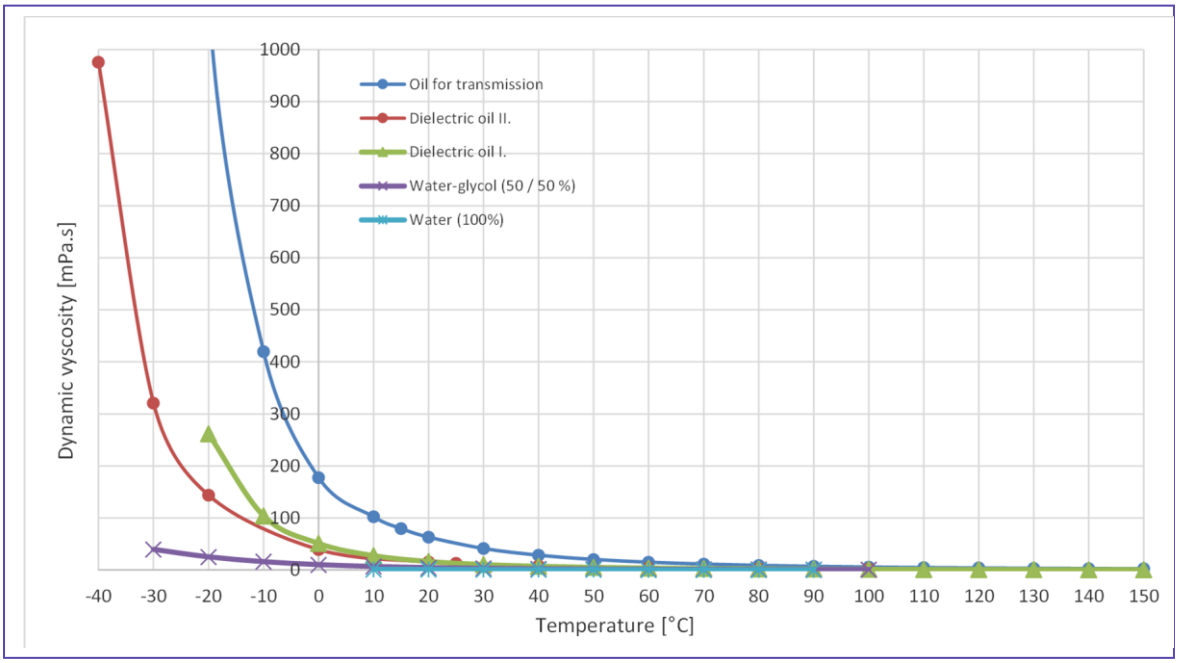

Figure 14: *Graph for Dynamic viscosity per temperature for cooling liquids [8], [9], [10], [11]*

3. CONCLUSION

This paper shows that investigation for alternative ways of cooling and/or alternative system architecture is relevant. Plastic HEXs shows potential up to 60% weight saving compared to aluminium made HEXs with comparable heat rejection. It allows usage of unique manufacturing methods (e.g. RIM or extrusion) to form very rare geometries of the HEX. Another alternative is to use a completely different cooling medium (dielectric oil) and utilize advantages of heat transfer though complete surface of battery cell to the surrounding liquid. The new component O-LTR is needed for direct immersion cooling and it needs a further investigation to reach optimal thermal performance and pressure drops. Mainly the tubes for dielectric oil and more effective heat transfer need to be optimized. The indirect immersion cooling needs coolant-to-oil HEX. This HEX will be unique for every application based on package and size of the oil pan and/or battery pack as well as it will be affected by oil flow pattern inside the oil pan. For some application large and thin planar aluminium brazed radiators would be optimal, while for different oil pan with complicated shape a hollow fiber coolers placed in every free space would be a best option.

REFERENCES

[1] [online]. In: . [cit. 2024-31-05]. Available from: https://www.schaeffler.com/en/media/dates-events/kolloquium/digital-conference-book-2022/thermal-management-system-electric-vehicles/

[2] [online]. In: . [cit. 2024-31-05]. Available from: https://www.emobility-engineering.com/ev-battery-cooling/

[3] ZARKADAS D.M., SIRKAR K.K., Polymeric Hollow Fiber Heat Exchangers. Ind. Eng. Chem. Res 2004, 43, 8093–8106, doi:10.1021/ie040143k.

[4] KUČERA J., HVOŽDA J., BARTULI E.; RAUDENSKÝ M., Polymeric Hollow Fibers Heat Exchangers and their potential application in automotive industry, KOKA 2023

[5] Technical reports for Technological Agency of Czech Republic, grant code TH04010031

[6] Hanon Systems Internal technical reports, 2018-2024

[7] [online]. In: . [cit. 2024-31-05]. Available from: https://www.heatlab.cz/

[8] Texaco corp., datasheet for water-glycol coolant

[9] Texaco corp., datasheet for Texamatic transmission oil

[10] Shell corp., datasheet for E-thermal fluids

[11] Mobil corp., datasheet for ThemElite oil

[12] HORÁK A., RAUDENSKÝ M., POHANKA M., BELLEROVÁ H., REICHARDT T., Research on cooling efficiences of water, emulsions and oil, Journal of Metallurgical and Mining Industry, 2010, Vol. 2, No.4, pp. 271-278, ISSN 2076-0507

ACKNOWLEDGEMENT

This work was supported by PD organization of Hanon Systems Autopal Services, sro, Czechia.

TECHNICKÁ UNIVERZITA V LIBERCI

55. mezinárodní vědecká konference zaměřená na výzkumné a výukové metody v oblasti vozidel a jejich pohonů

září 5. - 6., 2024 – Liberec, Česká republika
Technická univerzita v Liberci
Fakulta strojní, Katedra vozidel a motorů

APPROACHES TO MODELLING NO_X EMISSIONS FOR NH_3 ENGINES IN GT-SUITE

Štěpán Kyjovský[1], Valery Martyuk[2]

Abstract
Although far from a new idea, ammonia (as a hydrogen carrier) has recently re-emerged as a zero-carbon fuel for internal combustion engines. Direct combustion of ammonia is possible, albeit difficult. However, issues with modelling and prediction of the nitrogen oxides emissions arise, as the popular Zeldovich model does not account for the fuel bound nitrogen. Apart of the NOx thermal pathway included in the Zeldovich model, ammonia oxidation is accompanied by multiple other pathways for both production and consumption of different nitrogen oxides. This article covers the possibilities of modelling these phenomena in GT-SUITE using chemical kinetics in the burned zone and neural networks.

[1] Štěpán Kyjovský, Gamma CAE Technologies s.r.o., Dobrovského 1076/36, Praha, s.kyjovsky@gtisoft.com
[2] Valery Martyuk, Czech Technical University, Technická 4, Praha, valery.martyuk@fs.cvut.cz

1. INTRODUCTION

Ongoing concerns about human impact on climate are fuelling demand for carbon-neutral technologies. In the transport sector this is represented most notably by battery electric vehicles (BEV) and fuel cell electric vehicles (FCEV). However, both these technologies currently face limitations hampering their widespread adaption, furthermore their deployment in some applications seems currently unlikely. This conundrum strengthened the demand for zero carbon fuels for internal combustion engines (ICE), representing a reliable and mature technology.

As an answer to this call hydrogen reemerged as a possible fuel for ICEs with its many beneficial properties, most notably wide flammability limits – allowing for very low NOx emissions production, and no carbon content resulting in zero CO2 emissions [1]. Unfortunately, storage and transportation of hydrogen is complicated, while simultaneously achieving near zero NOx emissions and good drivability requires extreme levels of boosting.

To address some drawbacks of hydrogen, other fuels that could be considered hydrogen carriers are investigated, such as e-fuels and ammonia. So far, the e-fuel production seems to be costly and requires a source of carbon. The ammonia production is currently dominated by the mature Haber-Bosch process and there is abundance of nitrogen present in atmosphere. While production of ammonia appears to be less complicated, it poses a challenge for engine applications with its low heating value, low flame speeds and complex pathways for emission production [2].

While flame speeds and heating values are a practical complication, the emission production pathways are modelling issue and with the limited amount of experimental data available, modelling of ammonia engines is of high interest. As equilibrium chemistry is not enough to model NOx emissions in ICEs, the Zeldovich (1) mechanism is common practice in modelling where NOx predictions are required [3].

$$\begin{aligned} O + N_2 &= NO + N \\ N + O_2 &= NO + O \\ N + OH &= NO + H \end{aligned} \tag{1}$$

The results of Zhang et al. [4] illustrate that for combustion of ammonia there are multiple pathways leading to both NOx production but also depletion. Looking at (1) we observe that Zeldovich mechanism only considers the $\mathrm{N} + \mathrm{O}_2/\mathrm{OH}$ pathway, disregarding the paths originating from NH and NH_2 radicals (Figure 1).

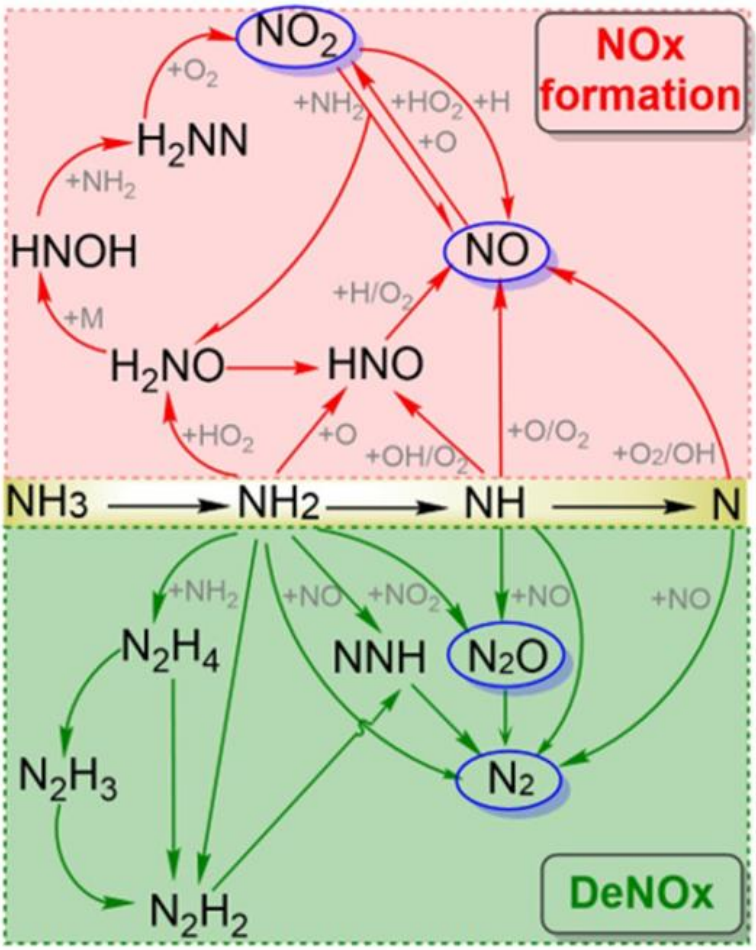

Figure 1: *NOx formation and depletion pathways in NH_3 oxidation. Reproduced from [4]*

It is evident that the Zeldovich mechanism is insufficient to model NOx emissions production from ammonia ICE. Accordingly a more complicated mechanism is required. Unlike the Zeldovich mechanism such mechanism must involve the oxidation of the fuel (ammonia) to evaluate concentrations of relevant radicals at each time step. With the increased complexity of the mechanism significant computational expense is expected driving a demand for an alternative approach.

This text investigates the possibilities of predicting NOx emissions from ammonia ICE using 1-D CFD tool GT-SUITE, using chemical kinetics and artificial neural networks (ANN) with an attempt to improve the runtime of the models.

2. MATERIALS AND METHODS

Following figures depict two methodologies investigated in this paper. The first one (Figure 2) directly couples the chemical mechanism for ammonia oxidation to multi cylinder engine model to calculate the engine out emissions.

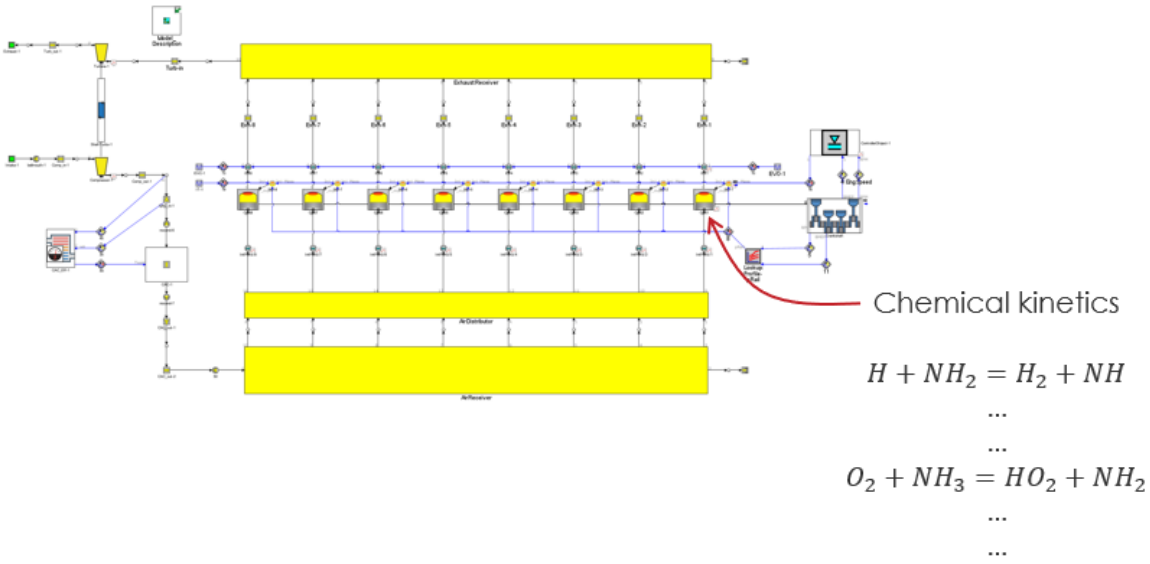

Figure 2: Direct coupling of chemical kinetics to multi cylinder engine model

In the second approach (Figure 3) we couple the chemical kinetics to simplified single cylinder engine model to generate cylinder-out emissions at different conditions (Table 1)[3], such model runs faster than the multi-cylinder model and allows for parallelization, being able to calculate the resulting 83 790 operating points in reasonable time.

This data is then used to train an artificial neural network with operating conditions as inputs and cylinder out emissions as outputs – in comparison to Table 1:

- pressure is replaced by the peak in-cylinder temperature

and additional inputs for:

- combustion phasing (CA50),
- duration (CA10-90)
- and residual fraction

are considered in the ANN training.

Finally, the neural network is coupled to the multi cylinder engine model (without chemical mechanism) actuating the cylinder-out emissions at exhaust valve opening. Drawback of this procedure is that it provides a single integral value for given set of integral inputs and therefore it can only provide cycle resolved emissions but can't provide crank angle resolved emissions concentrations in the cylinder. Also, since it provides a single value, individual ANNs have to be trained for each emissions component.

[3] For this investigation the backpressure was calculated using polynomial correlation fitted to data from the multi-cylinder engine model. While this lowers the number of operating points, it also limits predictivity in cases where the backpressure would vary significantly from the original model (i.e. turbo-matching studies)

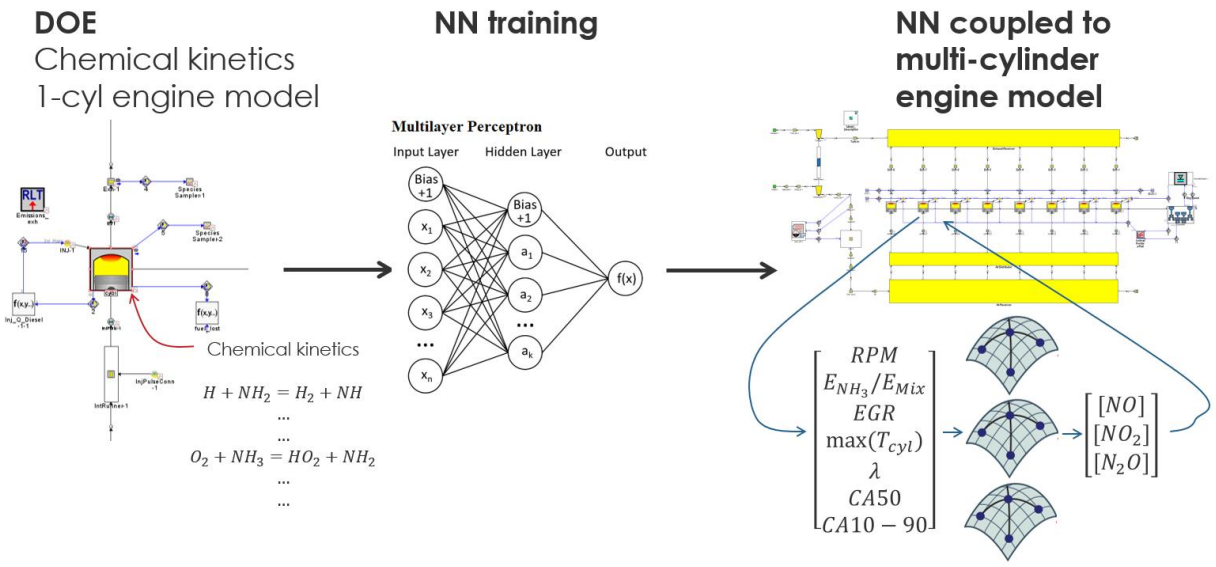

Figure 3: Process of utilizing neural network for engine out emissions

Parameter	Investigated range
RPM	[70,125] RPM
Inlet pressure	[1.05,5.3] bar
Start of injection	[0,15] bTDC
Air excess ratio	[0.7,2.5]
NH_3 energy fraction	[0.1,0.95]

Table 1: DOE parameters and ranges

2.1 1-D Engine Models

All results were obtained with 1-D CFD GT-SUITE model of two-stroke dual fuel (diesel/ammonia) marine engine. The engine is fuelled with ammonia in the intake port and the ignition is obtained by a pilot diesel injection. Parameters of the engine are in Table 2. Simplified single cylinder model of the engine is used to generate data for training of the artificial neural network.

Displacement 1-cyl	402 l
Bore/Stroke	500/2050 mm
Compression ratio	12
Ignition source	Diesel pilot
Fuel	Diesel + Ammonia

Table 2: Engine parameters

2.2 Chemical kinetics

The utilized chemical mechanism was developed by Liu et al. [5] for ammonia/n-heptane oxidation including 675 species and 3019 reactions. The chemical mechanism is used to calculate composition of the burned zone at each time step yielding emissions concentrations and heat release. While the combustion (as a transfer of mass from unburned zone to the burned zone) is governed by the Dual Fuel model in

GT-SUITE. This differs from a standard GT-SUITE engine simulation, where the burned zone chemistry would be governed by equilibrium chemistry.

2.3 Artificial neural network

Post processing tool of GT-SUITE (GT-POST) is used for the training of artificial neural network. In this context, ANN acts as a tool for nonlinear regression without understanding of the system. The trained ANN can be exported from GT-POST as .mmp file and plugged into the model through MetamodelHarness template which then feeds values to the Emissions map object in Engine Cylinder. Alternatively, the ANN can also be exported as .c code. Details about ANN training in GT-POST can be found in [6].

3. RESULTS AND DISCUSSION

To validate the training of neural network Figure 4 compares the engine-out NOx emissions of the single cylinder model using either chemical kinetics or neural network at full load and different engine speeds. We can observe that the approach using ANN to actuate cylinder-out emissions can follow relatively closely the results calculated using chemical kinetics directly. The error for NO is within few percent, while the relative error for NO_2 and N_2O can be 10-20% for some points, the absolute error is still within couple of ppm, which is an error that could be easily outweighed by measurement uncertainties on an actual engine.

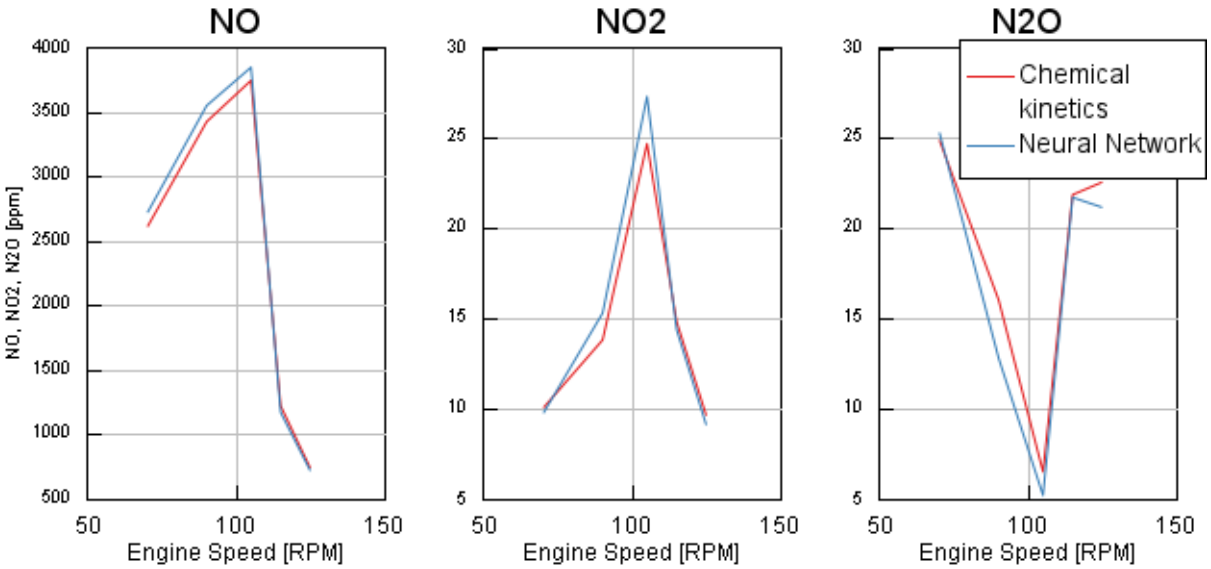

Figure 4: Emissions of the single cylinder engine predicted by direct solution of chemical mechanism against neural network

Figure 5 compares the engine-out NOx emissions of the multi-cylinder model using either chemical kinetics or neural network for emission prediction. The errors for lower engine speeds are within 2% while they increase to 10% at higher engine speeds. The Neural Network can still follow the trends very well and that is despite the fact the single cylinder model predicts lower emissions at identical operating points due to slower combustion (as can be observed from the comparison between Figure 4 and Figure 5) – seemingly that phenomena is sufficiently described by the selected ANN inputs.

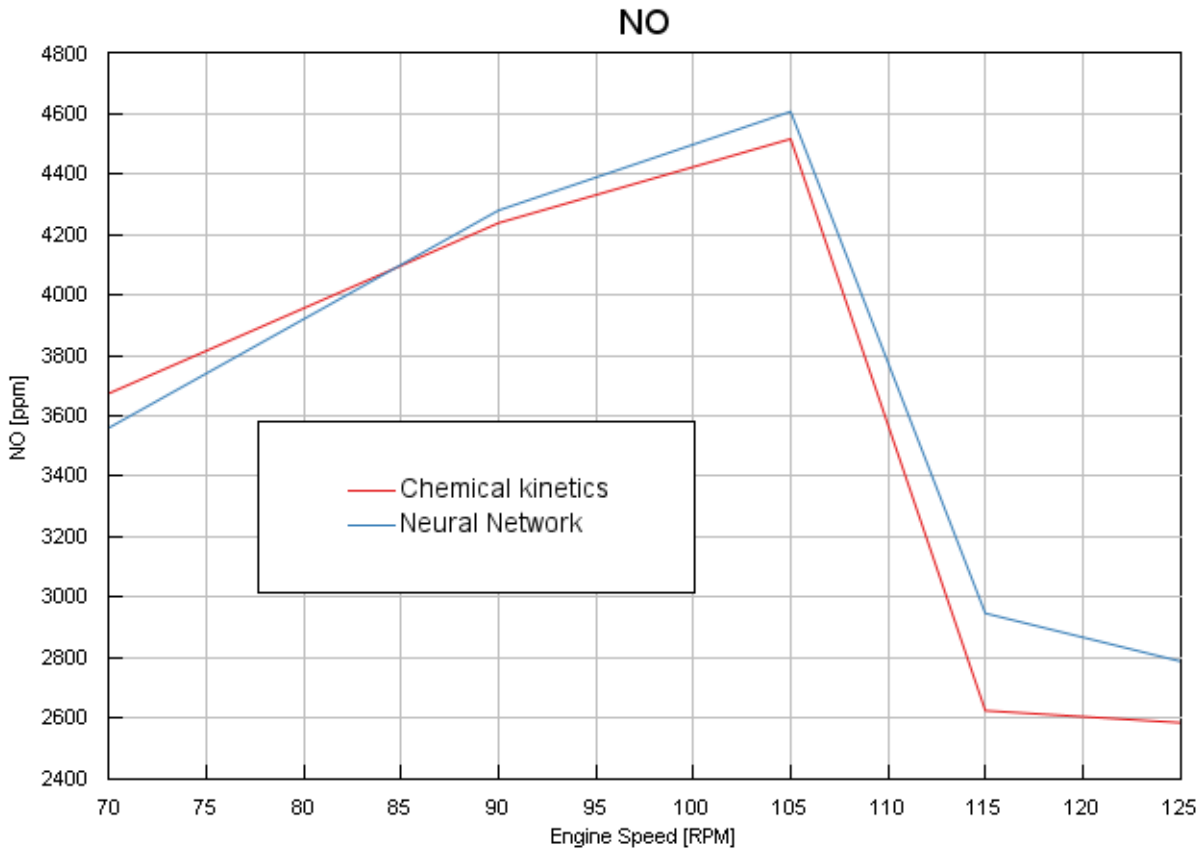

Figure 5: NO emissions of the multi-cylinder engine predicted by direct solution of chemical mechanism against neural network

As was expected, coupling the kinetic mechanism to the multi cylinder model results in an extremely slow running model restricting the use of the model for longer simulations such as drive cycles (or manoeuvres in the case of a marine engine). Considering for example a simple manoeuvre taking 80 minutes accelerating the ship from 5 to 13 knots, we can estimate the run time of different models. The factors of real time and computational time required for the specified manoeuvre for the models are in Table 3.

Model	Factor of real time	Manoeuvre computation time
Chemical mechanism	60	80 hours
ANN	1	1 hour 20 minutes

Table 3: Factor of real time of investigated models

Obviously, the data necessary for training of the ANN also require additional computational effort. In the presented study 83790 operating conditions were investigated on a single cylinder engine using chemical kinetics and the simulation took 63 hours on 20 cores. Unlike the multi-cylinder model with chemical kinetics, the generation of data for NN training can be easily parallelized.

4. CONCLUSION

The paper describes how NOx emissions in ammonia engines can be modelled in GT-SUITE using either chemical mechanism to solve the burned zone kinetics or actuating the cylinder-out emissions using ANN that was trained on a larger set of data generated beforehand using a simplified model.

The method utilizing ANN can replicate the results of chemical mechanism quite well and provides significant speed-up of the model. Such model can then be used for longer simulations like drive cycles and manoeuvres. Comparing the time needed to obtain results for a single manoeuvre using chemical kinetics, the approach utilizing neural networks can provide significant time savings, even when generation of the training data is considered. The extent of the time savings depends on the parallelization available. In the presented case, when running the simulation for training data on 20 cores, the total computational times was shorter than a single run of the manoeuvre with the multi-cylinder model including chemical kinetics. Also, the ANN can be reused for multiple simulations with the same engine, furthering its benefit.

When using neural networks for correlation there is no guarantee of quality results when extrapolating outside of the training data. Therefore, great care must be taken to ensure that training data reflect the intended use of the final model. Furthermore GT-SUITE allows enforcing limits on the Neural Network inputs when coupling it to the model using MetamodelHarness template.

Future work should focus on validating these methodologies on experimental data which are currently scarce.

REFERENCES

[1] Kyjovský, Š., Vávra, J., Bortel, I., & Toman, R. (2023). Drive cycle simulation of light duty mild hybrid vehicles powered by hydrogen engine. *International Journal of Hydrogen Energy*, *48*(44), 16885–16896. https://doi.org/10.1016/j.ijhydene.2023.01.137

[2] Elbaz, A. M., Wang, S., Guiberti, T. F., & Roberts, W. L. (2022). Review on the recent advances on ammonia combustion from the fundamentals to the applications. *Fuel Communications*, *10*, 100053. https://doi.org/10.1016/j.jfueco.2022.100053

[3] Heywood, J. (1988). *Internal Combustion Engine Fundamentals*.

[4] Zhang, X., Moosakutty, S. P., Rajan, R. P., Younes, M., & Sarathy, S. M. (2021). Combustion chemistry of ammonia/hydrogen mixtures: Jet-stirred reactor measurements and comprehensive kinetic modeling. *Combustion and Flame*, *234*, 111653. https://doi.org/10.1016/j.combustflame.2021.111653

[5] Liu, L., Wu, Y., & Wang, Y. (2022). Numerical investigation on the combustion and emission characteristics of ammonia in a low-speed two-stroke marine engine. *Fuel*, *314*, 122727. https://doi.org/10.1016/j.fuel.2021.122727

[6] Li, T., Ebrahimi, K., Gaukel, K., Roggendorf, K., & Fogla, N. (2024). Simulation study on laminar flame speed of Ammonia-Hydrogen blends using artificial neural networks. In *Proceedings* (pp. 241–255). https://doi.org/10.1007/978-3-658-44982-7_16

55. mezinárodní vědecká konference zaměřená na výzkumné a výukové metody v oblasti vozidel a jejich pohonů

září 5. - 6., 2024 – Liberec, Česká republika
Technická univerzita v Liberci
Fakulta strojní, Katedra vozidel a motorů

E-ASSISTED BOOSTING SYSTEM FOR H2 ICE

Valery Martyuk[1], Štěpán Kyjovský[2]

Abstract
Hydrogen internal combustion engine (H2 ICEs) powered vehicles offer the advantages of emitting zero carbon, while exploiting the existing infrastructure and the familiarity of conventional internal combustion engines. However, meeting near-zero emission targets is complicated. High AF ratios are required to limit production of NOx which requires high boost pressure. Lower exhaust gas temperatures and enthalpy makes turbo-matching complicated. To overcome these challenges, electrically assisted boosting system seems to be a reasonable solution. This paper explores advantages of e-Boosting systems utilizing comprehensive numerical analysis in 1D CFD solution GT-SUITE.

1. INTRODUCTION

Internal combustion engines (ICEs) have long been the predominant power source in the automotive and heavy-duty vehicle sectors. However, growing concerns about carbon dioxide (CO2) emissions and stringent regulations on pollutants have driven

[1] Valery Martyuk, Gamma CAE Technologies s.r.o., Dobrovského 1076/36, 170 00 Praha 7, v.martyuk@gtisoft.com
[2] Štěpán Kyjovský, Czech Technical University Prague, Technická 4, Praha 6, stepan.kyjovsky@fs.cvut.cz

the development of alternative propulsion technologies. Among these, battery electric vehicles (BEVs) and fuel cell electric vehicles (FCEVs) have gained traction. Despite these advancements, ICEs are expected to remain relevant for the foreseeable future due to their established infrastructure and ongoing technological enhancements.

Hydrogen, as a clean fuel, has garnered significant interest due to its potential to achieve near-zero CO2 emissions. When combusted in an ICE, hydrogen primarily produces water vapor, offering a substantial reduction in greenhouse gases compared to conventional fossil fuels. Nevertheless, hydrogen combustion presents unique challenges, particularly the need to maintain higher air-fuel ratios to mitigate NOx emissions. For hydrogen engines, a lambda value of 2.5 is often targeted to minimize NOx formation, which necessitates nearly double the air supply compared to diesel engines for the same power output [1].

This substantial air requirement complicates turbocharging strategies and exacerbates issues such as turbo-lag. Traditional variable geometry turbochargers (VGTs), while effective in many applications, struggle to provide the immediate air delivery needed for optimal hydrogen combustion, especially under dynamic operating conditions.

To address these challenges, this paper investigates the application of an e-assisted turbocharger (eTurbo) in a heavy-duty hydrogen internal combustion engine. The eTurbo integrates an electric motor to assist the turbocharger, offering rapid response and improved engine dynamics. Electrically assisted boosting has been successfully applied in high-performance applications, notably in Formula 1 since 2014. In this context, eTurbos have demonstrated significant advantages, including the elimination of turbo-lag, improved torque delivery at low engine speeds, and enhanced overall engine efficiency. These benefits make eTurbos an attractive solution for improving the performance and emissions characteristics of hydrogen-fueled engines.

This study utilizes a 1D CFD simulation model in GT-SUITE, focusing on a 6-cylinder, 11.7L, port-injected hydrogen engine. The model incorporates a predictive combustion model, extended Zeldovich mechanism for accurate NOx emissions prediction and control logic to optimize engine operation, including a knock control mechanism. The research methodology includes both steady-state and transient simulations. The steady-state analysis compares the performance of a standard VGT turbocharger with that of an eTurbo. Transient simulations are conducted to evaluate the dynamic response during load steps at constant engine speeds, assessing the potential for turbo-lag elimination. Additionally, the World Harmonized Transient Cycle (WHTC) is simulated to quantify NOx emissions reduction across a representative driving cycle.

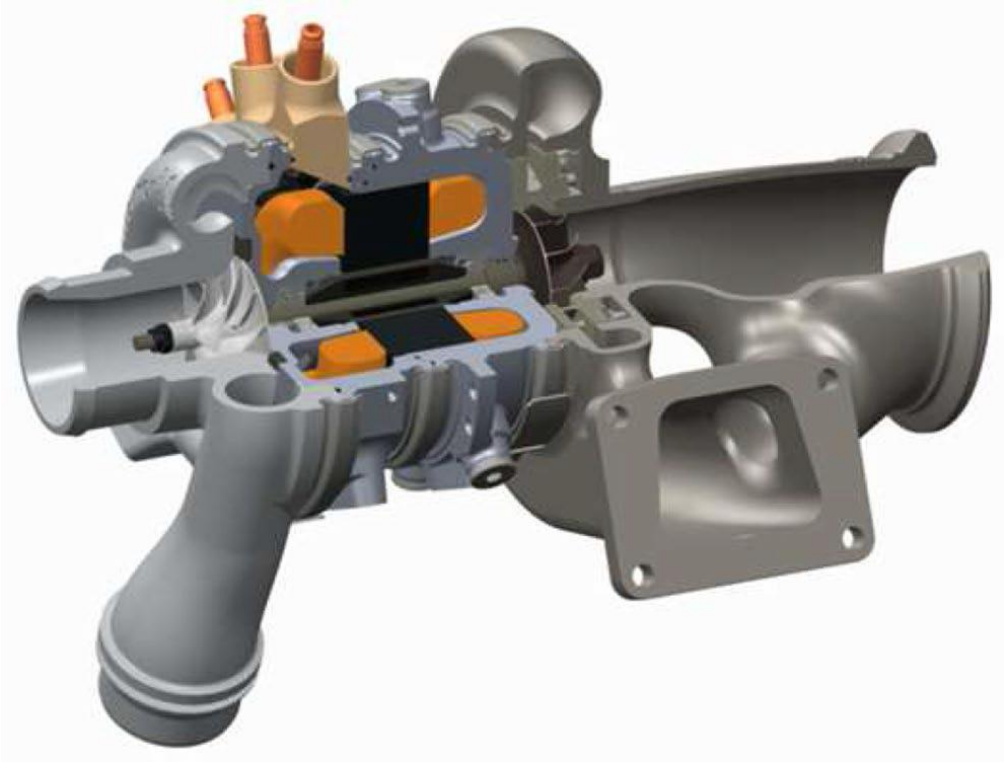

Figure 1: *BorgWarner eTurbo™* **[5]**

2. METHODOLOGY AND DESCRIPTION OF THE MODELS

A heavy-duty truck size engine is considered. This modelling activity sought to best combine the literature data and the values deriving from the authors' experience. Two models were prepared baseline with a standard single stage variable geometry turbine and same engine with eTurbo instead. In the first place steady-state simulations at different engine speeds and loads were made to generate engine performance maps. Subsequently models were modified to run transient simulations with loadsteps at constant speeds for driveability comparison and WHTC cycle. Electrical energy was considered as "free" here and is meant to be recuperated.

2.1 Baseline engine model

A 6-cylinder turbocharged engine derived from GT-SUITE example library was taken as a baseline. Initially diesel engine was modified to become a port injected, hydrogen fuelled engine partially calibrated to match mediocre engine of said size and application. In cooperation with Czech Technical University (CTU) measured data from experimental single cylinder engine was used to calibrate predictive turbulent combustion model. Combustion chamber properties were modified to comply with said engine, however base geometry was kept as in original diesel engine. Main characteristics are listed in *Table 1*. Engine was then calibrated to reach similar power and torque output as is expected from modern diesel engine of similar size.

	A
Engine type	SI, PFI, TC
Layout	R6
Bore x stroke [mm]	119
Total displacement [L]	175
Connecting rod length [mm]	300
Compression ratio	12
Max. brake power [kW]	240
Max. brake Torque [Nm]	1580

Table 1: *Main engine characteristics*

Turbocharger and its compressor and turbine maps were generated using *CompressorMapParam* and *TurbineMapParam* templates available in GT-SUITE. Single-stage variable geometry turbocharger was considered. *CompressorMapParam* template takes the compressor performance data from a single operating point and generates a fully extrapolated map using a set of physically-based parametric equations. This single operating point (referred to as the design point below) is assumed to be the peak efficiency point on the compressor map, and the inputs at the design point should be specified accordingly. These performance inputs may be specified either using typical performance variables (i.e. speed, mass flow, pressure ratio, and efficiency) or using non-dimensional parameters (i.e. Tip Speed Mach Number at Design Point, Work Input Coefficient at Design Point, Flow Coefficient at Design Point and Polytropic Efficiency at Design Point.). The method and correlations used to generate the compressor map are described in the paper from Casey and Robinson [2]. Turbine map is generated on a similar principle.

Load is controlled by model-based controllers. Throttle and rack controllers function as targeting controllers, analogous to the PID controller, but without the inconvenience of finding good gains for every operating condition. At every timestep, they calculate the rack position (or throttle position) based on several physical quantities of the engine and turbocharger system. Ignition timing is also adjusted during the run with a tuned PID controller acting as knock controller. Normalized knock induction time integral is targeted to 1 securing operation close to knock limit or an optimal value of CA50=8° ATDC.

Essential limitation of the turbocharger is compressor exiting gas temperature. Considering aluminum vanes, temperature was limited to 220°C. Another performance limit, due to lean mixture, is exhaust gas temperature which is relatively low (order of 500°C at full load) leading to low enthalpy and thus lack of available power for turbine. With this said for higher loads enrichment was applied with base lambda 2.5 linearly decreasing to 2 at 17 bar BMEP. That enrichment leads to increased NOx production penalty.

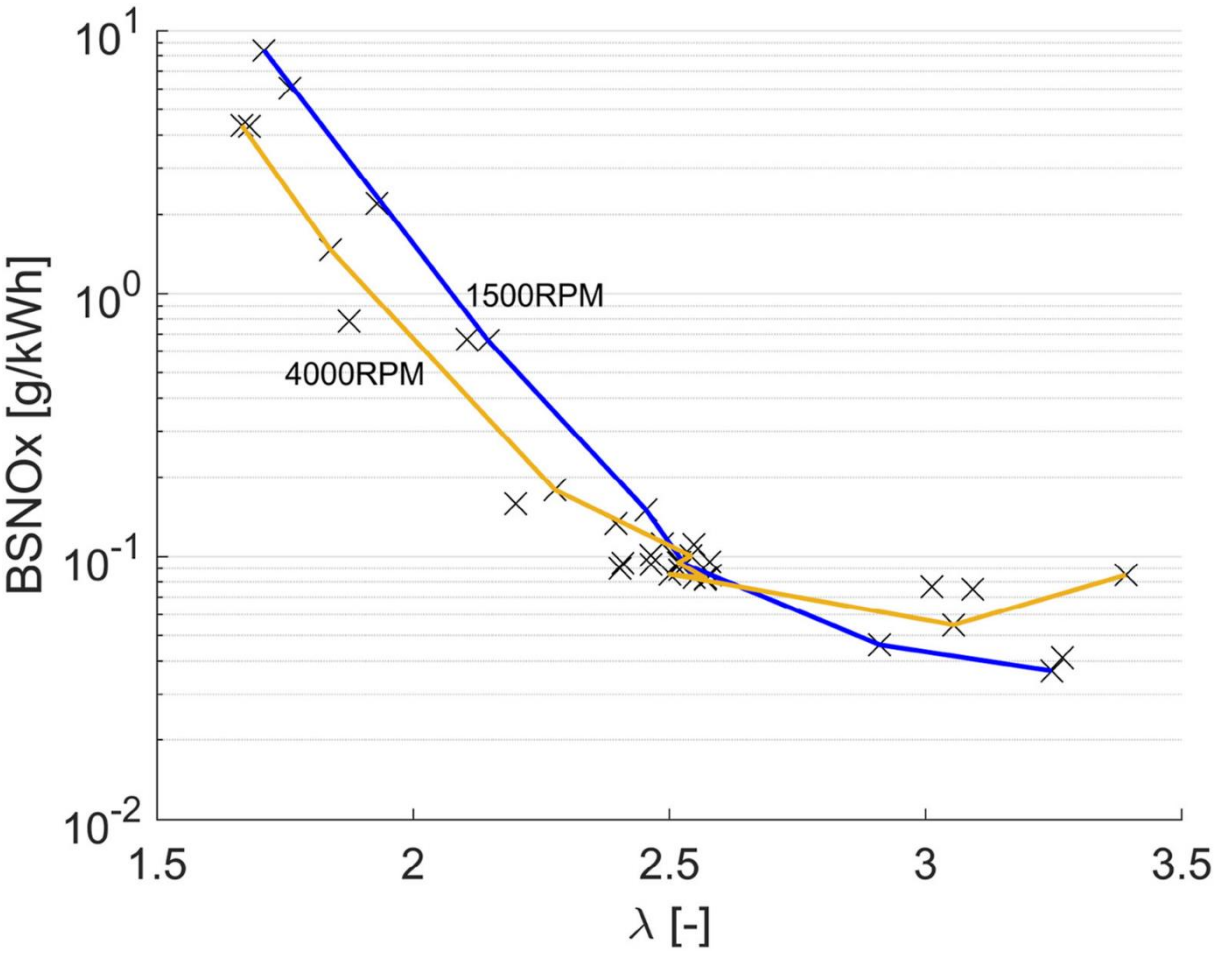

Figure 2: *Relation between air-excess ratio and measured NOx emissions* **[1]**

2.2 eTurbo engine model

Baseline engine was then equipped with eTurbo. Motor-generator with battery assembly was designed. Since electrical engineering side is not the focus of this paper, a simplified approach to modelling was chosen with electromechanical conversion efficiency map of the e-motor. Since application of e-assisted boosting on a hybrid vehicle is apparently most efficient, 48V system was chosen as a standard solution. 104 Ah battery with 14 serial and 8 parallel cells with 13Ah capacity was used. Electrical side was sized according to actual state of available technology limiting peak output power from battery to 40 kW [3].

Control strategy of eTurbo was developed. When requested load is low, boost pressure is controlled with rack position of VGT. However, contrary to a baseline engine, no enrichment was considered, hence engine is operated at constant lambda 2.5. When load request exceeds maximum possible load with just VGT, eTurbo controller is targeting requested load adjusting torque on a e-motor of eTurbo and rack controller is deactivated with rack moved to an optimal position resulting in lower back pressure, better gas exchange and thus higher efficiency. For a better comparison same compressor and turbine performance maps were used as in the baseline model.

3. RESULTS AND DISCUSSION

3.1 Steady-state comparison

Significant improvement in steady-state operation wasn't expected, however, due to specifics of H2 ICE, even here improvement is noticeable. Plots in *Figure 3* bellow show operation at full load. Engines full load curves were achieved with same limits (i.e. maximum temperature of exiting gas from compressor of 220°C and maximum back pressure of 4 bar).

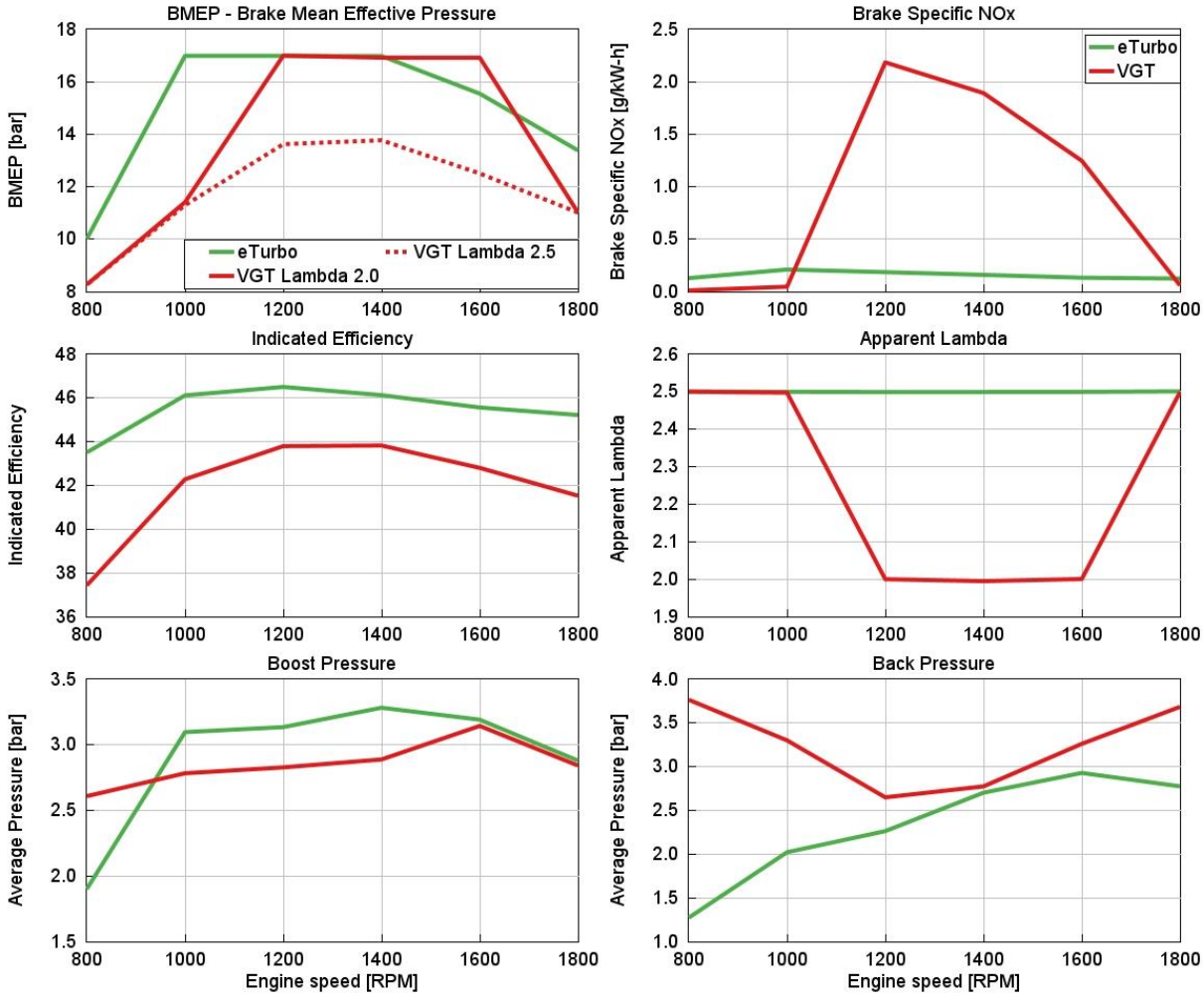

Figure 3: *Characteristics at full load*

As can be seen on a BMEP plot, with a conventional VGT turbocharger maximal achievable load is around 13 bar if λ is kept at 2.5 with no enrichment. Low end torque is limited due to lack of enthalpy in exhaust. Starting from 1200 RPM performance is limited with both exiting gas temperature and back pressure. That output if absolutely insufficient and therefore enrichment is necessary. With that approach, power output is comparable with a standard diesel truck engine, although low end torque is still affected with lean mixture low exhaust gas temperature and thus lack of available power on a turbine. Introducing eTurbo helps with low end torque, moving desired flat

torque curve towards lower engine speeds, however peak power is lower compared to VGT variant due to absence of enrichment and therefore necessity of higher boost pressure leading to higher compressor exiting gas temperatures.

Enrichment drastically increase NOx emissions which was expected based on measurements provided by CTU and simulation results corresponds well with these results.

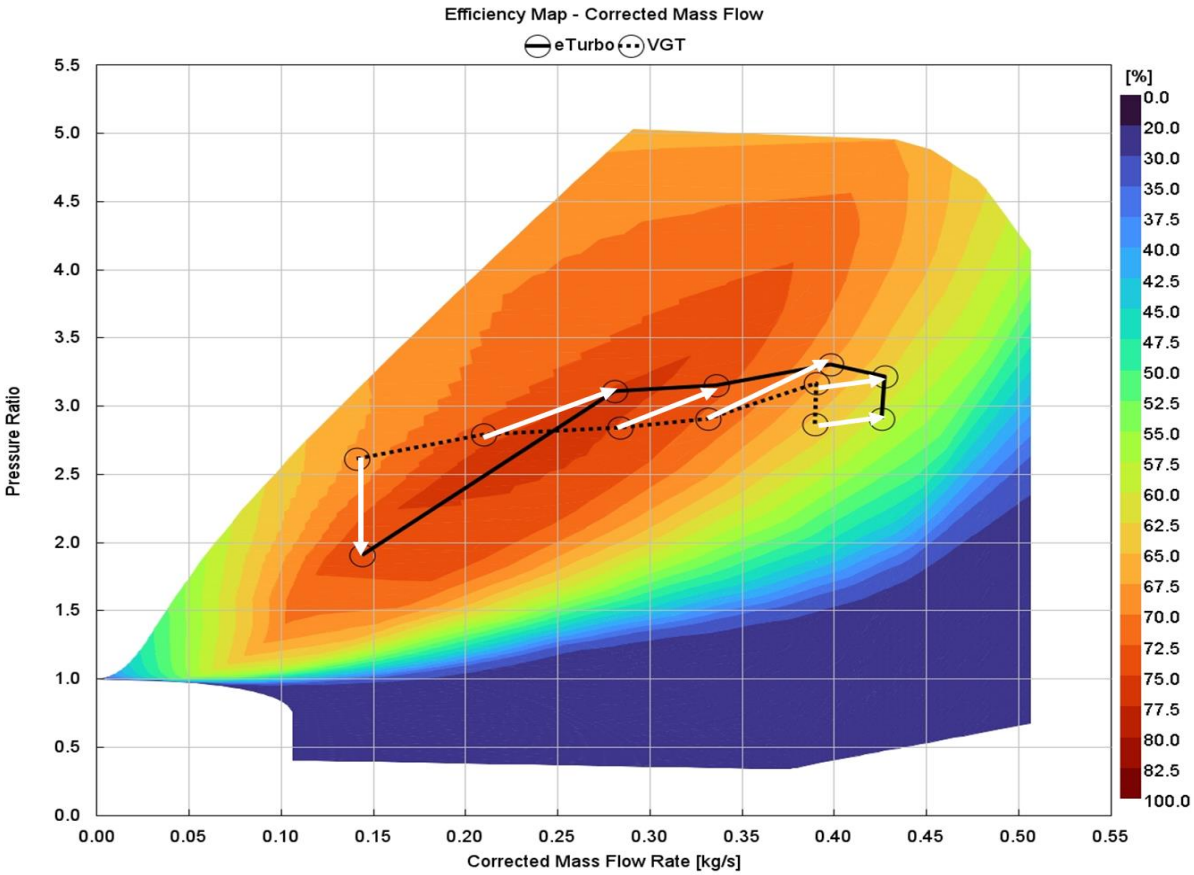

Figure 5: *Operating points*

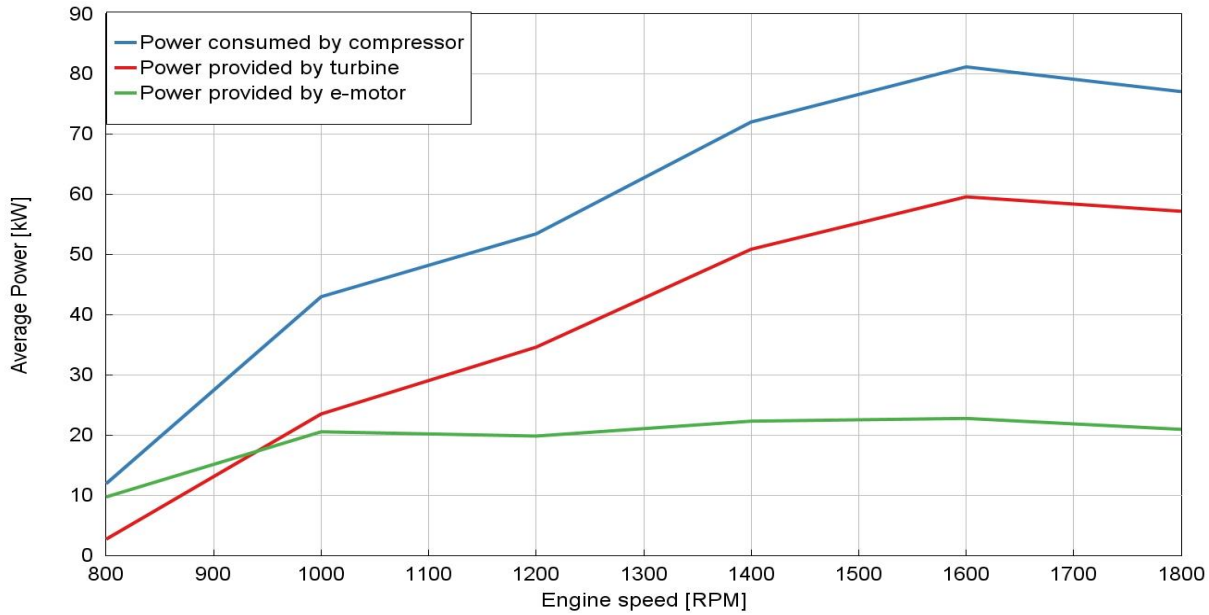

Figure 4: *Turbocharger power balance*

Another advantage brought by eTurbo is decrease of back pressure due to more opened rack position. That leads to substantial increase of indicated efficiency due to improved gas exchange. That effect is most noticeable at 800 rpm, where back pressure is reduced from mere 4 bar to 1.3 and higher BMEP is achieved even with lower boost pressure. Total efficiency is questionable though, since reduction of back pressure leads to higher demand on the eTurbo power though higher consumption of electrical energy that needs to be either recuperated or generated with motor-generator. However here we consider that energy to be provided by recuperation system and hence is “free”. Rack position at full load was optimized to give a reasonable compromise for power share between turbine and eTurbo.

3.2 Transient comparison

Driveability improvement is one of the main advantages of e-assisted boosting systems. Although in case of a truck engine driveability probably isn’t a main characteristic it’s still important. Loadsteps at constant speed show significant improvement in engine response time, reducing turbo-lag as shown in *Figure 6*.

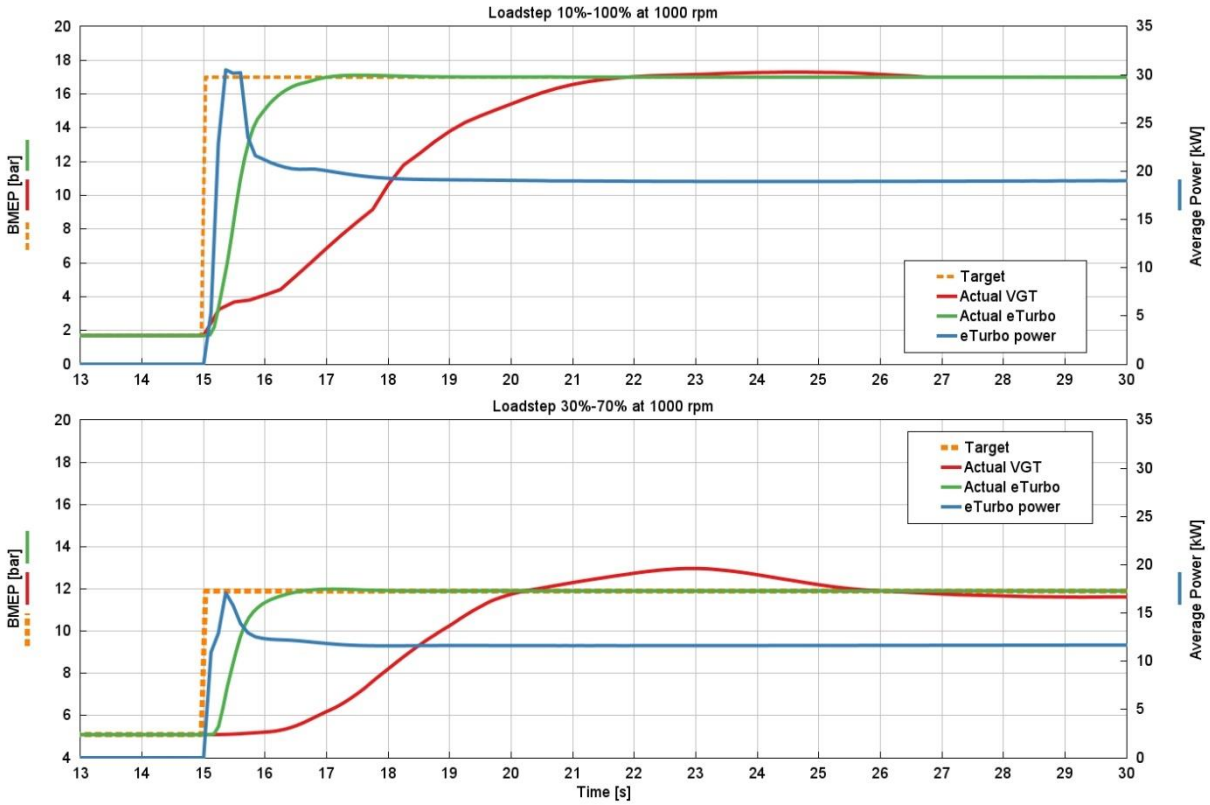

Figure 6: *Loadsteps*

Most interesting is comparison of driving cycle WHTC. Approximately first 1200 sec are not very demanding from load standpoint therefore NOx production is almost similar for both standard turbocharger and eTurbo, since VGT engine is operated bellow enrichment, however after 1200 sec load request is getting closer to full load and difference starts to be significant. In the end of the cycle difference between two

variants is almost 400mg NOx meaning reduction of NOx production by 20%. Slight increase of NOx production between 400 and 700 s is due to relatively dynamic change in load request when eTurbo is capable of almost instant reaction to these changes whereas VGT suffers from turbo-lag not reaching that target and staying at lower load, hence lower emissions.

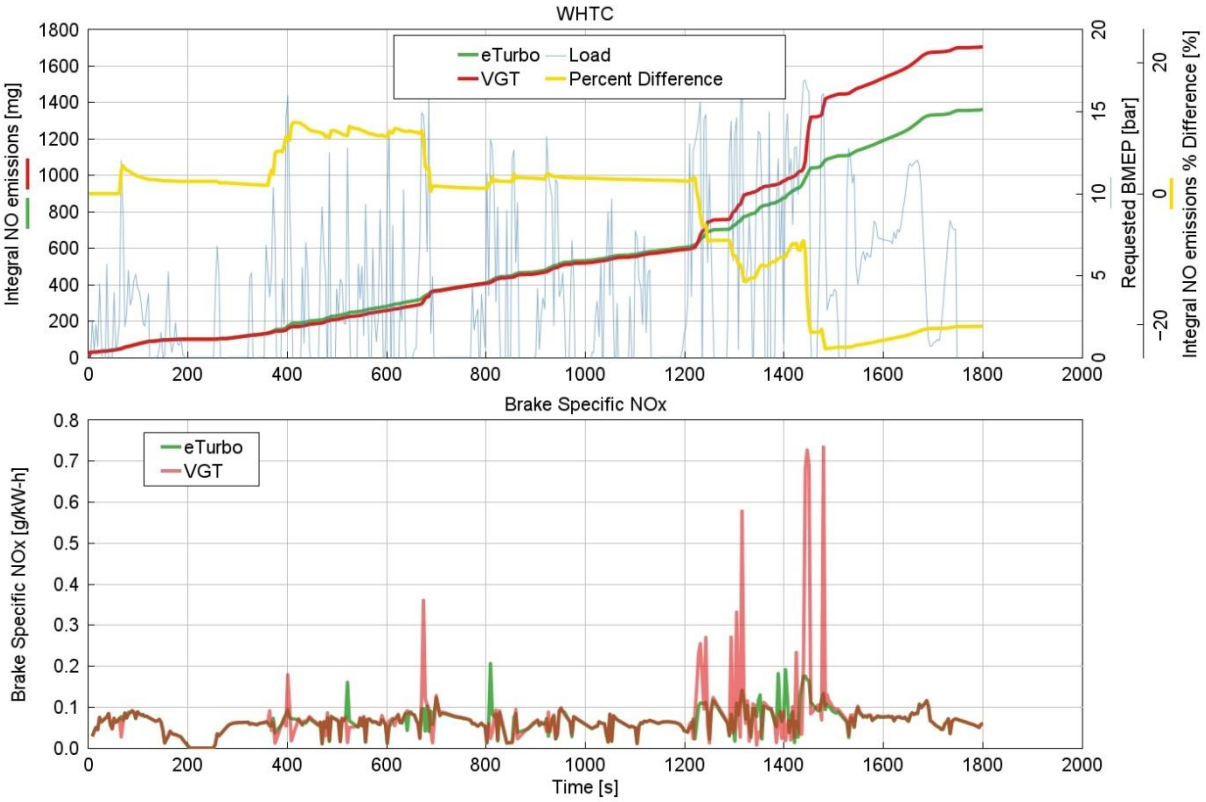

Figure 7: *WHTC cycle*

3. CONCLUSION

This study presents a detailed examination of the implementation and benefits of an electrically assisted turbocharger (eTurbo) in a hydrogen-fueled heavy-duty internal combustion engine. Using comprehensive 1D CFD simulations, we have demonstrated the eTurbo's significant advantages over traditional variable geometry turbochargers (VGTs).

The key findings from our research include:

1. **Enhanced Engine Performance**: The eTurbo effectively mitigates turbo-lag, providing a more immediate air supply that improves engine responsiveness and driveability, even under varying load conditions. This results in better torque delivery at low engine speeds, crucial for heavy-duty applications.

2. **Reduction in Emissions**: The optimized air-fuel ratio maintained by the eTurbo leads to a substantial reduction in NOx emissions. Our simulations of the World Harmonized Transient Cycle (WHTC) indicate a 20% reduction in NOx emissions

compared to the baseline VGT-equipped engine. This reduction is primarily due to the eTurbo's ability to maintain leaner combustion conditions without the need for fuel enrichment, which is a major source of NOx in engines.

3. **Improved Fuel Efficiency**: The decrease in back pressure facilitated by the eTurbo results in improved gas exchange and higher indicated efficiency. This is particularly evident at lower engine speeds, where the eTurbo reduces back pressure significantly and enhances BMEP.

In conclusion, the integration of eTurbo technology in hydrogen internal combustion engines represents a promising advancement towards cleaner and more efficient heavy-duty powertrains. The results of this study provide insights for future engine designs, highlighting the potential of e-assisted turbocharging to meet stringent environmental regulations while maintaining high performance. This research underscores the importance of continued innovation in boosting technologies to fully exploit the benefits of hydrogen as a sustainable fuel for heavy-duty applications.

REFERENCES

[1] J. V. I. B. R. T. Štěpán Kyjovský, “Drive cycle simulation of light duty mild hybrid vehicles powered by hydrogen engine,” *International Journal of Hydrogen Energy,* vol. 48, no. 44, pp. 16885-16896, 2023.

[2] M. a. R. C. Casey, “A Method to Estimate the Performance Map of a Centrifugal Compressor Stage,” *ASME Journal of Turbomachinery,* pp. Volume 135(2): 021034-1 - 021034-10, 2013.

[3] D. S. Lauer, M. Perugini, R. Weldle and F. G. (. Technologies), “48 Volt High Power – Much More than a Mild,” in *29th Aachen Colloquium Sustainable Mobility 2020*, 2020.

[4] BorgWarner, “https://www.borgwarner.com/technologies/electric-boosting-technologies,” 2024. [Online].

[5] A. Cooper, Bassett, M., Hall, J., Harrington, A. and et al., “HyPACE - Hybrid Petrol Advance Combustion Engine - Advanced Boosting System for Extended Stoichiometric Operation and Improved Dynamic Response,” *SAE Technical Paper,* no. doi:10.4271/2019-01-0325, 2019-01-0325, 2019.

55. mezinárodní vědecká konference zaměřená na výzkumné a výukové metody v oblasti vozidel a jejich pohonů

září 5. - 6., 2024 – Liberec, Česká republika
Technická univerzita v Liberci
Fakulta strojní, Katedra vozidel a motorů

AIR SPEED AND DIRECTION PROBE DESIGN AND CALIBRATION

Kamil Šebela[1], Michal Janoušek[2], Josef Štětina[3]

Abstract
For a proper design of the cooling packet, inputs are needed regarding the speed of the air and attack angle on vehicle. To measure air speed and attack angle in a real-scale vehicle, a pressure probe and an electronic module are designed. The probe is manufactured and characterised in a wind tunnel. Measurement is performed with air speeds from 5.8 to 40.1 m/s and attack angles from -46.08 to 46.08 °. Based on measured values, neural networks are trained, and air speed and attack angle are computed. For computing air speed and attack angle, measured ambient conditions are also used and air density is computed.

1. INTRODUCTION

In automotive testing and development, it is necessary to gain information and complement simulations with the real-world measurement. One of the most important

[1] Ing. Kamil Šebela, Brno University of Technology, Faculty of Mechanical Engineering, Institute of Automotive Engineering, Technická 2, Kamil.Sebela@vutbr.cz
[2] Ing. Michal Janoušek Ph.D., Brno University of Technology, Faculty of Mechanical Engineering, Institute of Automotive Engineering, Technická 2, Michal.Janousek@vutbr.cz
[3] prof. Ing. Josef Štětina Ph.D., Brno University of Technology, Faculty of Mechanical Engineering, Institute of Automotive Engineering, Technická 2, Josef.Stetina@vutbr.cz

areas of car design is related to car aerodynamics and thus resistances. This has a direct impact on fuel economy and car efficiency. While increasing the aerodynamic performance of the vehicle, some areas may suffer from reduced air supply. Cars with internal combustion engines increase overall drag by 5 – 10 % by using ambient air to cool the combustion engine and accessories [1].
For proper design of the car cooling packet, it is necessary to know the boundary conditions regarding engine performance, temperature limits of the components, and vehicle working conditions. As there are more and more stringent limits on vehicle pollution, and thus pressure to maximise efficiency, vehicles cooling packets are designed with lower margin to maximum considered design point. One boundary condition, that is sometimes neglected, is the angle of attack (AA) to the front vehicle face. During real-world driving there are never conditions like in aerodynamics tunnel with respect to flow stability and uniformity. The side wind or driving on a curved road causes air to approach the front of the car at a non-zero angle. This can cause different air distributions and AA on the heat exchanger (HX). When air is distributed at HX core nonuniformly, performance is deteriorated up to 25 % [2], [3] and air flow resistances increase due to the square relation with air speed. When HX is approached with non-zero air AA, performance also deteriorates [4], [5].
Air speed and direction are often measured with pressure probes, as they are inexpensive and robust compared to a hot wire or propeller anemometer. The simplest probe to measure air speed is Pitot probe [6]. This probe is fine for measurement with known air speed direction, however, when the car is moving, the air speed direction is not known. In small AA, it is possible to use a Pitot probe up to 20 ° within 1 % deviation from dynamic pressure [7]. By shielding the central tube according to Kiel design, it is possible to increase this working window to 40 – 55 ° [8] for open probes and up to 67 ° for closed probes [9]. For air speed directions measurement, different types of probes with multiple holes are used to sense air dynamic pressure at angled surfaces. The simplest one is the claw probe consisting of two separate tubes orientated at an angle towards the air stream. When the measured pressure difference is processed, AA can be determined.
The aim of this article is to make a sensor for measurement air speed and direction usable for vehicle measurement on the real scale using only two differential pressure sensors.

2. PROBE DESIGN AND CALIBRATION

Desing is separated into two standalone probes. One for sensing dynamic pressure and the other to measure dynamic pressure with respect to AA. The dynamic pressure measurement for air speed sensing should not depend on the yaw angle or should be at least not influenced at lower angles. This condition is met by the Kiel probe with open or closed design compared in Figure 1. There is clear that open style probe is less complicated to manufacture and can be built from common tubing. Due to these reasons, an open-design probe is manufactured.

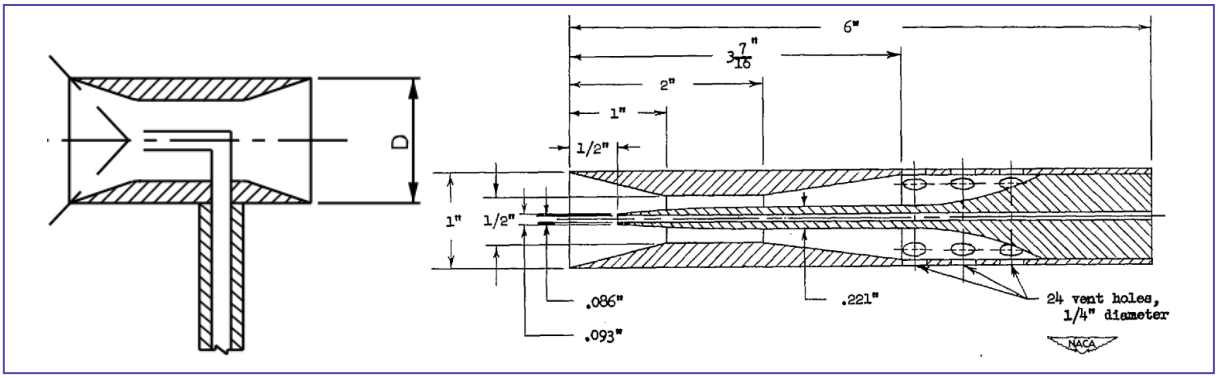

Figure 1: *Open style Kiel probe (left) and closed style probe (right) [10], [11]*

The second probe for yaw angle sensing consists of the two soldered tubes with a tip angle of 90 °, known as the claw probe. Spacing between probes is 15 mm and it is expected that no significant speed difference will occur in that distance. The complete probe design is shown in Figure 2 with important dimensions and details.

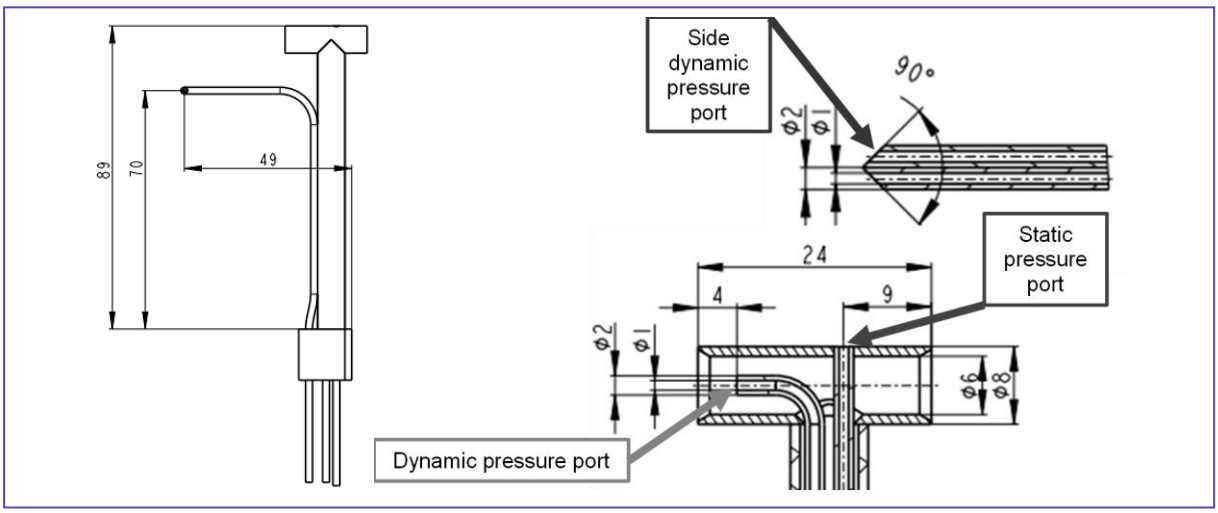

Figure 2: *Probes design and dimensions with details*

2.1 Probe calibration

The probe is calibrated in a closed-style wind tunnel with 500 × 700 mm measurement section dimensions and a length of 1 500 mm. Calibration is performed in steps with changing air speed and AA. The probe is positioned in the middle of the section and rotated using a step motor coupled with a pulleys with tooth belt for a finer angle setup. The probe is rotated with an increment of 3.84 ° from -46.08 to 46.08 °. The probe is turned and then the delay of two seconds is set to eliminate vibration or unsteady state measurement. For every AA are measured 200 points and then measurement continues with next AA. The air speed is set from 5.8 to 40.1 m/s with a 5 m/s increase. The wind tunnel with the inserted probe and the reference probe is presented in Figure 3. The reference probe is used for wind tunnel control and for initial probe check.

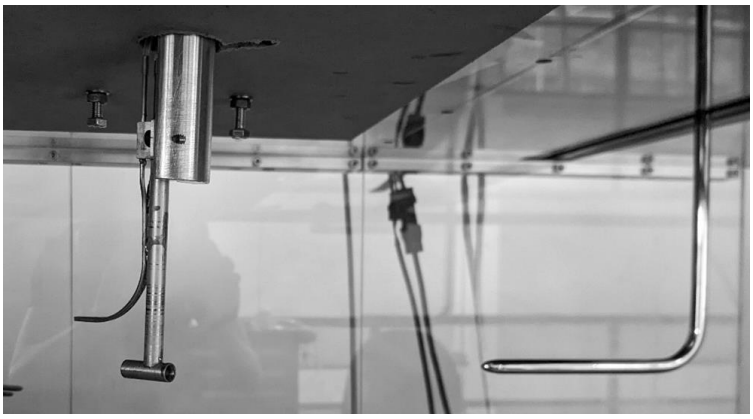

Figure 3: *Probe during calibration and tunnel pitot tube at right side*

2.2 Measured data post-processing

Measured data are processed for static characteristics and then for check and validation. For every angle and speed combination, 200 points are measured, which are averaged, and this value is used for regression. Averaging is especially important in higher AA, where oscillations are observed for the Kiel probe. The measured values are presented in Figure 4. There are two points selected for air speed 34.8 m/s and AA 0 and 42.24 °. From readings an average value is used and only differences from the average are presented. For null angle at Kiel probe there are only minor oscillations, however, at high angle pressure is oscillating as much as ± 7.8 %. The claw probe is less prone to oscillation in pressure, and there is no significant increase with increasing AA.

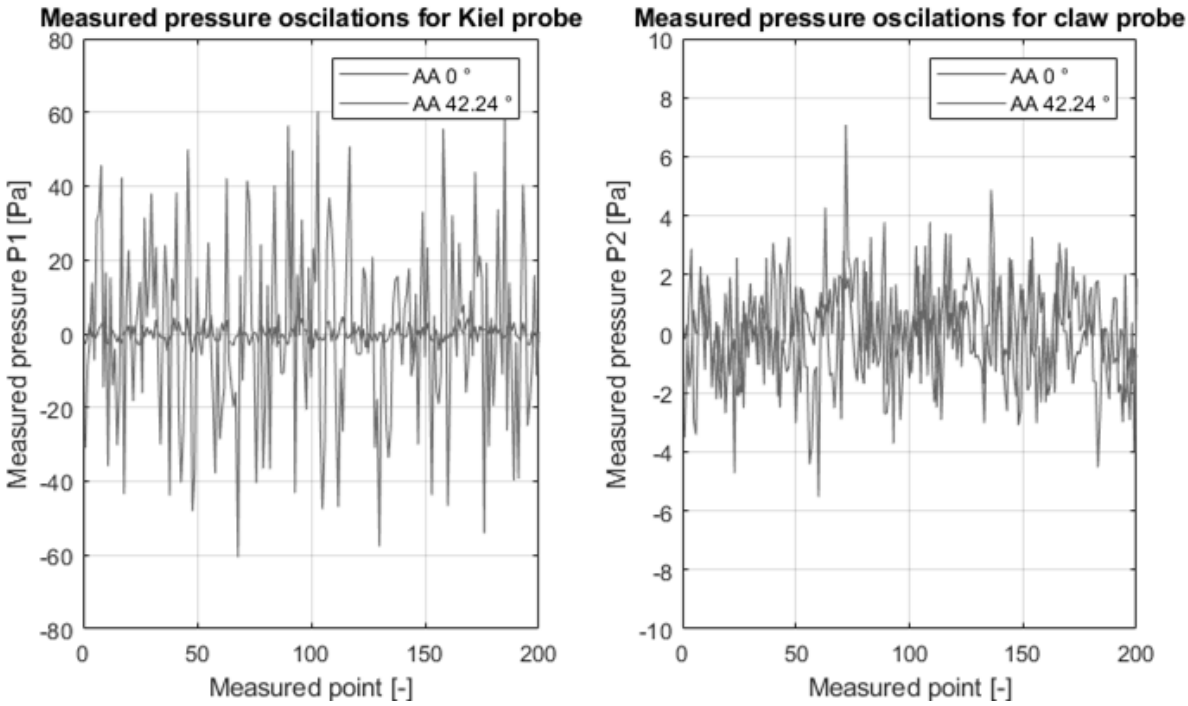

Figure 4: *Measured pressure differences for two points*

The standard deviation (STD) for the entire range of AA and air speed is plotted on Figure 5, computed from the measured pressure differences at each point. At small angles for the Kiel probe, the STD is lower than at higher angles. When speed and AA

are increasing, STD also is increasing. Dynamic pressures increase with square of the air speed and thus at higher speeds higher STD are expected. For claw probe, steady increase of STD with raising air speed is measured. A similar trend as for the Kiel probe is observed at higher AA, but not as steep increase is observed there. From computed STD are excluded not measured points due to error in positioner.

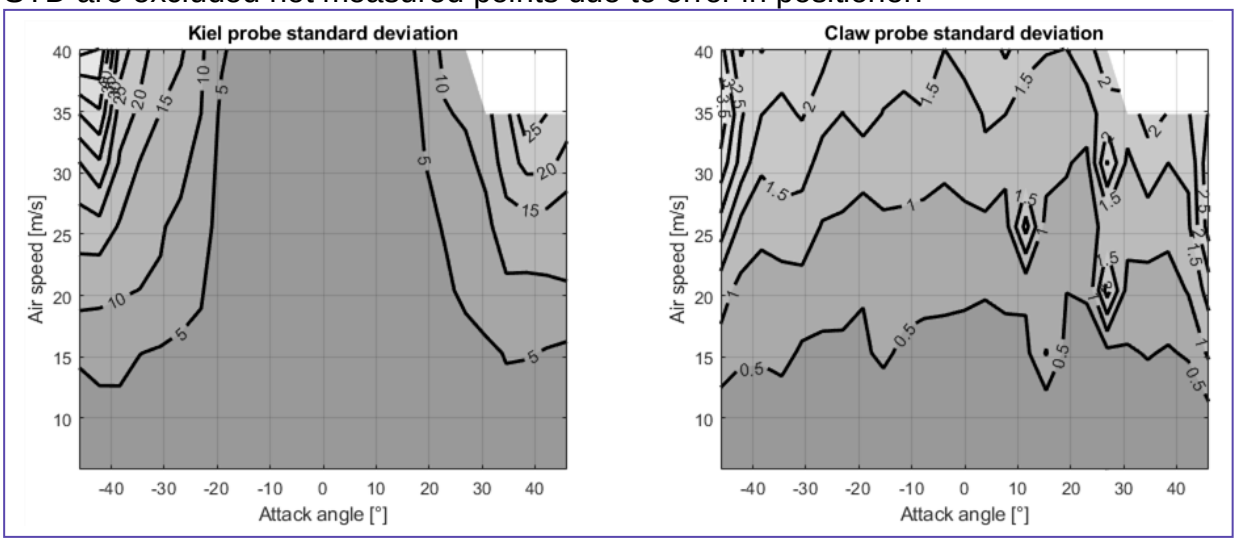

Figure 5: *Standard deviation for probes*

2.3 Probe characteristics

Characteristics are presented in *Cp*, which stands for coefficient of pressure equal to one for the Kiel probe aligned to air stream. For the claw probe *Cp* one equals reading dynamic pressure with pressure sensor. As AA changes, *Cp* is also changing. Ideally, it will be independent for the Kiel probe on AA, but this is only observed in the narrow AA window ± 10 ° for a difference less than 0.1 *Cp*. The claw probe intentionally is by design sensitive to AA and has a good response to AA for measured air speeds and AA. The measured values are symmetric, with zero *Cp* for null AA. The measured pressure difference at claw probe should be zero when the probe is aligned with air stream and if the probe is symmetric side-to-side.

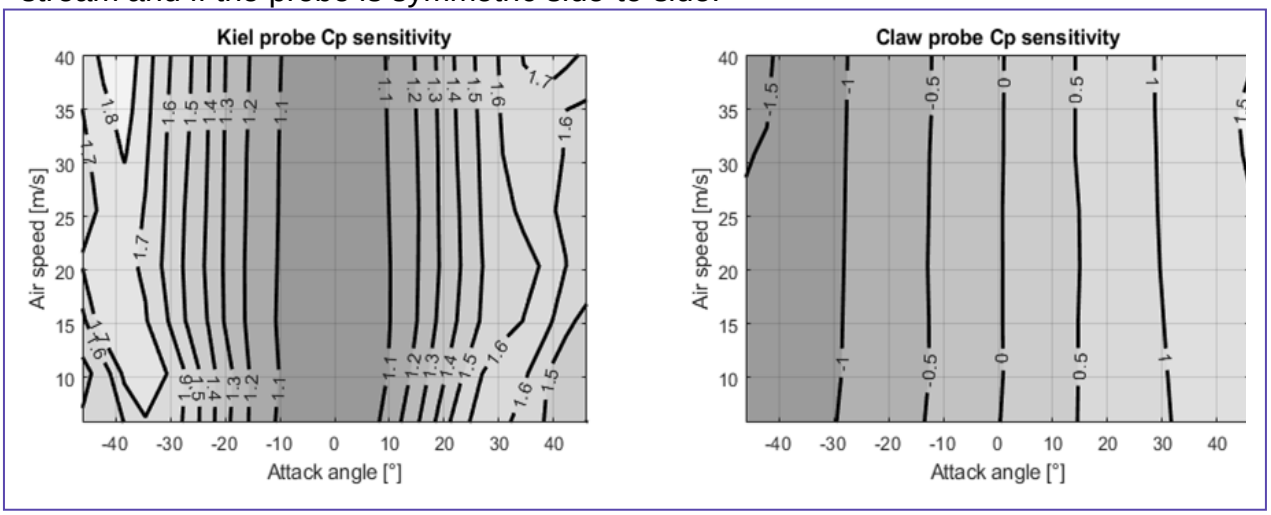

Figure 6: *Probes sensitivity to air speed and AA*

2.4 Air speed and angle computing

For computing air speed and AA, neural networks are trained on measured averaged values. The MATLAB application Regression learner is used with three inputs consisting of two pressure differences and air density. Based on these data, best-fit Gaussian process regression is used for AA and for air speed. The neural networks fit to the data are shown in Figure 7.

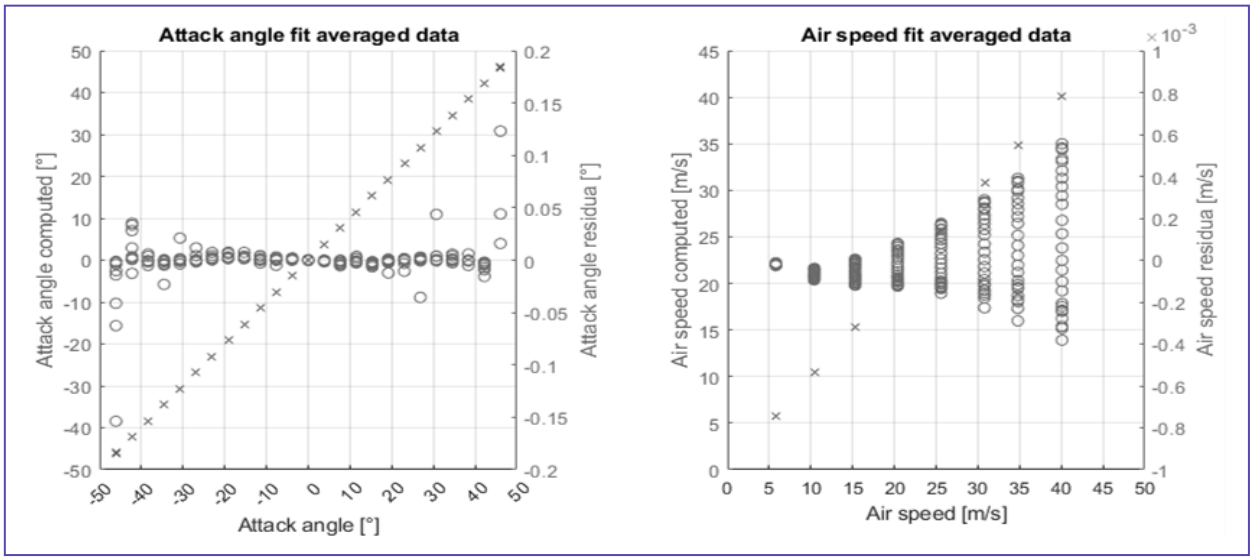

Figure 7: *Fit for averaged data with neural networks*

Neural networks work well to predict air speed and AA. With AA closer to zero, the difference between the measured and predicted angle is minor, even at the maximum AA, difference is lower than 0.2 °. For air speed prediction, there is increasing difference with air speed, but still even for maximum speed of 40.1 m/s is a difference lower than 0.0006 m/s. On the basis of these results neural networks are used for computing both air speed and AA.

2.5 Air speed and attack angle non-averaged data fitting

Based on measured data, AA and air speed are computed in the same way as intended for real usage. Two previously created neural networks are fed by two pressure differences and air density. The computed AA is more influenced by pressure reading of the Kiel probe and differences from the set value have a larger spread than expected on averaged data regression. Air speed, on the other hand, shows a similar trend as with averaged values. With increasing air speed, the difference increases, but there is only a small difference up to 0.0006 m/s, similar to average values. These comparisons for measured values show that for AA it is beneficial to measure more samples and averaging them to smooth out the final value. Air speed computing is not disturbed by oscillations such as AA and can be used without extensive averaging.

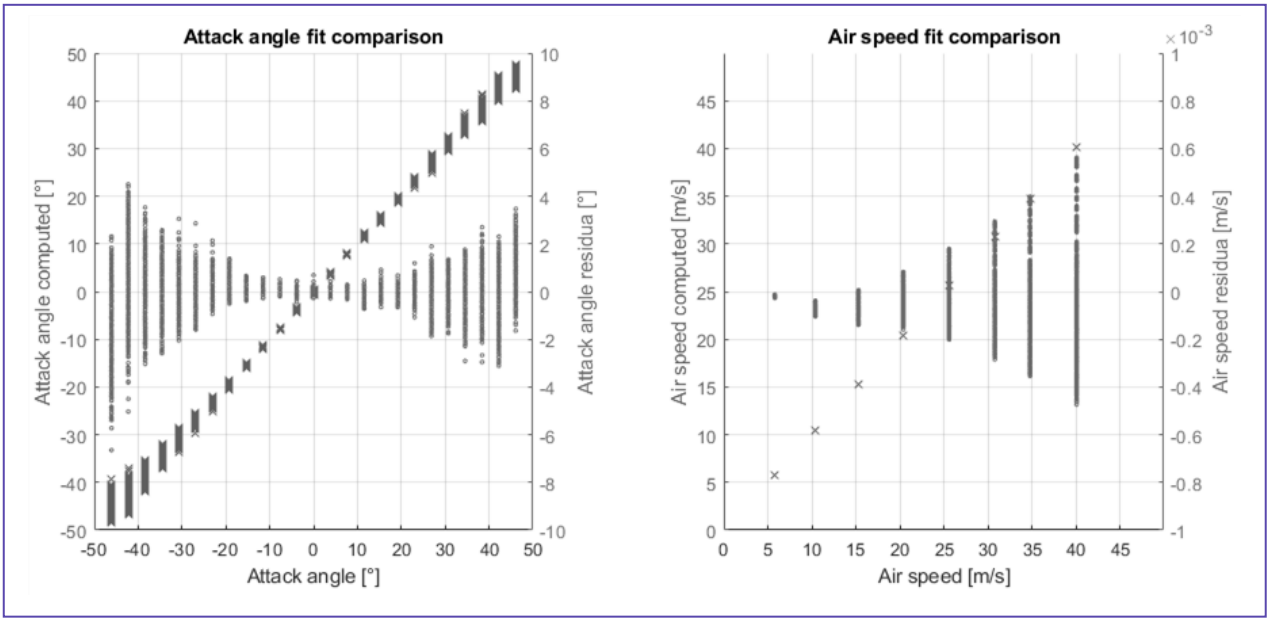

Figure 8: *Fit for non-averaged data with neural network*

3 CONCLUSION

To address air speed and AA measurement pressure probes were chosen and built for measurement of air speed and AA at full-scale vehicles. The setup of two probes was made and tested. From the measurement in the aerodynamics tunnel, the claw probe works as expected and with a change in AA *Cp* is equally changing. The Kiel probe on the other hand did not work as expected based on the literature. In a narrow window this probe is not sensitive to AA. This might be caused by a bad position of the static pressure tap. The static tap would be ideally on the surface of the wind tunnel, but in real conditions using such a tap might be impractical and can influence the measurement when not properly positioned. After measurement in the wind tunnel, the measured data are fed to neural networks, which compute air speed and AA. This regression works well and the air speed is predicted with a maximum difference of 0.0006 m/s. The AA is then predicted with a higher difference up to 7 ° for higher speeds and AA. This difference can be lowered with averaging and filtering when high data frequency measurements are not needed.

REFERENCES

[1] BARNARD, R. H. Theoretical and experimental investigation of the aerodynamic drag due to automotive cooling systems. *Proceedings of the Institution of Mechanical Engineers, Part D: Journal of Automobile Engineering*. 2000, **214**(8), 919-927. ISSN 0954-4070. Dostupné z: doi:10.1177/095440700021400810

[2] FARAJ, Ahmad, Mostafa MORTADA, Khaled CHAHINE, Jalal FARAJ, Bakri ABDULHAY a Mahmoud KHALED. Experimental Study of the Effect of Non-Uniform Airflow Velocity Distribution on the Thermal Performance of a Water-Air Heat Exchanger. *ICEREGA'19: Emerging and Renewable Energy Generation and Automation*. 2019, (19).

[3] ZHAO, Lanping, Bei WANG, Jianxin WANG et al. Effect of non-uniform airflow on the performance of a parallel-flow heat exchanger considering internal fluid distribution—Simulation studies and its experimental validation. *Applied Thermal*

Engineering. 2020, **180**. ISSN 13594311. Dostupné z: doi:10.1016/j.applthermaleng.2020.115685

[4] KIM, Nae-Hyun. Effect of inclination on thermal performance of a louver-finned aluminum heat exchanger having a drainage channel. *Journal of Mechanical Science and Technology*. 2021, **35**(1), 381-389. ISSN 1738-494X. Dostupné z: doi:10.1007/s12206-020-1238-5

[5] LISA, Henriksson, Dahl ERIK, Gullberg PETER a Lofdahl LENNART. Experimental Investigation of Heat Transfer Rates and Pressure Drops through Compact Heat Exchangers. *International Journal of Automotive Engineering*. 2015, **6**(1), 7-14. ISSN 2185-0984. Dostupné z: doi:10.20485/jsaeijae.6.1_7

[6] PITOT, Henri. Description d'une machine pour mesurer la vitesse des eaux courantes et le sillage des vaisseaux. *Histoire de l'Académie Royale des Sciences avec les mémoires de mathématique et de physique tirés des registres de cette Académie*. 1732, 363–376.

[7] GRACEY, William. *Wind-Tunnel Investigation of a Number of Total-Pressure Tubes at High Angles of Attack - Subsonic, Transonic, and Supersonic Speeds: Technical note* [online]. NATIONAL AERONAUTICS AND SPACE ADMINISTRATION HAMPTON VA LANGLEY RESEARCH CENTER, 1956, 32 s. [cit. 28.11.2023]. Dostupné z: https://apps.dtic.mil/sti/pdfs/ADA377664.pdf

[8] KIEL, G. *Total-head Meter with Small Sensitivity to Yaw* [online]. 12. Washington, 1935, , 11 s. [cit. 28.11.2023]. Dostupné z: https://ntrs.nasa.gov/api/citations/19930094642/downloads/19930094642.pdf

[9] UNITED SENSOR CORPORATION. *Kiel probes* [online]. In: . 2015 [cit. 2023-11-28]. Dostupné z: https://www.unitedsensorcorp.com/kiel.html

[10] PAKTECHPOINT. *Pitot Tube Design Requirement In Process Industry: Kiel Probe* [online]. In: PAKTECHPOINT. [cit. 2023-11-28]. Dostupné z: https://paktechpoint.com/pitot-tube-design-requirement-pitot-tube-types/

[11] RUSSEL, Walter R., William GRACEY, William LETKO a Paul G. FOURNIER. *Wind-Tunnel Investigation of Six Shielded Total-Pressure Tubes at High Angles of Attack: Subsonic Speeds* [NACA Technical Note]. NACA-TN-2530. 1951.

[12] THøGERSEN, Morten Lybech. *Modelling of the Variation of Air Density with Altitude through Pressure, Humidity and Temperature* [online]. 2005, 18 [cit. 2024-02-23]. Dostupné z: https://www.emd-international.com/files/windpro/WindPRO_AirDensity.pdf

LIST OF USED SYMBOLS AND ABBREVIATIONS

AA	Attack angle
HX	Heat exchanger
STD	Standard deviation
Cp	Pressure coefficient

ACKNOWLEDGEMENT

The authors gratefully acknowledge funding from the Specific research on BUT FSI-S-23-8235.

55. mezinárodní vědecká konference zaměřená na výzkumné a výukové metody v oblasti vozidel a jejich pohonů

září 5. - 6., 2024 – Liberec, Česká republika
Technická univerzita v Liberci
Fakulta strojní, Katedra vozidel a motorů

KONCEPT MOTOCYKLU S POHONEM VYUŽÍVAJÍCÍ FCEL

Pavel Brabec[1], Tomáš Němec[2], Robert Voženílek[3]

Abstract
The paper deals with the design of a motorcycle concept with a hydrogen fuel cell propulsion system, the installation of this fuel cell and all other necessary components into the frame of an existing JAWA motorcycle with minimal changes to the frame structure. The aim of the work was to develop a conceptual design of the layout of all selected components and the paper also includes a model calculation of the range of this concept motorcycle.

1. ÚVOD

Příspěvek se věnuje možnosti zastavění vodíkového palivového článku do rámu motocyklu s cílem vypracovat koncepční návrh rozložení všech zvolených komponent. Využití palivových článků pro motocykly je podstatně obtížnější, jelikož motocykly jsou

[1] Pavel Brabec, Technická univerzita v Liberci, Studentská 1402/2, 461 17 Liberec, pavel.brabec@tul.cz
[2] Tomáš Němec, Technická univerzita v Liberci, Studentská 1402/2, 461 17 Liberec, tomas.nemec@tul.cz
[3] Robert Voženílek, Technická univerzita v Liberci, Studentská 1402/2, 461 17 Liberec, robert.vozenilek@tul.cz

výrazně menší než automobily a autobusy. Právě v tom spočívá výrazné omezení, protože dostupné palivové články nedisponují příliš vysokým výkonem. Pravděpodobně první motocykl, který využívá k pohonu palivový článek, je motocykl navržený designeskou dvojicí Seymour&Powell. Jedná se o motocykl ENV, který je vybaven palivovým článkem od firmy Inteligent Energy, tento palivový článek je součástí sestavy, která obsahuje ještě vyrovnávací baterii, celá tato sestava je vyjímatelná z rámu motocyklu. Palivový článek, který je v tomto motocyklu použitý, má maximální výkon 1 kW a s použitou nádrží by měl schopen dodávat energii po dobu 4 hodin. Elektrický motor, použitý v tomto konceptu, je uložen v rámu motocyklu a jeho maximální výkon je 6 kW. Motocykl v tomto uspořádání dosahuje maximální rychlostí 80 km/h, a jeho dojezd měl být 160 km. Prvním jednostopým dopravním prostředkem s vodíkovým palivovým článkem, který dostal evropské schválení pro zahájení sériové výroby, byl skútr Suzuki Burgman Fuel-Cell. Tento stroj byl vyvinut ve spolupráci Suzuki s britskou firmou Inteligent Energy. Palivový vodíkový článek měl maximální výkon 2,5 kW, vodíková nádrž využívala tlaku 70 MPa s kapacitou 500 g vodíku a elektrický motor byl umístěný v zadním kole. Udávaný teoretický dojezd je 352 km. Tento dojezd byl předpokládán při průměrné rychlosti cca 35 km/h. Poprvé byl tento skútr představen v říjnu roku 2009 na Tokio Motor Show, schválení sériové výroby nastalo v roce 2011. Skútry provozovala například Londýnská policie [2]. V současné době vyvíjí firma Xiaomy motocykl Segway Apex H2, ovšem dodnes není známo mnoho parametrů k tomuto motocyklu. Dosud známé parametry motocyklu jsou: maximální rychlost 150 km/h, zrychlení z 0 na 100 km/h pod 4 sekundy, elektromotor o maximálním výkonu 60 kW [3, 4]. Nejaktuálnější projekt motocyklu na vodík představil Fraunhoferův institut, partnerem projektu je i ČVUT [11]

Figure 1: *Ukázky vodíkových motocyklů – a) ENV[5], b) Suzuki Burgman Fuel-Cell [2], c) Segway Apex H2 [3]*

2. KONCEPCE NAVRŽENÉHO MOTOCYKLU S FCEL

Následující část se věnuje popisu jednotlivých komponent, které jsou na navrhovaném motocyklu použity. Jedná se o součásti nutné pro zaručení funkčnosti pohonu konceptu. Hlavní částí motocyklu, která jej odlišuje od klasické elektrické koncepce je vodíkový palivový článek. Tato komponenta slouží jako další zdroj energie pro pohon motocyklu. Největším problémem při volbě palivového článku byly především jeho rozměry. Bylo nutné také počítat s ponecháním prostoru pro ostatní potřebné komponenty, především pro trakční baterii. Právě z tohoto důvodu byl zvolen palivový článek H-1000 XP od firmy Horison Fuel Cell Technologies, který má vzhledem k velikosti přiměřený výkon 1000 W při maximálním zatížení. Tento palivový článek je schopen dodávat maximálně 33,5 A a napětí se pohybuje v rozsahu od 25 V do 40 V, přičemž operační napětí se pohybuje od 48 V bez zatížení a 30 V při plném zatížení.

Výrobce doporučuje, aby článek pracoval právě při plném zatížení, tzn. při 33,5 A a 30 V. Při maximálním výkonu má tento palivový článek spotřebu 12,5 l/min. Základní rozměry palivového článku, které jsou velmi podstatné, především kvůli zástavbovému prostoru, jsou 104x203x264 mm. Celková teoretická energie, kterou získáme z palivového článku je 4 kWh v kombinaci s použitou nádrží na vodík. Nejdůležitější součástí sestavy komponent patřícím k palivovému článku je jeho kontroler. Tento kontroler se stará o jeho řízení, propojuje se přes něj palivový článek s trakční baterií, kterou napájí. Rozměry kontroleru bez vstupů kabeláže jsou 182x154x62 mm [6]. Další součásti jsou dva elektronicky řízené redukční ventily, jeden na vstupu a druhý na výstupu palivového článku.

Při volbě vodíkové nádrže se vyskytl obdobný problém jako u palivového článku. Tímto problémem tedy byla především velikost. Většina vodíkových nádrží je totiž založena na vysokotlaké technologii 70 MPa nebo 35 MPa, ale z důvodu rozměrů nejsou tyto nádrže vhodné, protože jsou příliš velké. Možnost, která byla zvolena pro tuto koncepci, je uložení vodíku při nízkém tlaku v tlakové nádrži s hydridy kovů v práškovém stavu, do kterých se vodík absorbuje. Tato technologie je pro naši koncepci vhodná především proto, že tato nádrž má dostatečně malé rozměry. Omezení v této technologii je ovšem rychlost uvolňování a absorpce vodíku. Byla zvolena nádrž MyH2 3000, která je schopná pojmout 3000 l vodíku, který je skladován při tlaku 1,2 MPa. Nominální kapacita nádrže je 270 g vodíku, což tedy odpovídá cca 3000 litrům vodíku za normálních podmínek. Maximální možný průtok vodíku z této nádrže je 18 l/min, což bez problémů dostačuje pro využití s palivovým článkem H-1000XP, který odebírá maximálně 12,5 l/min. Celková hmotnost této nádrže je 22 kg. Průměr lahve je 152 mm, její délka bez ventilu je 460 mm a včetně ventilu 530 mm. Tato lahev je dodávána firmou H2planet a je certifikovaná dle ISO 16111 – je tedy vhodná pro přepravování vodíku. [7, 8]

Velice důležitou součástí celé soustavy potřebné pro pohon motocyklu jsou baterie. Protože obecně palivové články „nestíhají“ dostatečně rychle reagovat na požadavky výkonu, proto jsou doplňovány vyrovnávací baterií. Ovšem v našem případě se jedná spíše o samostatnou trakční baterii, která je dobíjená palivovým článkem, ten totiž není schopný dodat dostatečný výkon pro samostatnou plnohodnotnou jízdu. Protože se k baterii bude připojovat palivový článek, je vhodné, aby trakční baterie operovala s obdobným napětím jako je výstupní napětí z palivového článku, ovšem je také nutné mít dostatečně vysoké napětí pro pohon elektromotoru. Na základě těchto dvou protichůdných požadavků bylo vybráno vyšší napětí baterie a za palivový článek se přidá DC/DC měnič. Maximální velikost boxů trakční baterie je určena především omezeným prostorem v rámu, a také není vhodné, aby boxy příliš přesahovali obrys rámu.

Výsledkem uvedených požadavků jsou dva bateriové boxy, každý s deseti bateriovými články. Celkové zapojení trakční baterie je 20s1p což znamená, že máme celkem dvacet článků zapojených sériově, tudíž v každém boxu deset článků v sérii a oba boxy jsou k sobě taktéž propojeny sériově. Rozměry bateriových boxů jsou určeny počtem umístěných článků a tloušťkou jejich stěn, boxy mají vnější rozměry včetně víka 282x196x137,5 mm. Boxy by byly vyrobeny pomocí 3D tisku a to z materiálu HiPS. Dále budou boxy vyztuženy pomocí kompozitního materiálu s uhlíkovými vlákny. Bateriové články, které byly použity, jsou články prismatické s rozměry 148x105x26 mm. Tyto články mají nominálním napětí 3,7 V a kapacitu 58 Ah. Při zvoleném zapojení 20s1p bude tedy celkové nominální napětí baterie 74 V a celková kapacita bude 58 Ah. Celkový uchovaný výkon, při použití těchto bateriových článků a zmíněného zapojení, bude při nominálním napětí 4292 Wh. Takovéto zapojení bylo

zvoleno z důvodu dosažení dostatečného napětí pro pohon použitého elektromotoru. Přičemž počet článků je určen především využitelným prostorem v rámu motocyklu. Elektromotor je v našem případě umístěn do zadního kola z prostorových důvodů. Pro koncept motocyklu byl zvolen elektromotor QS 273 50H, jedná se o stejnosměrný elektromotor bez mechanické komutace tzv. BLDC motor. Maximální výkon, který je tento elektromotor schopen dodat, je 8 kW a jeho maximální točivý moment je 330 Nm. Rychlost dosažitelná s použitím tohoto motoru se pohybuje na úrovni 120 km/h. Celková hmotnost elektromotoru je 22,5 kg.

Figure 2: *3D model konceptu motocyklu, Pohled na rozložení jednotlivých komponent hnacího ústrojí [1]*

Další důležitou součástí systému pohonu je měnič, který je nutné použít z důvodu řízení elektromotoru dle požadované charakteristiky. V našem případě se jedná o měnič Sevcon Dragon 8. Měnič je schopen operovat s nominálním napětím baterií od 48 V do 96 V, přičemž maximální operační napětí může být až 139 V a minimální operační napětí pouze 20 V. Pro zvolený koncept pohonu motocyklu se bude napětí pohybovat v optimální oblasti provozu měniče, jelikož baterie má nominální napětí 74 V. [9, 10]

Součástí konceptu je také nabíječka trakční baterie zabudovaná v motocyklu pro možnost externího nabíjení z elektrické sítě. Byla zvolena jednofázová nabíječka DCNE-Q2-3,3kW. Nabíječka je vzduchem chlazená a o toto chlazení se stará ventilátor umístěný ve středu žebrování na jejím povrchu. Celkové vnější rozměry nabíječky jsou 294x210x111 mm včetně kotvících částí. Hmotnost nabíječky je 6,5 kg. Koncept tohoto motocyklu vyobrazený na předchozím obrázku se všemi komponentami by měl mít celkovou hmotnost přibližně 150 kg, dále byla provedena i analýza změny polohy těžiště v porovnání s původní variantou využívající spalovací motor. Z analýzy vyplynulo, že nedošlo k významné změně polohy těžiště vůči původní variantě koncepce pohonu.
V původním rámu nebylo pro zastavění všech potřebných komponent dostatek místa a z tohoto důvodu bylo nutné provést dílčí úpravy. Byly provedeny tři zásadní úpravy, první v přední části rámu motocyklu, druhá v jeho středové části a třetí na spojení hlavního rámu s podsedlovou částí. Dále jsou také přidány další části, a to především pro uchycení nových komponent. Části sloužící k uchycení původního spalovacího motoru, případně jiných dílů na původním rámu, byly odstraněny z důvodu jejich nevyužití. Co se týče první zmiňované změny v přední části rámu, tak trubky bylo nutné upravit zejména proto, aby se zvětšil prostor v původní motorové části. Do tohoto prostoru se následně po úpravě umístí trakční baterie a její nabíječka. Samotná úprava trubek spočívá v tom, že se oproti původním trubkám přidá ještě jeden ohyb a trubka se tímto způsobem částečně narovná do vertikálního směru a dále se provede ohyb zpět do směru původní trubky. Ve středové části rámu byly přidány dvě kotvicí trubky. Tyto kotvící trubky slouží jako základní úchytná část rámu pro trakční baterii a palivový článek, a to je také hlavní důvod proč jsou do rámu přidány. Současně by také tyto kotvicí trubky měly zvýšit tuhost samotného rámu. Další změna rámu ve spojení hlavního a podsedlového rámu je v tom, že se odebere původní výztuha spojující pření a zadní část rámu, která je umístěná v podélné ose motocyklu. Tato výztuha se ovšem nahradí dvěma trubkami, umístěními mezi stejnými částmi rámu jako původní výztuha, ovšem ne ve středu ale po stranách. Změna byla nutná, protože výztuha v tomto místě bránila možnosti umístění vodíkové nádrže.

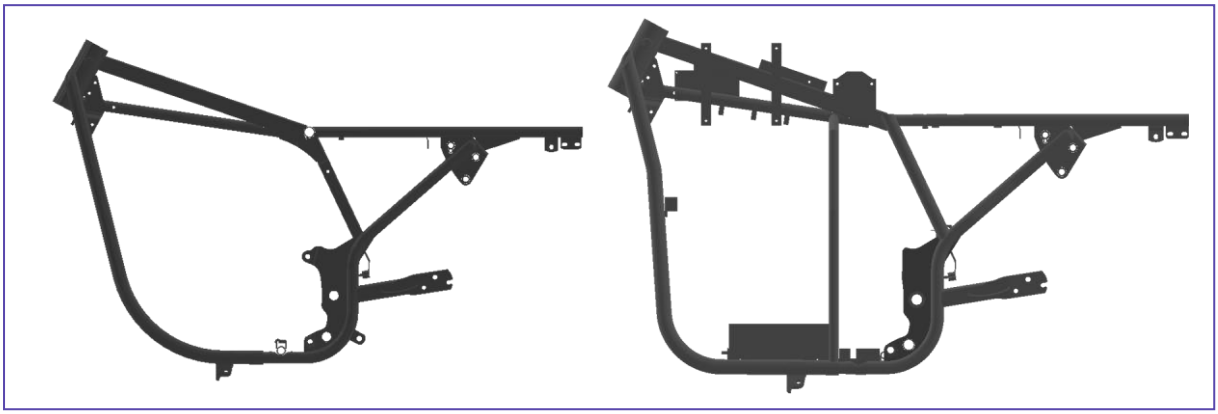

Figure 3: *Původní a nový upravený včetně všech úchytů rám motocyklu [1]*

Další důležitou částí bylo stanovení dojezdu motocyklu, výpočet byl proveden pro jízdní cykly WMTC, které jsou dnes platné pro homologaci motocyklů.
Jednalo se o výpočet, který používal několika zjednodušení, pro první odhad jsou ale výsledky dostačující. Na základě zvoleného jízdního cyklu (Class 1, 2 a 3) byl použit daný průběh rychlosti v závislosti na čase jízdy. Pro určení potřebného výkonu pro

jízdu je nutné vypočítat odporové jízdní síly, které vyvolávají požadavek výkonu. V našem případě uvažujeme odpor valení, odpor vzduchu a samozřejmě setrvačnou sílu. Zapnutí a vypnutí palivového článku bylo možno nastavit v závislosti na úrovni nabití trakční baterie. Při výpočtu byly použity dva extrémní případy, první byl předpoklad využití pouze provozních brzd pro dosažení potřebného zpomalení motocyklu. Druhým extrémem bylo využití jen rekuperace na všechna zpomalení v průběhu jízdy - čímž docházelo k nabíjení baterie a můžeme mluvit o maximálním možném dojezdu.
Při použití jízdního cyklu WMTC – Class 3, při kterém je dosaženo maximální rychlosti 125 km/h, docházelo k situaci, že palivový článek nestíhal dostatečně rychle dobíjet trakční baterii a ta se vybije dříve, než se spotřebuje všechen vodík v nádrži. Pro takto vysoké rychlosti jízdy není náš koncept vhodný, tzn. především by se mělo jednat o motocykl do města (obce), případně pro jízdu mezi obcemi. U jízdních cyklu WMTC Class 1 a 2 vyšly následující hodnoty dojezdů.

	Dojezd motocyklu s maximální rekuperací (km)	Dojezd motocyklu bez rekuperace (km)
WMTC Class 1	411	322
WMTC Class 2	302	257

Table 1: *Výsledky zjednodušeného výpočtu dojezdu motocyklu*

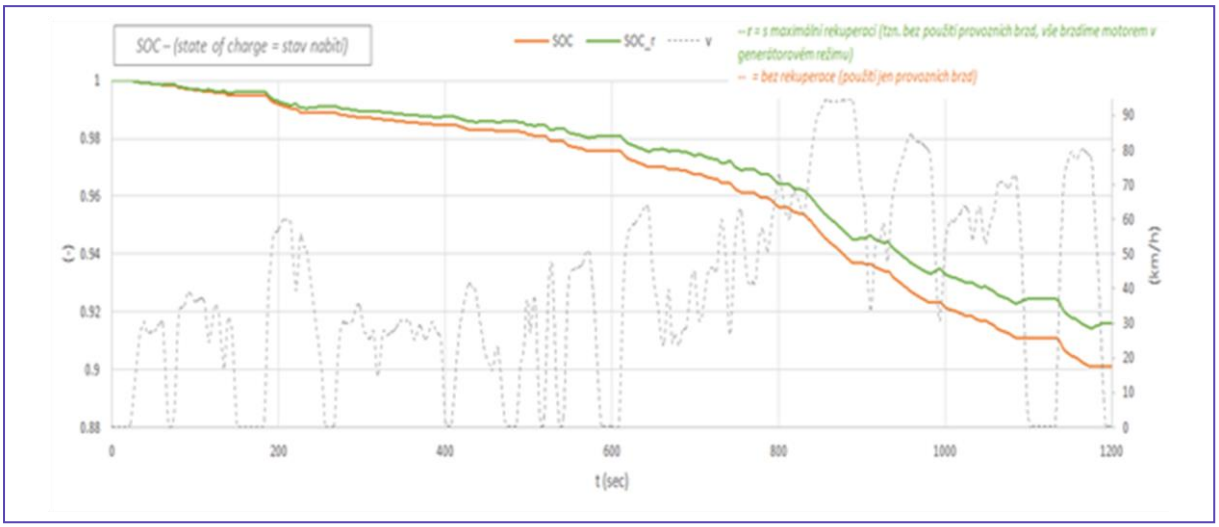

Figure 4: *Stav nabití baterie SOC po ujetí jednoho cyklu WMTC – Class 2 v závislosti na čase cyklu/jízdy*

3. ZÁVĚR / VYHODNOCENÍ

Dnes je v Evropě snaha snižovat emise (především CO_2), to se samozřejmě týká i motocyklů, které také musí splňovat zákonné předpisy. Pokud budeme porovnávat motocykly z pohledu vytvářených emisí při jízdě (tzv. analýza Tank-to-Wheel), jsou na tom samozřejmě motocykly využívající spalovací motory nejhůře, protože při spalování benzinu vznikají přímo emise, které jsou úměrné hodnotě spotřeby paliva. Pokud budeme uvažovat emise vytvářené pouze jízdou (tak jak uvažuje legislativa), jsou motocykly využívající elektrickou energii pro pohon bezemisní. Toto se týká i motocyklů s palivovými články, jako je náš koncept.

Běžný dojezd dnes prodávaných motocyklů, které využívají spalovací čtyřtaktní motor s průměrnou spotřebou benzinu cca 3 l/100km a nádrži o objemu 12 l, dosahuje úrovně okolo 400 km na jedno natankování. Dojezd elektrických motocyklů závisí především na velikosti baterie. Jako příklady pro porovnání dojezdů byly vybrány dva motocykly od výrobce Zero Motorcycles. Prvním z těchto motocyklů je typ Zero S, který má udávaný dojezd 193 km při kombinovaném provozu 50% město 50% dálnice (dálniční provoz při rychlosti 113 km/h výrobce udává dojezd 145 km a při provozu ve městě 288 km). Přičemž tyto dojezdy jsou dle testu SAE 2982 a pro velikost baterie 12,6 kWh. Druhý příklad elektrického motocyklu od stejného výrobce je typ Zero FX, který má baterii o kapacitě pouze 6,3 kWh. Dojezdy tohoto stroje jsou 146 km ve městě a 63 km na dálnici při 113 km/h, dle SAE 2982 tedy 87 km kombinovaně. Pro lepší porovnatelnost dojezdu výrobce udává v uživatelských příručkách dojezd podle evropské normy. Pro motocykl Zero FX je udávaný dojezd 104 km a pro motocykl Zero S udávají dojezd 200 km. U představeného konceptu motocyklu JAWA se zabudovaným palivovým článkem v kombinaci s elektrickým pohonem může být dosaženo dojezdu na úrovni přibližně 300 km za podmínek provozu v městském a příměstském režimu.
Pokud se budeme bavit o složitosti konstrukce, je na tom vodíkový motocykl určitě nejhůře, protože je u něj potřeba výrazně větší počet speciálních komponent. Co se týče cenovému srovnání, tak motocykly využívající vodíkové palivové články jsou jednoznačně nejdražší.

REFERENCES

[1] NĚMEC T. Koncept motocyklu s vodíkovým palivovým článkem. Diplomová práce. Technická univerzita v Liberci, 2023.

[2] Suzuki's fuel cell scooter gets mass-production approval - but should you want one?. Motorcycle News | Home of motorbike reviews, news and bikes for sale | MCN [online]. [cit. 2023-03-25]. Dostupné z: https://www.motorcyclenews.com/news/new-bikes/2011/march/mar0911-suzuki-fuel-cell-scooter-gets-mass-production-approval-/

[3] Segway Super Motorcycle Apex H2_Segway Motors Offical Global Website. Segway Motors Offical Global Website-Simply Moving! Segway Smart Electric Scooter [online]. [cit. 2023-03-25]. Dostupné z: https://motors.segway.com/product/SegwayAPEXH2

[4] Segway Apex H2: E-Motorrad mit Wasserstoffantrieb für 2023. Coolsten | Produkte, die wir lieben [online]. [cit. 2023-03-25]. Dostupné z: https://coolsten.de/segway-apex-h2-e-motorrad-wasserstoffantrieb-2023/

[5] Intelligent Energy ENV H2 Motorcycle [online]. [cit. 2023-01-24]. Dostupné z: https://www.hydrogencarsnow.com/index.php/intelligent-energy-env/

[6] H-1000XP User Manual - Uživatelská příručka H-1000XP [online]. [cit. 2023-03-25]. Dostupné z: https://www.horizoneducational.com/h-1000-xp-fuel-cell-stack/p1407

[7] Katalog produktu MyH2 3000 [online]. [cit. 2023-03-30]. Dostupné z: https://www.h2planet.eu/grk_files/catalogo/prodotti/presentazioni/MyH2_EN_S.pdf

[8] MyH2 3000. H2Planet - Re-evolution started - Hydrogen & fuel-cell experience [online]. [cit. 2023-03-25]. Do-stupné z: https://www.h2planet.eu/en/detail/MyH23000
[9] Datasheet SEVCON Dragon 8 [online]. [cit. 2023-03-25]. Dostupné z: https://electricdriveengineering.com.au/product/dragon-8/
[10] SEVCON Dragon 8 - Electric Drive Engineering. Electric Drive Engineering [online]. [cit. 2023-03-25]. Dostupné z: https://electricdriveengineering.com.au/product/dragon-8/
[11] https://www.iwu.fraunhofer.de/en/press/PM-2024-Hydrocycle-the-Motorcycle-for-the-Hydrogen-Age.html

ACKNOWLEDGEMENT

This publication was written at the Technical University of Liberec as part of the project 21588 with the support of the Specific University Research Grant, as provided by the Ministry of Education, Youth and Sports of the Czech Republic in the year 2024.

Název	KOKA 2024 55. mezinárodní vědecká konference zaměřená na výzkumné a výukové metody v oblasti vozidel a jejich pohonů
Vydavatel	Technická univerzita v Liberci Studentská 1402/2, Liberec
Schváleno	Rektorátem TUL dne 20. 8. 2024, čj. RE 35/24
Vyšlo	v srpnu 2024
Vydání	1.
ISBN	978-80-7494-711-7
Č. publikace	55-035-24